

Advanced Multi-Physics Methods for Safety Investigations of Research Reactors

Zur Erlangung des akademischen Grades eines
DOKTORS DER INGENIEURWISSENSCHAFTEN (Dr.-Ing.)

von der KIT-Fakultät für Maschinenbau des
Karlsruher Instituts für Technologie (KIT)
angenommene

DISSERTATION

von

M. Eng. / Dipl.-Eng. **Juan Carlos Almachi Nacimba**

Tag der mündlichen Prüfung: 18.12.2023

Hauptreferent: Prof. Dr.-Ing. Robert Stieglitz
Karlsruhe Institute for Technology (KIT)
Korreferent: Prof. Dr. Marat Margulis
Bangor University, United Kingdom

"In honor of my beloved father, Pablo Enrique Almachi Flores, The Original Mechanic, his inspiring spirit lives on in every page of this thesis."

"- Todo pasa mijo, todo pasa..."

11/10/2021

Acknowledgements

At this point, I would like to express my sincere gratitude to all the people who contributed significantly to the development and completion of this dissertation.

First and foremost, I would like to thank my main supervisor, Prof. Dr.-Ing. Robert Stieglitz, and Dr. Victor Hugo Sanchez Espinoza for giving me the opportunity to do my PhD at the Institute of Neutron Physics and Reactor Technology, and to benefit from the experience and knowledge of the RPD research group. Their guidance and helpful comments have undoubtedly contributed to this work. In addition, I am very grateful to Prof. Dr. Marat Margulis, whose knowledge and experience with research reactors contributed to the success of this work.

I would also like to thank Dr. Uwe Imke for his patient comments and contribution to the analysis and understanding of the thermal-hydraulic aspects of my research. Without his guidance, it would have been impossible to perform these analyses. I would also like to thank the McSAFER-2020 team, especially Diego Ferraro and Manuel Garcia, who played a key role in developing tools for high-fidelity analysis of power reactors.

I cannot fail to mention Petra Klug, Birgit Zagolla, and Ingeborg Schwartz, who provided valuable administrative and logistical support throughout the process. I also have no words to thank Dr.-Ing. Fabrizio Gabrielli and to describe what he has accomplished. In addition, I would like to thank my friends Onur, Mercan and Nuri for their constant support, encouragement and understanding during these years.

I want to thank my family: my Ito Pablo, my Mamita Elsa, my wife Jessy and my Carlitos for their love, unconditional support and for always being a source of inspiration to me.

Finally, I am grateful for the financial support from the National Secretariat of Higher Education, Science, Technology and Innovation (SENESCYT), AGREEMENT No. SENESCYT-2018-037.

Karlsruhe, February 2024

Juan Carlos Almachi Nacimba

Abstract

Advanced Multi-physics Methods for Safety Investigations of Research Reactor

The main objective of this thesis is to develop an analysis tool for plate-type research reactors capable of performing steady-state and transient calculations using a multiphysics approach between neutronics and thermal-hydraulics. Most research reactors have been licensed using legacy codes that have been developed specifically for those particular reactors. These codes are designed with low-level solutions, which means that certain limitations may exist in terms of accuracy and modeling capabilities. However, in recent years there has been a push to promote the use of more advanced codes, with more mature and highly validated architectures, which are used in power reactor analysis. While the application of these codes to research reactors allows the simulation of steady-state and transient problems, based on heuristic methods and simplifications, the results do not represent all the complexities and details of a real model. In addition, another drawback is that, in many cases, when extended or modified codes are used in research reactors, the verification and validation process is approached in a superficial manner. This implies that a thorough evaluation of the accuracy and reliability of the results obtained is not carried out. In this context, to address these new challenges, this dissertation extends and modifies the Serpent2/Subchanflow code. This state-of-the-art code, normally used for power reactor analysis, undergoes a rigorous verification and validation process using relevant experimental data obtained from reference research reactors. In this way, the quality and reliability of the results obtained in the analysis of research reactors is guaranteed.

The first step is to extend the Subchanflow thermal-hydraulic code to include a heat conduction solver for plate-type fuel elements and different correlations for predicting the heat transfer and pressure drop in narrow rectangular channels, typical for plate-type research reactors, as well as modifications to account for downward flow in addition to upward flows. This extension has been validated with experimental data relevant to the research reactors. The experimental data measured under steady-state conditions have been obtained from various technical reports of the RA-6 facility and IEA-R1 reactor.

Subsequently, the static simulation capabilities of the Monte Carlo Serpent 2 neutron code have been validated by comparison with experimental data of the thermal neutron flux measured in the SPERT IV D-12/25 reactor. In this analysis, static core parameters such as the criticality state and the control rod worth curve have been evaluated. This validation allows verifying the accuracy and reliability of the Serpent 2 code in reproducing the static nuclear characteristics of

the reactor, thus demonstrating its ability to accurately model and predict the behavior of the neutron flux under steady-state conditions.

The internal coupling of the Serpent2 and Subchanflow codes based on the master-slave approach is then established and validated using unique data. For the validation of the transient capability of the coupled Serpent2/Subchanflow code, experimental data from the SPERT IV D-12/25 reactor measured during transient control rod ejection tests are used. This work represents the first validation of the transient capability of Serpent2/Subchanflow using very detailed models of the SPERT IV core at the plate/subchannel level considering the local feedback between neutronics and thermal-hydraulics during static and transient simulations.

Then, the validated and coupled Serpent2/Subchanflow code is applied to analyze the generic IAEA 10 MW Benchmark reactor defined by the International Atomic Energy Agency, where a reactivity insertion accident scenario is assumed. The hypothetical transient scenarios encompass slow and fast reactivity insertions to the system.

The results predicted by Serpent2/Subchanflow show excellent agreement with the experimental values, considering a statistical uncertainty of ± 2 sigma. This is particularly apparent in the estimation of core power and critical plate temperature distribution. This high agreement enhances the reliability and accuracy of the code in predicting parameters that allow direct identification of the highest and lowest power plate, its location within the fuel assembly and core, as well as other safety parameters, such as the Departure from Nucleate Boiling Ratio (DNBR) and the temperature distribution at the hottest critical plate, without the need to apply correction factors for hot channel conditions. Consequently, the development of the Serpent2/Subchanflow code is positioned as a highly reliable and accurate numerical tool, enabling high-fidelity local analysis of MTR research reactors.

Kurzfassung

Fortgeschrittene Multiphysik-Methoden für Sicherheitsuntersuchungen von Forschungsreaktoren

Das Hauptziel dieser Arbeit ist die Entwicklung eines Analysewerkzeugs für plattenförmige Forschungsreaktoren, das in der Lage ist, stationäre und instationäre Berechnungen unter Verwendung eines multiphysikalischen Ansatzes zwischen Neutronik und Thermohydraulik durchzuführen. Die meisten Forschungsreaktoren wurden mit alten Codes lizenziert, die speziell für diese Reaktoren entwickelt wurden. Diese Codes wurden mit Low-Level-Lösungen entwickelt, was bedeutet, dass gewisse Einschränkungen hinsichtlich der Genauigkeit und der Modellierungsmöglichkeiten bestehen können. In den letzten Jahren wurde jedoch die Verwendung fortschrittlicherer Codes mit ausgereifteren und hochgradig validierten Architekturen gefördert, die in der Leistungsreaktoranalyse eingesetzt werden. Die Anwendung dieser Codes auf Forschungsreaktoren ermöglicht zwar die Simulation von stationären und instationären Problemen auf der Grundlage heuristischer Methoden und Vereinfachungen, doch die Ergebnisse geben nicht alle Komplexitäten und Details eines realen Modells wieder. Ein weiterer Nachteil ist, dass in vielen Fällen, wenn erweiterte oder modifizierte Codes in Forschungsreaktoren verwendet werden, der Verifizierungs- und Validierungsprozess nur oberflächlich angegangen wird. Dies bedeutet, dass eine gründliche Bewertung der Genauigkeit und Zuverlässigkeit der erzielten Ergebnisse nicht durchgeführt wird. In diesem Zusammenhang wird in dieser Dissertation der Code Serpent2/Subchanflow erweitert und modifiziert, um diesen neuen Herausforderungen zu begegnen. Dieser hochmoderne Code, der normalerweise für die Analyse von Leistungsreaktoren verwendet wird, wird einem strengen Verifizierungs- und Validierungsprozess unterzogen, bei dem relevante experimentelle Daten von Referenzforschungsreaktoren verwendet werden. Auf diese Weise wird die Qualität und Zuverlässigkeit der bei der Analyse von Forschungsreaktoren erzielten Ergebnisse gewährleistet.

Der erste Schritt besteht in der Erweiterung des thermohydraulischen Codes Subchanflow um einen Wärmeleitungslöser für plattenförmige Brennelemente und verschiedene Korrelationen zur Vorhersage des Wärmeübergangs und des Druckabfalls in engen rechteckigen Kanälen, wie sie für plattenförmige Forschungsreaktoren typisch sind, sowie um Modifikationen zur Berücksichtigung von Abwärts- und Aufwärtsströmungen. Diese Erweiterung wurde anhand von experimentellen Daten für die Forschungsreaktoren validiert. Die experimentellen Daten, die unter stationären Bedingungen gemessen wurden, stammen aus verschiedenen technischen Berichten der RA-6-Anlage und des IEA-R1-Reaktors.

Anschließend wurden die statischen Simulationsfähigkeiten des Monte-Carlo-Neutronencodes Serpent 2 durch Vergleich mit experimentellen Daten des im Reaktor SPERT IV D-12/25 gemessenen thermischen Neutronenflusses validiert. Bei dieser Analyse wurden statische Kernparameter wie der Kritikalitätszustand und die Steuerstabwertkurve bewertet. Diese Validierung ermöglicht es, die Genauigkeit und Zuverlässigkeit des Serpent 2-Codes bei der Reproduktion der statischen nuklearen Eigenschaften des Reaktors zu überprüfen und damit seine Fähigkeit zu demonstrieren, das Verhalten des Neutronenflusses unter stationären Bedingungen genau zu modellieren und vorherzusagen.

Die interne Kopplung der Codes Serpent2 und Subchanflow auf der Grundlage des Master-Slave-Ansatzes wird dann anhand einzigartiger Daten hergestellt und validiert. Für die Validierung der instationären Fähigkeit des gekoppelten Serpent2/Subchanflow-Codes werden experimentelle Daten aus dem SPERT IV D-12/25-Reaktor verwendet, die während instationärer Steuerstabauswurftests gemessen wurden. Diese Arbeit stellt die erste Validierung der Transientenfähigkeit von Serpent2/Subchanflow unter Verwendung sehr detaillierter Modelle des SPERT IV-Kerns auf Platten-/Teilkanalebene unter Berücksichtigung der lokalen Rückkopplung zwischen Neutronik und Thermohydraulik während statischer und transienter Simulationen dar.

Anschließend wird der validierte und gekoppelte Serpent2/Subchanflow-Code zur Analyse des von der Internationalen Atomenergie-Organisation (IAEO) definierten generischen 10-MW-Benchmark-Reaktors verwendet, bei dem ein Störfallszenario mit Reaktivitätseinbringung angenommen wird. Die hypothetischen transienten Szenarien umfassen langsame und schnelle Reaktivitätseinschübe in das System.

Die von Serpent2/Subchanflow vorhergesagten Ergebnisse zeigen eine ausgezeichnete Übereinstimmung mit den experimentellen Werten, wobei eine statistische Unsicherheit von ± 2 Sigma berücksichtigt wurde. Dies zeigt sich insbesondere bei der Abschätzung der Kernleistung und der Verteilung der kritischen Plattentemperatur. Diese hohe Übereinstimmung erhöht die Zuverlässigkeit und Genauigkeit des Codes bei der Vorhersage von Parametern, die eine direkte Identifizierung der Platte mit der höchsten und der niedrigsten Leistung und ihrer Position innerhalb des Brennelements und des Kerns ermöglichen, sowie von anderen Sicherheitsparametern, wie z. B. dem Departure from Nucleate Boiling Ratio (DNBR) und der Temperaturverteilung an der heißesten kritischen Platte, ohne dass Korrekturfaktoren für Heißkanalbedingungen angewendet werden müssen. Folglich ist die Entwicklung des Serpent2/Subchanflow-Codes als ein äußerst zuverlässiges und genaues numerisches Werkzeug positioniert, das eine hochgenaue lokale Analyse von MTR-Forschungsreaktoren ermöglicht.

Publications related to this thesis

As first author in peer review magazine papers

- Almachi, J., Sánchez-Espinoza, V., & Imke, U. (2021). Extension and validation of the SubChanFlow code for the thermo-hydraulic analysis of MTR cores with plate-type fuel assemblies. *Nuclear Engineering and Design*, Vol. 379, pp. 111221.
- Almachi, J., Sánchez-Espinoza, V., & Imke, U. (2022). High-Fidelity Steady-State and Transient Simulations of an MTR Research Reactor Using Serpent2/Subchanflow. *Energies*, Vol. 15(4), pp. 20.

As first author in peer review conference papers

- Almachi, J., & Sanchez-Espinoza, V. (2023). Preliminary validation of Serpent2/Subchanflow using the SPERT IV D-12/25 data. In European Research Reactor conference. Antwerp, Belgium. April 16-20. ISBN: 978-92-95064-39-3, pp. 409-419.
- Almachi, J., Sanchez-Espinoza, V., & Margulis, M. (2022). Validation of Serpent 2 using experimental data from the SPERT-IV D-12/25 Research Reactor Tests. In European Research Reactor Conference of innovative methods in reactor physics and thermal-hydraulics. Budapest, Hungary. June 6-10. ISBN: 978-92-95064-38-6, pp. 142-150.
- Almachi, J., & Sanchez-Espinoza, V. (2022). Extension of the validation basis of Subchanflow by using measured data from the IEA-R1 research reactor. In Annual Congress of the Mexican Nuclear Society, Nuclear Energy: The most efficient energy source to mitigate global warming. Veracruz, Mexico. Vol. XXXIII, pp. 1-13.
- Almachi, J., Sanchez-Espinoza, V., Imke, U. & Mercatali, L. (2021). High-fidelity analysis of MTR cores using Serpent2/Subchanflow. In European Research Reactor conference. Helsinki, Finland. September 24-29. ISBN: 978-92-95064-36-2, pp. 1-9.
- Almachi, J., Imke, U. & Sanchez-Espinoza, V. (2020). Extension of Subchanflow for thermal-hydraulic analysis of MTR-cores. In European Research Reactor conference. 100% Online. October 12-15. ISBN: 978-92-95064-34-8, pp. 72-81

Content

List of Acronyms	xvii
1 Introduction.....	1
1.1 Motivation.....	1
1.2 Description of material testing reactor with plate-type fuel	3
1.3 Main thesis objectives.....	8
1.4 Structure of the thesis and solution approach.....	8
2 Fundamentals of neutronic core analysis	9
2.1 The neutron transport equation	9
2.1.1 Time-dependent neutron transport equation	10
2.1.2 The time-dependent neutron transport equation without delay neutrons.	11
2.1.3 The steady-state neutron transport equation.....	12
2.1.4 K-Eigenvalue calculations	13
2.1.5 Power generation in a nuclear reactor	13
2.2 Deterministic methods to describe the neutron transport	14
2.3 The Monte Carlo method to describe the neutron transport	15
2.3.1 Precision and accuracy of Monte Carlo methods.....	18
2.3.2 Application of Monte Carlo methods in core analysis	19
2.3.3 Monte Carlo method for transient simulations.....	20
2.4 State-of-the-art of neutronic analysis	22
3 Fundamentals of thermal-hydraulic core analysis	25
3.1 Thermal analysis	25
3.1.1 Heat transport in the fuel, gap and cladding.....	26
3.1.2 Wall-liquid heat transfer	27
3.2 Hydraulic analysis.....	27
3.3 State-of-the-art of thermal-hydraulic analysis	29
3.4 Multiphysics approach for core analysis	30
4 Selected simulation tools.....	33
4.1 The thermal hydraulic Subchanflow code.....	33
4.1.1 Conservation equations.....	34
4.1.2 Heat conduction equation	36
4.2 The neutronic Serpent 2 code.....	37
4.3 The internal coupling of Serpent 2 and Subchanflow.....	39

4.3.1	The master-slave coupling approach.....	39
4.3.2	The thermal-hydraulic feedback exchange.....	41
4.3.3	Challenges of the coupling approach.....	43
4.4	Subchanflow limitation for the analysis of MTR-cores.....	43
5	Extension of Subchanflow for the analysis of MTR-cores.....	47
5.1	Implementation of heat conduction solver for plates.....	47
5.2	Description of the heat conduction solver.....	48
5.3	Heat transfer correlations for narrow rectangular channels.....	49
5.4	Extension to consider the effect of downward coolant flow.....	52
6	Validation of Subchanflow using the data of the RA-6 facility.....	55
6.1	Overall validation approach.....	55
6.2	Description of the RA-6 facility.....	55
6.2.1	Test section of experimental facility RA-6.....	56
6.2.2	Geometric dimensions of test section of facility RA-6.....	57
6.2.3	Material properties.....	58
6.2.4	Operating condition of RA-6 facility.....	58
6.2.5	RA-6 test conduction.....	59
6.3	Development of the Subchanflow model for the RA-6 test section.....	59
6.3.1	Assumptions for the Subchanflow model.....	59
6.3.2	Selected heat transfer and pressure drop correlations.....	60
6.4	Comparison of measured and predicted data.....	61
6.5	Final comments of Subchanflow using the RA-6 data.....	66
7	Validation of Subchanflow using the data of the IEA-R1 reactor.....	67
7.1	Description of the IEA-R1 Reactor.....	67
7.1.1	Measurement devices of IFA.....	68
7.1.2	Geometric dimensions of the IFA.....	70
7.1.3	Material properties.....	70
7.1.4	Operations conditions for tests performed at the IFA.....	70
7.1.5	IFA test conduction.....	71
7.2	Development of the Subchanflow model for the IEA-R1 test.....	72
7.2.1	Assumptions for the Subchanflow model.....	72
7.2.2	Selected flow friction pressure drops and heat transfer correlations.....	73
7.3	Comparison of measured and predicted data.....	74
7.4	Final comments of the Subchanflow validation using the IAE-R1 data.....	77
8	Validation of dynamic capability of Serpent2/Subchanflow using data of the SPERT IV reactor.....	79

8.1	Description of the SPERT IV reactor.....	79
8.1.1	Tests of the SPERT IV D-12/25 reactor	80
8.1.2	Geometric dimensions of SPERT IV D-12/25 reactor	82
8.1.3	Material properties.....	83
8.1.4	Operating condition of SPERT IV D-12/25 reactor	84
8.1.5	SPERT IV D-12/25 test conduction.....	85
8.2	Main assumptions for the SPERT IV reactor model	85
8.2.1	Subchanflow model.....	86
8.2.2	Serpent 2 model.....	86
8.2.3	Serpent2/Subchanflow model.....	87
8.3	Validation of the Serpent 2 using steady-state experimental data	87
8.3.1	Identification of the position of control rods for criticality state.....	88
8.3.2	Comparison of predicted and experimental results	88
8.4	Validation of Serpent2/Subchanflow using transient experimental data	90
8.4.1	Start-up of the SPERT IV reactor for transient tests	91
8.4.2	Transient rod movement scenarios for reactivity insertion	93
8.4.3	Comparison of global reactor parameters for test B-34	94
8.4.4	Discussion of local parameters predicted for test B-34.....	95
8.4.5	Comparison of global reactor parameters for test B-35	99
8.4.6	Discussions of local parameters predicted for test B-35	100
8.5	Final comments about the validation using the SPERT IV data.....	103
9	Analysis of reactivity insertion accidents in an MTR-core with Serpent2/Subchanflow code	105
9.1	IAEA MTR benchmark problem definition	105
9.2	Modeling of the IAEA-10 MW MTR reactor core.....	107
9.3	Definition of the fast/slow RIA transients.....	109
9.4	Convergence criteria	110
9.5	Discussion of global results for FRIA and SRIA	110
9.5.1	Global results for FRIA	110
9.5.2	Global results for SRIA	112
9.6	Discussion of local results for FRIA and SRIA.....	113
9.6.1	Local results for FRIA.....	113
9.6.2	Local results for SRIA.....	115
10	Summary and conclusions.....	119
11	Outlook.....	121
	Bibliography.....	123

Appendix A	Implementation of the conduction solver in SCF	137
Appendix B	Description of the SPERT IV reactor elements	139
B.1	Geometric details of the SPERT IV reactor components	139
B.2	Radial numbering of plates and cooling channels for SPERT-IV reactor.....	142
Appendix C	Additional data for the IAEA 10-MW reactor	143
C.1	Description of the benchmark IAEA 10 MW	143
C.2	Serpent 2 modeling results	144
C.3	Radial numbering of plates and cooling channels for IAEA 10 MW reactor	148

List of Acronyms

BOI	Beginning Of the Interval
BOL	Beginning Of Life
BWR	Boiling Water Reactors
CFA	Control Fuel Assemblie
CFD	Computational Fluid Dynamics
CPD	Cumulative Probability Distribution
CRP	Coordinated Research Project
DP	Differential Pressure
EOI	End Of the Interval
FDM	Finite Difference Method
FEM	Finite Element Method
FOM	Figure-Of-Merit
FRIA	Fast Reactivity Insertion Accident
FVM	Finite Volume Method
HEU	Highly Enriched Uranium
HFIR	High Flux Isotope Reactor, High-Flux Isotope Reactor
HPC	High-Performance Computing high-performance computing
IAEA	International Atomic Energy Agency
IAPWS	International Association for the Properties of Water and Steam
IFA	Instrumented Fuel Assembly
IFC	Interface File
IFP	Iterated Fission Probability
IPEN	Nuclear and Energy Research Institute
KIT	Karlsruhe Institute of Technology
LEU	Low Enriched Uranium
LOFA	Loss Of Flow Accidents
MC	Monte Carlo
MOC	Method Of Characteristics
MRR	Multipurpose Nuclear Research Reactor
MTR	Material Testing Reactor, Materials Test Reactor
NAA	Neutron Activation Analysis
NDL	Nuclear Data Libraries
PDF	Probability Density Function
PT100	Resistance temperature detectors

PWR	Pressurized Water Reactors
RAM	Random Access Memory
RIA	Reactivity Initiated Accident
RMSE	Root Mean Square Error
SCF	Subchanflow
SFA	Standard Fuel Assembly
SPERT	Special Power Excursion Reactor
SRIA	Slow Reactivity Insertion Accident
SSS2/SCF	Coupled version of Serpent 2 and Subchanflow
TC	Temperature of the Cladding
TF	Temperature of the Fluid
TFA	Transient Fuel Assembly
TMS	Target Motion Sampling
TR	Transient Rod
VVER	Water-to-Water Energy Reactors

1 Introduction

1.1 Motivation

Many research reactors are under operation worldwide and acts as centers of innovation and productivity for the development of nuclear science and technology for more than 60 years. Research conducted with these types of reactors is mostly related to various fields such as particle and nuclear physics, radiochemistry, nuclear medicine, materials characterization and testing, radioisotope production, computer code validation, or nuclear science and technology education programs (IAEA, 2014).

Currently, a total of 841 research reactors have been built in 70 countries, of which 223 are operating, 79 are about to close, and 24 are under construction or in planning, e.g., the Dutch government's PALLAS reactor and the Bolivian government's CIDTN reactor (see Figure 1.1), (IAEA, 2022), (Doval, et al., 2022), (Nogarin, 2016). Most of these reactors are more than 40 years old, and many of them must meet current technological standards and safety requirements in order to renew their operating licenses (Zuccaro-Labelarte and Fagerholm, 1996), (Schaaf, et al., 2011), (Doval, et al., 2022).



Figure 1.1: Number of research reactors per country, obtained from (IAEA, 2022).

Some research reactors, classified as multipurpose ones, are also used for testing of materials and fuels for nuclear power plants. This type of research ensures the continued operation, life extension, and safety of power plants (IAEA, 2019). Because these types of reactors are fundamental to advances in nuclear research and technology, improvements in their design, performance, and safety are essential. To meet these new challenges, the development of computer codes to simulate normal and off normal operating conditions of a research reactor are primordial for safety evaluations and design optimization. For thermal-hydraulic and neutronic analysis of

research reactors, dedicated codes or adapted power reactor codes are commonly used. Codes dedicated to research reactors are developed specifically for a particular reactor, which complicates its application to other research reactors (Doval A. , 1998), (Gaheen and Abdelaziz, 2019), (Castellanos-Gonzalez, et al., 2018). This issue has significantly slowed the development of these types of codes compared to codes used for power reactors, which typically have more general applications. In addition, many of these codes use low-level solvers, such as the use of lumped parameter approaches for plate heat transfer resolution or diffusion methods for neutron analysis. These simplified approaches allow faster and more efficient analysis, but are not as accurate, leading to certain limitations compared to more sophisticated methods (Ferraro, et al., 2020).

On the other hand, the codes used in power reactors have achieved a high level of development and reliability due to their extensive verification and validation process (IAEA, 2002). However, when applying these codes to the analysis of research reactors, it is often necessary to resort to heuristic methods and geometric approximations because power reactors and research reactors differ in their design and characteristics (Soares, et al., 2014), (Hainoun and Schaffrath, 2001), (Bousbia-Salah and Hamidouche, 2005). Although these simplifying assumptions have enabled steady-state and transient simulations to be performed to some extent, the verification and validation processes specific to research reactors have not yet been fully addressed. Therefore, rigorous verification and validation based on experimental data from formalized reference reactors is essential. This practice ensures the reliability and accuracy of the results obtained, thus increasing confidence in the use of these codes for research reactor analysis and design (IAEA, 2008).

Between 2008 and 2013, the International Atomic Energy Agency (IAEA) carried out a Coordinated Research Project (CRP) aimed at promoting the development of innovative methods for analyzing research reactors (IAEA, 2019). Under this project, eight research reactors of different design, power and applications have been selected as references to validate and verify codes. The IAEA shared the results obtained with the scientific community (IAEA, 2015). The report resulting from this project is intended to extend the use of codes used in power reactors to their application in research reactors. Deterministic and Monte Carlo codes have been used for neutron physics analyzes, as have system codes for thermal-hydraulic analysis. Most of the codes used for thermal-hydraulic analysis are based on the "best estimate" technique, and there is no evidence of the use of high-fidelity codes (IAEA, 2019), (IAEA, 2015), (Adorni, et al., 2007).

High-fidelity codes focus on a finer level of spatial and temporal detail and a more accurate representation of phenomena in nuclear reactors. These codes typically use advanced numerical methods, such as solving the Navier-Stokes equations and Monte Carlo simulations, to more accurately model the flow behavior, heat transfer, and neutron physics in reactors. The high-fidelity approach is based on a conventional coupling architecture between the equations

governing the behavior of neutrons and thermal-hydraulic parts of a system. This architecture allows detailed pin-to-pin and channel-to-channel analyzes at significant computational cost, requiring the use of high-performance computing (HPC) resources to perform such simulations (Ferraro, 2021), (Daeubler, et al., 2015), (Garcia, 2021).

At the Karlsruhe Institute of Technology (KIT), various coupled high-fidelity codes have been developed and validated for pressurized water reactors (PWR), boiling water reactors (BWR), and water-to-water power reactors (VVER). One such coupling approach between the thermal-hydraulic subchannel code Subchanflow (SCF) and the Monte Carlo code Serpent 2 is the internal master-slave interface, which has the unique ability to predict core behavior under transient conditions, i.e., rod ejection accidents (Ferraro, 2021). This dissertation addresses the use of Serpent2/Subchanflow tools for high-fidelity analysis of research reactors. Especially focusing on the study of fuel assemblies formed by plate-type fuel at the plate/subchannel level. The extensions and modifications made to the codes undergo exhaustive verification and validation to strengthen the basis of codes used in this field and to promote significant advances in research reactor design and analysis.

1.2 Description of material testing reactor with plate-type fuel

In the 1940s, work began on the design of a reactor that would provide a test environment with high thermal and fast neutron fluxes. The design evolved into a research reactor called a materials test reactor (MTR), which typically uses thin plates of nuclear fuel instead of the cylindrical fuel rods used in most power reactors (Russell, et al., 1956). An overall schematic of a typical MTR research reactor facility loaded with fuel plates is shown in Figure 1.2.

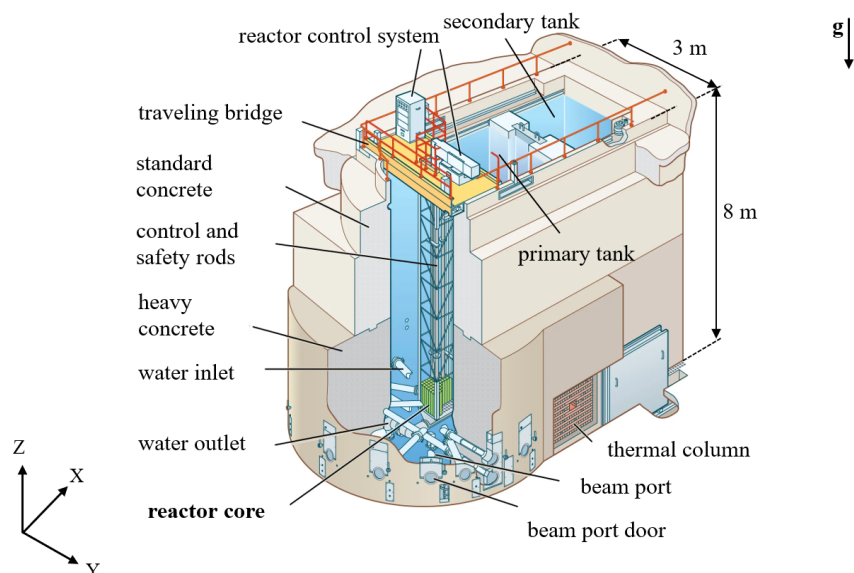


Figure 1.2: Typical 3-D presentation of a research reactor facility obtained from (Britannica, 1999).

These facilities contain two tanks filled with water, the reactor core housed in the lower part of the main tank. Tank dimensions range from 3 m to 6 m wide and 8 m to 20 m high. The main tank is equipped with a nozzle through which the coolant flows downward or upward. The control system for the poisoned rods is located on a bridge at the top of the tanks and they can move freely to the secondary tank (Russell, et al., 1956). Figure 1.3 shows a detailed view of the lower part of the INVAP RA-10 multipurpose reactor facilities, where horizontal and vertical piping can be seen around the core used to perform the various neutron beam or irradiation tests (Sánchez, et al., 2014).

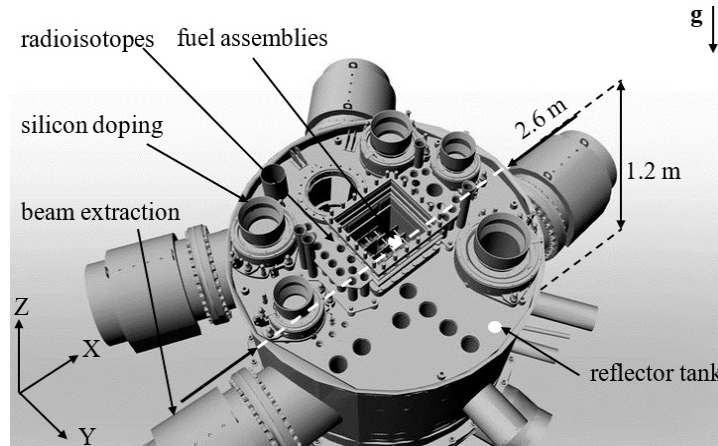


Figure 1.3: Schematic representation of the multipurpose reactor RA-10 obtained from (CNEA, 2017).

Figure 1.4 shows a 3D representation of the MTR reactor core, showing the fuel assemblies, the grid in which they are housed, and the fuel plates. The plates are made of enriched fuel material, usually uranium or plutonium, encapsulated in a matrix of aluminum or zirconium alloys. The plates are usually stacked in groups of 6 to 23 in a rectangular aluminum housing and form standard and control fuel assemblies. Control fuel assemblies consist of a smaller number of plates that provide space for the neutron poison material (B4C, AgInCd or Hf).

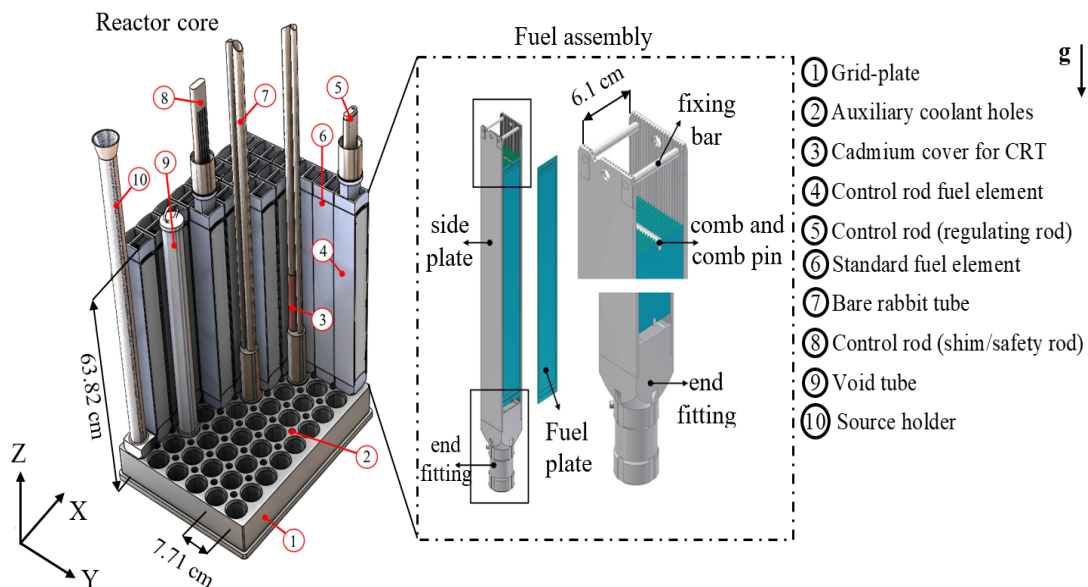


Figure 1.4: Grid with standard fuel elements, artwork extracted from (Bugis, 2020), (Kim, et al., 2014).

The geometrical characteristics of the fuel assemblies are determined by the configuration of the fuel plate. The fuel plate can take various shapes, such as rectangular thin plates, curved thin plates, and plates composed of layers of fuel-clad sandwich shells. When fuel assemblies are loaded with rectangular thin plates, the shape and dimensions of the resulting reactor core resemble the shape shown in Figure 1.4 and Figure 1.7. Research reactors loaded with curved thin plates are often compact in design and are used for isotope production and testing. An example of this type is the high-flux isotope reactor (HFIR) shown in Figure 1.5, which operates at a nominal power of 85 MW in Oak Ridge National Lab (Primm, et al., 2008).

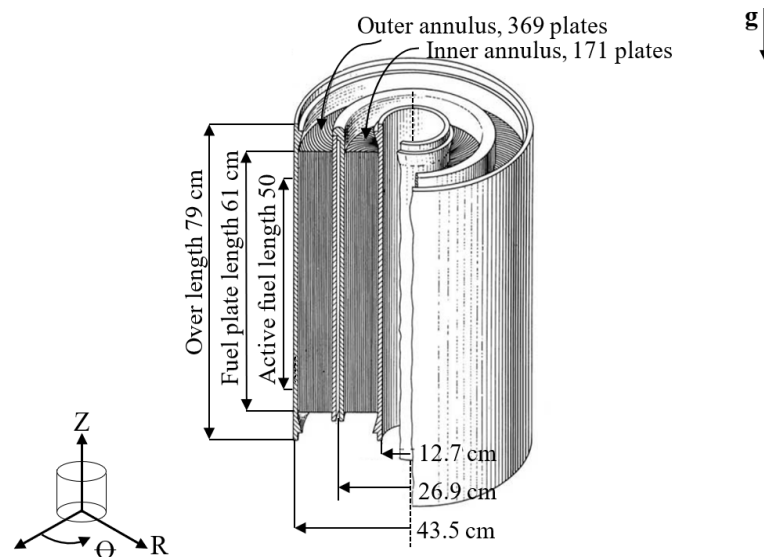
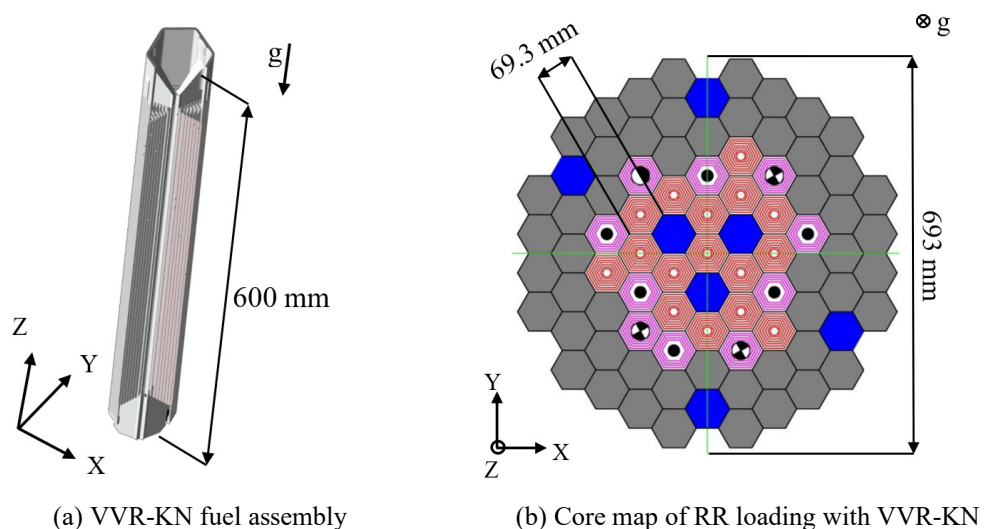


Figure 1.5: Schematic of HFIR reactor loaded with curved plates obtained from (Primm, et al., 2008).

When using fuel assemblies loaded with sandwich shells (aluminum-fuel-aluminum), as shown in Figure 1.6, rectangular and hexagonal fuel assemblies are obtained, which have some advantages, such as higher fuel density, homogeneous temperature distribution, improved cooling capacity, and less possibility of deformation due to structural rigidity. This type of fuel assemblies is used in the LVR-15 reactor and in the redesign of the MPRR reactor with VVR-KN fuel assemblies.



(a) VVR-KN fuel assembly

(b) Core map of RR loading with VVR-KN

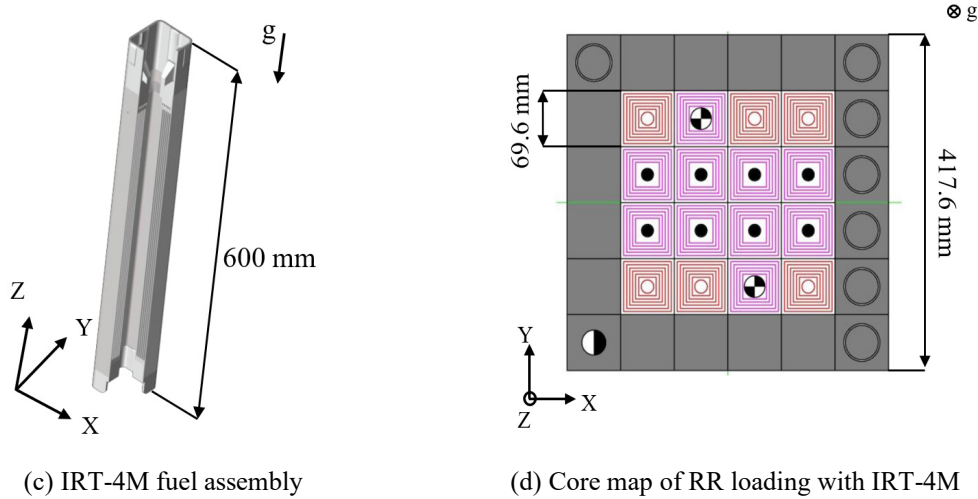


Figure 1.6: Different fuel assemblies and core configurations of the research reactors (RR), obtained from (Nhi-Dien, et al., 2020), (Osipovich, et al., 2011).

For research reactors, there is no predetermined standardization in terms of fuel element dimensions, reactor power, operating pressure, and temperatures reached. These parameters depend on the scope and objectives of the particular research project. However, it is possible to obtain information on the main fuel assembly dimensions in the various technical reports (IAEA, 1980). Figure 1.7 shows the main dimensions of a fuel assembly consisting of 18 plates for the IEA-R1 reactor. Specific data on the distance between the plates d forming the cooling channels, the height of the plates h , the width of the plates w , the width of the channel W and the thickness of the plates e can be seen in Table 1-1 (Doval A. , 1998), (Sudo, et al., 1990).

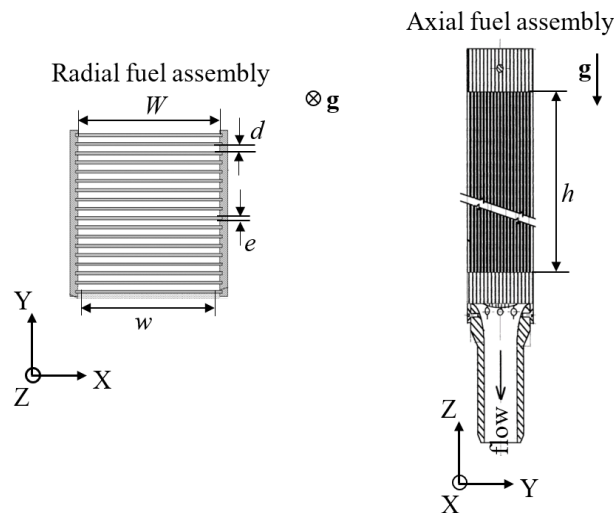


Figure 1.7: Radial and axial representation of the standard fuel assembly, obtained from (Castellanos-Gonzalez, et al., 2018), (Umbehaun, 2016)

Table 1-1: Main geometrical data of the plate and channel of a research reactor.

Geometric data	Registered dimensions
Coolant channel width (W)	range 38.0 - 71.0 [mm]
Coolant channel thickness (d)	range 1 - 50 [mm]
Fuel plate width (w)	range 35.0 - 69.0 [mm]
Total plate length (h)	range 600 - 1180 [mm]
Number of fuel plates per assembly	about 6 – 23
Thickness of the plate (e)	does not exceed 3 [mm]

The main boundary conditions for the analysis and design of research reactors are summarized in Table 1-2.

Table 1-2: Main boundary conditions for the analysis and design research reactors.

Parameters	Values registered
Coolant inlet temperature	range 17 - 70 [°C]
Pressure at channel exit	range 0.1566 – 0.186 [MPa]
Coolant	water or air
Coolant velocity	range 0 - 6 [m/s]
Flow direction	upward or downward
Power distribution	cosine shape or uniform

Several companies are currently engaged in the design and construction of research reactors with fuel plates for applications such as neutron activation analysis (NAA), neutron transmutation doping (NTD), radioisotope production, and neutron beam research (including cold neutron beams) (Villarino and Doval, 2011), (INVAP, 2023). Table 1-3 shows the classification of research reactors according to their criticality status and application. It should be noted that research reactors are cooled by natural or forced convection. If the reactor is operated by forced convection, downward or upward cooling is usually used; upward cooling is typical for reactors with power greater than 10 MW to avoid the phenomenon of backflow, such as at SPERT IV or RA-10, while downward cooling is used for reactors with lower power, such as at RA-6 or IEA-R1 (Silin, et al., 2009), (IAEA, 2015), (Umbehaun, 2016). More complex MTR research reactors, whose design exceeds 100 MW, are currently in greater demand because of the enormous need to test fuels for the next generation of power plants. Their design is similar to that of the OPAL reactor with the difference that the core is slightly pressurized (Villarino and Doval, 2011).

Table 1-3: Comparison of the uses of research reactors by criticality status, adapted from (Villarino and Doval, 2011).

Facility	Power	Experimental capability	Utilization
Sub-critical	0	Flexible	Training and education program
Zero power	< 1 W	Flexible	Training and education program and nuclear measures
Low power	< 100 kW	Flexible	NAA, low-scale radioisotope production
Medium power	< 10 MW	Flexible/production facility	NAA, NTD, several radioisotope productions, beams
High power	≥ 10 MW	Production facility	NAA, NTD, several radioisotope productions, high performance beams, material irradiation, loops

The aforementioned characteristics pose a huge challenge for the development of state-of-the-art codes. The codes developed by the various institutes are often useful only for their own configuration, so it is a priority to have a tool that allows a coupled neutron thermal-hydraulic analysis not only of a specific reactor but also of several reactors. The code developed must be flexible, accurate, reliable, and adaptable to multiple reactors. This technical challenge is addressed in the following chapters.

1.3 Main thesis objectives

The general objective of this work is to develop an analysis tool for plate-type fueled research reactors capable of performing steady-state and transient calculations using a combination of neutron Monte Carlo analysis and subchannel thermal hydraulic analysis. The development phase of this tool consists of extension, modification and validation phases, so the specific objectives of this work can be summarized as follows:

1. Extension of the thermal-hydraulic code for the analysis of plate-type research reactors with a plate-by-plate and channel-by-channel resolution focus on heat transfer, pressure drop, heat conduction solver, and downward flow.
2. Validation of the thermal-hydraulic subchannel code using experimental data obtained in dedicated tests (RA-6) and in a research reactor (IEA-R1).
3. Validation of the prediction capability of Serpent 2 to predict static reactor parameters using the unique data of the SPERT IV D-12/25 test.
4. Validation of the Serpent2/Subchanflow capability to predict transients using the unique data of the RIA-tests at the SPERT IV D-12/25 tests.
5. Application of the extended and validated couple code Serpent2/Subchanflow to analyze an MTR-core loaded with plate-type fuel under transient conditions typical of slow and fast reactivity insertions accidents.

1.4 Structure of the thesis and solution approach

This thesis consists of 11 chapters. In Chapters 2 and 3, the basic principles of the neutron transport and thermal-hydraulic equations are briefly explained. In Chapter 4, the computational tools used for the analysis of the research reactors are selected, and the limitations of the thermal-hydraulic code are demonstrated through a case study. Chapter 5 summarizes and discusses the extension of the thermal-hydraulic code, a description of the heat conduction solver for thin plates, and special heat transfer correlations relevant to research reactors. Chapters 6 and 7 begin the validation of the thermal-hydraulic code using relevant experimental data from the RA-6 device and the IEA-R1 reactor. In Chapter 8, the dynamic capabilities of the coupled neutron and thermal-hydraulic codes are validated using experimental data from the MTR SPERT IV D-12/25 reactor. In Chapter 9, the new extended and validated code is applied to a reference reactor defined by IAEA for reactivity insertion accident analysis. Finally, Chapter 10 and 11 contains the main summary and conclusions of this study and the main outlooks.

2 Fundamentals of neutronic core analysis

This section introduces the basic physics concepts of neutronics used to understand the behavior of a nuclear reactor. First, the basic neutron transport equations are described and how the Monte Carlo method is used to solve them is explained.

Neutron physics in nuclear engineering is a key expertise in the design, construction, operation, and optimization of nuclear reactors (Duderstadt and Hamilton, 1976). Its study is used to:

- Model and predict the motion of neutrons and their interaction with the nuclei of moderation and control materials such as fuel, coolant, and reactor structural materials.
- Determine the distribution and energy spectrum of neutrons in the reactor and thus the generation of fission power and the evolution of fuel during burnup.
- Optimizing, evaluating, and ensuring that the different types of materials used in the construction of the reactor allow its maximum performance.

In summary, neutron physics allows modeling the behavior of a neutron population in the core in terms of its spatial, angular, energetic, and temporal dependence.

2.1 The neutron transport equation

One of the central problems in the design and analysis of various nuclear reactors is the calculation of the neutron distribution throughout the reactor. The study of the neutron population allows conclusions to be drawn about the stability and operation of the reactor during fission chain. To determine the neutron distribution in the reactor, the neutron transport process, which describes how neutrons propagate within a multiplying system, must be studied (Duderstadt and Hamilton, 1976), (Prinja and Larsen, 2010).

To study neutron transport, basic physical parameters such as neutron streaming, neutron scattering, and neutron capture by nuclei, as well as the initiation of new neutron fission events as a result of the splitting of a nucleus, must be quantified (Duderstadt and Hamilton, 1976). Figure 2.1 is used to characterize the three-dimensional neutron transport process, which is composed of independent variables that specify the population of neutrons at an arbitrary position \vec{r} moving in an arbitrary direction $\hat{\Omega}$ with an energy E at an arbitrary time t .

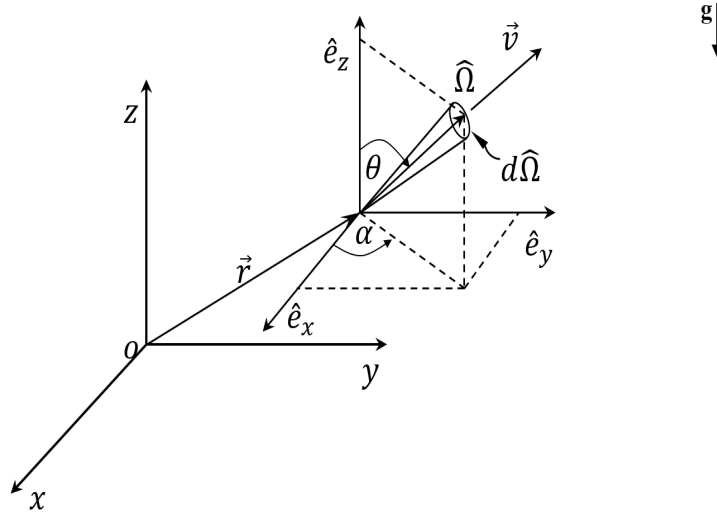


Figure 2.1: Three-dimensional space-angle coordinate system for characterizing neutron distribution.

The equations describing the neutron distribution in the nuclear reactor core result from an equilibrium between neutron production and neutron losses in a system; a detailed explanation of the derivation of the neutron transport equations with their various special features can be found in the literature (Duderstadt and Hamilton, 1976), (Bell and Glasstone, 1970), (Prinja and Larsen, 2010).

2.1.1 Time-dependent neutron transport equation

To understand the time-dependent reactor behavior, it is essential to obtain an equation describing the gain and loss of neutrons in each spacetime increment. The time-dependent neutron transport equation describing the above physical process is also known as the Boltzmann equation. In this equation, the delayed neutron precursors are considered, resulting in the following first-order integro-differential equation (Duderstadt and Hamilton, 1976), (Lewis and Miller, 1984), (Prinja and Larsen, 2010):

$$\begin{aligned}
 & \left(\frac{1}{v} \frac{\partial}{\partial t} + \hat{\Omega} \cdot \nabla + \Sigma_t(E) \right) \varphi(\vec{r}, E, \hat{\Omega}, t) \\
 &= \int_0^\infty \int_{4\pi} \Sigma_s(E' \rightarrow E, \hat{\Omega}' \cdot \hat{\Omega}) \varphi(\vec{r}, E', \hat{\Omega}', t) d\hat{\Omega}' dE' \\
 &+ \frac{\chi_p(E)}{4\pi} \int_0^\infty \int_{4\pi} [1 - \beta(E')] v_p(E') \Sigma_f(E') \varphi(\vec{r}, E', \hat{\Omega}', t) d\hat{\Omega}' dE' \\
 &+ \frac{1}{4\pi} \sum_{j=1}^N \chi_j(E) \lambda_j C_j(\vec{r}, t) + \frac{1}{4\pi} Q(\vec{r}, E, t);
 \end{aligned} \tag{2.1}$$

where

t = time,

\vec{r} = Position,

v = neutron velocity,

- φ = angular neutron flux,
 β = total delayed neutron fraction,
 $\hat{\Omega}$ = unit vector in direction of motion,
 E = energy,
 Q = internal neutron source,
 N = number of delayed neutrons precursors,
 ν_p = the average neutrons release per fission,
 χ_j = delayed neutron fission spectrum,
 Σ_t = total macroscopic cross section,
 λ_j = radioactive decay constant,
 χ_p = prompt fission spectrum,
 C_j = total number of precursors,
 Σ_f = macroscopic fission cross section,
 Σ_s = scattering cross section.

Additionally, the evolution of each precursor density is given by:

$$\left(\frac{\partial}{\partial t} + \lambda_j\right) C_j(\vec{r}, t) = \int_0^\infty \int_{4\pi} \beta_j(E') \nu_p(E') \Sigma_f(E') \varphi(\vec{r}, E', \hat{\Omega}', t) d\hat{\Omega}' dE'; \quad (2.2)$$

where

β_j = delayed neutron fraction for the precursor group j .

Eqs. (2.1) and (2.2) must be solved under the following boundary conditions:

$$\varphi(\vec{r}, E, \hat{\Omega}, t) = \varphi^b(\vec{r}, E, \hat{\Omega}, t), \quad \hat{\Omega} \cdot \hat{n} < 0, \quad 0 < E < \infty, \quad 0 < t, \quad (2.3)$$

and, the neutron angular flux φ and the precursor density C_j must satisfy the initial conditions:

$$\varphi(\vec{r}, E, \hat{\Omega}, 0) = \varphi^i(\vec{r}, E, \hat{\Omega}), \quad \hat{\Omega} \in 4\pi, \quad 0 < E < \infty, \quad (2.4)$$

$$C_j(\vec{r}, 0) = C_j^i(\vec{r}), \quad (2.5)$$

where φ^b , φ^i and C_j^i need to be specified.

2.1.2 The time-dependent neutron transport equation without delay neutrons

The time-dependent neutron transport equation without considering the delayed neutrons can be used to solve some problems where it is necessary to reduce the computational time of the calculation ($\beta \approx 0.01$), see (Prinja and Larsen, 2010). Since the total fraction of delayed neutrons is considered negligible, the terms β_j and C_j in Eq (2.1) can be eliminated. With these assumptions, the following expression is obtained

$$\begin{aligned}
& \left(\frac{1}{v} \frac{\partial}{\partial t} + \hat{\Omega} \cdot \nabla + \Sigma_t(E) \right) \varphi(\vec{r}, E, \hat{\Omega}, t) \\
&= \int_0^\infty \int_{4\pi} \Sigma_s(E' \rightarrow E, \hat{\Omega}' \cdot \hat{\Omega}) \varphi(\vec{r}, E', \hat{\Omega}', t) d\hat{\Omega}' dE' \\
&+ \frac{\chi_p(E)}{4\pi} \int_0^\infty \int_{4\pi} \nu_p(E') \Sigma_f(E') \varphi(\vec{r}, E', \hat{\Omega}', t) d\hat{\Omega}' dE' + \frac{1}{4\pi} Q(\vec{r}, E, t);
\end{aligned} \tag{2.6}$$

where the boundary conditions and initial conditions are presented in the following Eqs. (2.7) and (2.8)

$$\varphi(\vec{r}, E, \hat{\Omega}, t) = \varphi^b(\vec{r}, E, \hat{\Omega}, t), \quad \hat{\Omega} \cdot \hat{n} < 0, \quad 0 < E < \infty, \quad 0 < t, \tag{2.7}$$

$$\varphi(\vec{r}, E, \hat{\Omega}, 0) = \varphi^i(\vec{r}, E, \hat{\Omega}), \quad \hat{\Omega} \in 4\pi, \quad 0 < E < \infty. \tag{2.8}$$

2.1.3 The steady-state neutron transport equation

Several neutron analyses required for reactor licensing are performed when the reactor reaches steady-state, so it is very important to determine the neutron transport equation that describes this physical problem. To obtain this equation, first of all, the term describing the time evolution of the precursor density ($\partial C_j / \partial t = 0$) in Eq. (2.2) must be omitted, yielding the expression

$$\lambda_j C_j(\vec{r}) = \int_0^\infty \int_{4\pi} \beta_j(E') \nu_p(E') \Sigma_f(E') \varphi(\vec{r}, E', \hat{\Omega}') d\hat{\Omega}' dE'. \tag{2.9}$$

Then, the Eq. (2.9) is introduced in a modification of Eq. (2.1). The resulting equation does not include the derivatives and the time dependence of the neutron angular flux

$$\begin{aligned}
& (\hat{\Omega} \cdot \nabla + \Sigma_t(E)) \varphi(\vec{r}, E, \hat{\Omega}) \\
&= \int_0^\infty \int_{4\pi} \Sigma_s(E' \rightarrow E, \hat{\Omega}' \cdot \hat{\Omega}) \varphi(\vec{r}, E', \hat{\Omega}') d\hat{\Omega}' dE' \\
&+ \frac{\chi_p(E)}{4\pi} \int_0^\infty \int_{4\pi} [1 - \beta(E')] \nu_p(E') \Sigma_f(E') \varphi(\vec{r}, E', \hat{\Omega}') d\hat{\Omega}' dE' \\
&+ \frac{1}{4\pi} \sum_{j=1}^N \lambda_j \int_0^\infty \int_{4\pi} \beta_j(E') \nu_p(E') \Sigma_f(E') \varphi(\vec{r}, E', \hat{\Omega}') d\hat{\Omega}' dE' \\
&+ \frac{1}{4\pi} Q(\vec{r}, E).
\end{aligned} \tag{2.10}$$

Eq. (2.10) is subject to steady-state boundary conditions:

$$\varphi(\vec{r}, E, \hat{\Omega}, t) = \varphi^b(\vec{r}, E, \hat{\Omega}), \quad \vec{r} \in \partial V, \quad \hat{\Omega} \cdot \hat{n} < 0, \quad 0 < E < \infty, \tag{2.11}$$

if the term flux $\varphi^b = 0$, then ∂V is known as a vacuum boundary (Duderstadt and Hamilton, 1976), (Lewis and Miller, 1984), (Prinja and Larsen, 2010).

2.1.4 K-Eigenvalue calculations

Eigenvalue calculations are directly related to the calculation of criticality of nuclear reactors. One speaks of eigenvalue calculations when the steady-state neutron transport equation is converted into an eigenvalue equation in which the neutron source depends on the neutron flux itself. Eq. (2.12) introduces the multiplication factor $1/k$ into fission source of Eq. (2.10) as the source Q and the boundary source φ^b have zero value; this may be omitted, if there is a fixed external source and the system itself is subcritical. The multiplication factor, k , is a global value that allows inferring what type of reaction exists inside the reactor. When a value of k is equal to 1 it is said that the reactor is in a critical state with a stable chain reaction. On the other hand, if the multiplication factor, k , is greater than 1, e.g., $k = 1.0001$, this indicates a supercritical state. In the supercritical state excess neutrons due to fission are present, this state is mostly avoided in the power reactors normal operation. Finally, when the multiplication factor is less than 1 it indicates a neutron defect caused by fission causing a subcritical state (Duderstadt and Hamilton, 1976), (Lewis and Miller, 1984), (Prinja and Larsen, 2010).

$$\begin{aligned}
 & \left(\hat{\Omega} \cdot \nabla + \Sigma_t(E) \right) \varphi(\vec{r}, E, \hat{\Omega}) \\
 &= \int_0^\infty \int_{4\pi} \Sigma_s(E' \rightarrow E, \hat{\Omega}' \cdot \hat{\Omega}) \varphi(\vec{r}, E', \hat{\Omega}') d\hat{\Omega}' dE' \\
 &+ \frac{\chi_p(E)}{4\pi k} \int_0^\infty \int_{4\pi} [1 - \beta(E')] v_p(E') \Sigma_f(E') \varphi(\vec{r}, E', \hat{\Omega}') d\hat{\Omega}' dE' \\
 &+ \frac{1}{4\pi} \sum_{j=1}^N \chi_j(E) \int_0^\infty \int_{4\pi} \beta_j(E') v_p(E') \Sigma_f(E') \varphi(\vec{r}, E', \hat{\Omega}') d\hat{\Omega}' dE', \\
 &\varphi(\vec{r}, E, \hat{\Omega}, t) = 0, \quad \vec{r} \in \partial V, \quad \hat{\Omega} \cdot \hat{n} < 0, \quad 0 < E < \infty
 \end{aligned} \tag{2.12}$$

Because the values of the multiplication factor, k , are very low, it is usually used as part of the calculation of reactor reactivity ρ . Reactivity can be expressed in per-cent-mille ($\rho [pcm] = \frac{(k-1)}{k}$), or dollars, ($\rho [\$] = \frac{(k-1)}{k\beta}$), depending on the analysis. The criteria of $\rho < 0$, $\rho = 1$, $\rho > 1$ can be understood as subcritical, critical, supercritical respectively.

2.1.5 Power generation in a nuclear reactor

The energy released in a nuclear fission reaction takes place in the fuel pellets or plates from there it is transferred to the cladding and finally to the coolant. Hence, it is important to understand the thermal-hydraulic behavior of the core under normal operating conditions and under hypothetical accident conditions to ensure the safe operation of the nuclear reactor. The reactor typically uses uranium oxide as fuel. The nuclear fuel used in power reactors and some research reactors consists of solid uranium processed in the form of pellets stacked to form cylindrical rods. However, in most research reactors, a fuel assembly in the form of a plate is used. This fuel element is manufactured by the co-lamination process, in which the fuel and the cladding, usually

aluminum, are rolled together using high-pressure rollers. This process has advantages in terms of improved thermo-mechanical properties, as it allows a perfect integration between the fuel and cladding layers, minimizing thermal resistance at the boundaries of both materials (uranium-aluminum). There is a direct proportionality between the neutron flux produced by the fuel and the heat production i.e., around 200 MeV per fission of U-235 are released. Therefore, the study of reaction rate and thermal power generation in the reactor core are of important interest. For the study of the reaction rate, the first step is to define the scalar neutron flux

$$\phi(\vec{r}, E, t) = \int_{4\pi} \varphi(\vec{r}, E, \hat{\Omega}, t) d\hat{\Omega}, \quad (2.13)$$

to subsequently calculate the reaction rate, which is defined as the neutron flux multiplied by the probability of an interaction per centimeter path length (the macroscopic effective cross sections), the following expression is obtained

$$RR = \int_V \int_E \Sigma(\vec{r}, E) \phi(\vec{r}, E) dE dr^3. \quad (2.14)$$

Like the reaction rate, Eq. (2.14), the thermal power of the reactor is directly proportional to the neutron flux. The thermal power is equal to the total energy released during fission, including also the energy released by emerging particles. The thermal power is defined by the expression

$$P[W] = \int_0^{E_{max}} dE \int_V dr^3 H(\vec{r}, E) \phi(\vec{r}, E), \quad (2.15)$$

where V and $H(\vec{r}, E)$ are, respectively, the volume of the reactor core and the power factor, which gives the recoverable energy in terms of flux (Duderstadt and Hamilton, 1976), (Lewis and Miller, 1984), (Prinja and Larsen, 2010).

2.2 Deterministic methods to describe the neutron transport

In nuclear engineering, deterministic numerical methods are used to solve the neutron transport equation, but because of the high complexity of this equation (eight independent variables in the same system), several approximations and simplifications are required for the variables like position \vec{r} , direction $\hat{\Omega}$, energy E and time t . The independent variables within the transport equation mean that its solution must be treated using different discretization methods. Some of the methods used to solve the neutron transport equation are:

- For example, for the case of position \vec{r} , the following discretization methods are used: Finite Difference Method (FDM), Finite Volume Method (FVM), Finite Element Method (FEM).
- For the direction of flight $\hat{\Omega}$, the discretization is generally done with discrete coordinate methods, the collocation method (S_n) or the spherical harmonics method (P_n). The S_n -

based methods are generally the most commonly used because the resulting equations have a physical interpretation inherent in particle transport.

- For the discretization of the energy variable E , the multigroup method is often used. This method consists in replacing the calculation of the energy dependence of the neutron flux and reaction rates by a small number of intervals called energy groups. Each group is characterized by cross sections, fission spectra, and kinetic parameters condensed from continuous conservation data (Duderstadt and Hamilton, 1976), (Prinja and Larsen, 2010).
- The time variable t is discretized to handle time-dependent problems. The most common method for discretizing this variable is the implicit or backward Euler method.

As can be seen, a complete solution of the neutron transport equation is complex and requires a two-stage solution approach of condensation and homogenization. In the first stage, the relevant reaction rates must be preserved. To achieve this, continuous energy transport calculations are performed in 0- and 1-dimensional systems and stored in multi-group data libraries. The libraries consist essentially of cross sections and flows condensed into a few-group structure. In the second stage, the heterogeneous geometry of each representative subregion of the core is homogenized into an effective material and the nuclear data are condensed into two or three energy groups. Finally, a solution is obtained in which, for example, the entire reactor core is represented in a nodal-level geometry with a coarse energy structure (Duderstadt and Hamilton, 1976), (Prinja and Larsen, 2010). Although the neutron transport equation is an approximate solution (based on simplifications that do not always represent the real physical model), the results obtained have proven reliable for practical purposes, so the deterministic method is widely used in industry for conservative calculations (Prinja and Larsen, 2010), (Ferraro, 2021), (Garcia, 2021). Nowadays, the trend of analyzing nuclear reactor cores with higher order solutions has become very relevant due to the improvements in computer science and numerical algorithms in the last decade. A promising alternative to deterministic methods is the Monte Carlo method able to treat the reactor core without geometric simplifications and describing the physics of the interaction of neutrons with matter without approximations. Hence, these methods gaining increasing importance (Garcia, 2021).

2.3 The Monte Carlo method to describe the neutron transport

The Monte Carlo (MC) method is a stochastic method that uses mathematical techniques to simulate random events and predict probabilities e.g. of the interactions of neutrons with matter. The MC method is used in nuclear engineering to simulate the random behavior of particles, such as neutrons, and to calculate the probability of certain outcomes, e.g. neutron flux. The neutron transport equation (Eq. (2.1)) can be solved by the MC method, which is based on the repetition

of random events whose expected value is the solution of the given problem (Haghighat, 2020), (Bauer, 1958). Since the solution of the neutron transport equation depends on the number of random repetitions of the simulated event, the computation time is high and represents a parameter that must be considered when performing neutron calculations for the reactor. The main source of statistical error is related to the sample size. The larger the sample size, the smaller the statistical error, but the longer the simulation takes. In nuclear reactors, this method allows analyzing the individual behavior of a group of neutrons and their possible interaction with different materials. This approach has the advantage of allowing the modeling of a complex core with irregular geometry (X-5 Team, 2008).

MC simulations are applicable when the physical basis for a particular event, such as the flight path of a particle, is known. To understand the concept, imagine that a random variable x , determined by an underlying probability distribution, is subjected to a cumulative probability distribution whose outcome is now given over an interval of values. These distributions are usually referred to as the probability density function (PDF, $p(x)$) and the cumulative probability distribution (CPD, $P(x)$). The main idea is to determine the probability that x has a value between a and b . The cumulative distribution function is defined by

$$P(x \leq x' \leq x + \Delta x) = p(x)\Delta x, \quad (2.16)$$

where $\Delta x \rightarrow 0$, the probability density function $p(x)$ is always positive and the commutative distribution function $P(x)$ it is normalized in the range of $[0,1]$ (Lewis and Miller, 1984), (X-5 Team, 2008), (Haghighat, 2020). Eq. (2.16) can be rewritten as

$$P(a \leq x \leq b) = \int_a^b p(x) dx. \quad (2.17)$$

Figure 2.2 shows the representation of the commutative distribution. The sample ξ depends on the random variable x . To obtain the sample ξ , one must apply the inversion method function, a mathematical technique used to calculate the probability of certain outcomes when dealing with particles in nuclear engineering, see Eq. (2.18). The inversion method is not always possible, so alternative techniques are used that maintain the same principle (Haghighat, 2020), (Leppänen, 2007).

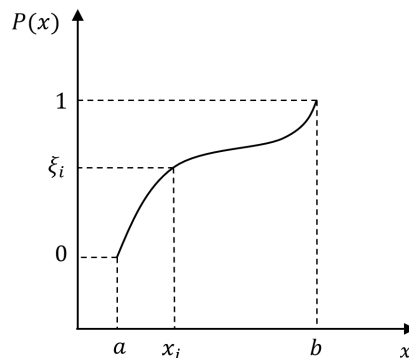


Figure 2.2: Commutative distribution, sampling of a random variable x .

$$P(a \leq x \leq b) = \xi \quad \rightarrow \quad x = \xi^{-1}. \quad (2.18)$$

The results of the MC method are obtained from a sample of possible random moves, each of which is assigned a score x_i . The estimates fall within a range of values calculated as a function of the sample and the chosen variance (X-5 Team, 2008). The expected value $E(x)$ of a known process, e.g., $x = \text{energy deposited}$, can be calculated using the probability density function $f(x)$ of the process value. The expected value can be defined as follows

$$E(x) = \int x f(x) dx. \quad (2.19)$$

If the function $f(x)$ is implicit, Eq. (2.19) can be expressed using the mathematical theorem of the law of large numbers, which affirms that if x_i are mean samples of a random variable, it will tend to approach the expected value, see Eq. (2.20).

$$E(x) \approx \bar{X} = \frac{1}{N} \sum_{i=1}^N x_i. \quad (2.20)$$

Eq. (2.20) states that the precision of an estimate of a quantity tends to improve when larger samples of observations are averaged. This means that the results are random in the short run, but become more reliable in the long run. The variance of the population σ^2 of x values is defined as

$$\sigma^2 = \int (x - E(x))^2 f(x) dx = E(x^2) - (E(x))^2. \quad (2.21)$$

The term $f(x)$ in Eq. (2.21) makes the standard deviation σ a function that may or may not be known consequently, the standard deviation can be determined by

$$S^2 = \frac{1}{N-1} \sum_{i=1}^N (x_i - \bar{X})^2, \quad (2.22)$$

$$= \frac{1}{N-1} \sum_{i=1}^N (x_i^2 - 2x_i \cdot \bar{X} + \bar{X}^2), \quad (2.23)$$

$$= \frac{1}{N-1} \left(\sum_{i=1}^N x_i^2 - 2\bar{X} \sum_{i=1}^N x_i + \sum_{i=1}^N \bar{X}^2 \right), \quad (2.24)$$

$$= \frac{N}{N-1} (\bar{X^2} - \bar{X}^2), \quad (2.25)$$

where the factor $1/(N-1)$ is used for large samples ensuring that S^2 is an unbiased estimator for the true variance. However, for larger number of $N \rightarrow \infty$ the term $\frac{N}{N-1}$ of Eq. (2.25) tends to be one. And Eq. (2.25) is expressed as

$$S^2 = (\bar{X^2} - \bar{X}^2). \quad (2.26)$$

And the estimated variance of \bar{X} is given by

$$S_{\bar{X}}^2 = \frac{S^2}{N}. \quad (2.27)$$

The term $1/\sqrt{N}$ of Eq. (2.27), where N is the number of the histories, determines the sample deviation in Monte Carlo calculations. This term indicates that the largest the number of histories used in MC calculations the smaller the sample deviation as a result improves the precision but not the accuracy.

2.3.1 Precision and accuracy of Monte Carlo methods

Figure 2.3 shows the difference between precision and accuracy. Precision depends on the number of histories used in the representative model. The number of histories cannot be infinite, a large particle sample ensures that the calculated values are close to the expected value $E(x)$. Usually, $\pm S_{\bar{x}}$ values are used to describe the precision. Simulation precision is also referred to as MC uncertainty and is valid when the physical phase space is adequately sampled. Factors affecting precision include the type of tally, variance reduction techniques, and the number of runs simulated (X-5 Team, 2008), (Prinja and Larsen, 2010).

On the other hand, accuracy is a measure of how close the sample mean \bar{X} is to the true mean. The true mean usually refers to experimentally determined values such as neutron flux, reactor power, or coolant and fuel temperature profiles. It may be the case that the uncertainty of the expected value is small, i.e., a large number of historical values have been used, but the difference of the expected value from the true value is large. In this case, one could deduce that the Monte Carlo calculations are acceptable, but the physical representation of the model is not good enough to reach the true values. For a proper simulation using the MC method, a detailed physical description of the problem is required; this includes an accurate knowledge of the parameters such as material type, geometric dimensions and boundary conditions.

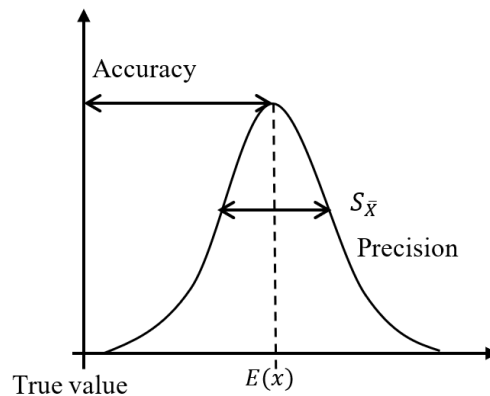


Figure 2.3: Schematic of the definition of accuracy and precision in MC calculations.

The values that result from the gap between the true mean and the sample mean are called systematic errors. For the calculation of MC, it is useful to define the estimate of an error, the most common being the relative squared error R^2 and the figure-of-merit (FOM).

The relative squared error estimate R^2 is used to measure the precision of an estimate. It can be used to compare different estimates and determine which one is more accurate. The relative error is proportional to $1/N$ and can be calculated using the following expression

$$R = \frac{S_{\bar{X}}}{\bar{X}} . \quad (2.28)$$

Another parameter used to compare different systems or processes is the figure-of-merit (FOM), which is a measure of the performance of a system or process. It is usually expressed as a ratio or percentage and indicates the reliability of the count. If the FOM is approximately constant, ignoring the statistical fluctuations at the beginning of the iterations, the quality of the results can be considered good. On the other hand, if the FOM is not constant, the confidence intervals may not contain the expected value $E(x)$. FOM can be expressed as

$$FOM = \frac{1}{R^2 T} , \quad (2.29)$$

where the term T is the total computer time and R can be calculated using the Eq. (2.28). The multiplication of $R^2 T$ should be approximately constant (Chan, 2013), (Olsher, 2006).

2.3.2 Application of Monte Carlo methods in core analysis

In this section, a brief discussion of the application of the MC method in nuclear physics is given. To solve the neutron transport equation, the tracking routine is usually used, which attempts to follow the nuclear reaction process. This routine simulates the random walk process that transports neutrons from one iteration to the next through the geometry (X-5 Team, 2008), (Viitanen and Leppänen, 2012). The path length between two collision points is exponentially distributed as follows

$$p(En, x) = \Sigma_{total}(En) e^{-x \Sigma_{total}(En)}, \quad (2.30)$$

where the $\Sigma_{total}(En)$ is the macroscopic total cross section of a medium. Eq. (2.30) will be known as probability density function *pdf*. Using the approach described in Eq. (2.17) the cumulative distribution function *cdf* will be

$$P(En, x) = \int_0^x p(En, x') dx' = 1 - e^{-x \Sigma_{total}(En)}, \quad (2.31)$$

and using the inversion technique to the cumulative distribution function, Eq. (2.18), is obtained by

$$x = P^{-1}(En, \xi) = -\frac{1}{\Sigma_{total}(En)} \ln(1 - \xi). \quad (2.32)$$

Finally, if a N random number ξ are sampling, the average track length can be calculated with Eq. (2.20)

$$\bar{X} = \frac{1}{N} \sum_{i=1}^N -\frac{\ln(1 - \xi)}{\Sigma_{total}(En)} \quad (2.33)$$

Examination of Eq. (2.33) shows that the total cross section must be constant over dx for the mathematical expression to be valid. If this is not the case, Eq. (2.30) is not statistically valid. Another limitation in using this approach is that the representative geometries of the model are defined using homogeneous materials with no variation in their cross-sectional efficiencies (Viitanen and Leppänen, 2012).

2.3.3 Monte Carlo method for transient simulations

The solution of the neutron transport equation with time dependence is a fundamental part of the analysis of reactor core behavior. When transient state simulations are required, the neutron population requires special importance. Prompt and delayed neutrons are the main players in the production of fission energy. A prompt neutron is released in about 10^{-14} s, a very short time, so its release can be considered instantaneous (Sjenitzer and Hoogenboom, 2011). On the other hand, there are delayed neutrons that are released by the beta decay of a fission fragment known as a delayed neutron precursor. Figure 2.4 shows the production of both types of neutrons, one almost instantaneous and the delayed neutrons produced some time after the initial nuclear reaction.

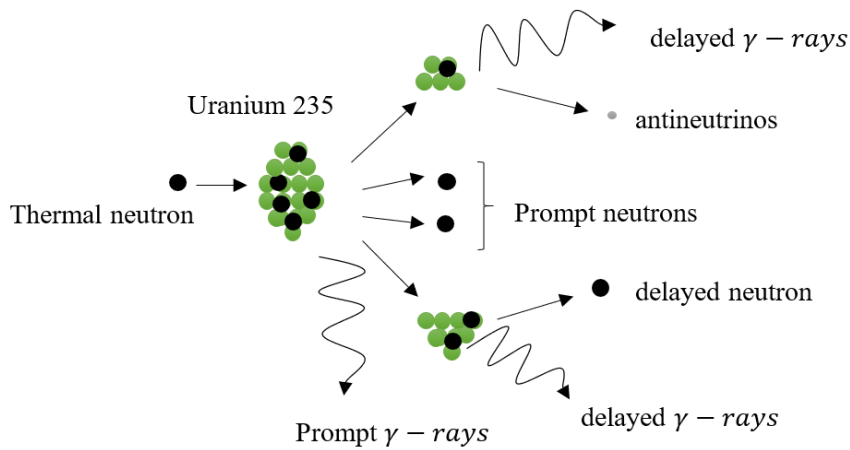


Figure 2.4: Sketch of the nuclear fission process with the associated particle and energy release chain.

To address transient problems with the MC method, it must be taken into account that its application is analogous to a fixed source computation, which means that it is necessary to perform a time-binning to capture the time associated with the particle trajectories, with the consequence that the control of the particle population must be performed for each time bin (Ferraro, 2021). In addition to the fixed source, delayed neutrons from precursor fractions must be treated analogously, for which an external source similar to the one proposed by (Sjenitzer B. , 2013) is used. At this point, an issue arises as to how to deal with the modeling of delayed neutrons. To this purpose, instead of sampling the delayed neutron emission during fission, the delayed neutron

precursors are produced so that the precursor population is tracked instead and delayed neutrons are emitted from them (Valtavirta, et al., 2016).

In a transient simulation, it is critical to know the initial distributions of the system sources. To understand how a distribution works, one must imagine that a snapshot of the distribution is taken at a random time. In this snapshot, the *live* neutrons and the delayed neutrons are observed. The *live* neutrons move with an energy E corresponding to their position and direction of motion, while the delayed neutrons wait in the precursor atoms at a certain position with a decay constant λ (Valtavirta, et al., 2016).

Random neutrons at a point in their lifetime are stored to create the source of *live* neutrons. These random points are uniformly distributed over time. However, the neutron interactions are not uniformly distributed in time, so the average interaction frequency must be calculated using Eq. (2.34),

$$f_{mean} = \frac{1}{t_{mean}E} = \Sigma_{total}(E)v(E). \quad (2.34)$$

To generate the delayed neutron source, the time domain is divided into n intervals. Each interval consists of a beginning of the interval (BOI) and an end of the interval (EOI). Not all delayed neutrons survive to the end of the interval, and geometric parameters such as control rod position, temperature, and fuel and coolant density can be changed in the time domain, altering the BOI considerations. To model this behavior, MC codes can be used to calculate the weight associated with the fraction of surviving neutrons using the decay law, Eq. (2.35),

$$w_{tal} = w_0 e^{-\lambda_g(t_* - t_0)}, \quad (2.35)$$

where λ is known as the decay constant of the precursor. The neutron portion emit during the interval will be calculated by

$$w_{emit} = w_0(1 - e^{-\lambda_g(t_* - t_0)}). \quad (2.36)$$

Figure 2.5 taken from (Leppänen, et al., 2022) represents schematically the different portions of neutrons in a time interval.

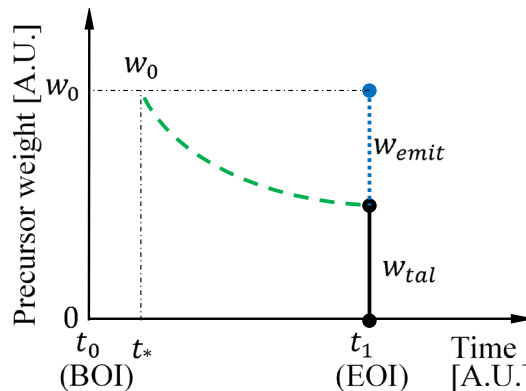


Figure 2.5: Representation of precursors decay within MC code Serpent 2.

Finally, the *live* and delayed neutron sources are obtained from a steady-state criticality calculation $k_{eff} = 1$. The criticality state should fully represent the desired physical model. The criticality or steady-state simulation should be performed with a good neutron population so that the uncertainty is small. In this work, the Monte Carlo code Serpent 2 is used. The transient calculations of Serpent 2 use the external source of *live* and delayed neutrons obtained from a critical steady-state simulation. This approach is referred to as two-step and is shown in Figure 2.6.

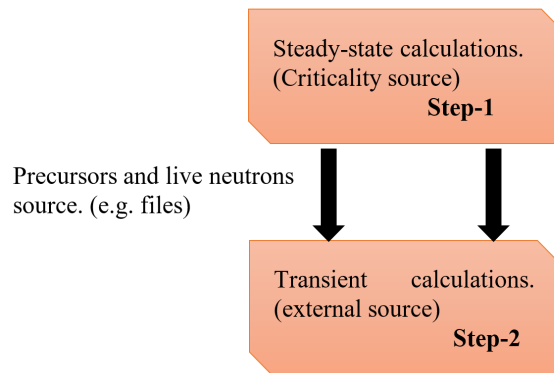


Figure 2.6: Two-step scheme for transient simulation.

2.4 State-of-the-art of neutronic analysis

Currently, deterministic and Monte Carlo codes are commonly used for neutron analysis of nuclear reactors. Both methods are constantly evolving, and the choice of one of them will depend on several factors, such as the application, the available computational resources, and the level of detail (Pecchia, et al., 2012).

Neutron codes are used in industry, research and development. Established standard deterministic codes are used in industry for power reactor simulation. Some of these codes are CASMO (Rhodes, et al., 2006), HELIOS (Wemple and Simeonov, 2017), SCALE (Rearden and Jessee, 2016), SIMULATE-5 (Bahadir and Lindahl, 2009). On the other hand, Monte Carlo codes are mainly used for research and development of new reactors because they allow modeling of complex geometries with a high level of detail for both power and research reactors. MC Codes such as Serpent 2 (Leppänen, 2007), MCNP (Werner, et al., 2018), TRIPOLI (Nimal and Vergnaud, 1990) and KENO-VI (Rhodes, et al., 2006), have been tested and validated for steady-state, transient, and fuel burnup calculations.

In terms of computational resources, this is a critical issue to consider since the results of the codes can be efficient (short simulation time) but not as accurate (results with large discrepancy) or vice versa, in any case, in certain applications it is sufficient that the results are reliable. One of the disadvantages of MC codes compared to deterministic codes is that dynamic calculations are computationally intensive. Therefore, to realize their full potential, parallelization methods

must be used in HPC architectures (Dietrich and Boyd, 1996). Currently, there are several techniques to speed up MC computations, such as stratified sampling, the walk algorithm for time dependence between samples, and variance control techniques, which are among the most commonly used (Lai, et al., 2019).

In terms of level of detail, the current trend is to simulate all fuel elements in the core, so the use of MC codes has become very popular. Although deterministic codes are the most widely used in the industry, their condensation and homogenization approach to solving the neutron transport equation represents their major limitation when dealing with high level of detail simulations, so new deterministic codes with high accuracy have been developed in recent years (Smith and Forget, 2013). One approach using these new codes is based on two-dimensional (2D) and one-dimensional (1D) numerical schemes. In a 2D/1D scheme, the principal components are modeled in detail in two dimensions using the Method of Characteristics (MOC) solver and axially coupled with low-order methods such as diffusion or SP_N ; some examples of codes inspired by this methodology are: DeCART (Joo, et al., 2004), MPACT (Cao, et al., 2015), MICADO (Fevotte and Lathuiliere, 2013) and Proteus-MOC (Marin-Lafleche, et al., 2013).

Another technique to improve the simulation capability of deterministic codes is the implementation of SP_3 solvers, as provided by the codes PARCS and DYN3D (Beckert and Grundmann, 2008). This new development brings some limitations, such as the dependence on precomputed cross sections and the need for computational resources almost similar to those of the MC codes.

In summary, although deterministic codes with high fidelity can currently model a complete core with a certain level of detail, their results do not seem to be more accurate than those of MC codes, so MC codes are currently preferred when high fidelity simulations are required (Daeubler, et al., 2015), (Ferraro, et al., 2019), (Garcia, 2021).

3 Fundamentals of thermal-hydraulic core analysis

In nuclear engineering, thermal-hydraulic analysis is used to evaluate the safety of nuclear reactors. The study of thermal-hydraulics is a fundamental part of understanding the behavior of the fluid under the influence of heat (Duderstadt and Hamilton, 1976). A set of equations describing the thermal and hydraulic parts is used to deal with thermal-hydraulics coupling. The thermal analysis is related to the power distribution resulting from the nuclear fission process and allows to obtain the radial and axial temperature profiles of the fuel element, cladding and gap by heat transfer through conduction and the temperature profiles of the coolant by convection. On the other hand, hydraulic analysis is used to determine the fluid condition, flow patterns, and pressure losses in the core. The hydraulic part is the most challenging to solve because it deals with the equations for conservation of mass, momentum, and energy. Numerical integration methods or analytical solutions are used to solve this first set of equations (Lahey and Moody, 1993). The numerical integration method is most commonly used because the equations can be broken down into smaller parts and solved using numerical calculation methods. Depending on the scope of the hydraulic analysis, the equations for conservation of mass, momentum, and energy can be discretized in 3, 2, or 1 dimension. Nowadays, different types of codes are used to perform thermal hydraulic analysis. Among the most commonly used and accepted codes by industry and researchers are, Computational fluid dynamics (CFD), subchannel, and system codes.

3.1 Thermal analysis

The thermal energy released during nuclear fission in the fuel is transferred in the form of heat from the source that generates it to a cooler sink (coolant). In the thermal analysis of the reactor core, heat transfer by conduction and convection is considered (Lahey and Moody, 1993), (Van Uffelen, et al., 2010). Figure 3.1 shows a typical representation of the temperature distribution within an axial slice of a fuel element. Assuming that the boundary conditions are the same on both sides of the cladding (black colored area), the maximum temperature T_{max} is in the central part of the fuel (yellow colored area). The heat passes through the fuel until it reaches a gap with a temperature T_F . Inside the gap, the heat transfer coefficient must be calculated to obtain the temperature of the inner cladding temperature T_{ci} , and then the heat conduction process is used to determine the temperature distribution in the cladding. Finally, the heat is transferred to the coolant, which circulates upward as part of the convective flow pattern imposed on the system.

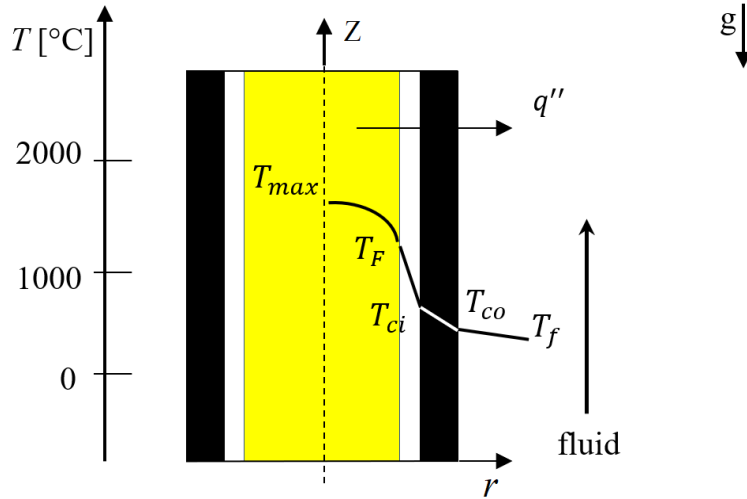


Figure 3.1: Typical 1.5D schematic representation of the temperature distribution of a fuel element.

3.1.1 Heat transport in the fuel, gap and cladding

Heat transfer through the fuel and the cladding is described by the heat conduction, Eq. (3.1), known as Fourier's law, which can be used to solve the heat conduction problem. This law states that the volumetric heat source q''' is equal to the time change t of the temperature distribution T as a function of the thermo-physical properties density ρ , heat capacity C_p and thermal conductivity K_c (Duderstadt and Hamilton, 1976), (Incropera and DeWitt, 1996)

$$\frac{\partial}{\partial x} \left(K_c \frac{\partial T}{\partial x} \right) + \frac{\partial}{\partial y} \left(K_c \frac{\partial T}{\partial y} \right) + \frac{\partial}{\partial z} \left(K_c \frac{\partial T}{\partial z} \right) + q''' = \rho C_p \left(\frac{\partial T}{\partial t} \right). \quad (3.1)$$

The temperature difference in the gap between fuel-cladding, $\Delta T_{F,ci}$, is defined by (Lassmann and Hohlefeld, 1987):

$$\Delta T_{F,ci} = \frac{q''}{h}, \quad (3.2)$$

where q'' is the heat flux and h is known as the *gap conductance* and is calculated using the expression

$$h = h_{rad} + h_{gap} + h_c. \quad (3.3)$$

The heat transfer coefficient h consists of a radiative component h_{rad} , gap component h_{gap} , and contact term h_c . The heat transfer by convection in the gap can be considered negligible (Lassmann and Hohlefeld, 1987), (Van Uffelen, et al., 2010).

3.1.2 Wall-liquid heat transfer

For analyzing the heat transfer from the fuel surface to the coolant, the Eq. (3.4) known as Newton's law is used. There q'' is the heat flux through the clad, T_{co} represents the outside temperature of the cladding, T_f is the fluid temperature and, h_{coef} is the heat transfer coefficient, see Figure 3.1.

$$q'' = h_{coef}(T_{co} - T_f). \quad (3.4)$$

The heat transfer coefficient h_{coef} is calculated in a simplified form assuming axis-symmetry using the Nusselt number Nu , the hydraulic diameter, and the conductivity of the coolant C . The Nusselt number is taken from relevant experimental correlations such as Dittus-Boelter (Dittus and Boelter, 1985) for power reactors Sudo for research reactors (Sudo, et al., 1985).

$$h_{coef} = \frac{Nu C}{D_h}. \quad (3.5)$$

3.2 Hydraulic analysis

Hydraulic analysis evaluates and predicts the behavior of the coolant under various pressure, temperature, and mass flow conditions. This requires understanding the basic principles of fluid dynamics and using advanced computational tools such as CFD and subchannel codes. The equations for conservation of continuity, momentum, and energy are commonly used. The usual approach is to calculate the equations for continuity, momentum, and energy as a coupled system. The numerical techniques used to solve these equations are based on the finite volume method or the finite element method. Figure 3.2 shows a cooling channel cell between different fuel elements. The left side of the figure shows a coolant channel between 4 parallel fuel rods typically used in power reactors, while the right side shows that the coolant channel is between two parallel fuel plates, a configuration observed in research reactors.

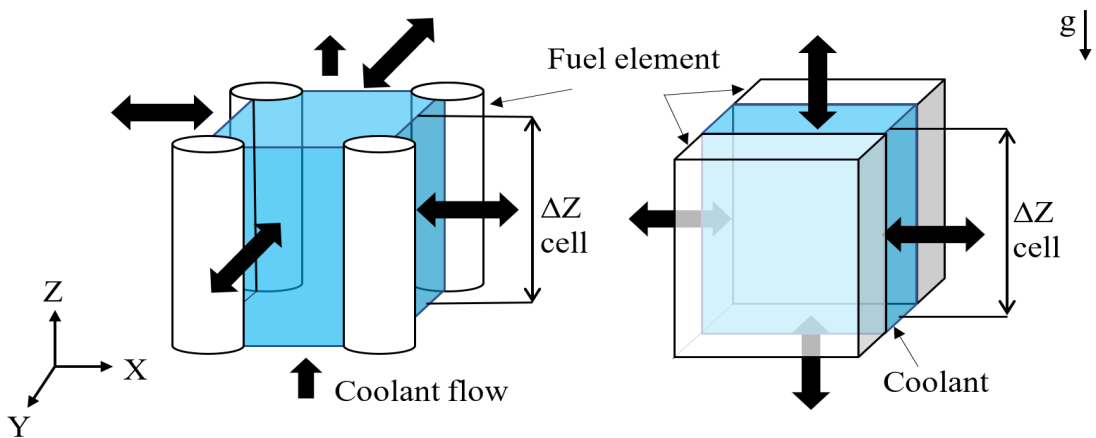


Figure 3.2: Axial representation of a subchannel cell, for the rod fuel (left) and plate fuel (right) elements.

The coolant channels seen in Figure 3.2 are narrow and thin, so from an applicability and computational resource standpoint, subchannel codes are the most appropriate. The continuity, momentum, and energy equations are applied to the subchannel along the axial direction, since the main focus of using subchannel codes is the imaginary radial subdivision of the main channel into small subchannels. Figure 3.3 shows the different types of subchannels that communicate with each other in the lateral direction by cross-flow. The cross-flow occurs in a space between the fuel elements known as a *gap*. As a result, the original three-dimensional problem is reduced to a one-dimensional problem with lateral components (Wheeler, et al., 1976).

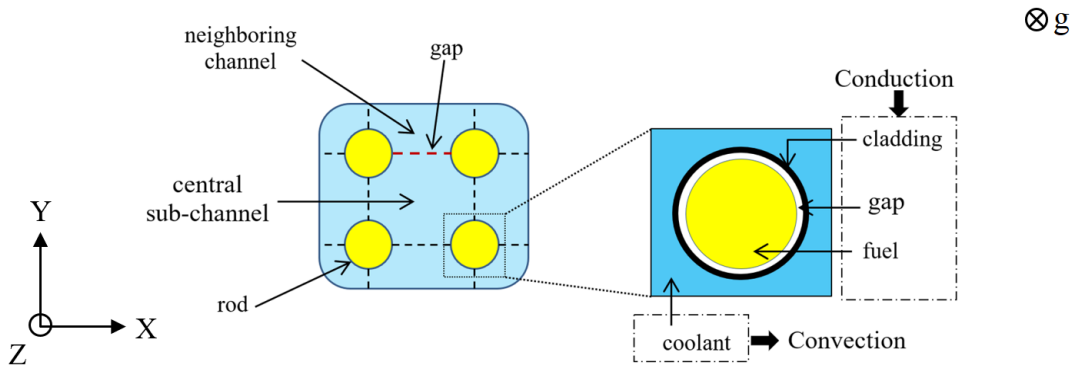


Figure 3.3: Schematic XY cut of an arrangement of 4 fuel rods next to the cooling fluid.

The basic equations of the mathematical model applied to subchannels, which have been proposed by (Rowe, 1973), are presented below:

Continuity:

$$A \frac{\partial \rho}{\partial t} + \frac{\partial m}{\partial z} + [DC]^T w = 0. \quad (3.6)$$

Energy:

$$A \frac{\partial \rho h}{\partial t} + \frac{\partial m h}{\partial z} + [DC]^T h^* w = q'. \quad (3.7)$$

Axial momentum:

$$\frac{\partial m}{\partial t} + \frac{\partial m u}{\partial z} + [DC]^T v^* w + \frac{\partial P}{\partial z} = F'. \quad (3.8)$$

Lateral momentum:

$$\frac{\partial w}{\partial t} + \frac{\partial v^* w}{\partial z} - [DC] P = c. \quad (3.9)$$

Where:

A = axial flow area,

m = axial mass flow rate,

w = cross flow rate,

t = time,

P = subchannel pressure,

F' = axial friction,

c = lateral friction,

u = axial velocity,

q' = total heat source,

where in addition the term $[DC]$ expressed in the above equations is a matrix operator that carried out the lateral finite difference operation, and $[DC]^T$ is the transposed matrix of $[DC]$ (Wheeler, et al., 1976).

3.3 State-of-the-art of thermal-hydraulic analysis

Currently, system, CFD - and subchannel codes are used for the thermal-hydraulic analysis of nuclear reactors. In industry, the use of system codes for thermal-hydraulic analysis of power reactors is in high demand, and few of these code types can model research reactors without the need for customization and heuristic approaches. Some types of system codes are RELAP (Khedr, et al., 2005), TRACE (Zhang, et al., 2021), ATHLET (Hainoun and Schaffrath, 2001), and Flownex ® (Slabbert, 2011).

On the other hand, CFD codes are also used to simulate fluid dynamics and heat transfer in the reactor. These codes are very sophisticated and use finite element and volume control techniques to solve the thermal hydraulic equations. CFD codes are commonly used for applications that require a high degree of three-dimensional detail and are therefore used to model parts of the reactor core. Although advances in computer technology have made it possible to use CFD codes to model an entire reactor core, two-phase flow problems are limited to small academic application examples. Some of the most commonly used codes are: ANSYS-FLUENT (Hedayat and Davari, 2022), OpenFOAM (Liu, et al., 2021), and COMSOL (Almachi and Montenegro, 2016).

Finally, subchannel codes are usually used for industry and research. These types of codes are mostly from the COBRA family (Moorthi, et al., 2018). The simplest ones allow modeling two-phase flows by solving 3 mixing equations and one cross-flow equation. These types of codes are used to model power reactor cores, and only a few with certain extensions can model research reactors. Some of these codes are MATRA (Yoo, et al., 1999) and Subchanflow (Imke and Sanchez-Espinoza, 2012), the latter of which has been chosen in this dissertation to model research reactors by extending the heat transfer modules. There are more sophisticated Subchannels codes that involve the solution of six and nine conservation equations for modeling two fluids in two and three fields, respectively, including the analysis of the film, droplet, and vapor phases of the fluid (Salko Jr, et al., 2019).

In summary, computational tools for thermal hydraulic analysis are essential for predicting the behavior of nuclear reactors under different initial conditions. The use of each technique depends on the level of detail of the elements to be modeled and the reliability and adaptability of each code. Many of the subchannel codes are very popular because they have proven to be very versatile when coupled with Monte Carlo codes for high-fidelity analyzes (Daeubler, et al., 2015), (Ferraro, 2021), (Garcia, 2021).

3.4 Multiphysics approach for core analysis

Regardless of the type of reactor, the neutronic and thermal-hydraulic effect must be included for the analysis of a core to be considered realistic. The interaction between both fields is usually related to the feedback effect on the neutronics arising from the core thermal-hydraulics.

In particular, when changes in thermal-hydraulics occur, the overall impact on neutron moderation and absorption is affected. Typically, when a nuclear facility relies on a fission chain reaction that depends on the induction of a neutron in a heavy atomic nucleus, such as uranium, the isotopes U-235 and U-238 are used.

Here, the probability of interaction of neutrons with matter in space is studied, based on neutron cross sections. The concept of neutron cross section is used to express the probability of interaction between an incident neutron and a target nucleus, and is expressed in units of area called barn ($1b = 10^{24} [cm^2]$). If a neutron is absorbed a composite nucleus with higher energy is created, e.g., U-235 becomes U-236, this nucleus exists for some time and the contained energy is released through other mechanisms such as elastic scattering (σ_s), radioactive capture (σ_γ), fission (σ_f) and other reactions involving secondary particles ($\sigma_{(n,\alpha)}$), Eq. (3.10) (Björn, 2010).

$$\sigma_{total} = \sigma_\gamma + \sigma_f + \sigma_s + \sigma_{(n,\alpha)} + \dots; \quad (3.10)$$

Neutrons released from fission have high energy ($>1MeV$) so that they will interact with moderator material (elastic collisions) to loss energy in a thermal reactor core. Neutrons with low energy have a high probability to fission a U-235 nucleus. Such kind of reactions are desired to maintain a stable chain reaction.

The kinetic energy of thermal neutrons, which correspond to low energy neutrons, is comparable to the energy of atomic motion. This implies that molecular structure and temperatures are relevant factors to consider in low energy situations. In the specific case of the U-235 isotope, temperature effects on the total cross section for high energy neutrons may be less significant compared to low energy neutrons. At extremely high temperatures the value of the cross sections for U-235 decreases especially for low energy neutrons (Zheng, et al., 2020).

Another way to maintain the criticality of the reactor core is to use a fuel with higher enrichment. However, most reactors in the world, about 81%, use low enriched uranium U-235 (due to safety regulations) that varies between 3 to 4.5 % (Doligez, et al., 2017). The main effect of decreased fuel enrichment (due to increased U-238) is that more neutrons will be absorbed in U-238 than in U-235. Figure 3.4 (Nelson, et al., 2021) the fission and capture microscopic cross section in U-235 and U-238 in dependence of then energy of the incident neutrons is shown. In reality, most of these feedback mechanisms are affected mainly by neutron leakage than by enrichment decrease. The coolant density has a direct effect on neutron moderation and non-fission-related absorptions affecting the leakage.

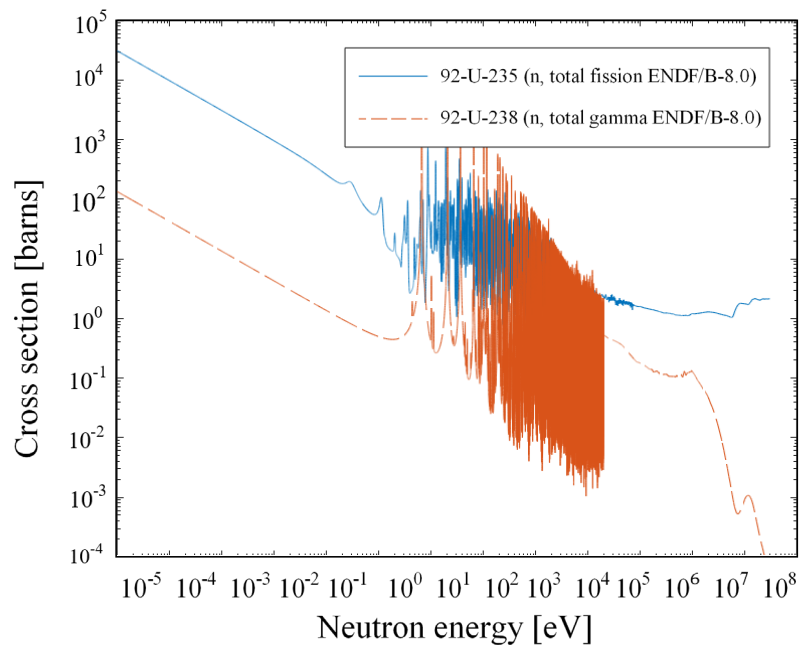


Figure 3.4: Cross section of U-235 (n , fission) and U-238 (n , γ), from (Nelson, et al., 2021).

An increase in temperature leads to a decrease in the density of the coolant and thus to a decrease in the moderating capacity, which leads to an increase in absorption in the epithermal energy spectral zone. In addition, in the case of using dilute burnable poisons, changes in coolant density alter the number of neutrons absorbed (Ferraro, 2021).

The feedbacks between the neutronic and thermal-hydraulics due to fuel temperature variations correspond to the neutron Doppler effect. This effect is considered as an intrinsic reactor safety feature. Note that the variation of the neutron captures cross section of U-238 isotope in the epithermal domain is strong, see Figure 3.4. The excessive resonances present in U-238 are called resonance-forests which vary in amplitude with fuel temperature. Not that in a PWR core, high-energy fission neutrons are slowed down by the moderator passing into the thermal domain through the epithermal area. As the temperature increases, the *resonances broaden* and therefore the sterile neutron captures increase causing a reduction in the fissile neutron flux and thus a decrease in reactor power, see Figure 3.5. This self-stabilizing effect is beneficial because it is an

intrinsic safety property of reactors. The Doppler broadening is calculated according to the Breit-Wigner formula (Duderstadt and Hamilton, 1976).

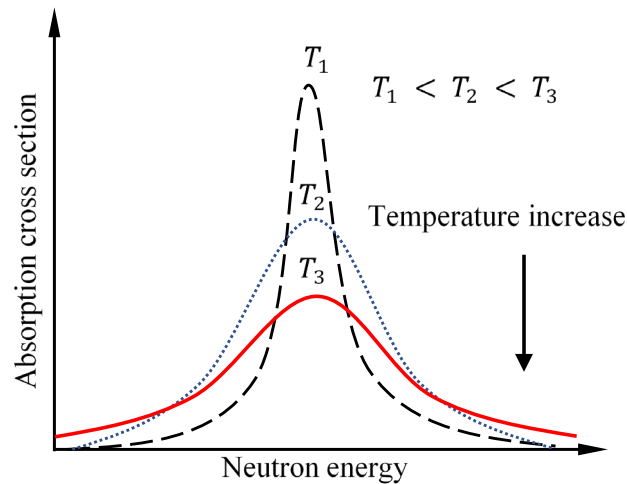


Figure 3.5: Doppler broadening of the absorption cross section of U-238, profiles at different temperatures, scheme adapted from (Duderstadt and Hamilton, 1976).

The values for the Doppler reactivity feedback effect depend on the type of isotope used. The Doppler feedback for U-235 can be slightly positive, negative, or negligible. For the U-238 isotope, however, it is always negative, which is why it is commonly used to make fuel from low-enriched uranium (LEU) for thermal reactors. Reactors fueled by highly enriched uranium (HEU) have much less negative Doppler feedback than reactors loaded with LEU, so that power control depends entirely on the absorber rod control system (Nelson, et al., 2021).

4 Selected simulation tools

In this section, the selected codes for neutron and thermal-hydraulic analysis are briefly described. For the neutron analysis, the Monte Carlo code Serpent 2 has been used for its ability to simulate complex steady-state and transient cores at very detailed level. For the thermal-hydraulic analysis, the Subchanflow code has been chosen, which has been developed in-house for fuel assembly/pin level analysis of power reactors. For the multiphysics analysis, the internal coupled code Serpent2/Subchanflow based on the master-slave approach is selected.

4.1 The thermal hydraulic Subchanflow code

Subchanflow is a subchannels thermal-hydraulic code that has been developed at the Karlsruhe Institute of Technology (Imke and Sanchez-Espinoza, 2012). The code is capable of performing steady-state and transient calculations for thermal-hydraulic analysis of BWR, PWR, and VVER reactors (Calleja, et al., 2014). It is written in a modular and platform-independent manner so that it can be easily compiled and run in both WINDOWS and LINUX operating systems. A standard Fortran 2003 compiler is required.

In Subchanflow, a three-equation two-phase flow model that is a mixture equation for mass, momentum and energy balance is implemented. Additionally, momentum equation for the cross flow between neighbor subchannels is used and a set of empirical constitutive correlations closes the system. It includes relations for the wall friction, pressure drop and wall/liquid heat transfer for an upward flow. The mixture conservation equations for mass and energy are solved in the subchannel approach for a specific spatial discretization of the computational domain, either centered at the fuel rod or centered at the coolant channel. In Figure 4.1, the different subchannel types in a bumble with nine pins are exhibited.

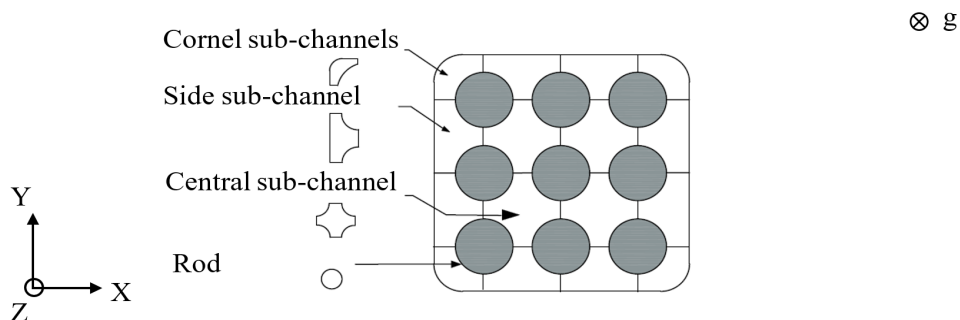


Figure 4.1: Types of subchannels for a squat lattice of 3x3.

For the steam/water state properties the IAPWS-97 formulation is used. In addition, property functions for liquid metals (sodium and lead) and gases (helium, air) are available. The two-phase flow (boiling) is implemented for water and sodium.

Subchanflow works with an input file called input.txt. This file contains keywords that can be easily read by the user of Subchanflow. The input.txt must be edited with an ASCII editor or similar. The input has simple tables and numerical values must be given in SI units, only temperatures are in °C (Sánchez, et al., 2010). The results of the simulations are printed to output.txt and if an error in the input.txt file is encountered the code stops the calculations and prints the error to output.txt. The extra files with extension “vtk” can be used for further processing using ParaView software or similar tools.

4.1.1 Conservation equations

The mixture conservation equations (mass, momentum and energy) are solved numerically within subchannel approach using finite-difference scheme. A fully implicit method is used to solve steady-state and transient problems. The bundle is divided into subchannels, in the radial direction and in axial zones along with the height. In Figure 4.2, the key parameters for the sub-channel approach are indicated: for an axial volume (j) in the channel (i) surrounded by volumes of neighboring channels (n) through gap (k).

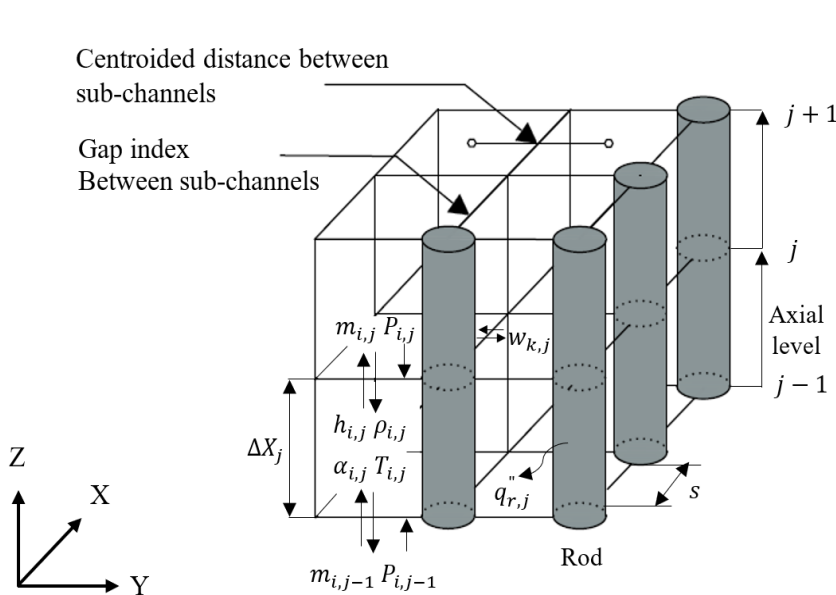


Figure 4.2: Scheme of the control volumes for the axial and radial discretization of Subchanflow.

The mixture mass conservation Eq. (3.6) is written as follows:

$$A_i \frac{\Delta X_j}{\Delta t} (\rho_{i,j} - \rho_{i,j}^{old}) + (m_{i,j} - m_{i,j-1}) + \Delta X_j \sum_{k \in i} w_{k,j} = 0, \quad (4.1)$$

where:

A = axial flow area,

- ρ = mixture density,
 m = axial mass flow rate of the mixture,
 w = cross flow rate,
 Δt = time step,
 ΔX = length of axial cell.

The momentum equation is divided in two components: the axial and lateral momentum. The momentum Eq. (3.8) along the axial direction is given by the following expression:

$$\begin{aligned}
 \frac{\Delta X_j}{\Delta t} (m_{i,j} - m_{i,j}^{old}) + m_{i,j} U'_{i,j} + \Delta X_j \sum_{k \in i} w_{k,j} U'_{k,j} \\
 = -A_i (P_{i,j} - P_{i,j-1}) - g A_i \Delta X_j \rho_{i,j} \cos \theta \\
 - \frac{1}{2} \left(\frac{\Delta X_j f \Phi^2}{D_h \rho_l} + K v' \right) |m_{i,j}| \frac{m_{i,j}}{A_i} - f_T \Delta X_j \sum_{k \in i} w'_{k,j} (U'_{i,j} - U'_{n(k),j}),
 \end{aligned} \quad (4.2)$$

where:

- P = Pressure,
 g = gravitational constant,
 θ = angle of the subchannel in vertical direction,
 f = friction coefficient,
 Φ = two phase flow multiplication factor,
 K = local pressure loss coefficient for spacers,
 f_T = factor for lateral turbulent momentum exchange,
 v' = specific volume,
 w' = turbulent cross flow.

Additionally, the donor cell velocity, with its variants form, vertical $U'_{i,j}$ and lateral $U'_{k,j}$ are calculated by the equation shown below:

$$U' = \frac{m}{A} v', \quad (4.3)$$

and the turbulent cross flow between channel i and channel n through gap k is defined by:

$$w'_{k,j} = \beta_{i,n} S \frac{\dot{m}_i + \dot{m}_n}{2}, \quad (4.4)$$

where:

- β = mixing coefficient,
 \dot{m} = mass flux,
 S = coolant gap width.

The lateral momentum conservation Eq. (3.9) is written as follows:

$$\begin{aligned}
 \frac{\Delta X_j}{\Delta t} (w_{k,j} - w_{k,j}^{old}) + (\bar{U}'_{k,j} w_{k,j} - \bar{U}'_{k,j-1} w_{k,j-1}) \\
 = \frac{S_k}{l_k} \Delta X_j \Delta P_{k,j-1} - \left(K_G \frac{\Delta X_j v'_k}{S_k l_k} \right)_j |w_{k,j}| w_{k,j},
 \end{aligned} \quad (4.5)$$

where:

K_G = lateral pressure loss coefficient for spacer,

l = distance between neighbor subchannels.

The energy Eq. (3.7) in terms of subchannel enthalpy is defined as follows:

$$\begin{aligned} \frac{A_i}{\Delta t} [\rho_{i,j}(h_{i,j} - h_{i,j}^{old}) + h_{i,j}(\rho_{i,j} - \rho_{i,j}^{old})] + \frac{1}{\Delta X_j} (m_{i,j}h_{i,j} - m_{i,j-1}h_{i,j-1}) \\ + \sum_{k \in i} w_{k,j} h_{k,j} = \sum_{r \in i} p_r \Phi_{i,r} q''_{r,j} \\ - \left[\sum_{k \in i} w'_{k,j} (h_{i,j} - h_{n(k)j}) + \sum_{k \in i} C S_k (T_{i,j} - T_{n_j}) \right] \\ + \sum_{r \in i} r_Q \Phi_{i,r} q'_{r,j}, \end{aligned} \quad (4.6)$$

where:

q'' = heat flux from fuel rod to coolant,

q' = linear fuel rod power,

w' = turbulent cross flow,

T = temperature,

p_r = heated perimeter,

Φ_r = fraction of heater perimeter,

C = heat conductivity,

r_Q = total power directly deposited into the coolant,

h = specific mixture enthalpy.

4.1.2 Heat conduction equation

To deal with heat conduction Eq (3.1) is used. In this equation the temperature is expressed as $T(x, y, z, t)$ where (x, y, z) indicates the temperature variations in the x , y , and z directions and t indicates the variation in time. Some variables, such as x , y , and z , can be simplified by assuming that the temperature varies with time, but not with position. The latter assumption is known as the "lumped parameter method" and is commonly used by system codes where the accuracy of the temperature distribution within the fuel element is not the subject of analysis (Aksan, et al., 2017). The lumped parameter method simplifies Eq (3.1) and this is reflected in the fact that the computational requirements are not as demanding, so it is essential to know when to use it. The Biot number is commonly used to determine when it is convenient to use this method. A small Biot number represents little resistance to heat conduction and, therefore, small temperature gradients within the target body. Generally, if a range of Biot ≤ 0.1 is obtained it is considered acceptable for the application of the lumped parameter method (Cengel and Ghajar, 2015).

Another option to solve Eq. (3.1) is to employ more advanced numerical methods. In this case, the Biot number can also help determine in how many dimensions Eq. 3.1 can be expressed.

For example, if the Biot number ≤ 1 , a one-dimensional analysis can be used without losing accuracy in the temperature results, while if the Biot number > 1 , a two-dimensional analysis is appropriate. When studying fuel element thermo-mechanics, two-dimensional analysis is recommended (Lahey and Moody, 1993).

The Subchanflow code uses the standard finite volume method to solve for heat transfer in the fuel rod. It is assumed that radial heat conduction is dominant compared to axial conduction, which allows to express Eq. (3.1) in its radial form through Eq. (4.7) (Masterson, 2020). This allows obtaining the temperature distribution in the radial direction without losing accuracy. To numerically simulate the heat conduction inside the rod, which is coupled to the heat transfer to the coolant in direct contact with its outer surface, an axial discretization into zones is performed, while the fuel and cladding are subdivided into thin zones in the radial direction.

Consequently, the heat conduction in the cylindrical fuel rod is expressed as follows

$$\nabla \cdot K \nabla T + q'''(r, t) = \rho C_p \left(\frac{\partial T}{\partial t} \right). \quad (4.7)$$

The temperature difference in the gap between the fuel and the cladding is treated by Eq. (3.2). In addition, the heat transfer from the rod to the coolant is carried out with Eq. (3.4). The heat transfer coefficients are calculated using Eq. (3.5), where the Nusselt number is obtained from relevant experimental correlations. The correlations available in Subchanflow are: Gnielinski and Dittus-Boelter. The current heat conduction solver and the heat transfer correlations implemented in Subchanflow do not allow to describe the heat conduction and convection for plate-shape fuel elements.

4.2 The neutronic Serpent 2 code

The Monte Carlo code Serpent 2 has been developed at VTT Technical Research Center of Finland and is widely used for neutron physics in nuclear reactors (Leppänen, et al., 2015). This simulation tool is a multi-purpose 3D Monte Carlo transport code for continuous energy and is therefore very useful for simulating complex geometries. Static, burnup and transient calculations are performed using the ACE format Nuclear Data Libraries (NDL) (Chadwick, et al., 2006). Serpent 2 can be compiled under the Linux operating system and is designed to allow massive parallelization of the code. Serpent's parallelization allows HPC clusters to process OpenMP, MPI, or hybrid compilations, which is essential for tackling large and complex problems that require large computational loads.

The ray tracing algorithm used by Serpent 2 is based on the method known as delta-tracking, which samples the next collision point of a particle without handling surface intersections. This

method is proposed by (Woodcock and Murphy, 1965) and is commonly used in Monte Carlo codes. To understand this method, consider an interaction in which the neutron is not absorbed and both energy and direction of flight are preserved. Such an interaction is called a virtual collision $\Sigma_0(r, E)$. In this method, an appropriate virtual collision cross section is added to the cross section of each material such that the total modified cross section has the same value for all materials. As a result, the total interaction probability is the same for all. This approach eliminates the need to adjust and calculate the free path length each time the neutron interacts with a new material. Eq. (4.8) shows the value of the virtual collision cross section

$$\Sigma_0(r, E) = \Sigma_m(E) - \Sigma_t(r, E), \quad (4.8)$$

where $\Sigma_t(r, E)$, is the total physical cross section of the material, $\Sigma_m(E)$ is the maximum of all cross sections, the so-called majorant, whose value is the same for all materials and therefore independent of the spatial coordinates. The main advantage of the delta tracking method is the simplified treatment of the geometry, which can speed up the calculation to some extent (Leppänen, 2007).

The effect of coolant density and fuel temperature on neutron multiplication is handled in Serpent 2 through rejection sampling techniques combined with target motion sampling (TMS). This second technique is a stochastic method and is used to treat material temperatures on-the-fly addressing even to account for Doppler effect resonances broadening. Additionally, this technique is based on sampling the target velocities at each collision location and treating collisions in the rest-target frame using cross sections below the actual nuclide temperature (Viitanen and Leppänen, 2014). This implementation serves as a universal multiphysics interface for coupling Monte Carlo with thermal hydraulic and fuel performance codes (Viitanen and Leppänen, 2012).

The iterated fission probability (IFP) method is used to calculate point kinetic reactor parameters such as effective generation time and delayed neutron fractions. The concept behind iterated fission probability looks at the number of neutrons produced in the system when fission chains are traced several generations into the future, instead of looking at the number of source neutrons produced in the next fission (Leppänen, et al., 2014).

Finally, for transient state calculations the two-step approach described in Section 2.3.3 is used. A critical state calculation together with the source of the precursor and live neutrons are used as the first step. During each time step, updates of the geometric parameters are allowed to handle transient problems where the control rods move with constant or variable velocity or a combination thereof, this feature, for example, is used to address reactivity insertion problems.

4.3 The internal coupling of Serpent 2 and Subchanflow

The concept of internal coupling, where there is a degree of interdependence between the Serpent 2 and Subchanflow codes, has been introduced in its test phase by (Daeubler, et al., 2015) for the analysis of LWR reactors. The results obtained showed that the internal coupling approach can perform steady-state, burnup, and transient calculations within realistic operating configurations. However, some disadvantages have been found by (Ferraro, 2021) noted some as the limitation of performing HPC calculations and the limited versatility in the geometrical construction of complex cores such as MTR reactors. This initial approach with the development of high-fidelity simulation tools does allow full exploitation of the ability to build complex cores within Serpent 2, so a new internal coupling approach, called master-slave, has been developed at the Karlsruhe Institute of Technology (Ferraro, 2021).

4.3.1 The master-slave coupling approach

The internal master-slave coupling, where Serpent 2 is the master and Subchanflow is the slave, is designed to allow easy compilation and use of the codes. The main advantage is that it allows maintenance and extension of certain routines of each code without having to modify the coupling architecture which is developed in the C programming language. The conceptual implementation of the Master-slave coupling can be seen in Figure 4.3, where the coupling routines interact with certain high-level subroutines generating an interdependence in selected fields such as convergence calculations, errors checks, relaxation, and exchange of thermal-hydraulic fields.

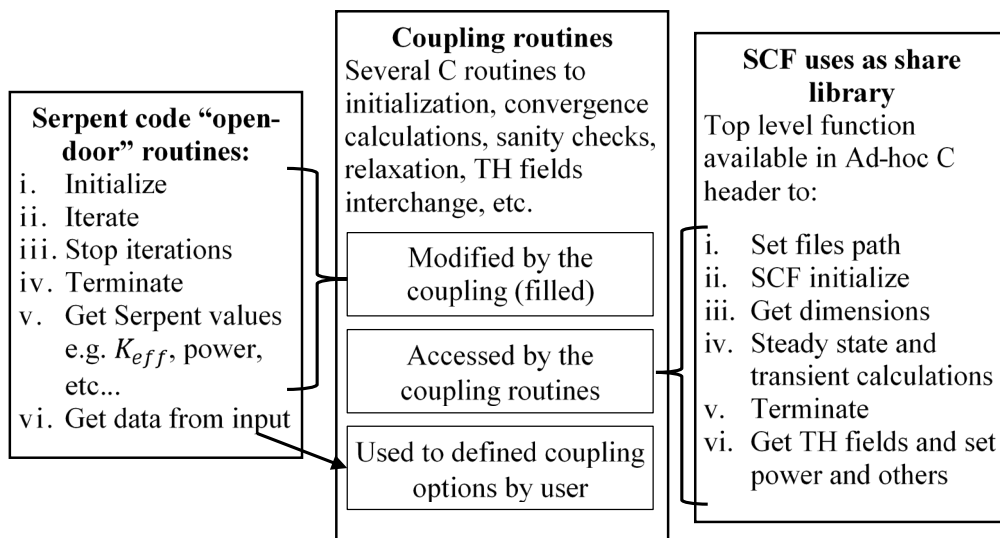


Figure 4.3: Implementation of Master-slave internal coupling approach, adapted from (Ferraro, 2021).

The routines for performing coupled computations in Serpent 2 are designed to solve multiphysics problems based on the Picard iteration method. As can be seen in Figure 4.4, the thermal-hydraulic and neutron solvers operate separately and can be further iterated until convergence is achieved.

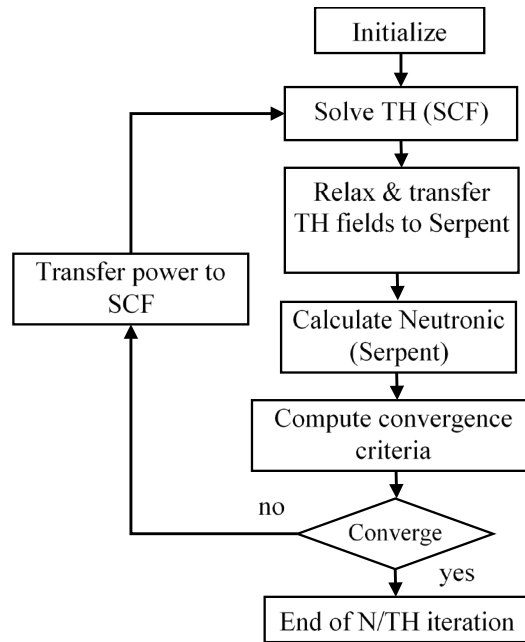


Figure 4.4: Picard iteration scheme Serpent2/Subchanflow, adapted from (Ferraro, 2021).

For transient calculations, explicit coupling is required, the convergence goal criteria are set for reactivity in pcm, fuel and coolant temperature in $^{\circ}\text{C}$ and coolant density in g/cm^3 . The evolution of the time step for transient calculations is shown in Figure 4.5, where the thermal-hydraulic and neutronic parameters are solved at time step i , this does not mean that the solvers operate in parallel at the same time.

At the beginning of the simulation, Subchanflow starts the calculations for a time step i and transfers the thermal-hydraulic fields to Serpent 2 for the same time step. Serpent 2 then adjusts the cross sections based on the internal storage of the density and temperature fields using interface files (IFC) containing the coolant and fuel temperatures and densities, performs linear interpolation with respect to time and obtains the actual temperature and density values for time step i , after these Serpent 2 updates the geometries, this option is very useful in transient analyses when the control rods change position as a function of time; finally, Serpent 2 passes the next time step $i + 1$.

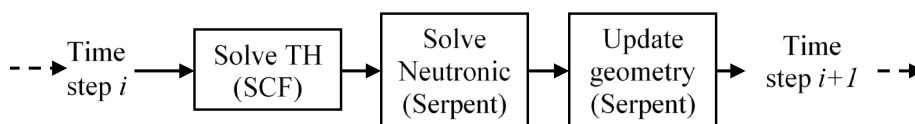


Figure 4.5: Flow to transient calculations master-slave approach, adapted from (Ferraro, 2021).

4.3.2 The thermal-hydraulic feedback exchange

The exchange of thermal-hydraulic fields from Subchanflow to Serpent 2 is done by means of IFC files. These files contain information about the temperature and density of coolant and fuel in the form of a meshes. These meshes are overlaid on the geometric model created for Serpent 2 and Subchanflow. Square and hexagonal lattice structures can be created for PWR and VVER type reactors. A power field remapping matrix is required for the design of complex cores with more than one type of fuel assemblies. The power remapping from Serpent 2 to Subchanflow is created node by node using high-level functions.

The concept of field interchange within the coupled code is shown in Figure 4.6, where two IFC files are observed, one for fuel and one for coolant. The model created in Serpent 2 provides the power values generated by neutron fission to the Subchanflow thermal-hydraulic code. The power provided by Serpent 2 is an average value per pin that is reordered if necessary and transmitted to Subchanflow. The thermal-hydraulic code then performs the fuel, cladding, and coolant temperature calculations where upon reaching the convergence values it transfers to Serpent 2 the average values of fuel temperature, coolant temperature, and coolant density. The matrices are updated at each iteration, allowing for transient simulations where the control rods move on-the-fly are allowed. All fields are stored in Random Access Memory (RAM), which allows fast data exchange.

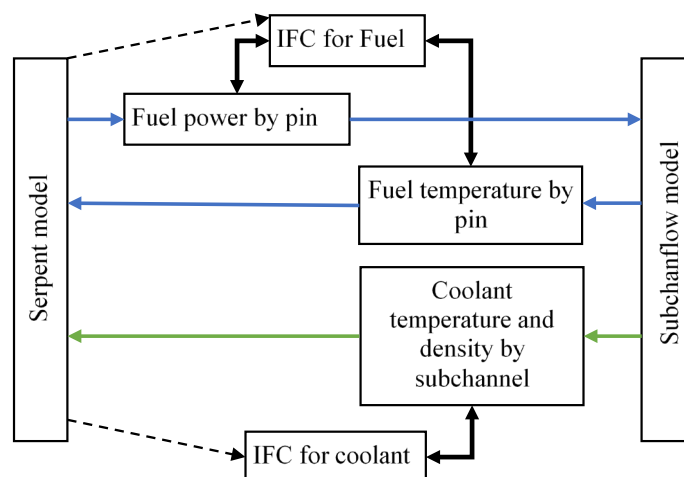


Figure 4.6: Concept of thermal-hydraulic field exchange in a coupled model, adapted from (Ferraro, 2021).

The main physical parameter to consider in the exchange of thermal hydraulic feedbacks is the temperature Doppler effect. This parameter is important in reactors because it can affect the rate of nuclear fission and thus reactor power. The Doppler effect is caused by the capture of neutrons with epithermal energy in U-238 and acts as self-shielding (see Figure 3.5) (Duderstadt and Hamilton, 1976). As the temperature increases, thermal expansion of the nuclear fuel occurs,

resulting in an increase in the distance between U-238 atoms. This decreases the probability of fission of the fuel nuclei, and in addition, at high temperatures there is increased neutron absorption and leakage through the moderator and reactor structure materials, which also decreases the amount of neutrons available for fission. A Doppler-weighted average is used to calculate the temperature feedbacks of the fuel in Serpent2/Subchanflow, and the feedback temperature is determined by the following equation.

$$T_{fuel}^{doppler} = \alpha T_{fuel}^{surface} + (1.0 - \alpha) T_{fuel}^{center}, \quad (4.9)$$

Here $T_{fuel}^{surface}$ and T_{fuel}^{center} are the temperatures calculated by Subchanflow and $T_{fuel}^{doppler}$ is the effective Doppler temperature or the Doppler-weighted temperature used by Serpent 2 to determine the effective cross sections. There is considerable spatial self-shielding of 238-U absorption, and much of the absorption occurs near the surface of the fuel where steady-state temperatures are lower, so assuming an average of temperatures between $T_{fuel}^{surface}$ and T_{fuel}^{center} is not entirely accurate. For them, a weight $(1.0 - \alpha)$ is assigned to the center temperature and (α) to the surface temperature, this value being aimed at evaluating the magnitude of the Doppler coefficient mainly in the surface part of the fuel. A value of $\alpha = 0.7$ or $\alpha = 5/9$ are highly recommended according to the studies of (de Kruijf and Janssen, 1996), (Goltsev, et al., 2000).

The convergence criteria and relaxation schemes used to ensure the stability of the iterative process are also implemented in Serpent2/Subchanflow and are specified by the user-defined. In the first case, the convergence criteria, the L_2 and L_∞ norms are enabled for both the fuel and the coolant by Eqs. (4.10) and (4.11)

$$\epsilon_T^{L_2} = \frac{\sqrt{\sum_{i,j,k} (T^t[i,j,k] - T^{t-1}[i,j,k])^2}}{\sqrt{ijk}}; \quad (4.10)$$

$$\epsilon_T^{L_\infty} = \max_{(i,j,k)} \{|T^t[i,j,k] - T^{t-1}[i,j,k]|\}; \quad (4.11)$$

where t is the iteration step, i, j, k denotes the position and ϵ is the convergence scalar.

However, cases have been reported where the above convergence criteria do not ensure that Picard iteration converges without changing the scheme. In these cases, some issues have been observed, such as unstable iteration processes and oscillations in the flux and fuel temperature. For e.g., when there are large power peaks, this leads to large temperature peaks, but in the subsequent iteration, this temperature rise leads to a local increase in neutron absorption due to the Doppler effect, which causes a local depression of the flux and another peak as power is conserved. The simplest method to solve this issue in the neutron and thermal-hydraulic systems is to use a relaxation scheme described in Eq. (4.12)

$$\tilde{T}^t[i,j,k] = T^{t-1}[i,j,k]\omega + (1 - \omega)T^t[i,j,k]; \quad (4.12)$$

here, T is the target thermal-hydraulic field, which can be the fuel temperature, the coolant temperature, or the coolant density. The value of ω is called the relaxation factor and ranges from 0 to 1. A value of $\omega = 1$ means that no relaxation is considered in the Picard system. For smaller values of ω , convergence is achieved more quickly. A value of $\omega = 0.5$ seems to give stable results, as confirmed by (Gill, et al., 2017). The use of this type of relaxation of the thermal-hydraulic parameters provides a very efficient coupled solution for steady state, theoretically it could also be used for transient simulations, although this would significantly increase the computational effort required (Gill, et al., 2017).

4.3.3 Challenges of the coupling approach

In the Serpent2/Subchanflow coupling system, the IFC files transfer their results from node to node and, if necessary e.g. in case of complicated geometries, the nodes can be remapping. This approach and the superposition of meshes on complex models for abstract cores is one of the features used in the analysis of research reactors design (Ferraro, 2021).

4.4 Subchanflow limitation for the analysis of MTR-cores

Subchanflow is a thermal-hydraulic code developed for power reactor analysis that does not provide thermal-hydraulic analysis of plate-type research reactor fuel assemblies (Imke and Sanchez-Espinoza, 2012). Using the “equivalent plate” approach, a fuel assembly can be represented by Subchanflow in a simplified manner as it is done by the system thermal-hydraulic codes. The application of this approach to analyze an MTR-core with Subchanflow as it is showing the limitations and the need for code extensions.

According to the "equivalent plate" approach, the dimensions of a “rod” are determined based on the dimensions of the plate. For it, it is necessary to identify the perimeter of the plate, identify the perimeter of the fuel (meat), use the general equation of the perimeter of a circle to obtain the diameter of the “rod”, see Figure 4.7.

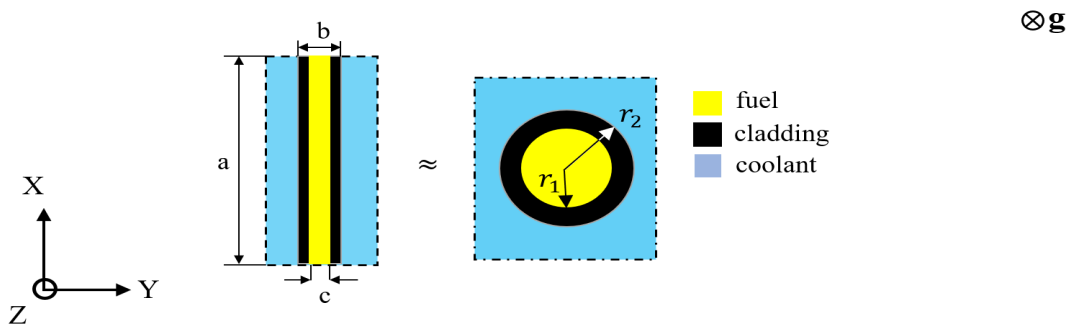


Figure 4.7: Sketch of the equivalent plate approach.

Table 4-1 lists the overall dimensions of a generic IAEA 10 MW reactor loaded with plate-type fuel assemblies and the corresponding dimensions for a rod (IAEA, 1980), (IAEA, 1992b). The full description of this reactor used to test the prediction capabilities of thermal-hydraulic codes, can be found in Appendix C.

Table 4-1: Typical dimensions of a plate and rod.

Perimeter (plate)	Diameter (rod)
Cladding, 0.1328 [m]	0.0423 [m]
Fuel, 0.1259 [m]	0.0401 [m]

In this exercise, the Dittus-Boelter and Blasius correlations for heat transfer and pressure drop as implemented in Subchanflow are used. The 60 cm long fuel assembly is axially discretized into 10 nodes. The representative fuel rod is radially subdivided in three nodes within the fuel and two nodes for the aluminum cladding. Table 4-2 contains the initial operating conditions for the case study of a simple fuel assembly.

Table 4-2: Single fuel assembly, operational conditions.

Parameter	Value
Pressure out [Pa]	1.56e5
Inlet temperature [°C]	38
Inlet flow rate [kg/s]	8.169
Total Power [W]	417.422

The MTR-core exercise is described in (Slabbert, 2011) for comparative analysis of the code's prediction capabilities using the "equivalent plate" approach. In Figure 4.8, the axial core averaged temperature of the coolant, cladding, and fuel as predicted by Subchanflow based on the "equivalent plate" approach is shown. There can be observed that the peak of the fuel temperature is around 154.66 °C and the one of the cladding is about 78.38 °C. The maximum coolant temperature is around 50.23 °C.

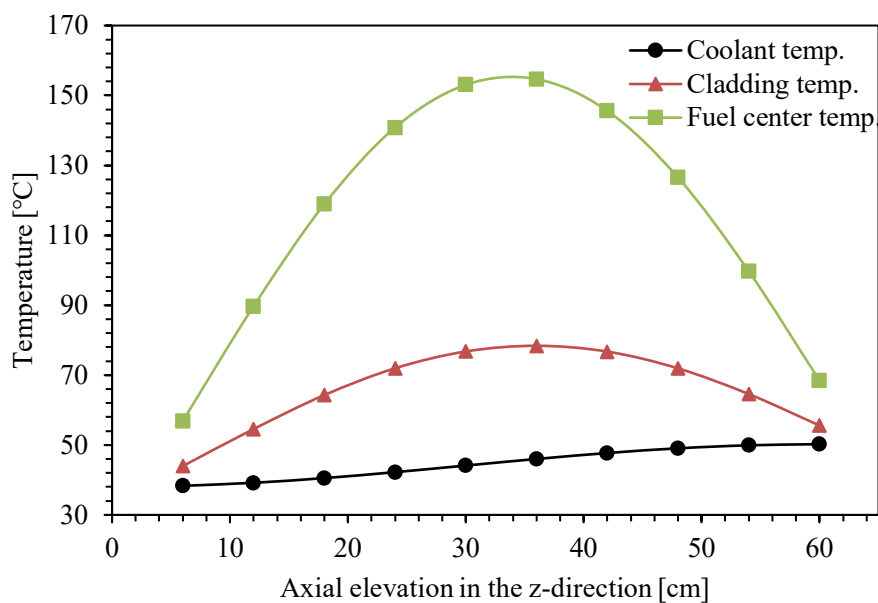


Figure 4.8: Coolant, cladding and fuel center temperature profiles of a single fuel assembly using Subchanflow.

Contrary to Figure 4.8, Figure 4.9 shows the axial averaged temperature profiles of the coolant, cladding, and fuel predicted by the dedicated thermal-hydraulic code Flownex® version 8.0, specifically developed for thermal-hydraulic analysis of plate type reactors (Slabbert, 2011).

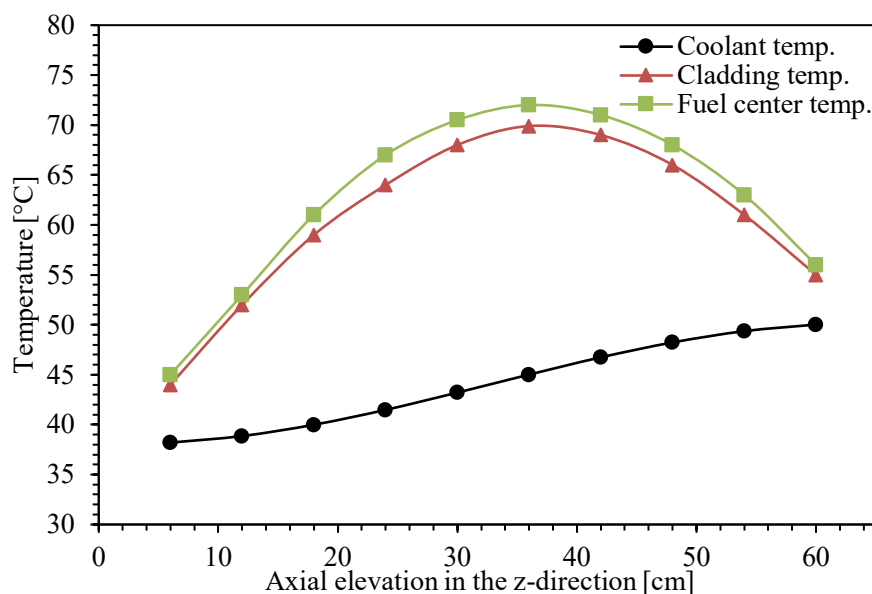


Figure 4.9: Coolant, cladding and fuel center temperature profiles of a single fuel assembly using Flownex® (Slabbert, 2011).

Based on Figure 4.8 and Figure 4.9, it can be concluded that the "equivalent plate" approach is not sufficient to predict the key parameters of cores loaded with plate-type fuel. The temperatures estimated by Subchanflow of the cladding and fuel are not comparable with the reference values of the Flownex® code. However, for the coolant temperature profile calculated by Subchanflow, there is remarkable consistency with the results obtained using the Flownex® code, suggesting proper operation of the energy conservation equation. In order to achieve accurate description and comprehensive thermal-hydraulic analysis of fuel plates and coolant channels in research reactors, it is necessary to extend the capabilities of the Subchanflow code. These extensions will make it possible to perform analyses without approximations and, moreover, will facilitate the coupling of the Subchanflow code with neutron codes for high-fidelity analyses. In this way, it will be possible to obtain a more accurate and detailed assessment of the thermal-hydraulic aspects in the research reactors and to optimize the understanding and analysis of their behavior. Consequently, the following extensions and improvements of Subchanflow have been identified for realistic analysis of research reactors with MTR cores: a) heat conduction for thin plates, b) specific heat transfer correlations for narrow rectangular channels that can be found in MTR cores such as the one developed for the JRR-3 reactor (Sudo, et al., 1990), and c) pressure drop correlations that apply to square and narrow cooling channels. In addition, some research reactors with a thermal power of less than 10 MW operate with downward flow along the core. Therefore, it is necessary to extend the range of coolant channel orientation described in Eq. (4.2), which will allow thermal-hydraulic analysis of both downward and upward cores.

5 Extension of Subchanflow for the analysis of MTR-cores

In order to extend the capabilities of Subchanflow for the analysis of plate-type reactors, the following code extensions are necessary: a heat conduction solver for plates, heat transfer correlations relevant for narrow rectangular channels and downward coolant flow.

5.1 Implementation of heat conduction solver for plates

Figure 5.1 shows the overall flowchart of the steady-state and transient solution approach of Subchanflow, where a highlighted box indicates the heat conduction solver for rods and the new solver implemented for plates.

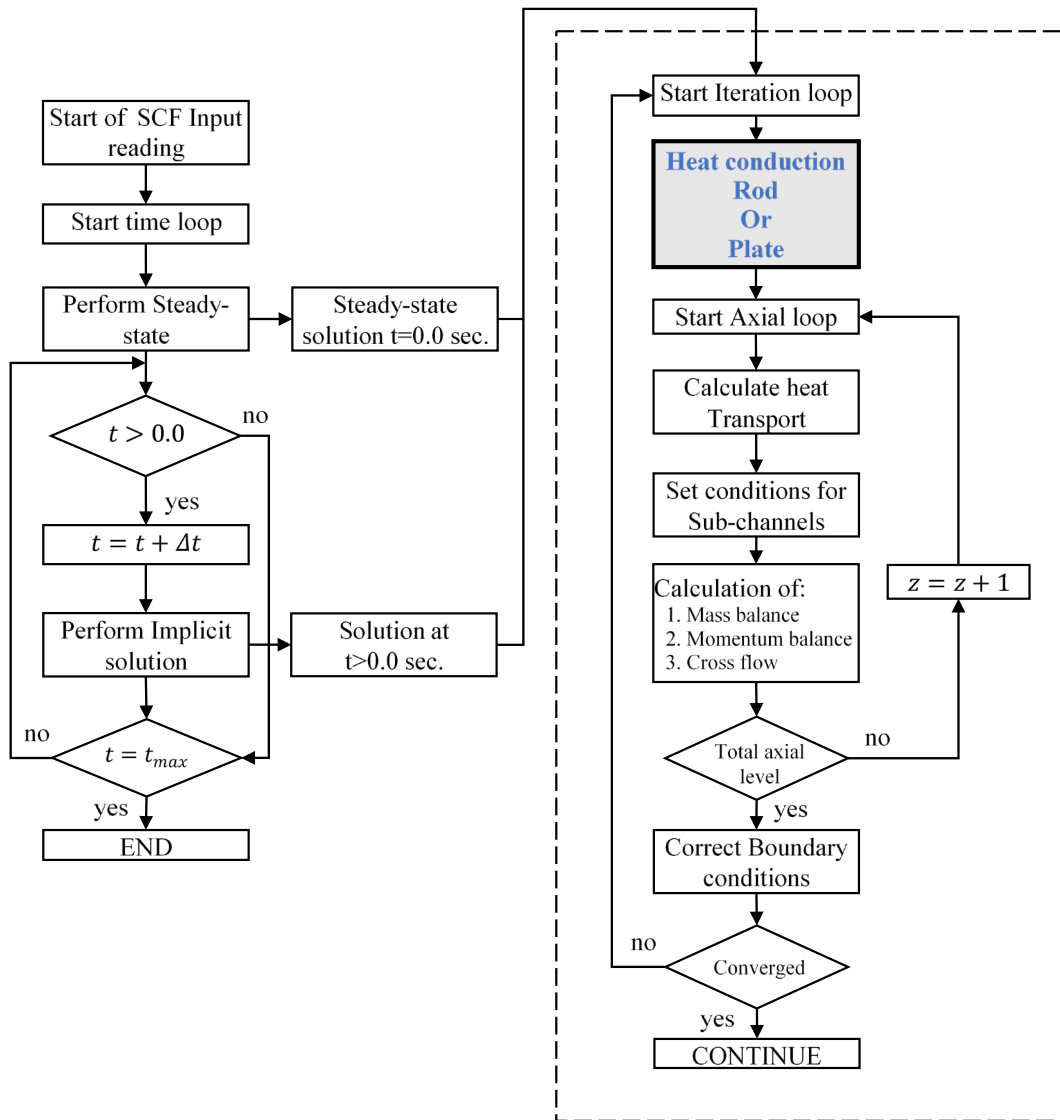


Figure 5.1: Subchanflow flowchart of solution procedure.

In the flowchart, it can be seen that Subchanflow always calculates a steady-state in a first step and, followed by a transient simulation if necessary. Within the iteration loop, which depends on the fuel geometry (now plate or rod), temperatures are calculated along the entire axial length. For more information on the heat conduction solver, please refer to Appendix A. Subsequently, subchannel conditions are then established to solve the mass, momentum and energy equations at the axial cell level in the z -direction. The stationary and transient conditions are completed when the solution converges within certain accuracy criteria for the main variables. The convergence limits must be given by the user and range from $1.0e-5$ - $1.0e-3$ for flow convergence and about $1.0e-3$ if a pressure boundary condition must be met. The number of iterations required to achieve the convergence values varies between 20 and 50, although it may be higher for more complex or larger scale system analyses.

5.2 Description of the heat conduction solver

Eq. (3.1) is used to deal with heat conduction in a plate-type fuel element (Duderstadt and Hamilton, 1976), (Incropera and DeWitt, 1996). However, for its application, the assumptions mentioned in Section 4.1.2 must be considered. First, the lumped parameter method is not appropriate because it does not provide detailed information about the temperature distribution within the material, although the Biot number for a fuel plate has a value of about 0.05 (El-Khatib, 2013). However, assuming that a one-dimensional analysis is accurate for Biot numbers less than 1, it is reasonable to assume that if the fuel plate is thin in one axis and expands considerably in the other two remaining axes of a three-dimensional system, heat conduction will occur mainly along the shorter dimension, simplifying the study from three dimensions to one (Lahey and Moody, 1993). Figure 5.2 shows an example of a plate-type fuel element where heat conduction occurs in one dimension in the y -direction. The fuel and cladding are assumed to be in perfect contact, so the thermal resistance between the two can be considered negligible. The heat (q''') generated by the fuel passes to the cladding, and assuming that the cladding thickness (δ_c) and downward mass flow rate is the same in the both side of plate, the maximum temperature (T_{max}) will be found at the center. The downward flowing coolant with a temperature T_f dissipates the heat deposited in the fuel. T_{ci} and T_{co} are the temperatures inside and outside the plate (Todreas and Kazimi, 1990).

If the fuel plate is thin and extends in the x and z directions considerably more that it does in the y direction, the heat conduction in the x and z directions can be eliminated by assuming

$$K_c \frac{\partial T}{\partial x} \cong K_c \frac{\partial T}{\partial z} \cong 0 \quad (5.1)$$

simplifying the general heat conduction Eq. (3.1) by a homogeneous partial differential equation of second order:

$$\rho C_p \left(\frac{\partial T}{\partial t} \right) = \frac{\partial}{\partial y} K_c \left(\frac{\partial T}{\partial y} \right) + q''' \quad (5.2)$$

where, C_p is the heat capacity, K_c the heat conductivity and ρ the density.

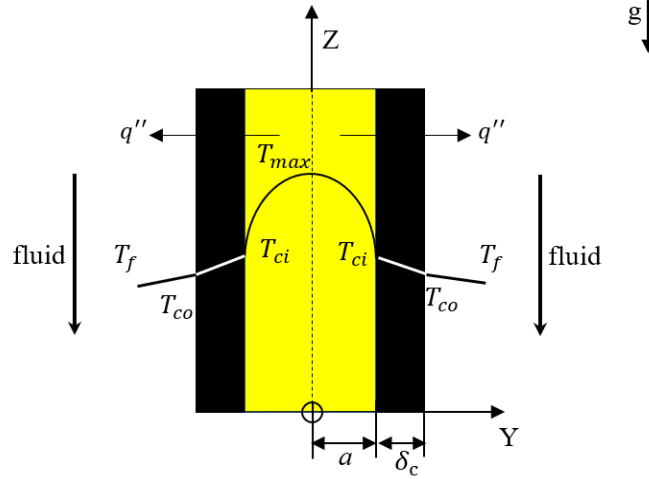


Figure 5.2: Sketch of plate fuel element with symmetrical boundary conditions.

Eq. (5.2) describes the mechanism of one-dimensional conduction heat transfer in a transient state in which the temperature is dependent on the position y and time t . To perform a steady-state heat conduction analysis, the $\rho C_p \left(\frac{\partial T}{\partial t} \right)$ term of Eq. (5.2) is simplified to obtain a new expression in which the temperature will depend entirely on the y -position,

$$\frac{\partial}{\partial y} K_c \left(\frac{\partial T}{\partial y} \right) + q''' = 0. \quad (5.3)$$

In the absence of any heat source or sink at $y = 0$, no heat flux should cross the plane. Hence:

$$K_c \left. \frac{dT}{dy} \right|_{y=0} = 0. \quad (5.4)$$

Applying the boundary condition given in Equations (5.4) to (5.3), the following expression describing the heat conduction in the fuel is obtained,

$$k_{fuel}(T_{max} - T_{ci}) = q''' \frac{a^2}{2}. \quad (5.5)$$

The heat conduction in the cladding can also be assumed to be a one-dimensional, so that Eq. (5.3) also applies in the cladding. The heat conduction equation is given by:

$$T_{co} = T_{ci} - q'' \frac{\delta_c}{K_{clad}}. \quad (5.6)$$

5.3 Heat transfer correlations for narrow rectangular channels

The fuel elements used in research reactors consist of a series of thin plates spaced parallel to each other. The coolant flows up or down through the narrow rectangular channel formed between

the plates. Convective heat transfer studies in narrow rectangular channels are limited compared to those performed in circular geometries because the experimental setups are more complex to construct, measure and test. Research reactors often have rectangular channels with very different aspect ratios. E.g., consider the ratio r between the width w and thickness d of the channel, as shown in Figure 1.7. If $r = w/d \ll 1$, the channel is classified as narrow. However, to be more specific, (Kandlikar and Grande, 2003) proposes a classification based on the minimum channel dimension d . This classification distinguishes between nanochannels and mini-channels. In the case of MTR research reactors, narrow channels would be classified as mini-channels according to the scale proposed by (Kandlikar and Grande, 2003). A mini-channel is defined as a channel whose minimum dimension is in the range of $200 \mu\text{m} < d \leq 3\text{mm}$. However, it is important to note that this value may be questionable, as there are experimental data from reactors where the minimum channel dimension is 4.547 mm (IAEA, 2019). Therefore, based on the available experimental data, it can be established that an $r < 0.07$ is considered a narrow channel.

In most reactors, the coolant flowing through the channels formed by the surrounding walls may be a simple liquid such as water or, in more complex systems, carbon dioxide, helium, or liquid metal. The coolant always flows through a channel and can never flow freely through the reactor core, so the flow behavior follows closed flows. Closed flows are characterized by viscosity dominating the entire flow field. This means that the frictional forces generated at the channel walls cause the different layers of the fluid to move at different speeds. The slower layer tries to slow down the faster one, resulting in a loss of kinetic energy. This kinetic energy is converted into small vortices that form at the boundary between the opposing layers (Masterson, 2020).

Figure 5.3 shows the phases through which an upward flowing fluid pass. When a moving fluid presents turbulence in both its velocity and temperature distributions, and these distributions remain constant as the fluid moves along the channel, the flow is said to be fully hydrodynamically and thermally developed turbulent flow. In this type of flow, turbulence significantly enhances heat transfer compared to laminar flow. The presence of vortices and eddies in a turbulent flow agitates the fluid in motion and promotes more effective mixing by increasing heat transfer between the fluid and the walls of the fuel elements. The agitation of the fluid in the turbulent flow promotes a more uniform temperature distribution in the fluid and avoids the formation of stagnant thermal layers near the fuel element walls. For these reasons, most attempts to understand the behavior of the fluid in rectangular channels wait until a state of fully developed turbulent flow conditions is reached to perform measurements and tests.

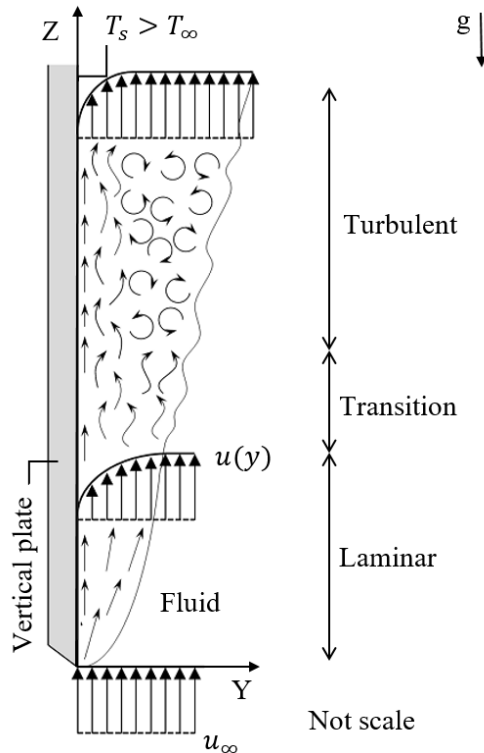


Figure 5.3: Boundary layer development on a hot vertical plate with velocity profiles (u); artwork obtained and adapted from (Frei, 2017).

The heat transfer from the plate to the fluid follows the convention given in Eq. (3.4). The term h_{coef} in Eq. (3.4) is known as the heat transfer coefficient and is obtained by Eq. (3.5). The terms of hydraulic diameter D_h and fluid conductivity C are easily determined. The term Nu , called the Nusselt number, can be obtained from correlations obtained from experiments. In the past, the McAdams correlation, commonly known as the (Dittus and Boelter, 1985), and its derivative forms, Sieder-Tate and Colburn, have been used for the design and safety analysis of the cooling channels of MTRs, although they have been developed for circular tubes (Sudo, et al., 1985).

Since 1959, several experimental devices have been constructed to evaluate the suitability of applying correlations for circular tubes to rectangular channels. E.g., results presented by (Levy, et al., 1959) showed that heat transfer rates under fully developed turbulent flow conditions are 30% to 45% lower than those predicted by the Sieder-Tate equation and 15% to 30% lower than most values reported for flow in circular tubes. Later experiments conducted in 1961 by (Gambill and Bundy, 1961) for the study of the high flux isotope reactor (HFIR) showed that the measured heat transfer coefficients ranged from 10% to 20% higher than those predicted by the Sieder-Tate correlation.

In 1969, further studies have been performed in rectangular channels, this time focusing on the MITR reactor. Single-phase heat transfer coefficients 12% higher than those obtained with the modified Colburn correlation are obtained. Water properties are evaluated at film temperature

(Spurgeon, 1969). Later, between 1985 and 1990, (Sudo, et al., 1985) and (Sudo, et al., 1990) performed studies for the JRR-3 reactor using downward and upward flows. In this series of experiments, Sudo & team recommend the use of the Dittus-Boelter correlation and suggests its correlation for turbulent flows with a dispersion of $\pm 20\%$. Recent studies for the RA-6 and HFIR reactors suggest the use of the Gnielinski correlation. In the case of the RA-6 device, the use of the Gnielinski correlation is recommended with modifications depending on the value of the Reynolds number obtained with a dispersion range of $\pm 8\%$ (Silin, et al., 2012). On the other hand, (Bodey, 2014) uses the Gnielinski correlation without modifications and obtains a dispersion of $\pm 7.1\%$.

Finally, based on these previous studies, Table 5-1 shows a summary of the reported heat transfer correlations for flow development in a narrow vertical channel (Forrest, et al., 2016). However, there are conflicting data and experimental data are still lacking to fully understand the heat transfer characteristics in narrow channels (Jo, et al., 2014). It should also be emphasized that the studies are very old and the effects of roughness and defects such as wear blisters on the plates are still being investigated (Li, et al., 2019).

Table 5-1: Heat transfer correlations used to analysis of narrow rectangular channels.

Institution/Reactor	Pressure (MPa)	Correlation	Reynolds/Prandtl	Name/Ref
ORNL/HFIR	0.1-3.95	$Nu = 0.027Re^{0.8}Pr^{\frac{1}{3}}(\mu_b/\mu_w)^{0.14}$ The bulk-to-wall viscosity factor, 1.02	$1.14 \times 10^4 < Re < 1.65 \times 10^5$ $1.7 \leq Pr \leq 2.8$	Sieder-Tate / (Gambill and Bundy, 1961)
MIT/MITR	~0.1	$Nu = 0.023Re^{0.8}Pr^{1/3}$	$6.5 \times 10^3 < Re < 20 \times 10^3$ $0.71 \leq Pr \leq 5.7$	Colburn / (Spurgeon, 1969)
JAERI/JRR-3	~0.1	$Nu = 0.023Re^{0.8}Pr^{0.4}$	$500 < Re < 50 \times 10^3$	Dittus-Boelter / (Sudo, et al., 1985)
JAERI/JRR-3	~0.1	$Nu = \frac{0.0296Re^{0.8}Pr}{[1 + 1.54Pr^{-\frac{1}{4}}Re^{-0.1}(Pr - 1)]}$	$2200 < Re < 16 \times 10^3$ $3 \leq Pr \leq 6$	Y. Sudo / (Sudo, et al., 1990)
ORNL/HFIR	~0.13	$Nu = \frac{(f/8)(Re - 1000)Pr}{[1 + 12.7(f/8)^{1/4}(Pr^{2/3} - 1)]}$	$2100 < Re < 5 \times 10^6$ $2.2 \leq Pr \leq 5.4$	Gnielinski / (Bodey, 2014)

5.4 Extension to consider the effect of downward coolant flow

In research reactors, control of coolant flow is critical to the safe and efficient operation of the system. Coolant flow can be either upward or downward, and each of these options has its own characteristics and limitations.

Most high-power research reactors (greater than 20 MW) operate with upward flow similar to power reactors (El-Din El-Morshedy, 2011). Reactors cooled with upward forced convection have the main advantage of avoiding the phenomenon of flow reversal in the core. Upward flow can provide adequate core cooling, but requires adherence to a strict protocol if the reactor needs

to be shut down for maintenance. When the reactor must be shut down the coolant pumps gradually stop supplying coolant so that, in the absence of the neutron control rods to regulate power, the coolant will start to boil on the fuel element walls, drastically changing the pressure and temperature conditions. Under these conditions, the coolant can no longer be considered incompressible and new phenomena must be addressed to characterize the coolant. If an event such as the one described above occurs, the cooling of the core would be mainly by natural convection flow. Natural convection flow is determined by the dimensionless Grashof number, which describes the relationship between the buoyancy force and the viscous force acting on the fluid. These parameters assume that the thermodynamic properties of the fluid, such as density, change in response to temperature at constant pressure. This simplification is known as the Boussinesq approximation. Since the effects of buoyancy are limited to the momentum equation, the mass and energy conservation equations are not changed with respect to forced convection (Incropera and DeWitt, 1996).

On the other hand, there is downward flow, which is limited to low-power research reactors such as RA-6 (Villarino and Doval, 2011) and IEA-R1 (Castellanos-Gonzalez, et al., 2018) for safety reasons. In the fluid is downward the flow reversal phenomenon can occur either due to a blocked cooling channel at the top or due to a low velocity of the cooling fluid, resulting in Reynolds numbers in the laminar region below 700. Thus, if it is ensured that the fluid has no obstructions in the channel and the Reynolds number is in the turbulent range (> 4000), the momentum equation would be approached in the same way as if the fluid is ascending. Also, consider that the effects of increased fluid velocity within the channel are irrelevant due to gravity acceleration (Sudo, et al., 1985). To distinguish whether a reactor is cooled with downward or upward flow, the thermal-hydraulic code of Subchanflow expands the θ term that handles the channel orientation in Eq. (4.2) from $0^\circ \leq \theta \leq 90^\circ$ to $0^\circ \leq \theta \leq 180^\circ$ (see Figure 5.4). This expansion means that if the flow is downward, the reference point $z = 0$ is at the top of the core and the increments are from top to bottom. In contrast, if the reactor is cooled with an upward flow, the reference point $z = 0$ is at the bottom of the core and the increments will be upward. This allows a clear distinction between the two types of flows and a correct adjustment of the calculations and considerations in the thermal-hydraulic code of Subchanflow.

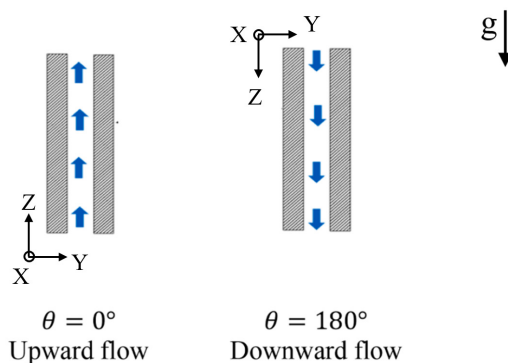


Figure 5.4: Schematic of the mass flow directions available in the extended Subchanflow code.

6 Validation of Subchanflow using the data of the RA-6 facility

6.1 Overall validation approach

Before entering into a validation of the Subchanflow thermal-hydraulic code, either alone or in its coupled version with the Monte Carlo Serpent 2 code, it is first necessary to verify the correct implementations and code extensions. It has been done after each modification/extension of the code, where it has been demonstrated that the code modifications do not deteriorate the numerical calculation schemes. A very important step is the validation of the code's capability by using appropriate and relevant experimental data gained either in test facilities or in research reactors.

Figure 6.1 shows the strategy followed for the validation of Subchanflow as stand-alone and of the coupled Serpent2/Subchanflow code. Experimental data have been collected from the literature and published by various research institutes, e.g., the RA-6 experimental facility, the Instrumented Fuel Assembly (IFA) of the IEA-R1 reactor and the SPERT IV D-12/25 reactor, and the solutions of the generic IAEA-10 MW reactor.

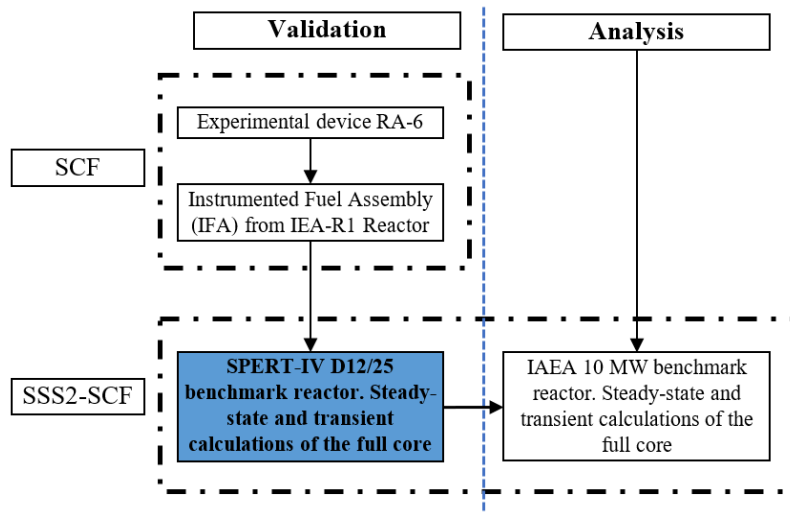


Figure 6.1: Strategy to follow for Subchanflow and Serpent2/Subchanflow validation.

6.2 Description of the RA-6 facility

To support the design and construction of MTR research reactors, Centro Atómico Bariloche, together with the Balseiro Institute of Argentina developed an experimental facility between 2000 and 2005 called RA-6. The experimental facility, RA-6, is a 1:1 scale representation of a coolant channel formed by the typical fuel plates of an MTR reactor. Tests have been performed in this

facility to investigate the thermal behavior of MTR fuel assemblies during transient and steady-state operation. Part of the experimental results obtained have been published and used to validate and improve thermal hydraulic codes (Silin, et al., 2009). Figure 6.2 shows a representation of the RA-6 experimental circuit, which consists of a pressurized hydraulic loop, electrical systems, and data acquisition systems. The hydraulic loop system has two water tanks, a main tank that supplies water to the system and an auxiliary tank that stores water coming from the test section. The water is circulated through 20- and 50-micron filters to deionize it and retain particles. Pressure is measured with a JUMO pressure transducer and a differential pressure level gauge (DP cell). The flow rate is controlled by a valve downstream of the test section (Silin, et al., 2010). The Bruker power supply BMN 70/700 provides the electrical power to the system, which is responsible for heating the walls of the test section. Temperature measurements are performed using K-type thermocouples and TP100 sensors. The analog signals are converted into digital signals, which are then analyzed and stored (Masson, et al., 2008).

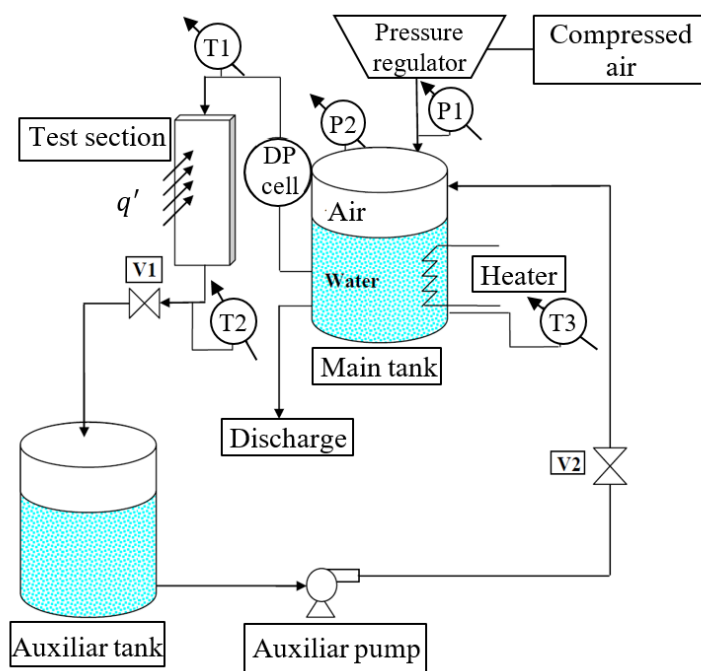


Figure 6.2: Experimental facility RA-6 setup scheme, obtained from (Masson, et al., 2008).

6.2.1 Test section of experimental facility RA-6

The top view of the test section is shown in Figure 6.3. The cooling channel consists of a rectangular section 2.7 mm thick and 60 mm wide. The height of the experimental unit is 76 cm, of which only 62 cm are electrically heated by using heating bands. The aluminum plates that form the channel are thermally and electrically insulated on the back to prevent energy loss and electrical inconvenience. Type K thermocouples are placed along the heated aluminum plates at a depth of 2 mm from the surface. The thickness of the heated aluminum plates can vary from 5

mm to 6 mm, and depending on the type of analysis, the axial position of the thermocouples can vary (Masson, et al., 2008), (Silin, et al., 2009).

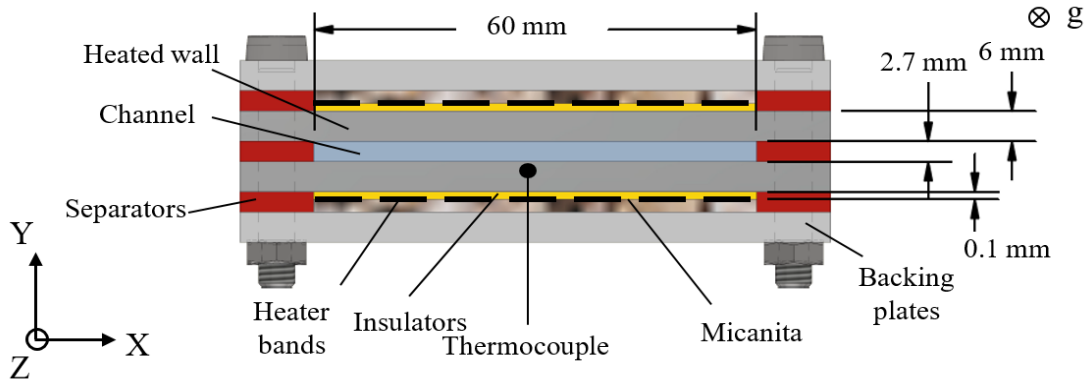


Figure 6.3: Schematic of the top view of the test section, obtained from (Masson, et al., 2008).

Resistance temperature detectors (PT100) are used to measure the coolant temperature at the inlet and outlet of the test section. According to the international standard IEC 751, these sensors provide a tolerance range of ± 0.15 °C (Meijer and Voorwinden, 1991). Aluminum silicate (Micanite) electrically insulates the heating bands of the aluminum plates to prevent short circuits, and post-silicate insulation is also used to prevent heat loss. Regarding the margin of error in temperature measurements, several studies indicate that properly calibrated type K thermocouples have a measurement error on the order of ± 1.1 °C according to ASTM E230 standards (Chen, et al., 2017).

6.2.2 Geometric dimensions of test section of facility RA-6

The overall test section dimensions for three studies cases have been documented and published by (García, et al., 2008), (Silin, et al., 2009) and are summarized in Table 6-1. With the exception of test one, the dimensions of tests two and three are identical. The dimensions of the heater bands together form the width and length of the "fuel dimension". This arrangement is intended to ensure uniform heat distribution over the entire surface of the aluminum plates. The schematic drawing of the test section RA-6 with the axial distribution of thermocouples for the case studies is shown in Figure 6.4.

Table 6-1: Main dimensions for the channel flow, plate and heater bands.

Device parts	Dimensions [m]	Test 1	Test 2	Test 3
Channel flow	Width	0.0600	0.0600	0.0600
	Height	0.7600	0.7600	0.7600
	Thickness	0.0027	0.0027	0.0027
Plate	Width	0.060	0.060	0.060
	Height	0.620	0.620	0.620
	Thickness	0.006	0.005	0.005
Heater bands	Width	0.056	0.06	0.06
	Height	0.62	0.62	0.62
	Thickness	0.0001	0.0001	0.0001

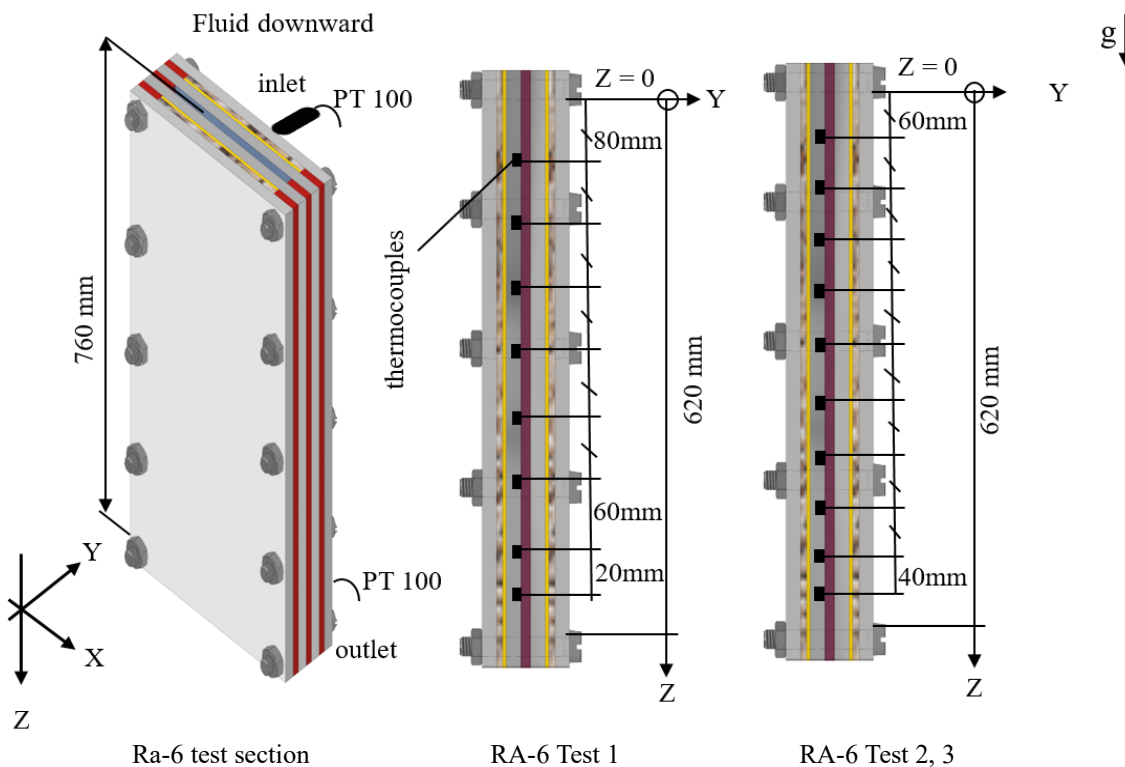


Figure 6.4: Sketch of the axial distribution of the thermocouples installed to measure the temperature of the plates for Tests 1, 2 and 3.

6.2.3 Material properties

To solve the heat conduction in the fuel plate, it is required to know the heat capacity, thermal conductivity and density of the aluminum plate and the heating bands. The heater plates are made of 6061 aluminum and the heater bands are made of 20/80 CrNi alloy. For the specific heat of CrNi alloy, the heat capacity of pure nickel is used because the alloy is the predominant element with 80%. The values are given in Table 6-2.

Table 6-2: Material properties evaluated at 25 °C.

Parameters	Al 6061	CrNi
Conductivity [W/mK]	180	15
Specific heat [J/kgK]	892	130
Density [kg/m^3]	2700	8400

6.2.4 Operating condition of RA-6 facility

Three tests have been designed and carried out with different thermal-hydraulic parameters and different geometrical dimensions., as shown in Table 6-3. The total power supplied for Test 1 is 24 kW (losses to the environment of between 7 and 10% have been reported) (García, et al., 2008). The power supplied for Test 2 and 3 is derived from the heat balance in the flow channel, this value also corresponds to the directly measured electrical power (heat losses have not been reported). To obtain a continuous flow of the coolant, a hydraulic circuit pressurized to 170 kPa is added at the inlet of the test section (upper part, see Figure 6.2), (Silin, et al., 2009).

Table 6-3: Operating conditions for three case studies carried out at the RA-6 experimental facility.

Measurements	Test 1 *	Test 2 **	Test 3 **
Power [W]	21600	19000	25000
Pressure [Pa]	170000	170000	170000
T inlet [°C]	38	38	38
Mass flow rate [kg/s]	0.1615	0.1243	0.1615
Flow direction	Downward	Downward	Downward
* (García, et al., 2008), ** (Silin, et al., 2009)			

6.2.5 RA-6 test conduction

The cooling channel of the RA-6 experimental device consists of two parallel side plates heated by electric heating bands. The heating bands are pressed against the heating plates by a back plate to improve the contact between them. To reduce heat flow to the back plate, the heating bands are electrically and thermally insulated. The heat generated electrically by the Bruker BMN 70/700 source flows through the aluminum plate by heat conduction and from there into the coolant by heat convection. The experimental values obtained during the performance of these tests have been published by (García, et al., 2008) and (Silin, et al., 2009), the results have been digitized using *Digitzelt* software and are presented in Table 6-4.

Table 6-4: Experimental fluid and plate temperature data measured for the three case studies.

RA-6 Measured parameters	Test-1	Test-2	Test-3
Coolant temperature at inlet [°C]	38.00	38.00	38.00
Coolant temperature at outlet [°C]	70.00	75.21	74.9
Pressure at core inlet [MPa]	0.17	0.17	0.17
C.T. at Position-1 [°C]	83.59	92.79	93.87
C.T. at Position-2 [°C]	87.56	97.81	98.31
C.T. at Position-3 [°C]	87.56	98.47	98.05
C.T. at Position-4 [°C]	91.12	101.18	101.34
C.T. at Position-5 [°C]	91.54	102.41	102.98
C.T. at Position-6 [°C]	96.57	104.80	106.27
C.T. at Position-7 [°C]	97.82	105.53	107.25
C.T. at Position-8 [°C]	99.50	106.85	109.06
C.T. at Position-9 [°C]	-	109.32	112.01
C.T. at Position-10 [°C]	-	111.95	114.89
C.T.= Cladding Temperature (position of top to bottom)			

6.3 Development of the Subchanflow model for the RA-6 test section

6.3.1 Assumptions for the Subchanflow model

It is important to note some assumptions and limitations when performing steady-state modeling of the RA-6 device. First, it is assumed that the system is in a steady-state of thermal and fluid equilibrium and that the refrigerant properties and boundary conditions given in Table 6-2 and Table 6-3 are maintained constant over time. In addition, a geometric simplification of the test section RA-6, as shown in Figure 6.5, is required by adjusting the dimensions of the actual

model to those allowed by Subchanflow. Parameters such as channel area, wetted perimeter and heated perimeter must be maintained.

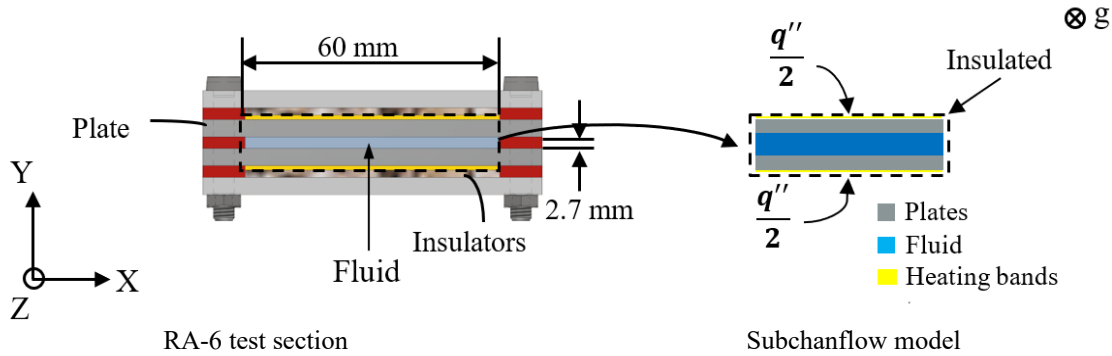


Figure 6.5: Subchanflow model representation.

The test section RA-6, shown on the right side of Figure 6.5, consists of a single cooling channel and two plates. Since the computational cost is not a constraint in this simulation, it is proposed to use 100 axial nodes to achieve higher accuracy and to evaluate the thermal-hydraulic properties in more detail in the axial direction. Figure 6.6 shows the distribution of axial and radial nodes in the array. In this case, 3 nodes are assigned for the heating bands (fuel) and 2 nodes for the aluminum cladding, which allows a more accurate coverage of the thermal properties of these components.

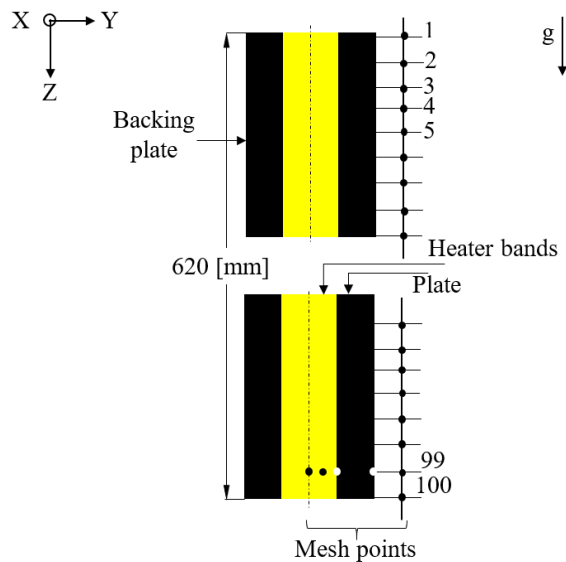


Figure 6.6: Axial and lateral (y-direction) discretization of the heater bands and plate.

6.3.2 Selected heat transfer and pressure drop correlations

Five Subchanflow simulations per Test have been performed with the previously described model using five different heat transfer correlations implemented in Subchanflow: Colburn, Dittus-Boelter, Gnielinski, Sieder-Tate, and Y-Sudo, see Table 5-1. In all simulations performed,

the specific Blasius correlations recommended by (Li and Zhang , 2010) have been used to calculate the friction factors in laminar and turbulent flow regimes. These correlations are summarized in Table 6-5.

Table 6-5: Friction factor for rectangular channels.

Friction factor	Correlation
Laminar	$f = 96Re^{-1}$
Turbulent	$f = 0.3164Re^{-0.25}$

6.4 Comparison of measured and predicted data

Table 6-6 shows the experimental temperature results along with the temperature values predicted by Subchanflow for Tests 1, 2, and 3. The measured experimental data correspond to the fluid temperature at the outlet of the RA-6 test section. It can be seen that the increase in fluid temperature that occurs throughout the test section is due to the heat provided by the heater plates. A margin of error in the measurement of the temperatures of ± 1.1 °C is considered, which, together with the calculated absolute error (which varies between 0.11 °C and 0.66 °C), shows that the Subchanflow predictions have excellent agreement with the experimental values. The simulations show that the values calculated by Subchanflow predict the coolant temperatures with acceptable accuracy. It is important to note that these validation tests have been carried out at different operating conditions, as shown in Table 6-3.

The experimental power measured for Test 1 is 21.6 kW at a mass flow rate of 0.1615 kg/s; the fluid temperature gradient calculated with Subchanflow between the inlet and outlet of the RA-6 test section is 31.89 °C, assuming a specific heat of water of 4.186 J/g-K; the calculated power is 21.56 kW. The relative error between both powers is 0.18%, indicating that the values calculated by Subchanflow are satisfactorily close to the experimental values. The calculated power for Tests 2 and 3 is 19.01 kW and 25.02 kW, respectively. This results in a relative power error of 0.05% for Test 2 and 0.08% for Test 3. It can be seen that the calculated power overestimates with respect to the experimental power in Tests 2 and 3, and slightly underestimates in Test 1. These results strongly support the conclusion that the energy conservation equation used in Subchanflow converges exceptionally well overall, demonstrating its ability to reliably and accurately predict the powers in the study system.

Table 6-6: Comparison of channel outlet temperature predicted by the code Subchanflow vs experimental data.

Case study	Outlet temperature fluid [°C]		
	Experimental	Subchanflow	Absolute error
Test 1	70.00 \pm 1.1°C	69.89	0.11
Test 2	75.21 \pm 1.1°C	74.55	0.66
Test 3	74.90 \pm 1.1°C	75.01	0.11

The experimental temperature values measured on the heating plate surface are presented below together with the temperature values calculated by Subchanflow. The 5 correlations listed in Table 5-1 have been used for each of the Tests.

Figure 6.7 shows the experimental and calculated temperature values of the heater plate for Test 1. It can be observed that the measured values increase from the upper to the lower part of the RA-6 test section (z-axis, see Table 6-4), which is due to the fact that the coolant flow is downward. It can also be observed that the measured temperature values do not develop in a sustained manner, presenting a fluctuating behavior. This behavior may be due to power losses to the environment between the elements supplying electrical energy and the heating bands (recorded in 7% by (García, et al., 2008) for Test 1) or to the formation of aluminum oxide layers on the surfaces of the plates (Masson, et al., 2008). Comparing the measured values and the predictions, it is found that the Colburn correlation has a higher overprediction of the plate temperature compared to the Y-Sudo correlation. Subchanflow predicts the plate temperatures very close to the experimental values when the Dittus-Boelter and Gnielinski correlations are used. The Sieder-Tate correlation tends to predict temperatures near the inlet slightly below the mean, but agrees with experimental values at the outlet of the RA-6 device.

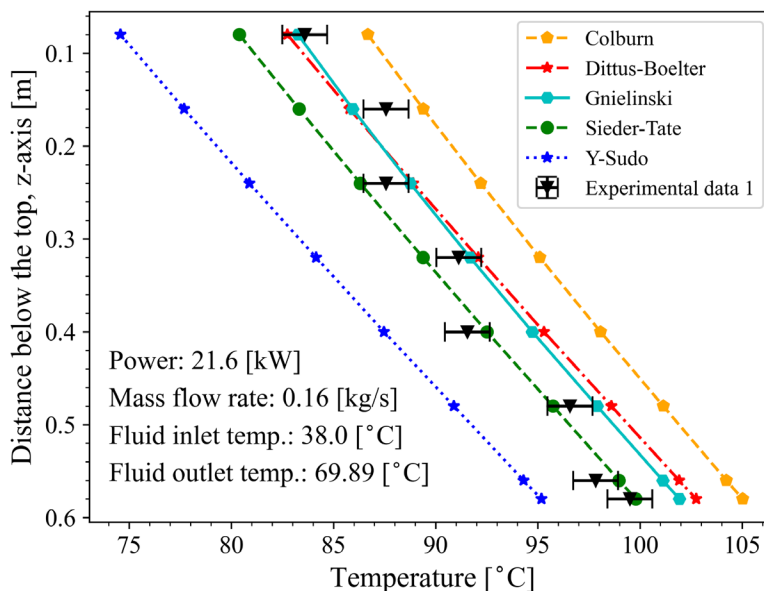


Figure 6.7: Comparison of measured plate temperature with predicted temperature using different correlations for the Test 1.

Figure 6.8 and Figure 6.9 show the comparison of the heating plate temperature values, obtained by Subchanflow, with experimental data corresponding to Test 2 and Test 3. When the Colburn correlation is used, excellent agreement is observed between the values predicted by Subchanflow and the experimental values. However, when the Y-Sudo correlation is used to calculate the plate temperature, results significantly different from the experimental values are obtained at all points studied.

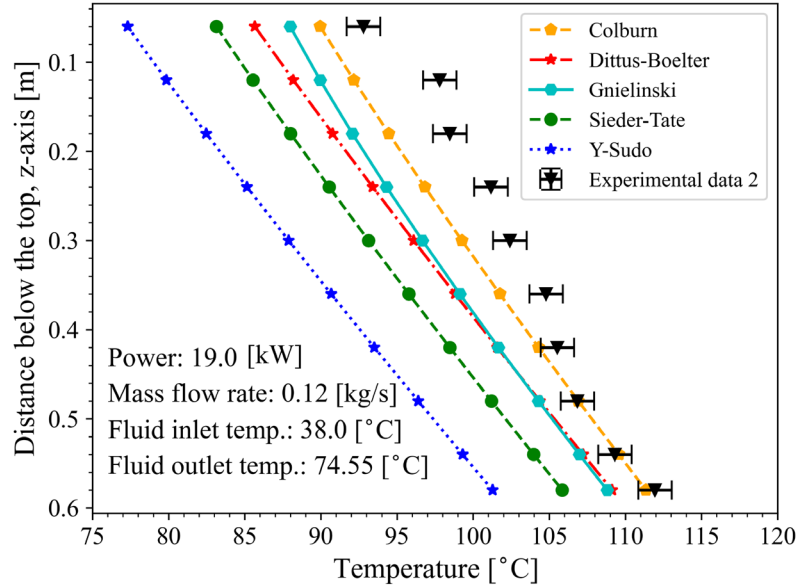


Figure 6.8: Comparison of measured plate temperature with predicted temperature using different correlations for the Test 2.

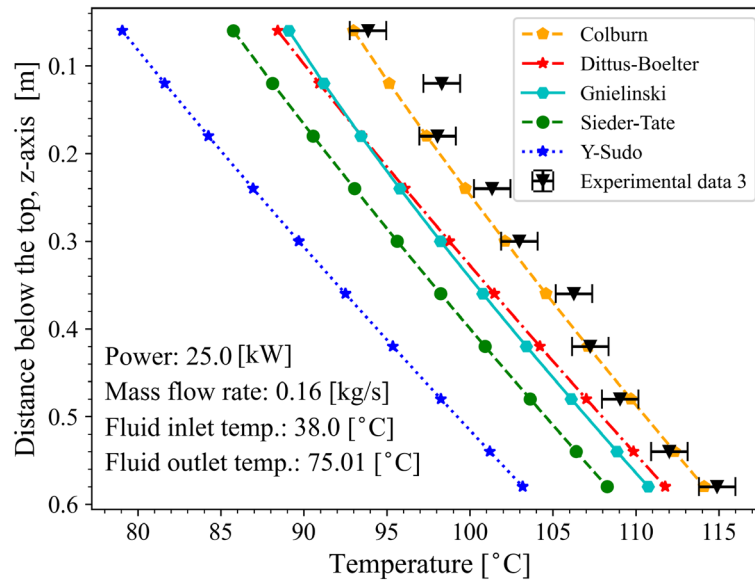


Figure 6.9: Comparison of measured plate temperature with predicted temperature using different correlations for the Test 3.

Figure 6.10 shows the axial variation of the temperature difference, represented as d , for each of the five correlations used in the study. The temperature difference is calculated by a simple mathematical expression: $d = T_{pre.} - T_{ext.}$, where $T_{pre.}$ is the temperature predicted by Subchanflow and $T_{ext.}$ is the measured experimental temperature. When the Colburn correlation is used, all deviations of the predictions from the data are within ± 7 °C, Figure 6.10 (a). Subchanflow predictions for Test 3 have the smallest deviation from the data, followed by Test 2 and Test 1.

When the Dittus-Boelter correlation is used, Figure 6.10 (b), under-prediction and over-prediction of the cladding temperature are observed. The range of deviation of the simulations from

the data is about ± 10 °C. Figure 6.10 (c) shows the deviation of the predictions from Subchanflow using the Gnielinski correlation compared to the data. It can be seen that the measured data are below/above the predictions and that the deviation is in the range of ± 8 °C. For the Sieder-Tate and Y-Sudo correlations, the deviations are the largest, i.e., in the range of ± 13 C and ± 18 °C, Figure 6.10 (d) and (e). The deviations between the predictions and the data obtained for Test 2 and Test 3 clearly show an underestimation of the data by Subchanflow.

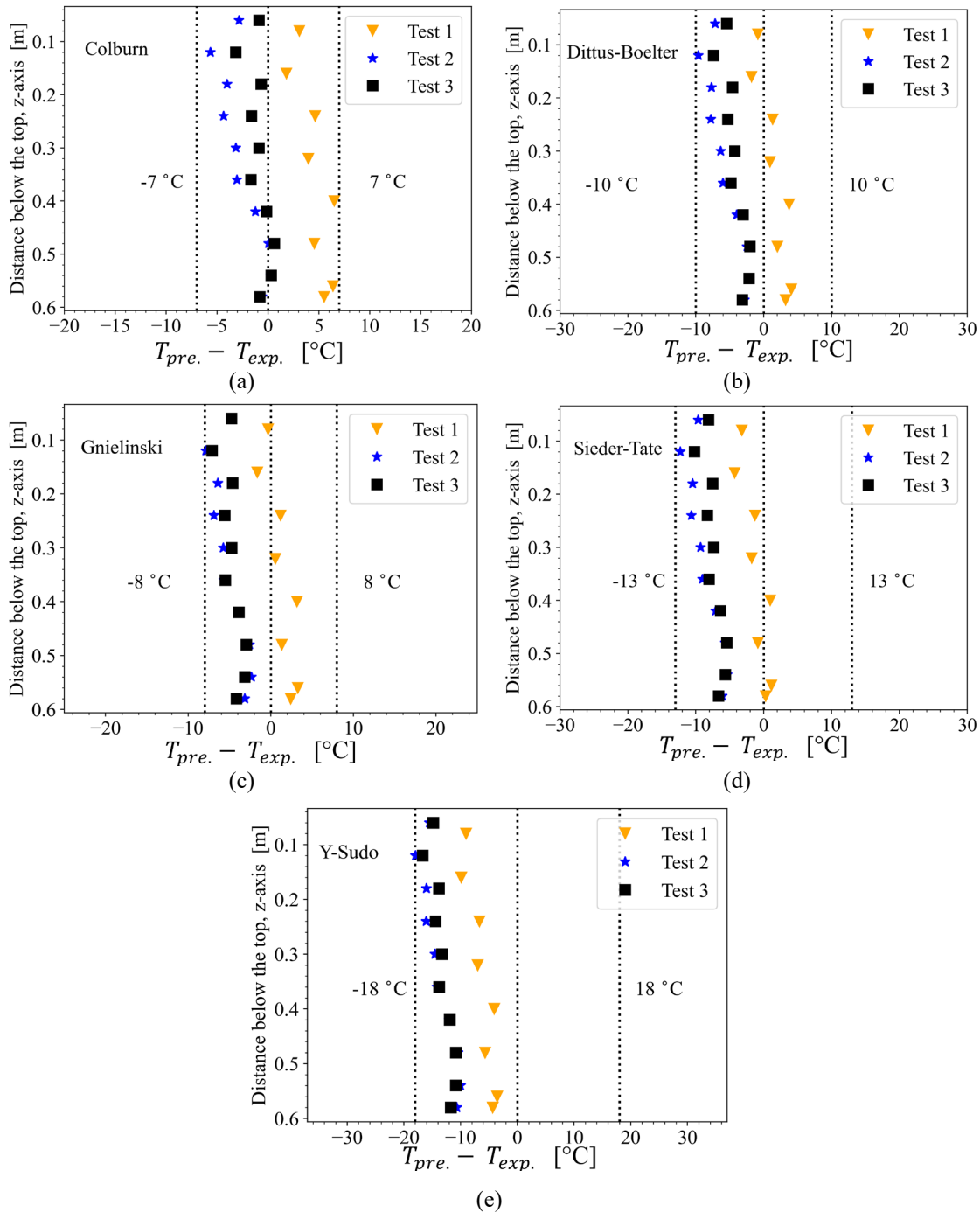


Figure 6.10: Difference between predicted and measured temperature for the three tests using different correlations: (a) Colburn; (b) Dittus-Boelter; (c) Gnielinski; (d) Sieder-Tate; (e) Y-Sudo.

Table 6-7 correspond to the root mean square error (RMSE) calculated by Eq. (6.1) for each of the correlations used in the different tests. This table shows that the Colburn correlation is the one closest to the experimental values, with the highest mean square discrepancy for Test 1 with a value of 4.53 °C. With the Colburn correlation, the lowest RMSE values are obtained, which is 1.36 °C for Test 3. The Y-Sudo correlation, on the other hand, has the highest mean square discrepancy in all cases, with the highest value obtained for Test 2 (13.94 °C), followed by Test 3 (13.31 °C) and Test 1 (6.25 °C). Intermediate values are obtained for the Gnielinski correlation with values of 1.91 °C, 5.24 °C and 4.78 °C for Tests 1, 2 and 3, respectively.

$$RMSE = \sqrt{\frac{1}{N-1} \sum_{i=1}^N (d)^2} . \quad (6.1)$$

Table 6-7: Global results of RMSE for different correlation.

Correlation	Test	RMSE [°C]
Colburn	1	4.53
	2	3.09
	3	1.36
Dittus-Boelter	1	2.4
	2	6.1
	3	4.48
Gnielinski	1	1.91
	2	5.24
	3	4.78
Sieder-Tate	1	2
	2	8.83
	3	7.47
Y-Sudo	1	6.25
	2	13.94
	3	13.31

It is expected that the use of different correlations in Subchanflow will produce different temperature profiles for the heater plate. Each of the correlations used has been developed for specific problems, so it is not accurate to assume that they can be applied globally to all problems. It is assumed that these correlations have been developed for fluids that have hydrodynamically and thermally well-established inlet lengths. The hydrodynamic inlet length depends on the Reynolds number, while the thermal inlet length depends on the Prandtl number. The variation of these parameters has a direct influence on the determination of the heater plate temperature (Everts and Meyer, 2020). The information on the hydrodynamic and thermal inlet lengths for the RA-6 la test section is not entirely clear for this data set (Silin, et al., 2012), (Silin, et al., 2010). This may explain why the heater plate temperature values in Test 2 and Test 3 at the inlet of the test section show a fluctuating behavior compared to the experimental values at the outlet of the device.

6.5 Final comments of Subchanflow using the RA-6 data

The results presented in this chapter are part of a strategy to validate the Subchanflow thermal-hydraulic code, showing good agreement in terms of temperatures and powers. It is found that the Subchanflow predictions are satisfactorily adjusted to the experimental values of refrigerant temperature, showing that the values predicted by the code are accurate and reliable for the system under study.

However, it should also be mentioned that the predicted axial temperature profiles for the heater plate differ significantly from each other because different heat transfer correlations have been used. The Colburn correlation has shown the best agreement with the experimental results, with 100% of the experimental values within ± 7 °C. Correlations such as Dittus-Boelter and Gnielinski showed deviations of ± 10 and ± 8 °C, respectively. The Sieder-Tate and Y-Sudo correlations show the largest deviations from the experimental values. It appears that the latter two correlations are not as recommendable under these initial conditions and geometric features. This highlights the importance of selecting the most appropriate correlation for each case based on flow conditions and power distribution.

These results are an important step towards the validation of Subchanflow and contribute to a better understanding of thermal phenomena. In the next chapter, the temperature and pressure drop values of a fuel assembly from IEA-R1 reactor are discussed.

7 Validation of Subchanflow using the data of the IEA-R1 reactor

7.1 Description of the IEA-R1 Reactor

The IEA-R1 is a pool-type light research reactor developed by Babcock & Wilcox and has been the first reactor in the Southern Hemisphere to be commissioned on September 16, 1957. The reactor is currently located at Nuclear and Energy Research Institute (IPEN) on the campus of the University of Sao Paulo (Maiorino, 2000). The reactor core is submerged at a depth of 7 meters in a pool of water. It is surrounded by horizontal irradiation tubes used for radioisotope production, neutron transmutation doping, neutron activation analysis, and materials and fuel testing. An overview of the reactor pool structures is shown in Figure 1.2, (Russell, et al., 1956), (Britannica, 1999).

Figure 7.1 shows a typical configuration of the IEA-R1 reactor; included in this sketch are the pneumatic system and the irradiation boxes. The fuel assemblies, (graphite) reflectors, and irradiation elements are housed in an 8×10 grid plate suspended from a structure connected to a bridge at the top of the pool. Currently, the reactor core consists of 20 standard fuel assemblies (SFA) and 4 control fuel assemblies (CFA) that are located around the center. The fuel (enrichment $< 19.75\%$) type used can be U_3O_8Al or U_3Si_2Al with aluminum cladding. The material used as neutron absorber is Ag-In-Cd.

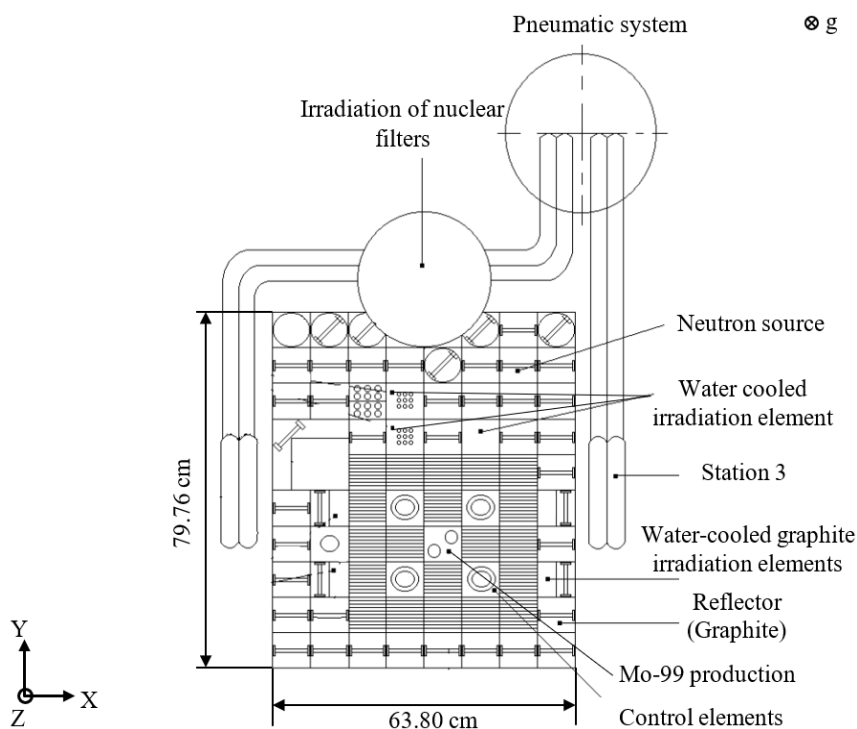


Figure 7.1: Top view of the typical IEA-R1 reactor configuration, obtained from (Maiorino, 2000).

For the thermal-hydraulic analysis, in the lower right corner, at position (6, 8) of Figure 7.2, is the Instrumented Fuel Assembly, called IFA. The IFA has been developed by IPEN researchers for testing purposes in the IEA-R1 reactor core, this instrument has all the geometric dimensions of an SFA and is used to measure coolant and fuel plate temperatures. The measurements acquired by the IFA are taken when the reactor is fully operational, so it is used to perform steady-state and transient analyses (IAEA, 2015).

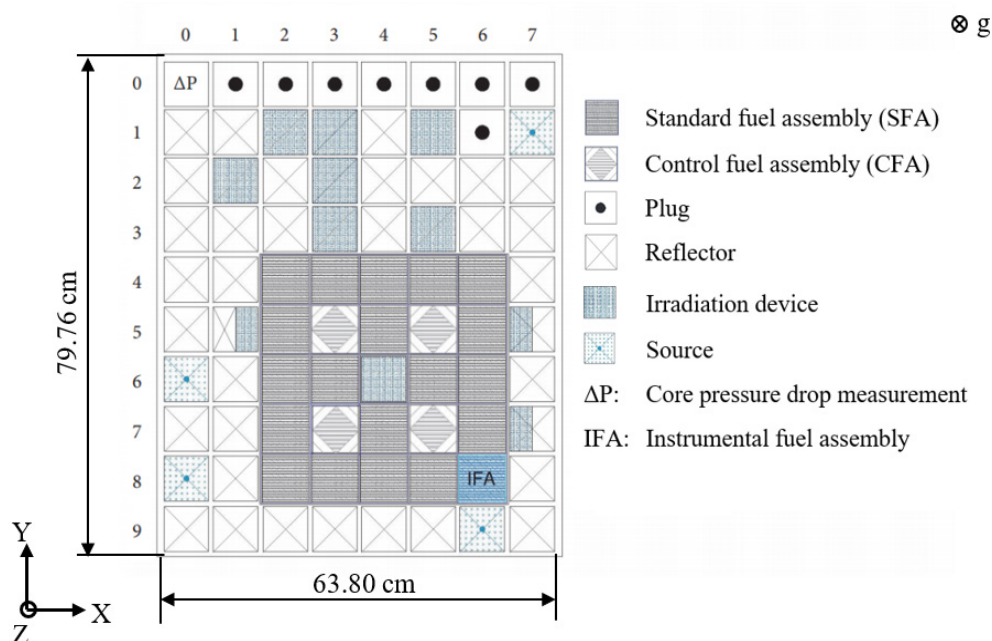


Figure 7.2: The top view of the IEA-R1 reactor core. It shows the location of the fuel elements, the irradiation positions, the reflector and the control rods, obtained from (IAEA, 2015).

7.1.1 Measurement devices of IFA

The Instrumental Fuel Assembly (IFA) has 18 fuel plates distributed at a distance of 2.89 mm, forming 17 internal channels and two external channels whose dimension corresponds to half a channel. It has 14 thermocouples distributed in three areas: reflective side channel, central channel and side channel of an adjacent unit. The IFA is equipped with sensors for measuring and monitoring the coolant temperature (TF) and the surface of the fuel plate (TC). For this purpose, type K thermocouples have been installed in three areas: on the reflector side, in the center, and on the side AF. The positions listed in Table 7-1 and the schematic drawing of the IFA with the thermocouples and respective position is shown in Figure 7.3.

Table 7-1: Locations and symbols of thermocouples in the IFA.

Position from top [mm]	Reflector side	Central	FA side
252.5	TC2	TC3	TC4
432.5	TC5	TC6	TC7
552.5	TC8	TC10	TC12
552.5	TF9	TF11	TF13
TC= clad temperature, TF= fluid temperature			

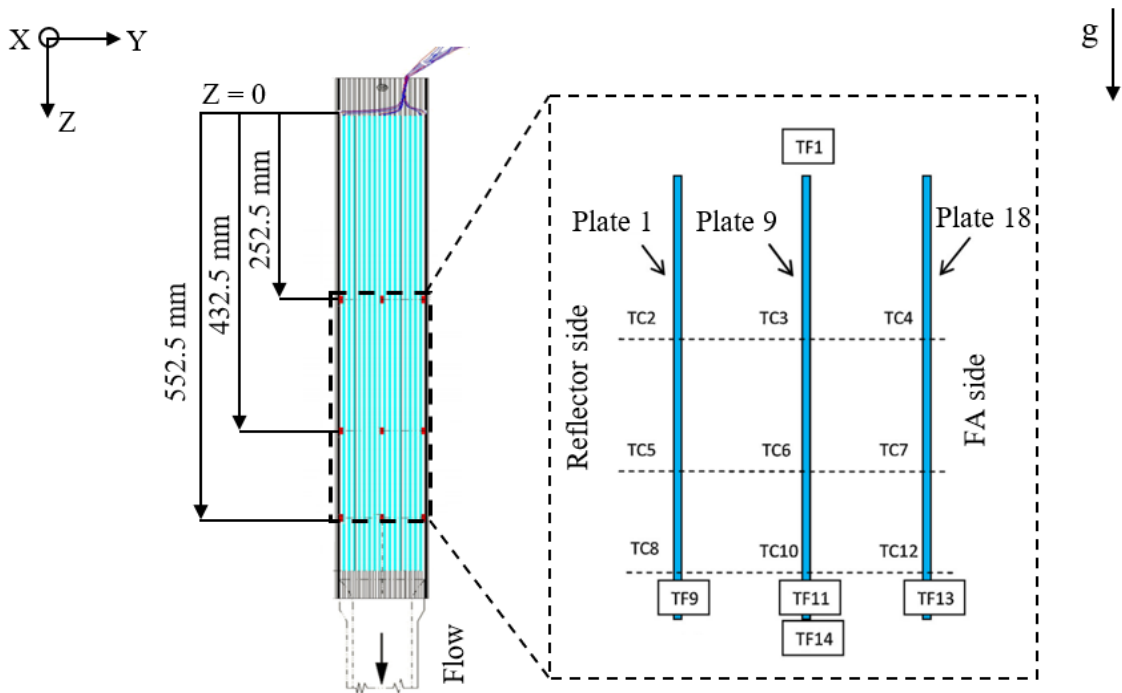


Figure 7.3: Schematic of the vertical section of an instrumented fuel assembly (left) and details of the thermocouple position symbols (right), obtained from (IAEA, 2015).

Regarding the temperature measurement, two type K thermocouples, one for the coolant and one for the cladding, are encapsulated in an aluminum pad 10 mm in diameter and 3 mm thick (Figure 7.4). The aluminum pads are located between the fuel plates and the side supports, which contain small slots that serve two functions: first, to hold the aluminum pad, and second, to reduce the interaction of the aluminum pad with the coolant flow. The measurement error when using the thermocouple is less than $\pm 0.5\text{ }^{\circ}\text{C}$ for temperatures below $50\text{ }^{\circ}\text{C}$ and $\pm 0.8\text{ }^{\circ}\text{C}$ for temperatures between 50 and $100\text{ }^{\circ}\text{C}$.

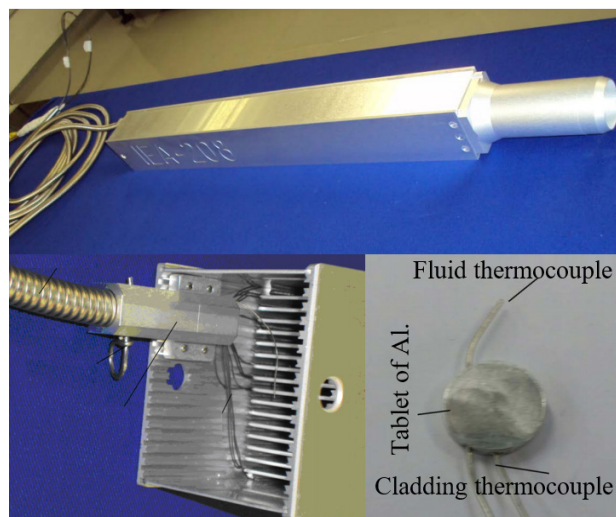


Figure 7.4: IFA and thermocouples encapsulated in aluminum pad; figures adapted from (Umbehaun, 2016).

7.1.2 Geometric dimensions of the IFA

The geometric dimensions of the IFA correspond to those of a standard fuel assembly. The axial and radial dimensions of the IFA have been taken from the literature reports presented in (Umbehaun, 2016), (IAEA, 2015) and these are present in Figure 7.5.

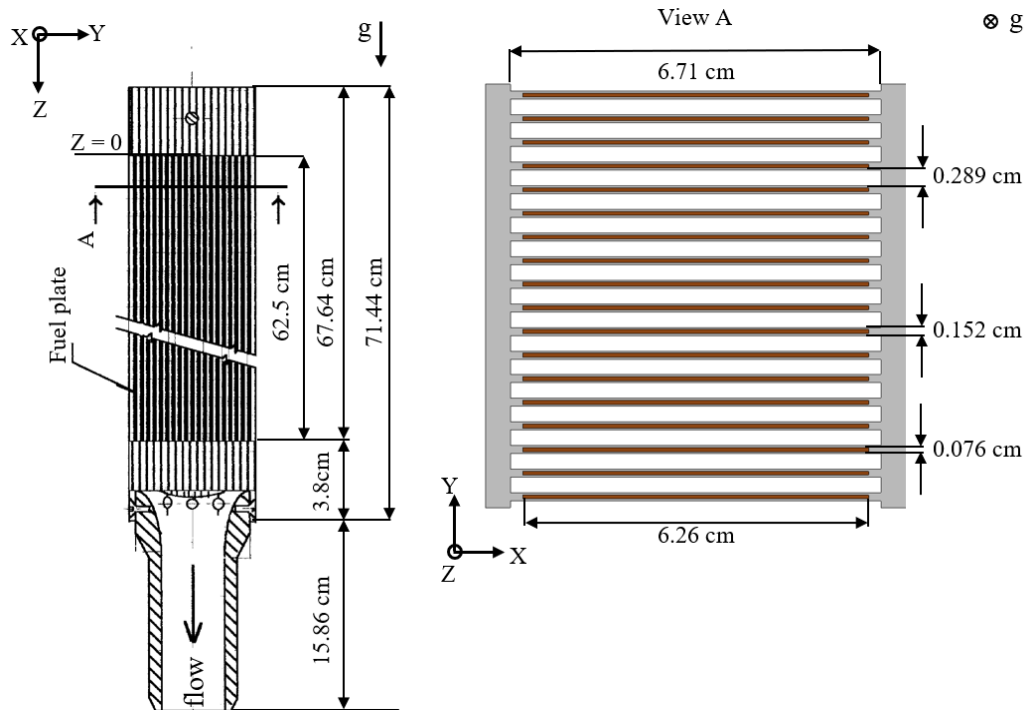


Figure 7.5: Front and top view of a standard fuel assembly with 18 fuel plates, obtained from (Umbehaun, 2016).

7.1.3 Material properties

The parameters important for heat conduction, such as thermal conductivity, specific heat and density have been obtained from (Nasir, et al., 2015), (IAEA, 1992a) and (Hainoun, et al., 2014) for the fuel, while the cladding the values given for aluminum (Al-6061) have been used. These values are summarized in Table 7-2.

Table 7-2: Material properties for IEA-R1 reactor.

Material	Fuel ($U_3O_8 - Al$)	Plate (Al)
Conductivity [W/mK]	11.0	180
Specific heat [J/kgK]	123.02	892
Density [kg/m^3]	2300	2700

7.1.4 Operations conditions for tests performed at the IFA

Several steady-state and transient analysis tests have been performed on the IEA-R1 reactor. Temperature, pressure, and mass flow rate data have been measured in the instrumented IFA. Details of these experimental investigations have been presented by (Durazzov, et al., 2019),

(Umbehaun, 2016), and (Hainoun , et al., 2014). Two experimental cases documented by (Hainoun , et al., 2014) are used in this work. The power output of the IFA for Test 1 and 2 are 128kW and 147.61 kW, respectively. The mass flow distribution within the IFA is measured using a dummy FA. The measurements showed a parabolic mass flow distribution within the IFA (Umbehaun, et al., 2018). Based on this work, the mass flow distribution parameters for each of the 18 channels have been extrapolated for an average mass flow of 6.27 kg/s. The initial conditions for performing Tests 1 and 2 are summarized in Table 7-3.

Table 7-3: Operations conditions of IFA, Test 1 and 2.

Parameter	Test 1	Test 2
Pressure outlet [Pa]	162165	162165
Reactor power [MW]	3.5	4.0
Power (IFA) [MW]	0.128	0.1474
Temperature inlet [°C]	32.69	31.61
Inlet flow rate (IFA) [kg/s]	6.27	6.27
Flow direction	downward	downward

7.1.5 IFA test conduction

Temperature, pressure, and mass flow measurements are made once the reactor reaches a steady-state. The core is cooled by downflow forced convection, and heat generated by nuclear fission is removed by primary and secondary cooling systems. Figure 7.6 shows that the pump located at the bottom absorbs the hot fluid and diverts it into a water-to-water heat exchanger. The coolant is reintroduced into the reactor pool after the heat has been removed. The secondary system has the task of dissipating the heat to the atmosphere by means of cooling towers. The experimental values obtained for Tests 1 and 2 are summarized in Table 7-4.

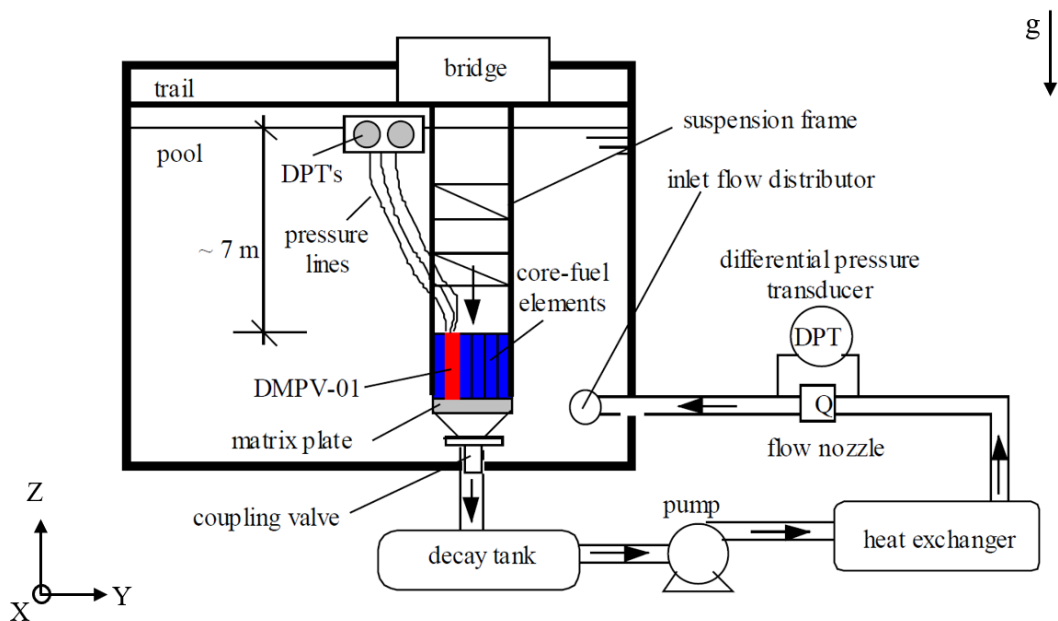


Figure 7.6: Simplified drawing of the primary cooling system, obtained from (Hainoun , et al., 2014).

Table 7-4: Experimental values measured for Tests 1 and 2.

IFA Measured parameters	Test 1	Test 2
Coolant temperature at inlet [°C]	32.69	31.61
Coolant temperature at outlet [°C]	37.57	37.23
Core pressure drop [kPa]	7.835	7.835
TC2 [°C]	43.8	44.41
TC3 [°C]	37.5	37.28
TC4 [°C]	44.5	45.27
TC5 [°C]	48	49.25
TC6 [°C]	42.5	42.95
TC7 [°C]	49.2	50.51
TC8 [°C]	45.2	45.99
TC10 [°C]	41.7	42.02
TC12 [°C]	46.6	47.64

7.2 Development of the Subchanflow model for the IEA-R1 test

7.2.1 Assumptions for the Subchanflow model

Modeling the Instrumental Fuel Assembly (IFA) with the Subchanflow thermal-hydraulic code requires certain assumptions and simplifications. First, both power and coolant flow are considered to be steady-state, which means that fluctuations or dynamic changes in these parameters are not considered. Also, pressure losses caused by acceleration in a downward flow are assumed to be negligible and can be disregarded since little information is available. As for the plate configuration in the Subchanflow model, a channel-centered arrangement is used. This means that a total of 18 cooling channels are considered, each of which is divided into 100 equidistant axial cells. For the plate itself, a symmetric nodalization is performed along the y-axis, specifically, 3 nodes are considered for the fuel section and 2 nodes for the cladding section; 100 equidistant axial cells are also used (see Figure 7.7).

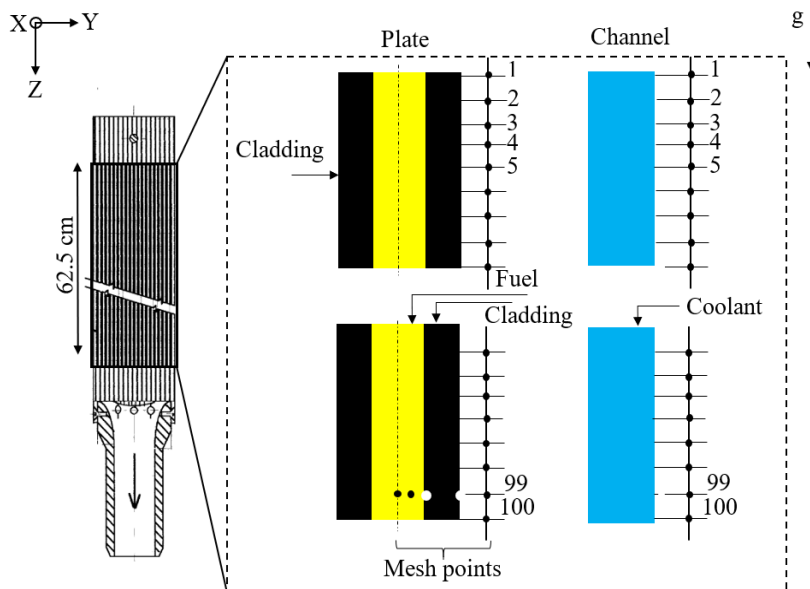


Figure 7.7: Lateral and axial representation of nodalization for fuel plate and coolant channel.

Additionally, the axial heat flux distribution for the 18 plates in the Instrumental Fuel Assembly (IFA), obtained from the study of (Umbehaun, et al., 2018) is shown in Figure 7.8. This representation shows that the lowest values of the relative heat flux are found at the coolant inlet, i.e., at the top of the active length of the IFA. On the other hand, the central area of the IFA shows the highest values of the relative heat flux, almost in the middle of the active length. At the lower end of the active length, the relative heat flux decreases slightly. This variation in heat flux distribution along the IFA is due to the presence of the control rods and the drag of the downward moderating fluid.

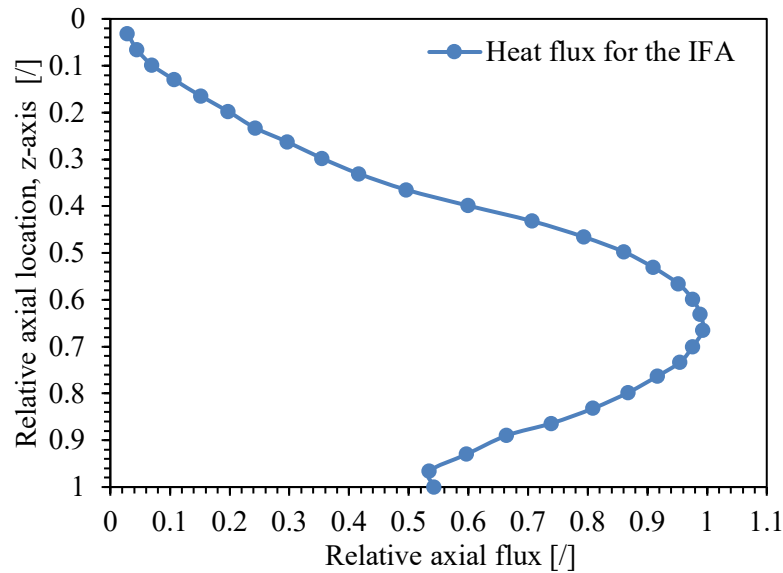


Figure 7.8: Axial relative heat flux for the IFA.

7.2.2 Selected flow friction pressure drops and heat transfer correlations

Pressure drop is a crucially important factor in pool-type research reactors because it is composed of losses generated by the fluid above the core, losses that occur at the bottom of the core, and losses that occur inside the core (as shown in Figure 7.6). In this dissertation, only the contribution of losses inside the core is considered (IAEA, 1980). For the pressure loss, the friction factors for the laminar and turbulent regions in a rectangular channel are given in Table 7-5 (Li and Zhang, 2010), (Rohsenow, et al., 1998).

Table 7-5: Pressure drop correlations for IEA-R1.

Friction factor	Correlation
Laminar	$f = 96Re^{-1}$
Turbulent	$f = 0.0791Re^{-0.25}$

In previous studies conducted by independent teams from different institutes and countries, a large discrepancy in the calculated data has been observed when simulating the heat conduction in the fuel plates at steady state in the IFA of the IEA-R1 reactor. For e.g., the Argentine team using the code RELAP determined an absolute error of 8.5 °C for the central plate (see Figure

7.3, TC6), (IAEA, 2019). These discrepancies arise from the use of the general forms of McAdam correlation (Dittus-Boelter) used in power reactors and a possible bias in the measured data, so in the studies conducted by (Hainoun , et al., 2014) the comparison, verification and improvement of the correlations used in the codes is proposed. In this context, the use of the correlation developed by (Sudo, et al., 1990) specifically for research reactors is considered (see Table 5-1).

7.3 Comparison of measured and predicted data

Global and local parameters of temperature and pressure drop have been calculated by Subchanflow and compared with experimental results. The global measured values correspond to the fluid temperature and pressure drop, and the local values correspond to the surface temperature of three plates forming the IFA (see Figure 7.3). Table 7-6 shows the experimental temperature values at the outlet of the IFA compared to the values predicted by Subchanflow. The calculated values tend to overestimate the temperatures, but remain within the experimental error range given for this series of Tests, which is ± 0.5 °C. The results are in excellent agreement with each other.

Table 7-6: Global parameter predicted by the code Subchanflow, outlet temperature fluid.

Case study	Exp. [°C]	Subchanflow [°C]	Absolute error [°C]
Test 1	37.57 ± 0.5	37.58	0.01
Test 2	37.23 ± 0.5	37.30	0.07

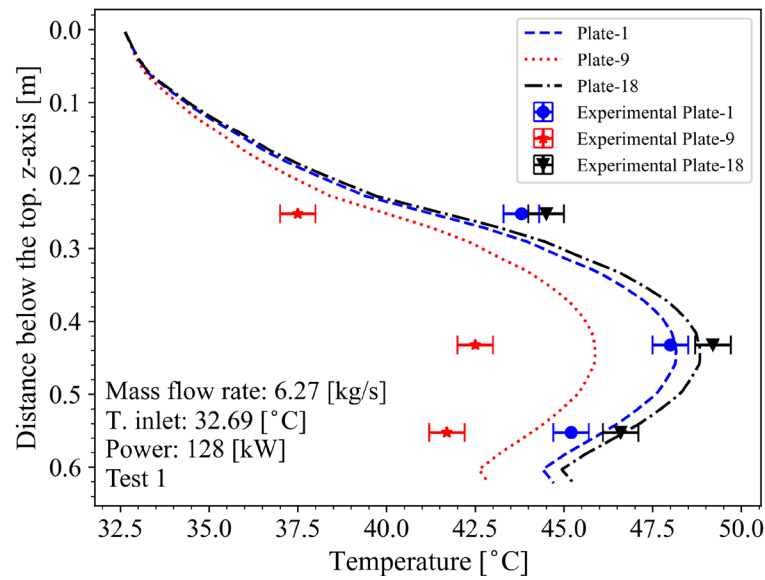
Table 7-7 shows the measured pressure drop values along with the values calculated by Subchanflow. It can be observed that Subchanflow underestimates the pressure drop values, with a relative error of -4.43% for Test 1 and -4.52% for Test 2. It should be noted that the pressure drops at the core inlet and outlet have a direct impact on the measured experimental value, which explains why the measured values are higher than the calculated ones. Although no experimental error bands have been reported for this series of Tests, with a conservative relative error margin of 5%, it can be concluded that Subchanflow shows acceptable agreement with the experimental values in terms of pressure drop.

Table 7-7: Global parameter predicted by the code Subchanflow, pressure drop.

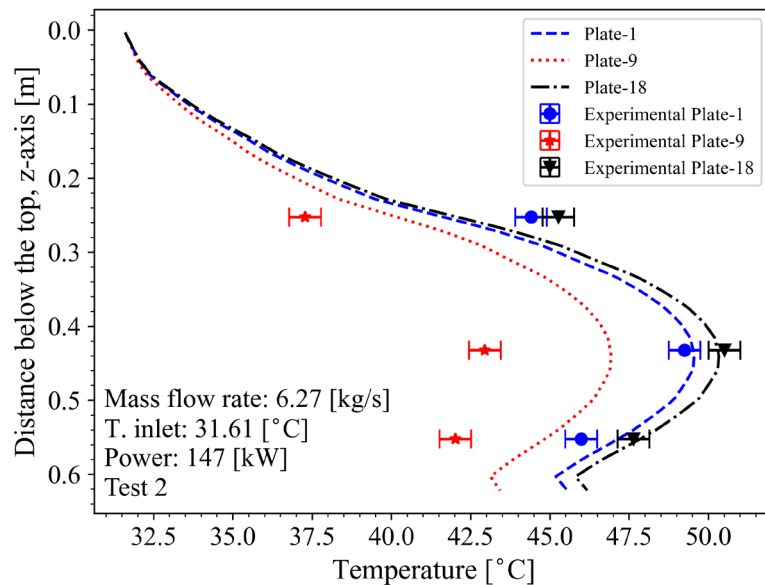
Case study	Exp. [Pa]	Subchanflow [Pa]	Relative error %
Test 1	7835	7488	-4.43
Test 2	7835	7481	-4.52

Figure 7.9 shows the calculated cladding temperature profiles along with the experimentally measured values for Tests 1 and 2. It can be seen that in both Tests, the measured values corresponding to plate 1 and 18 are higher than those for plate 9. This variation is due to the axial and radial power distribution, which changes as the control rods are inserted into the core from above. The error derived from the experimental results for this Tests set is ± 0.5 °C.

Regarding the axial cladding temperature profiles calculated by Subchanflow, an increase is observed from the top to the bottom of the IFA. The simulated temperature differences for plates 1 and 18 differ slightly from each other, in contrast to plate 9, which has lower temperature values. It can be noted that the temperature profiles for plates 1 and 18 show a good agreement with the experimental values, and only the temperature values measured in the middle and outlet regions of the IFA are within the error range of ± 0.5 °C. However, the temperature profiles for plate 9, located in the central part of the IFA, show a significant discrepancy with the results calculated by Subchanflow. In this case, none of the calculated values are within the experimental error range of ± 0.5 °C.



(a) Experimental and calculated temperature values for Test 1



(b) Experimental and calculated temperature values for Test 2

Figure 7.9: Axial temperature distribution for different plates for: (a) Test 1; (b) Test 2.

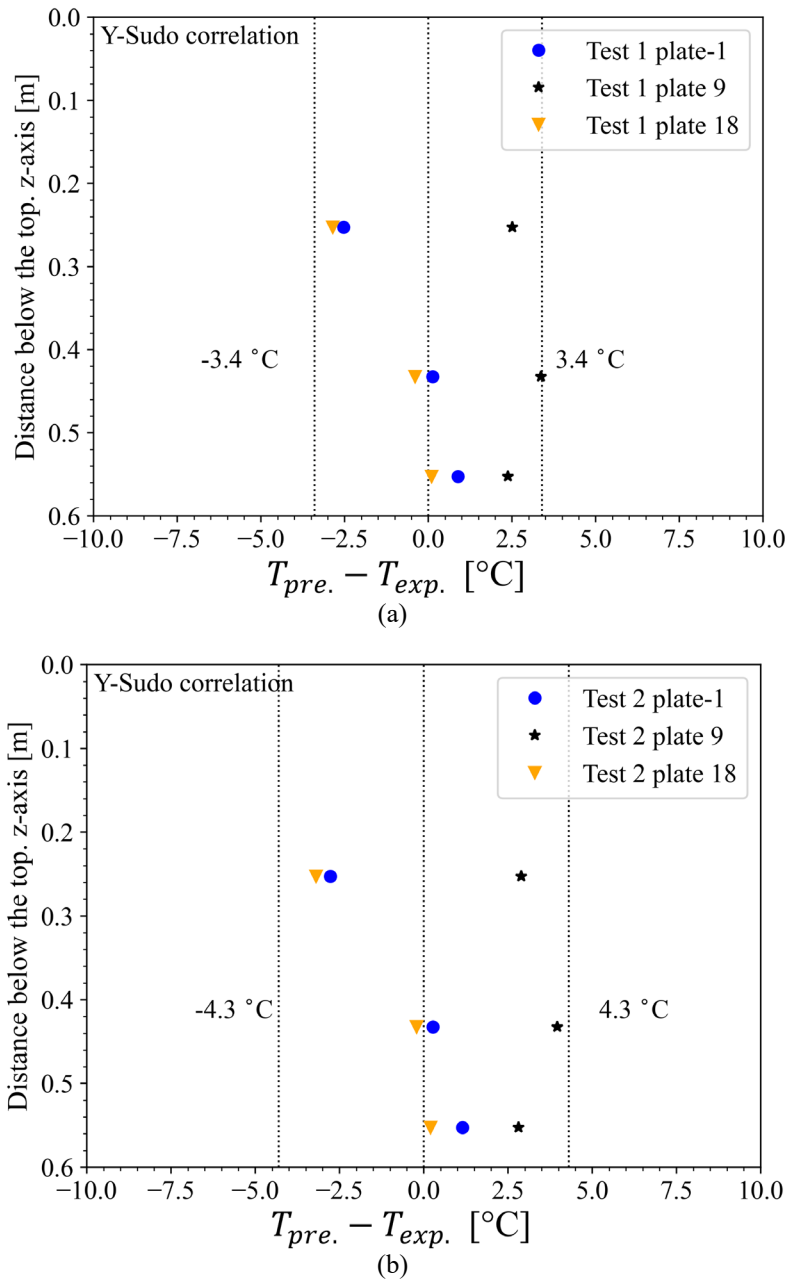


Figure 7.10: Difference between predicted and measured temperature for: (a) Test 1; (b) Test 2.

Analyzing Figure 7.10, which complements the information given in Figure 7.9, it can be seen that the temperature differences between the predicted values and the measured values are in a range of ± 3.4 °C for Test 1 and ± 4.3 °C for Test 2. For plates 1 and 18, the temperature differences are close to 0 °C at some points near the exit of the IFA. However, in both Tests, it can be seen that Subchanflow overestimates the temperature values, so that the temperature difference for the central plate is considerably higher compared to the others, ranging from 2.5 °C to 4.3 °C. It is important to emphasize that the high discrepancy observed for the central plate has also been recorded by other research teams, suggesting that there may be a bias in the experimental data associated with this particular plate (Castellanos-Gonzalez, et al., 2018), (Hainoun, et al., 2014). However, when comparing the temperature differences obtained by Subchanflow

(TC6 = 3.4 °C, Test 1) to the reported reference values of 8.5 °C (TC6,) for the central plate, it can be found that the calculations performed by Subchanflow represent a significant improvement of up to 60% (Hainoun , et al., 2014). Although a larger discrepancy is observed for the central plate, these results demonstrate the ability of Subchanflow to significantly improve the temperature estimates compared to the reported reference values.

7.4 Final comments of the Subchanflow validation using the IAE-R1 data

The simulations performed by Subchanflow have been compared with the experimental IFA values of the IEA-R1 reactor. It can be concluded that the global results of the fluid temperature and pressure drop, together with the local results of the fuel plate cladding temperature predicted by Subchanflow, agree well with the experimental data. In the case of the fluid temperature at the outlet of the IFA, the maximum absolute error between the calculated and experimental values is 0.07 °C. On the other hand, the percentage error of the experimental pressure drops with respect to the value calculated by Subchanflow is $\pm 4.52\%$. As for the local results, the values obtained for this series of experiments show a maximum temperature difference between predicted and measured values of ± 4.3 °C. The simulations carried out confirm the predictive ability of the thermal-hydraulic parameters of Subchanflow for MTR type reactors.

8 Validation of dynamic capability of Serpent2/Subchanflow using data of the SPERT IV reactor

Before using the developed coupled code to study the behavior of MTR cores in transient situations, it is important to validate the ability of Serpent 2 to predict static parameters. Subsequently, the capability of Serpent2/Subchanflow under transient conditions is validated. These validations are carried out using experimental data from the SPERT IV reactor.

8.1 Description of the SPERT IV reactor

Figure 8.1 shows the Special Power Excursion Reactor (SPERT) built under the U.S. Atomic Energy Commission's reactor safety program. This facility has been operated by the Atomic Energy Division of Phillips Petroleum Company (Crocker, et al., 1963). In July 1962, the first core used in the so-called SPERT IV tests is SPERT IV D-12/25. A series of tests have been conducted to verify the stability of the reactor under static and transient conditions, which are summarized in (Crocker and Stephan, 1964).

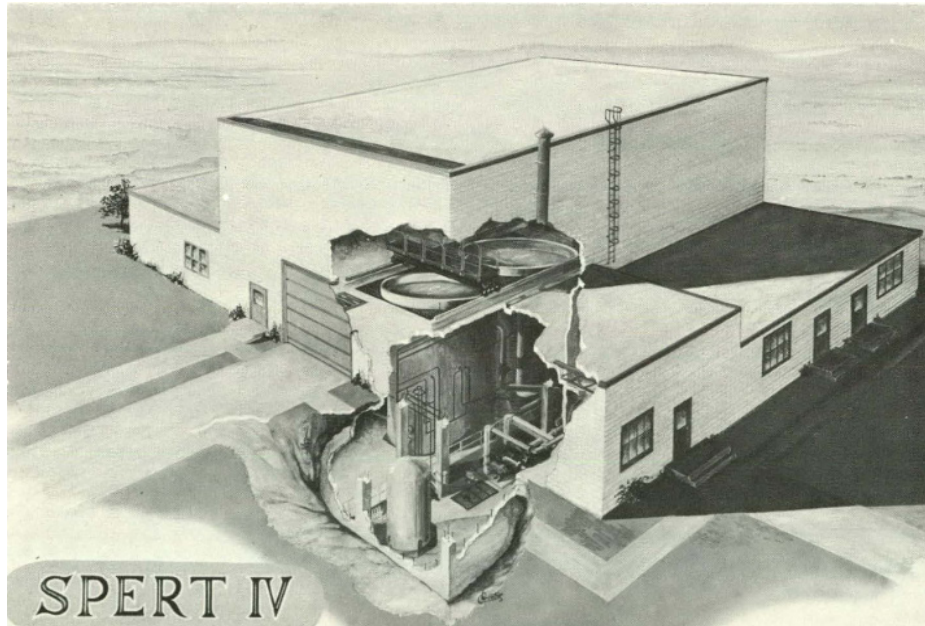


Figure 8.1: SPERT IV Building Schematic (NRTS-60-4264), obtained from (Heffner, et al., 1962).

As can be seen in Figure 8.2, the reactor core is located at the bottom of the north tank. The diameter of the tanks is 6.096 m and 7.62 m deep. At the bottom of the north tank, there is a 0.1064 m flanged nozzle in the center that allows velocities of up to 5000 gpm (3.87 m/s), through the core. To stabilize the pool temperature during operation, the cooling system consists of a 1 MW heat exchanger (Crocker, et al., 1965).

The drives for the control rods and the transient rod are mounted on the drive base plate, which is located on the control bridge. Since the drive bridge is not automated, base plates are used to level and square the control units. A Graham Model 190 MWG variable speed transmission has been used to drive the rods. This transmission has an output speed range of 0 to 200 rpm and is controlled by an electric remote control (Heffner, et al., 1962).

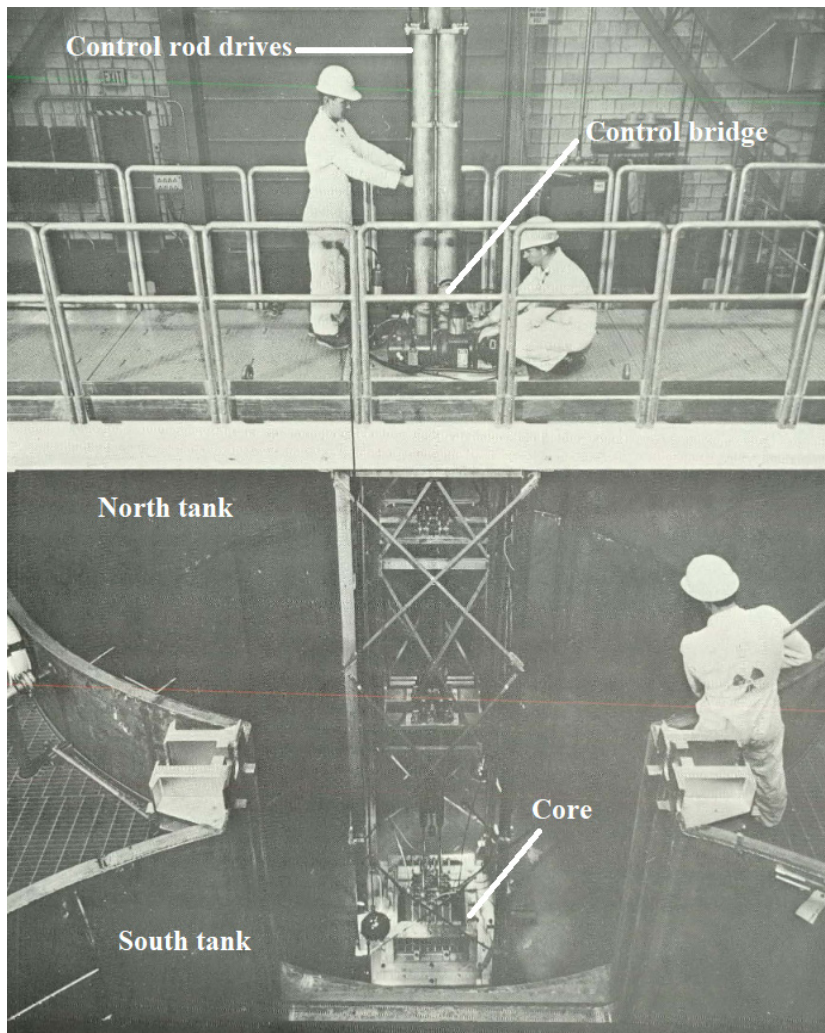


Figure 8.2: SPERT IV reactor tanks, obtained from (Heffner, et al., 1962).

8.1.1 Tests of the SPERT IV D-12/25 reactor

The SPERT IV D-12/25 reactor facility is designed to study the kinetic and static behavior of a variety of MTR-type reactors. The tests performed with this reactor have been conducted in two programs. The first experimental program, called “Nuclear Start-up of the SPERT IV Reactor,” collects the measured steady-state thermal neutron flux data and serves to determine the initial criticality state and reactivity insertion values (Crocker, et al., 1963). The second experimental program, called "Reactor Power Excursion Test in the SPERT IV Facility," collects a total of 46 transient tests with reactivity insertion, where the measured values are the evolution of: core power and cladding temperature of the main fuel plate (Crocker and Stephan, 1964).

Results from the first phase of the SPERT IV D-12/25 program are very valuable to validate neutronic codes. Recent studies, such as those presented by (Margulis and Gilad, 2018) and (Motalab, et al., 2014) have shown the usefulness of these unique data for validation of Monte Carlo codes. Figure 8.6 shows a radial cut of the reactor core SPERT IV D-12/25 where the control fuel assemblies (CFAs) and the transient fuel assembly (TFA) can be identified. It can be seen that the arrangement of the four CFAs is symmetrical from the central position where the TFA is located. Additionally, the activating cobalt wires used to measure the thermal neutron flux, are placed in different locations of the reactor, so that considering the symmetry of the CFAs and the location of the sensors, the experimental data measured at positions E-5 and D-4, corresponding to the CFA and the TFA, are used to validate the code MC Serpent 2.

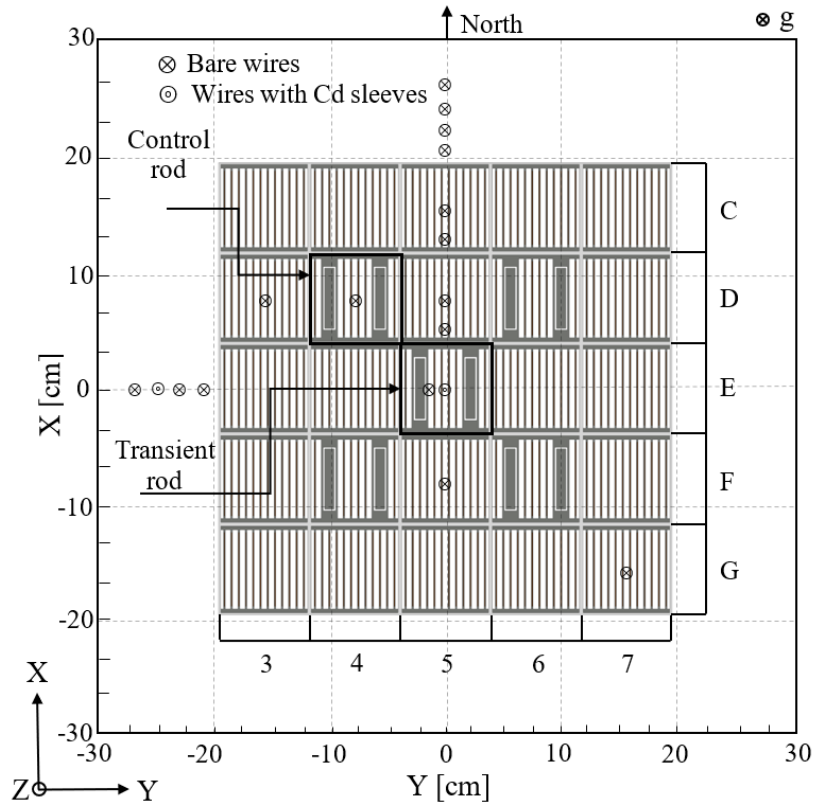


Figure 8.3: Top view of the reactor core SPERT IV with the control and standard fuel assemblies together with the radial positions of the cobalt wires for measuring the thermal flux.

The second phase of the SPERT IV D-12/25 program includes a total of 46 transient tests with reactivity insertion. The experimental values measured in this phase can be found in (Crocker and Stephan, 1964). Currently, some research groups involved in the development of codes for the thermal-hydraulic analysis of research reactors are using these results for code validation. Among the most common and challenging tests are the so-called B-34 and B-35 tests, which, according to recent research, require more sophisticated computational methods or extensions of their correlations to reduce the large discrepancy between simulated and measured data (Margulis and Gilad, 2018), (Labit, et al., 2021). In this dissertation, both tests are used to validate the dynamic capabilities of the Serpent2/Subchanflow code.

8.1.2 Geometric dimensions of SPERT IV D-12/25 reactor

Figure 8.4 shows a brief geometric representation of the main elements of the reactor SPERT IV D-12/25. On the right side of the figure is the reactor core, which rests on the 1.022 m square aluminum lattice; the elements that drive the control rods and the transient rod are located on top of the core. The reactor core configuration is of a 5 x 5 square grid that houses 20 standard fuel assemblies, 4 control fuel assemblies, and 1 transient fuel assembly; a top view of the fuel assembly arrangement is shown in Figure 8.3. The standard fuel assemblies consist of 12 plates stacked 4.54 mm apart. Each of the plates is made of 93% enriched HEU and, together with the support box, forms a height of 0.638 m.

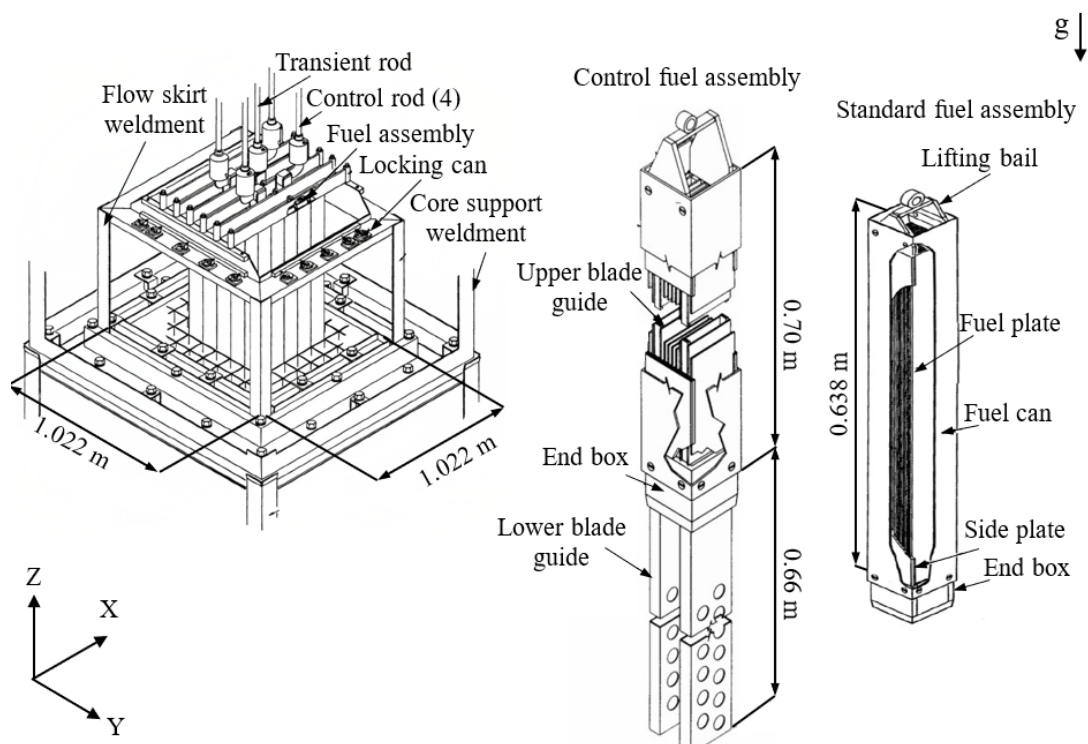


Figure 8.4: SPERT IV core support structure (left), and representation of the control fuel assemblies and standards (right); the images have been modified from (Crocker, et al., 1963).

Figure 8.4 (right) also shows the control fuel assemblies (the figure also applies to the transient fuel assembly). These configurations have a total of six fuel plates, distributed among four plates in the center and one plate at each end. The control and transient fuel assemblies are equipped with a rectangular guide tube through which the absorber material called Binal (aluminum alloy with 7 wt% boron, manufactured by Sintercast Corporation) is moved. A detailed description of each of these elements can be found in Appendix B.1.

The control rod and the transient rod are shown in Figure 8.5; the main difference between the two is the location of the absorbing material. The Binal absorbing material of the control rod is at the top, while that of the transient rod is at the bottom. The transient rod is used to introduce reactivity, and it should be noted that due to the position of the Binal on the transient rod, the

reactivity of the core decreases when the rod is raised, and reactivity is added to the system when the rod is lowered this difference can be seen in Figure 8.6.

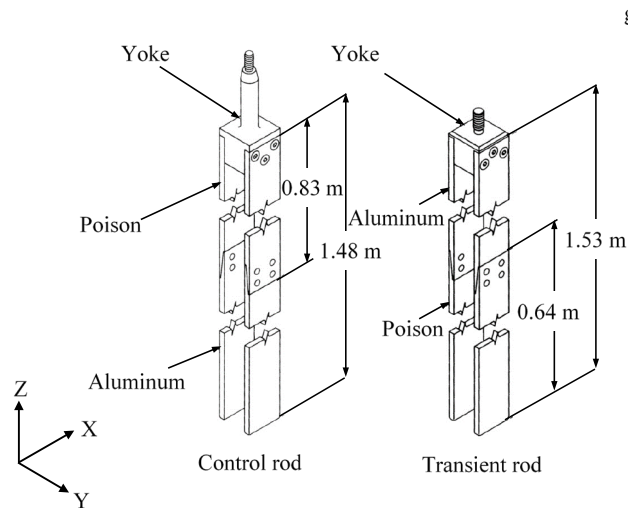


Figure 8.5: Control and transient rods, obtained from (IAEA, 2015).

8.1.3 Material properties

To perform the heat conduction calculations for the fuel (*UAl alloy*) and aluminum cladding, the material properties shown in Table 8-1 have been taken from (IAEA, 2019) and (IAEA, 1980).

Table 8-1: Material properties for SPERT IV D-12/25.

Material	Fuel (UAl alloy)	Plate (Al 6061)
Conductivity [W/m-K]	158	180
Specific heat [J/kg-K]	728	892
Density [kg/m^3]	1100	2700

The material specifications for the neutron calculations have been taken from (IAEA, 2015). The composition of the fuel in atom density is given in Table 8-2. The fuel is highly enriched uranium at 93% and is the same for all fuel assemblies. No burnup tests have been performed, so the fuel is considered fresh throughout the core. The nominal fuel porosity reported is 4%, and no data on material impurities are available.

Table 8-2: Fuel material specifications.

Isotope	Atom density (atoms/(b·cm))	Isotopic wt% in U
U-235	$1.861\ 29 \times 10^{-3}$	93
U-238	$1.205\ 43 \times 10^{-4}$	6.1
U-234	$1.205\ 98 \times 10^{-5}$	0.6
U-236	$5.978\ 69 \times 10^{-6}$	0.3
Al-27	$5.475\ 02 \times 10^{-2}$	-

Atomic densities for aluminum and absorber material are given in Table 8-3 and Table 8-4, respectively. For aluminum, a nominal mass density for generic alloys is assumed, and the nominal impurity composition is in the midpoint of the maximum limit. The absorber material is a combination of aluminum powder and boron carbide. The trade name is Binal and it is essentially a 7% boron alloy.

Table 8-3: Al 6061 material specifications in atom density (atoms/(b·cm)).

Isotope & Impurities	Nominal	Max	Isotope & Impurities	Nominal	Max
Al-27	$5.863\ 76 \times 10^{-2}$	-	Mn-55	$2.219\ 71 \times 10^{-5}$	$4.439\ 42 \times 10^{-5}$
Cr-50	$2.463\ 05 \times 10^{-6}$	$4.420\ 87 \times 10^{-6}$	Si-28	$3.203\ 68 \times 10^{-4}$	$4.271\ 57 \times 10^{-4}$
Cr-52	$4.744\ 35 \times 10^{-5}$	$8.515\ 50 \times 10^{-5}$	Si-29	$1.622\ 16 \times 10^{-5}$	$2.162\ 88 \times 10^{-5}$
Cr-53	$5.379\ 08 \times 10^{-6}$	$9.654\ 76 \times 10^{-6}$	Si-30	$1.076\ 81 \times 10^{-5}$	$1.435\ 74 \times 10^{-5}$
Cr-54	$1.336\ 28 \times 10^{-6}$	$2.398\ 45 \times 10^{-6}$	Ti-46	$2.037\ 53 \times 10^{-6}$	$4.075\ 07 \times 10^{-6}$
Cu-63	$4.867\ 10 \times 10^{-5}$	$7.079\ 41 \times 10^{-5}$	Ti-47	$1.859\ 25 \times 10^{-6}$	$3.718\ 50 \times 10^{-6}$
Cu-65	$2.169\ 33 \times 10^{-5}$	$3.155\ 39 \times 10^{-5}$	Ti-48	$1.879\ 63 \times 10^{-5}$	$3.759\ 25 \times 10^{-5}$
Fe-54	$5.910\ 22 \times 10^{-6}$	$1.182\ 04 \times 10^{-5}$	Ti-49	$1.400\ 80 \times 10^{-6}$	$2.801\ 61 \times 10^{-6}$
Fe-56	$9.346\ 31 \times 10^{-5}$	$1.869\ 26 \times 10^{-4}$	Ti-50	$1.375\ 34 \times 10^{-6}$	$2.750\ 67 \times 10^{-6}$
Fe-57	$2.241\ 81 \times 10^{-6}$	$4.483\ 62 \times 10^{-6}$	Zn-64	$1.510\ 58 \times 10^{-5}$	$3.021\ 15 \times 10^{-5}$
Fe-58	$2.853\ 21 \times 10^{-7}$	$5.706\ 42 \times 10^{-7}$	Zn-66	$8.671\ 83 \times 10^{-6}$	$1.734\ 37 \times 10^{-5}$
Mg-24	$5.284\ 26 \times 10^{-4}$	$6.341\ 11 \times 10^{-4}$	Zn-67	$1.274\ 35 \times 10^{-6}$	$2.548\ 71 \times 10^{-6}$
Mg-25	$6.689\ 78 \times 10^{-5}$	$8.027\ 74 \times 10^{-5}$	Zn-68	$5.843\ 38 \times 10^{-6}$	$1.168\ 68 \times 10^{-5}$
Mg-26	$7.365\ 45 \times 10^{-5}$	$8.838\ 54 \times 10^{-5}$	Zn-70	$1.864\ 91 \times 10^{-7}$	$3.729\ 82 \times 10^{-7}$

Table 8-4: Absorber material specifications in atom density (atoms/(b·cm)).

Isotope	Nominal
B-10	2.08×10^{-3}
B-11	8.37×10^{-3}
C-natural	2.61×10^{-3}
Al-27	5.45×10^{-2}

8.1.4 Operating condition of SPERT IV D-12/25 reactor

The initial conditions for testing the first phase of the program SPERT IV D-12/25 are summarized in Table 8-5. The test values have been recorded when the reactor reached steady-state operation (Crocker, et al., 1963).

Table 8-5: Main operating conditions of the reactor SPERT IV D-12/25 for the static calculation.

Parameter	Reference values
Fuel type	UAl alloy Al clad flat plate fuel
Enrichment	HEU 93 % 14.0g 235 U
Initial temperature	20 [°C]
Coolant, moderator, reflector	Light water
Poison material	Binal (B-Al)
Initial power	1 [W]

In addition, to validate the dynamic capabilities of Serpent2/Subchanflow, the two experimental tests B-34 and B-35 are used. The initial conditions before transient recording are summarized in Table 8-6 (Crocker and Stephan, 1964).

Table 8-6: Initial conditions for SPERT IV D-12/25 for the transient calculations.

Parameter	Test B-34	Test B-35
Inlet pressure [Pa]	140000	140000
Reactor power [W]	62548	68495
Temperature inlet [°C]	21.9	22
Inlet coolant flow rate [m/s]	3.87	3.87
External reactivity [\$]	0.88	1.05

8.1.5 SPERT IV D-12/25 test conduction

The heat generated during nuclear fission is removed by the reactor cooling systems. The primary cooling system uses deionized water that flows upward through the core at a rate that can vary depending on the type of test being performed. A secondary cooling system, equipped with a heat exchanger, is used to maintain a stable temperature in the reactor pools. Two parallel cooling pumps (located under the north tank, see Figure 8.2) are responsible for circulating coolant through the core via a 40.64 cm flanged inlet nozzle. The coolant flows upward and exits the reactor through the 30.48 cm bottom nozzle.

The heat exchanger is designed with a heat removal capacity of 1.1869 MW. The maximum operating pressure, temperature, and flow rates are 620.52 kPa, 54 °C, and 5000 gpm (3.87 m/s), respectively. For experimental temperature measurements, several thermocouples composed of 0.254 mm diameter alumina-chromium wire have been distributed around the reactor core. The temperature values reported for tests B-34 and B-35 correspond to those of the cladding. The positioning of the thermocouples in tests B-34 and B-35 is marked with a special label. For e.g., the label E5 7W-4 means that the thermocouple is placed in grid position E5 (transient rod assembly), the 7th plate, west side, 10.16 cm (4 in) below the centerline of the active core which translated to x, y, z coordinate system means (0, -0.03, 35.08) cm (see Figure 8.6).

Thermal neutron flux measurements have been determined by activating cobalt wires located at different positions as shown in Figure 8.3. The results are digitized in (IAEA, 2015) and are part of the IAEA CRP project. The control and transient rods are driven by a variable speed drive that has an operating range of 0 to 0.508 cm/s. The pitch accuracy of the control and transient rods is 0.254 mm. The control rods are pulled upward, while the transient rod works in reverse. The control and transient rods can also be independently programmed to perform a "ramped" reactivity addition using a sequence timer.

8.2 Main assumptions for the SPERT IV reactor model

A series of transient and steady-state experiments have been performed with the SPERT IV reactor, most of which are summarized and published in (Crocker and Stephan, 1964) and (Crocker, et al., 1963). The dimensions, material properties, and initial conditions are described in detail in Section 8.1. The measured values correspond to the thermal neutron flux, the core power and the temperature of the plate cladding. The main assumptions and aspects for the construction of the models in Serpent 2 and Subchanflow are presented below.

8.2.1 Subchanflow model

To create a representative model of the reactor SPERT IV D-12/25 with the Subchanflow code, a radial map showing the location of each plate and channel has been created (see Appendix B.2). Then, as in previous experiments such as RA-6, IEA-R1, the following assumptions are made:

- Center plate model is used for thermal-hydraulic information transfer,
- the number of nodes for heat conduction is divided into 3 nodes for the fuel and two nodes for the cladding (see Figure 6.6),
- the axial discretization for IFC information transfer is 20 cells for both the fuel plate and the coolant channel.

As in the case of the IEA-R1 reactor, it has been observed in several investigations that the use of standard heat transfer correlations, such as Dittus-Boelter or similar, results in high values for plate cladding temperature (Margulis and Gilad, 2018), (IAEA, 2019). To mitigate these discrepancies, correction factors are applied or modified correlations are used (Labit, et al., 2021). For this reason, the use of the Y-Sudo correlation is considered (see Table 5-1), which has shown good results as explained in Chapter 7. In addition, the friction factors used for laminar and turbulent flows are listed in Table 7-5. These considerations allow to improve the accuracy of the results and to minimize discrepancies in the heat transfer calculations.

8.2.2 Serpent 2 model

A Serpent 2 model is developed for detailed three-dimensional representation of all components of the SPERT IV D-12/25 reactor. The following aspects are used for the static neutron calculations:

- The composition of major materials is studied using the nuclear data library ENDF/B-VIII.0.
- To obtain the thermal neutron flux, a 1x60 mesh at the D-4 and E-5 positions has been used. The radial section of the mesh consists of a square with a side of 0.1016 cm and a height of 77.15 cm, divided into 60 equidistant cells. This discretization has been implemented to ensure the accuracy of the results obtained.
- Each calculation is performed with 200 inactive cycles followed by 1000 active cycles, with neutron per generation of 1E6, and the boundary conditions for all outer boundaries of the geometry are of the type vacuum.

8.2.3 Serpent2/Subchanflow model

A Serpent2/Subchanflow model is developed for the three-dimensional representation of the SPERT IV D-12/25 reactor. The investigations are divided into static and dynamic calculations using the nuclear data library ENDF/B-VIII.0. Due to the high complexity of the reactor core, additional files for axial and radial remapping of nodes are used in both cases. Also, the boundary conditions for all outer boundaries of the geometry are of the type vacuum. Additionally, following aspects are considered:

For the static calculations:

- A square detector of 0.1016 cm has been used to record the values of thermal neutron flux,
- the axial discretization for the acquisition of neutron heat flux values at positions D-4 and E-5 is 60 cells,
- the axial discretization for the information transfer (IFC-type 22) is 20 cells for both the fuel plate and the coolant channel, and
- the calculations are performed with 200 inactive cycles followed by 1000 active cycles, with neutron per generation of 1E6.

For the dynamic calculations:

- For the tests B-34 and B-35, the total number of particles is 4E6 divided into 200 batches,
- the axial discretization for the information transfer (IFC-type 22) is 20 cells for both the fuel plate and the coolant channel, and
- the combined movement of withdrawal and inserting the transient rod ensures the reactivity of the system.

To ensure good feedback of the thermal-hydraulic information with the least statistical noise for the coupled Serpent2/Subchanflow calculations, the convergence criteria proposed in (Ferraro, 2021) and (Ferraro, et al., 2019) have been used ($\epsilon_{T_{fuel}}^t = 5$ [°C], $\epsilon_{T_{cool}}^t = 1$ [°C] and $\epsilon_{\rho_{cool}}^t = 0.01$ [g/cm³]). In addition, a factor $\omega = 0.5$ has been used to relax the thermal-hydraulic parameters for the steady-state calculations and $\omega = 0.0$ for the transient calculations.

8.3 Validation of the Serpent 2 using steady-state experimental data

The following is a brief description of the model of the reactor SPERT IV D-12/25 created by Serpent 2 for validation.

8.3.1 Identification of the position of control rods for criticality state

Figure 8.6 shows two axial cuts, corresponding to sections D-4 and E-5 (see Figure 8.3). In section D-4 shows four control rods, with the poison section located at the top and represented by a dark area. The poison section is located at a distance of 51.46 cm from the lowest part of the reactor. The lower part of the control rods is made of aluminum. In contrast, cut E-5 on the right side of Figure 8.6 shows two transient rods. In this case, the poison section (also in dark color) is located at the bottom and is completely outside the active region. The active region of the core has a length of 60.96 cm.

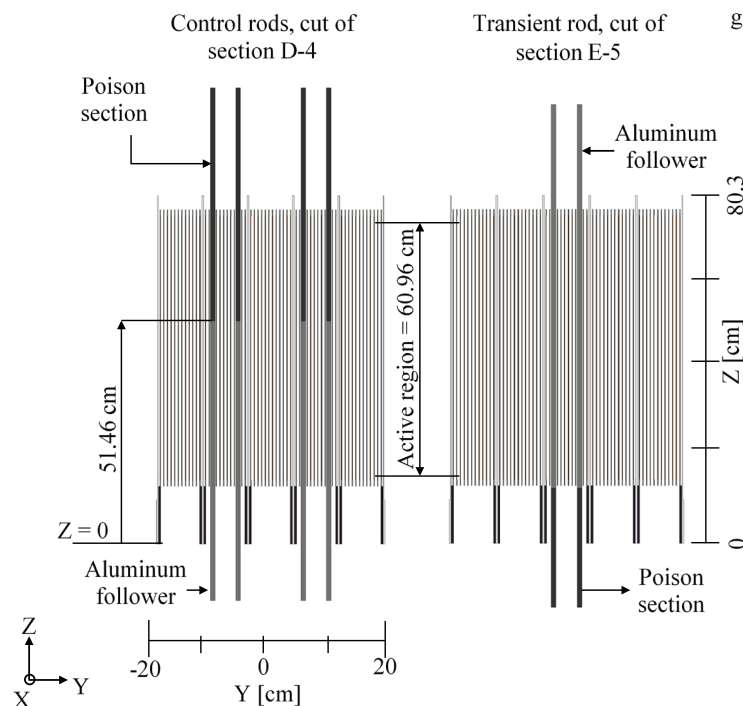


Figure 8.6: Representation of the SPERT IV reactor using Serpent 2 together with axial sections for the control (section D-4) and transient (section E-4) rods.

8.3.2 Comparison of predicted and experimental results

Figure 8.7 and Figure 8.8. show the normalized values of the thermal neutron flux, both measured and calculated by Serpent 2, for sections D-4 and E-5. In both cases, two peaks can be seen. The main peak indicates that the maximum thermal neutron flux is at a height of 40 cm, measured from the lowest part of the reactor. A second, smaller peak is located at a height of about 10 cm. Comparing the values measured at D-4 and E-5, it is observed that the neutron flux is lower in the upper part of D-4, which is due to the presence of control rods where the poison area is located, which absorbs neutrons to reduce nuclear fission. The secondary peak at the bottom, on the other hand, is due to the interaction of neutrons with the aluminum lattice where the reactor core is housed.

The results calculated by Serpent 2 show a similar trend to the measured values. The statistical error increases at the maximum and minimum peak values. The maximum normalized statistical error values for D-4 and E-5 are ± 0.051 and ± 0.048 , respectively. Overall, it can be stated that the values calculated by Serpent 2 agree satisfactorily with the experimental values, with about 95% of the experimental values falling within the statistical error bands. This proves the reliability of Serpent 2 for simulating research reactors and ensures that the model created is suitable for transient state calculations.

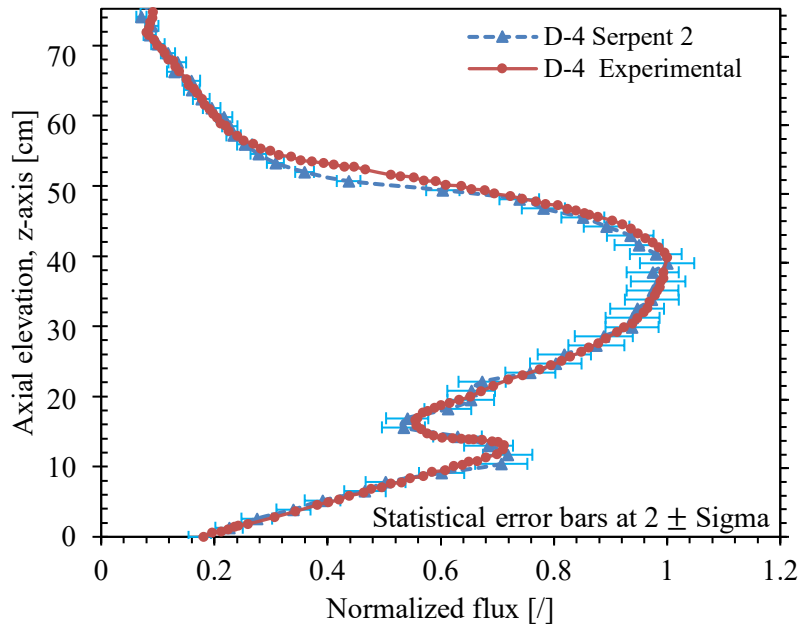


Figure 8.7: Comparison of thermal neutron flux detector at location D-4.

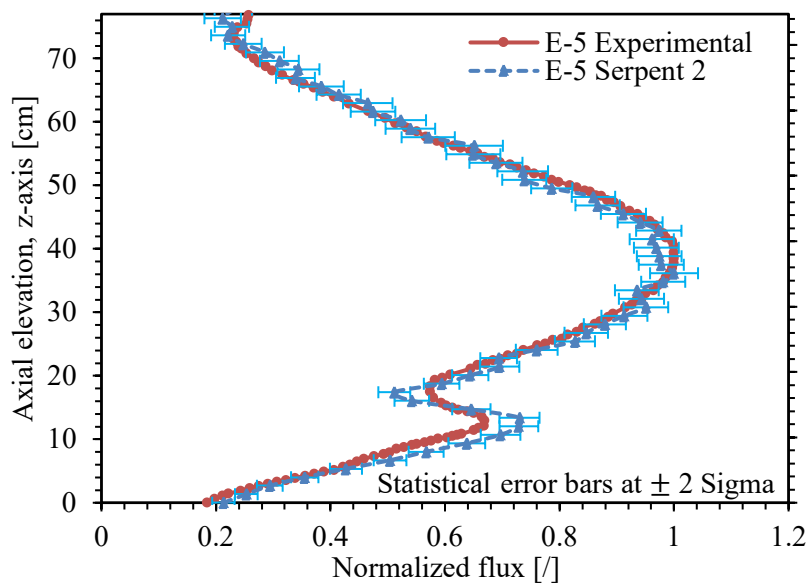


Figure 8.8: Comparison of thermal neutron flux detector at location E-5.

Figure 8.9 shows the reactivity added to the reactor when the control rods are drawn stepwise in the z-direction. The simulations have been performed at six different axial positions, measured from the lowest part of the active region of the plate, see Figure 8.6.

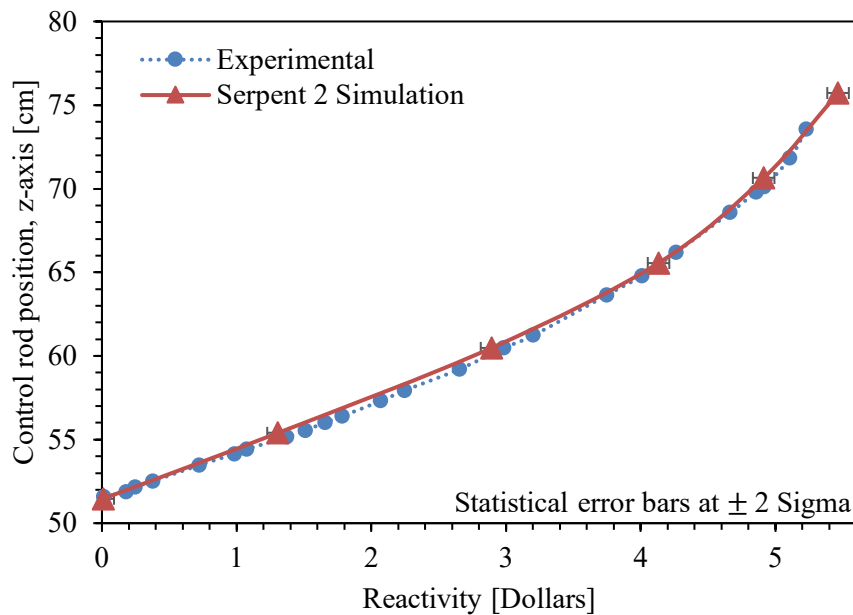


Figure 8.9: Integral control rod worth.

Finally, the main neutronic parameters calculated with Serpent 2, such as the k_{eff} factor, the β_{eff} factor (by Meulekamp method), and the excess reactivity, have a statistical error of ± 2 sigma and are compared with the available experimental values in Table 8-7. In general, a very good agreement with the experimental values can be observed (Meulekamp and van der Marck, 2006).

Table 8-7: Comparison between experimental and predicted values for the main neutron parameters.

Item	β_{eff} [pcm]	k_{eff}	Critical position with TR fully out [cm]	Excess reactivity [\$]
Experiment	N/A	~ 1	51.46	5.27
Serpent 2	749 ± 2	1.00007 ± 0.00014	51.46	5.27 ± 0.04

8.4 Validation of Serpent2/Subchanflow using transient experimental data

A transient simulation using the coupled code Serpent2/Subchanflow consists of two-steps. In the first step, the sources for live neutrons and precursors (external sources) are generated and stored by performing a criticality calculation. In a second step, a fixed source simulation is performed that uses the external sources generated in the step-1. The criticality state for reactor startup is not the same as that presented in Section 8.3, so the recommendations of (Crocker and Stephan, 1964) and (Crocker, et al., 1963) are used to determine an appropriate criticality state for the transient tests.

8.4.1 Start-up of the SPERT IV reactor for transient tests

The procedure for initiating transient testing is described in detail in (Crocker and Stephan, 1964) and (Spano and Miller, 1962). A procedure similar to the one used to establish the initial starting positions of the control rods and the transient rod is described below:

1. *A criticality condition is reached:* In this case, the model validated in Section 8.3 is used, where the positions of the control rods and the transient rod are known (see Figure 8.6).
2. *The exact position of the control rods required for the insertion of the desired excess reactivity is determined from the control-rod-worth-curves:* At this point, the reactivity addition for the SPERT IV D-12/25 tests vary from 0.88 to 2.14 \$, so the maximum value of 2.14 \$ is taken as a reference, allowing an overestimation of 23.36%.
3. *Insertion of the poison section of the transient rod (TR) into the reactor core:* The transient rod is inserted into the reactor core until the criticality value is reached, i.e., a value of 2.64 \$ is extracted from the system. At this time, the initial positions of the control rods and the transient rod are recorded and the velocities required transient rod withdrawal or insertion velocities for the tests are determined.

The sequence of steps proposed above has been tackled with the coupled Serpent2/Subchanflow code given the initial conditions of Table 8-5 and the assumptions of Section 8.2.3. First, using the curve shown in Figure 8.9, the position of the transient rods is determined for a reactivity of 2.64 \$. Then, the poisonous section of the transient rod is gradually inserted until a criticality state relevant to the transient tests is reached. During the insertion of the transient rod, the TR worth curve is constructed starting from seven different axial positions. Figure 8.10 shows the TR worth curve of the reactor SPERT IV D-12/25 with an uncertainty of ± 2 sigma.

Figure 8.11 shows the Serpent2/Subchanflow model created to simulate the SPERT IV D-12/25 reactor, showing the axial sections to illustrate the position of the control rods and the transient rod. In slice D-4, it can be seen that the position of the control rods is 59.7187 cm measured from the bottom and has been determined using the control rod-worth curves (Figure 8.9); in slice E-5, the transient rod can be seen at a distance of 36.678 cm measured from the bottom.

The distances given in this section correspond to a criticality state pertinent to the performance of transient tests, so this configuration is used for the calculation and storage of the external sources of live neutrons and precursors required for the dynamic calculations.

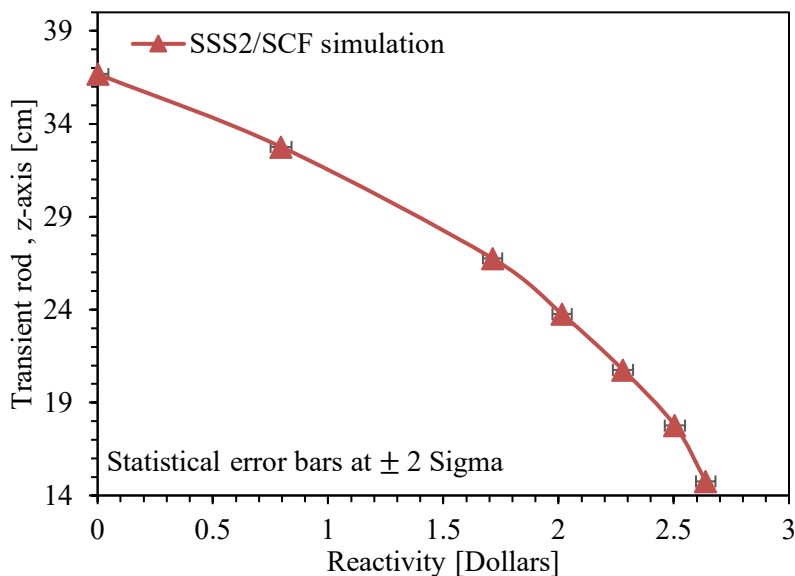


Figure 8.10: TR worth curve for SPERT IV D-12/25 reactor calculated by Serpent2/Subchanflow.

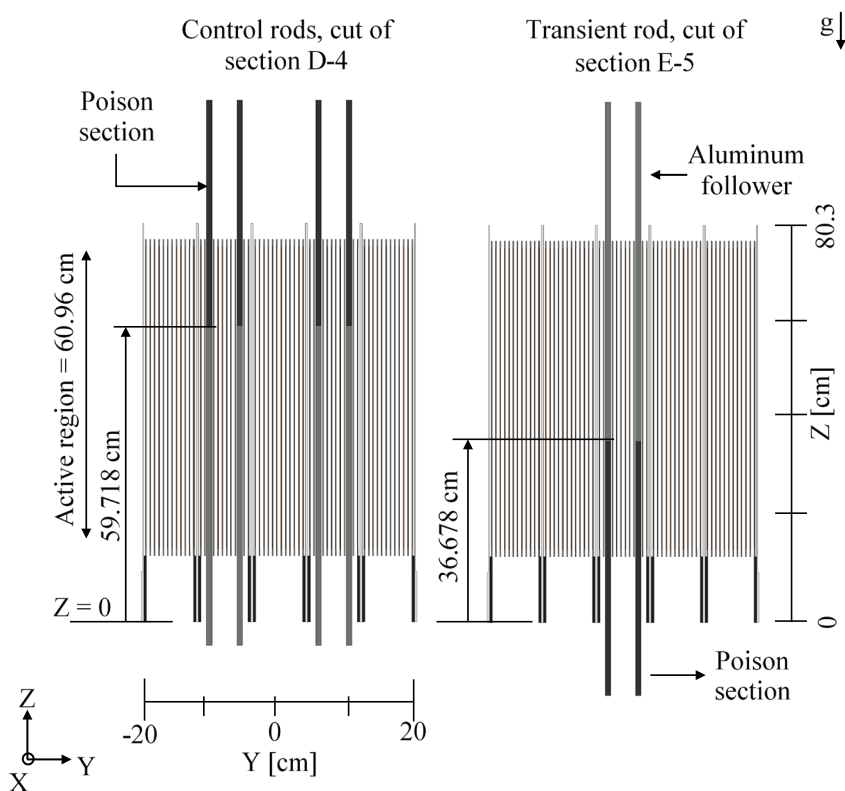


Figure 8.11: Representation of the SPERT IV reactor using Serpent 2 along with axial slices for the control (section D-4) and transient (section E-4) rods; model used for transient simulations.

Figure 8.12 shows the normalized thermal neutron flux at positions D-4 and E-5, calculated by Serpent 2. Maximum and minimum peaks can be seen in both curves. Compared to Figure 8.7 and Figure 8.8, it can be seen that the peak thermal neutron fluxes for D-4 and E-5 have moved upward due to the removal of the control rods and the introduction of the transient rod. The values calculated at the E-5 position retain their peak values. The maximum statistical error recorded for

D-4 and E-5 at ± 2 sigma is approximately ± 0.045 [/] and ± 0.044 [/], respectively, and is at a height of 45.5 cm. These values indicate that the calculations performed by Serpent 2 are conservative and show that the model can be used for transient simulations.

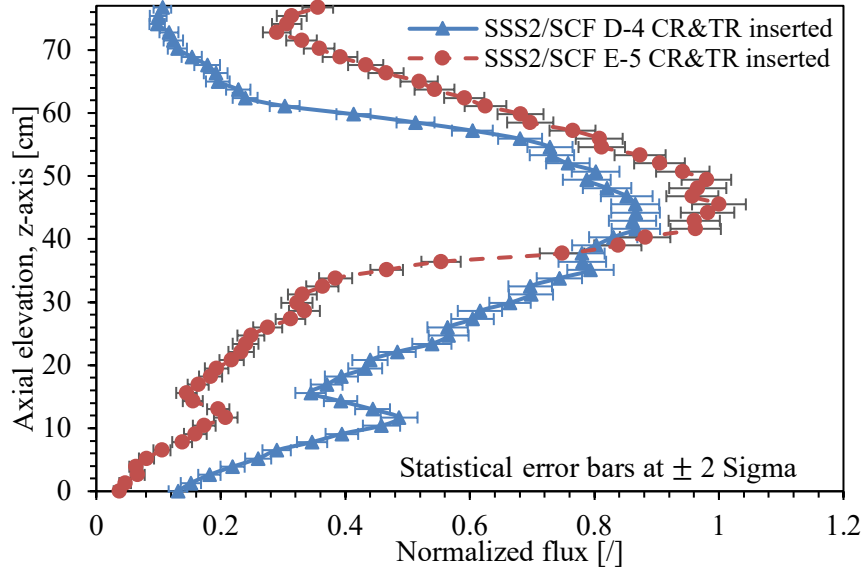


Figure 8.12: Simulated normalized thermal neutron flux normalized from inserted control and transient bars (CT & TR).

8.4.2 Transient rod movement scenarios for reactivity insertion

Since there is little information explaining in detail the movement of the transient rod during the dynamic tests, the transient rod movement scenarios are proposed considering the constraints found for the reactor SPERT III (Ferraro, 2021), (Ferraro, et al., 2020). It is not clear why this important parameter has been omitted, it could be due to the low power of the reactor or the main objectives of the project. However, Table 8-8 summarizes the scenarios for the transient rod motion based on the arrangements presented by (Almachi, et al., 2022a).

Table 8-8: Proposed transient rod movement scenarios for the reactivity insertion of tests B-34 and B-35.

ID	Vel1 Time scope	Vel2 Time scope	Vel3 Time scope	Reactivity [β]
B-34	-5.0 0.89 - 1.70	-1.5 2.24 - 2.33	N/A	0.88
B-35	-32 0.89 - 1.05	3.0 1.61 - 1.73	3.0 2.73 - 2.85	1.05
Vel [cm/s], Time scope [s].				

The experimental times required to perform the experiments in both cases are summarized in Table 8-9. The entire time interval is considered for the B-34 test ($\Delta t_{B-34} = 9$ s), while only a portion of the time interval is considered for the B-35 test ($\Delta t_{B-35} = 4$ s). For the transient simulation, the time intervals of both cases are divided into 100 bins, thus obtaining time steps for B-34 of 0.09 s and for B-35 of 0.04 s.

Table 8-9: Experimental time and simulation Δ time for cases B-34 and B-35.

ID	Experimental time [s]	Simulation Δt [s]	Bins	Step-time [s]
B-34	0.89 - 9.89	9 [s]	100	0.09
B-35	0.89 - 4.89	4 [s]	100	0.04

8.4.3 Comparison of global reactor parameters for test B-34

Figure 8.13 shows the results calculated by Serpent2/Subchanflow for the evolution of the total reactor power and the reactivity of the system. A consistent behavior is observed for the power, which increases when reactivity is added to the system. The sudden removal of the transient rod produces an increase in reactivity that places the reactor core in a supercritical state. The increase in power leads to an increase in fuel and coolant temperature (see Figure 8.14), causing negative reactivity feedback. Since the reactor core is loaded with highly enriched uranium (U-235), the Doppler effect is negligible (small amount of U-238) as an inherent reactor safety system, so the power still increases slightly despite the decrease in reactivity of the system (see Section 4.3.2). The experimental data are mostly within the statistical error band of ± 2 sigma, it can be observed that the statistical error increases with time. The peak reactivity calculated with Serpent2/Subchanflow is 0.746 ± 0.04 \$ at a time of 1.96 seconds. To obtain a better approximation of the calculated values to the experimental values, a more detailed description of the transient bar movements is needed. Despite the lack of information on this subject, no additional adjustment of the transient rod has been necessary in this case.

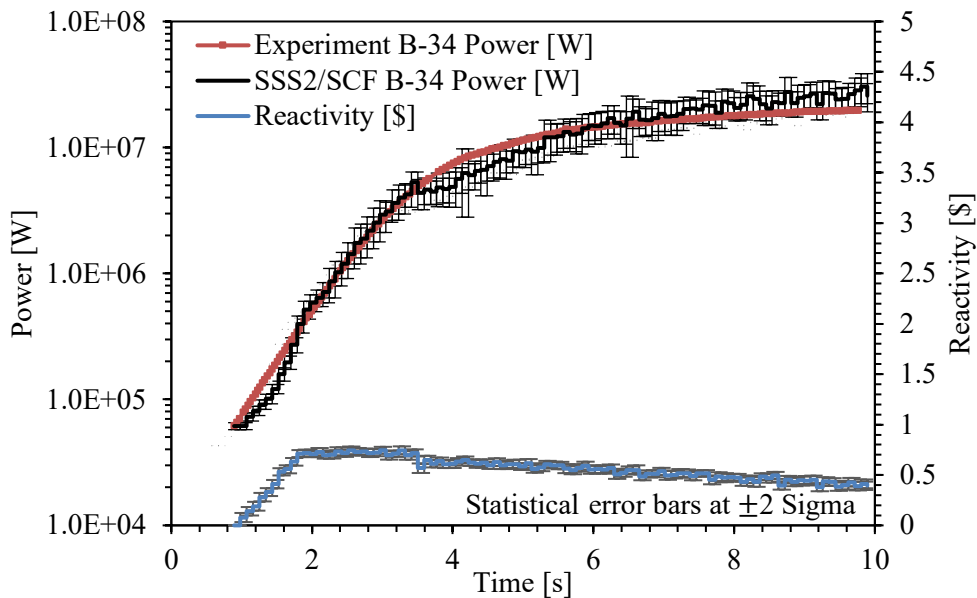


Figure 8.13: Evolution of total reactor power and total system reactivity of the reactor SPERT IV, only power values are compared with experimental measurements reported for B-34.

Figure 8.14 shows the evolution of the average fuel and coolant temperature over time. The average fuel temperature profile shows a slight instability compared to the fluid temperature profile. The maximum temperature values reached at the end of the time period ($t = 9.89$ s) are 83.14 °C for the fuel and 31.10 °C for the coolant. The instability of the average fuel temperature profile is attributed to the power fluctuations observed in Figure 8.13.

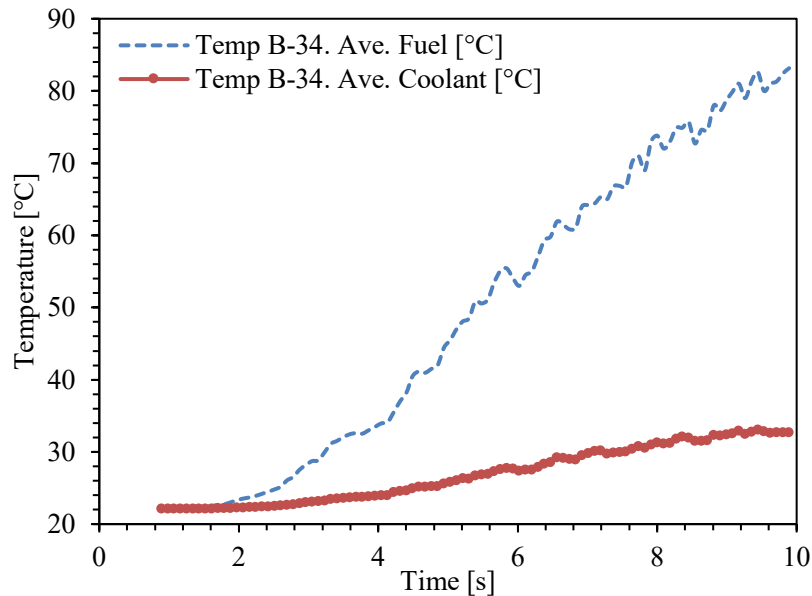


Figure 8.14: Evolution of averaged fuel and coolant temperature calculated by Serpent2/Subchanflow for the SPERT IV reactor tests B-34, no experimental results are provided for comparison.

8.4.4 Discussion of local parameters predicted for test B-34

A major advantage of the Serpent2/Subchanflow code is its capability to calculate parameters at the local level, i.e., at the plate/subchannel level, considering the feedback between neutronics and thermal-hydraulics. Figure 8.15 shows the radial distribution of the average power per plate. It can be seen that the power is concentrated around the center of the core. The empty areas within the core, shown in white, correspond to the water channels through which the control and transient rods move in the axial direction. Due to the high local resolution of the simulation, it can be seen that not all plates within a fuel assembly have the same power. Plates near the water channels have higher power due to increased moderation by the water, while plates away from the water channel have lower power. The plates identified as # 182 and # 5 show the highest and lowest power, with values of 118030 W and 66995 W in a time of 9.89 s, respectively.

Furthermore, by post-processing the data calculated with Serpent2/Subchanflow, it is possible to display the temperature values of fluid, cladding and fuel in three dimensions. Figure 8.16 shows the three-dimensional temperature distribution, in this case for the cladding of each plate of the test reactor SPERT IV D-12/25 B-34 at a time of 9.89 s. Simulations carried out with Serpent2/Subchanflow show the presence of temperature peaks in both radial and axial directions, which are concentrated in the center of the core in response to the power distribution shown in Figure 8.15. In addition, lower temperature values are observed at the radial ends, both at the bottom and top of the core, where the fission density is lower, leading to a decrease in power generation and consequently in temperature. It is of great interest to identify and analyze the temperature profiles corresponding to the peak power currents shown in Figure 8.15. These profiles

provide detailed information about the temperature distribution in the areas with the highest heat generation.

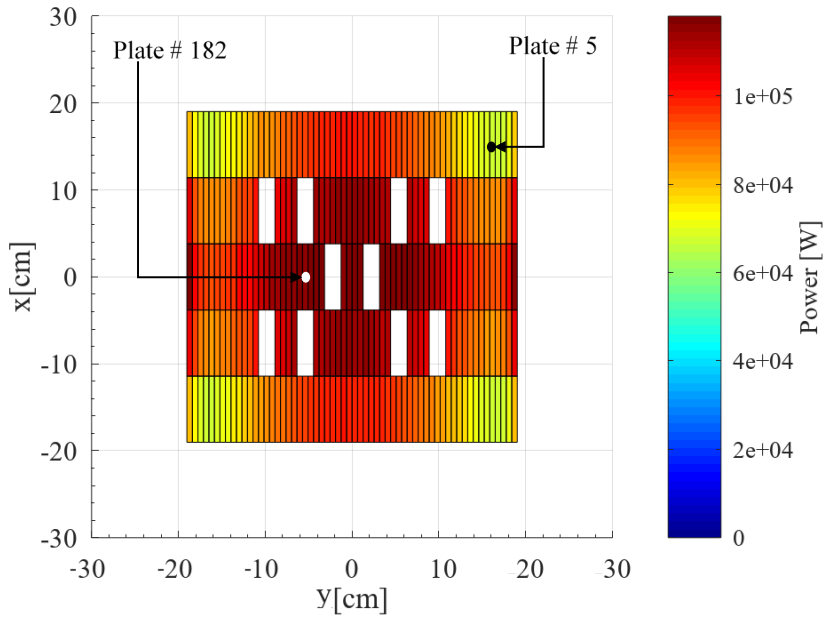


Figure 8.15: Radial power distribution for the SPERT IV reactor calculated by Serpent2/Subchanflow, test B-34 at a discrete time of $t = 9.89$ s after reactivity insertion.

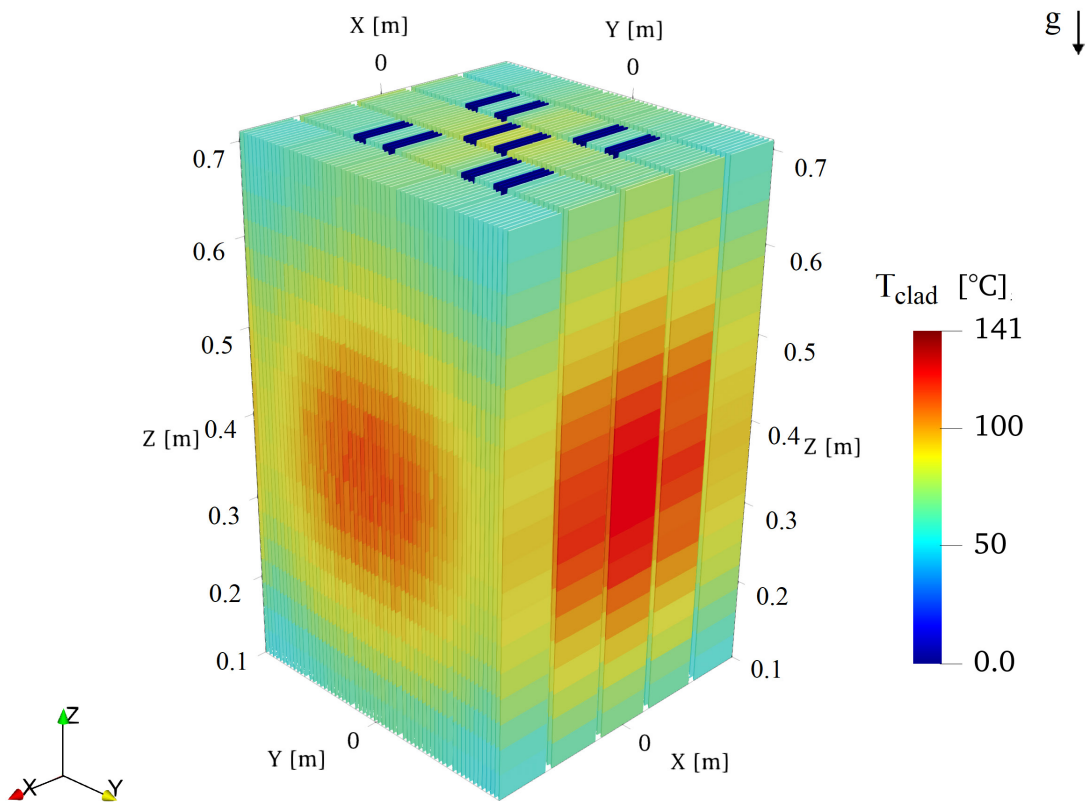
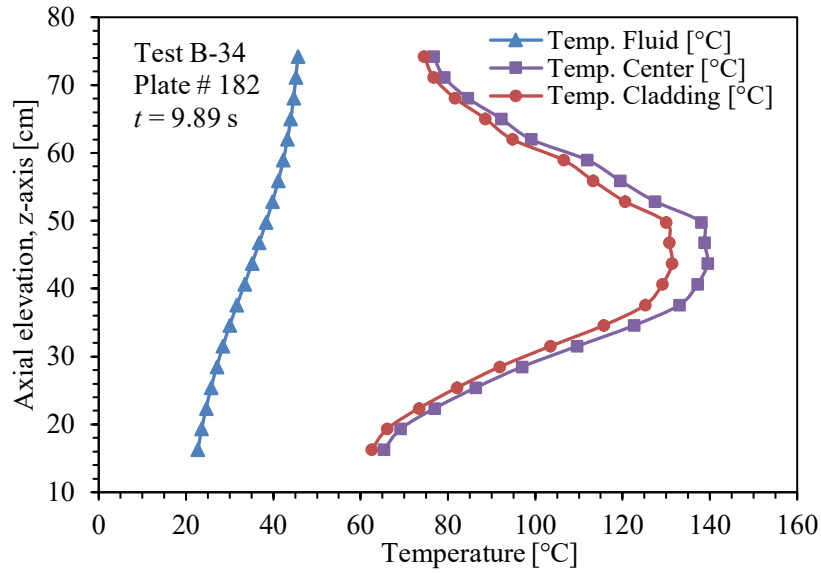
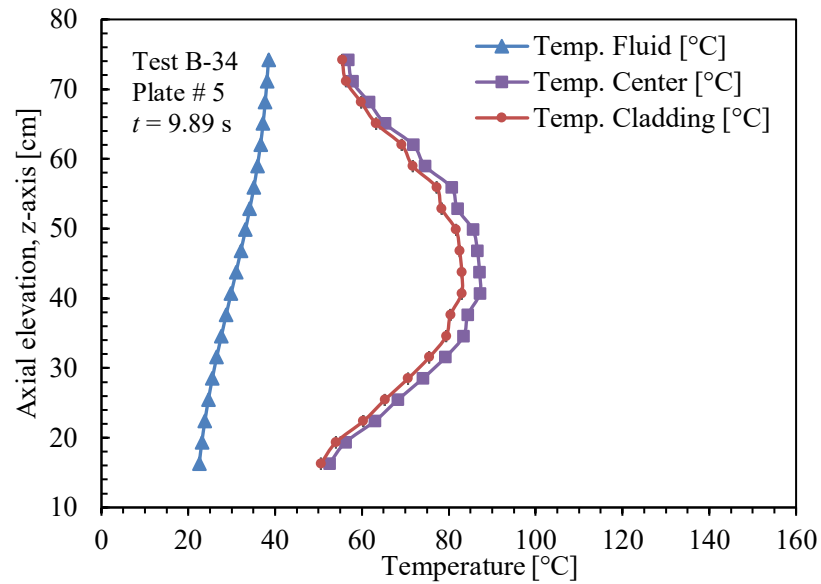


Figure 8.16. 3D cladding temperature distribution of reactor SPERT IV D-12/25 test B-34, predicted using Serpent2/Subchanflow at $t = 9.89$ s.



(a)



(b)

Figure 8.17: Test B-34, axial temperature distribution for coolant, cladding and fuel for: (a) maximum power plate # 182; (b) minimum power plate # 5 at $t = 9.89$ s after reactivity insertion.

Figure 8.17 shows the axial temperature distribution in plate/channel # 182 and plate/channel # 5. The values calculated by Serpent2/Subchanflow correspond to the coolant temperature, the cladding temperature and the fuel temperature. In both cases, it can be observed that the coolant temperature increases in the flow direction, i.e., upward and the maximum values are 45.62 °C for channel # 182 and 38.47 °C for channel # 5. The temperature peaks are located at 44 cm height in plate 182 and at 40 cm height in plate 5. In plate 182, the maximum temperature values are 139.46 °C for the fuel and 131.33 °C for the cladding. On the other hand, in plate # 5, the maximum temperatures are 87.16 °C for the fuel and 83 °C for the cladding.

The above results show that plate # 182 has a higher temperature and power distribution compared to plate # 5. This is due to the fact that plate # 182 is located close to the reactor core (see Figure 8.15), where the neutron concentration is higher, which in turn increases the number of fissions and energy production. On the other hand, the difference in axial thermal peaks between plate # 182 and plate # 5 is due to the presence of the poisonous section of the transient rod, shown in Figure 8.12, which tends to be located at the top, significantly affecting plate # 182.

Finally, for test B-34, Figure 8.18 shows a comparison between the experimental temperature values and the values calculated by Serpent2/Subchanflow. The measured values correspond to the temperature evolution of the cladding of plate # 136 up to a $t = 9.89$ s. The temperature measurements have been performed by a thermocouple located at coordinates (0, -0.03, 35.08) cm according to the reference frame (x, y, z) shown in Figure 8.3. The maximum value of the cladding temperature reached at $t = 9.89$ s is 72 °C. As for the values calculated by Serpent2/Subchanflow, it can be noted that the temperature values are overestimated and underestimated compared to the experimental values. From $t = 8.6$ s, the overestimation of the calculated temperature values becomes more evident, and a maximum difference between the predicted and experimental temperature of 7 °C is observed at $t = 9.89$ s. The time-dependent temperature increase observed for plate # 136 is due to the power increase shown in Figure 8.13, which is the result of the reactivity insertion in the system. An uncertainty of $\pm 10\%$ is considered for the experimentally measured values; this value combines the measurement uncertainty and the digitization of the results. The comparison between the calculated and experimental values shows that about 98% of the calculated values are within the established error band. This good agreement proves the ability of the Serpent2/Subchanflow code to perform calculations under transient conditions in research reactors.

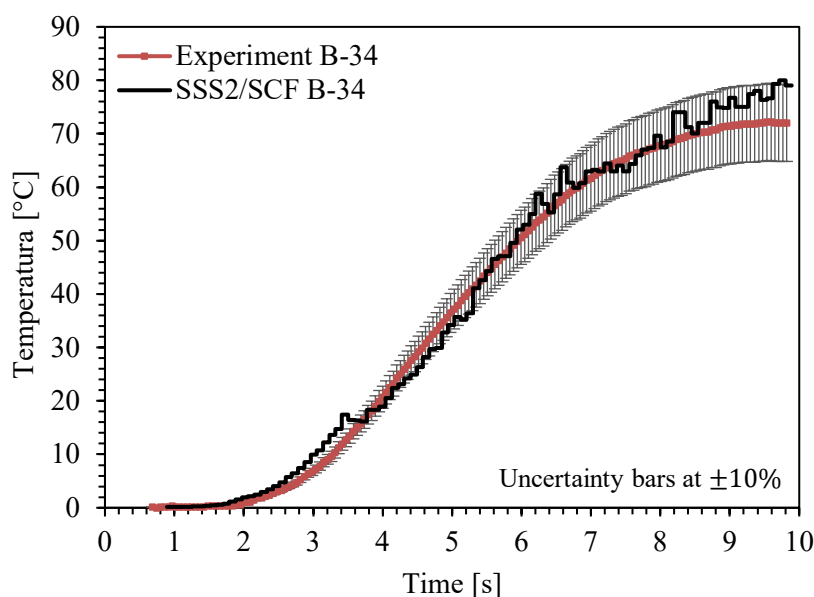


Figure 8.18: Comparison of temporal evolution of the cladding temperature between Serpent2/Subchanflow calculation and experimental data for the plate # 136, test B-34.

8.4.5 Comparison of global reactor parameters for test B-35

Figure 8.19 shows the measured power values along with the power and reactivity values calculated by Serpent2/Subchanflow for a transient condition. It can be seen that the measured power values increase in two intervals. In the first-time interval, the power increases rapidly and reaches a value of 8.65 MW for $t = 1.56$ s. Thereafter, the power continues to increase at a lower intensity, reaching a value of 21 MW at $t = 4.89$ s. The values calculated by Serpent2/Subchanflow correspond to the power and reactivity supplied to the system. The statistical error for the calculated power and reactivity values is estimated to be ± 2 sigma. While the calculated power values show both overestimation and underestimation, for the most part they follow the same trend as the experimental data, i.e., an abrupt increase followed by a gradual increase. The reactivity curve, located at the bottom of Figure 8.19, shows an increase to a maximum of 0.95 ± 0.04 \$ at $t = 1.13$ s and then begins to decrease until it reaches a value of 0.55 ± 0.044 \$ at $t = 4.89$ s. The power increases observed in the measured and calculated values are due to the insertion of reactivity into the system. The transient rod responsible for the change in neutron flux due to neutron absorption moves according to the scenarios described in Table 8-8 (Almachi, et al., 2022a). An increase in power indicates that the poisonous section of the transient rod is moving away from the nucleus, increasing fissions and thus power. Once the rod stops moving, the reactivity begins to decrease until equilibrium is reached. It is found that more than 95% of the experimental power values are within statistical error, confirming good agreement between experimental and calculated values.

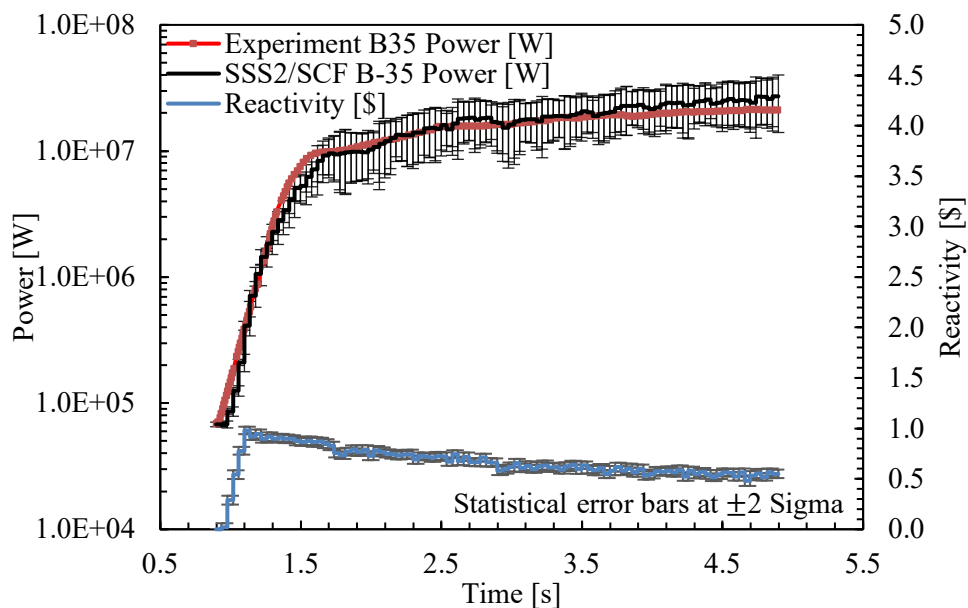


Figure 8.19: Evolution of total reactor power and total system reactivity of the reactor SPERT-IV, only power values are compared with experimental measurements reported for B-35.

Figure 8.20 shows the evolution of the average temperatures calculated by Serpent2/Subchanflow for the fuel and the coolant up to a time of 4.89 s. It can be observed that the coolant and fuel temperatures reach their maximum values of 34.0 °C and 84.0 °C, respectively,

at the end of the test period. Slight fluctuations in the temperature profile can be observed starting at 2.9 s. The increase in fluid and fuel temperature is due to the power increase shown in Figure 8.19. The fluctuations observed in the fuel temperature profile are inherent to the Monte Carlo approach and may be due to the fact that the particle contribution is small from $t = 2.9$ s onwards. The particle contributions are related to the change in the geometrical configurations of the core due to the movement of the transient rod (see Table 8-8), which alters the neutron flux and thus the effective sections, adding uncertainties to the results. It is worth noting that in this case no experimental data are available for comparison, so these results serve as a reference for calculations performed with lower level solvers, such as deterministic methods.

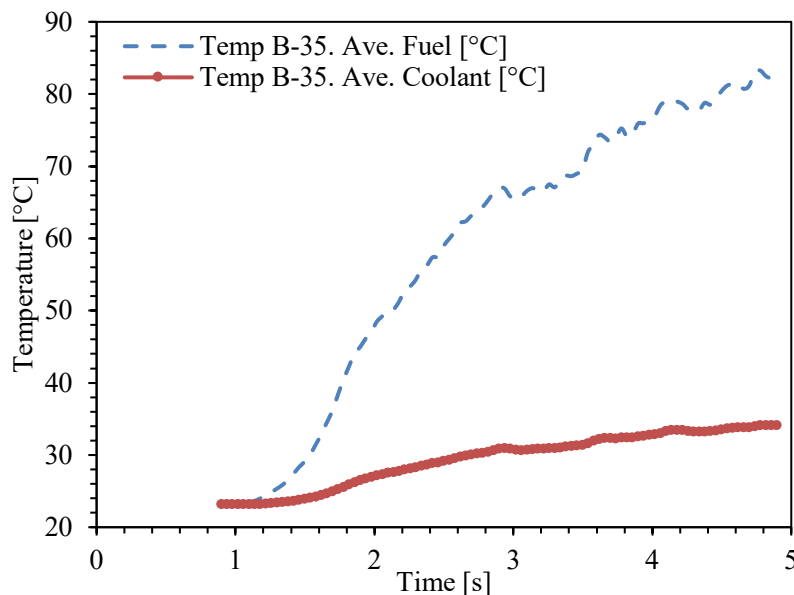


Figure 8.20: Evolution of averaged fuel and coolant temperature calculated by Serpent2/Subchanflow for the SPERT IV reactor tests B-35, no experimental results are provided for comparison.

8.4.6 Discussions of local parameters predicted for test B-35

Figure 8.21 shows the radial power distribution in the SPERT IV D-12/25 reactor core for the B-35 test. A concentration of power is observed in the center of the core, as well as in the areas where the tubes housing the control rods and the transient rod are located, and at the central ends. The maximum and minimum power values calculated for this test can be identified in the figure. Plate # 246 at the far-left center has the highest power of 116240 W, while plate # 219 at the upper left end has the lowest power of 65304 W. The power concentration in the center of the core is due to the higher density of the fissile material, which leads to a higher rate of nuclear reactions and thus higher power generation. On the other hand, for the plate # 246, the cold water in the extreme regions of the core acts as a moderator, which means that the neutrons are slowed down more efficiently and are more likely to initiate nuclear reactions in these regions, resulting in higher power generation. The major advantage of using high level codes such as Serpent2/Subchanflow is that they allow a detailed analysis of the case described above. Standard

low-level codes would not be able to provide the same level of accuracy and information. Similar to case B-34, Figure 8.22 shows the three-dimensional representation of the cladding temperature distribution for each of the plates of the SPERT IV D-12/25 test B-35 reactor. Radial and axial temperature peaks are observed, which are due to the power distribution shown in Figure 8.21.

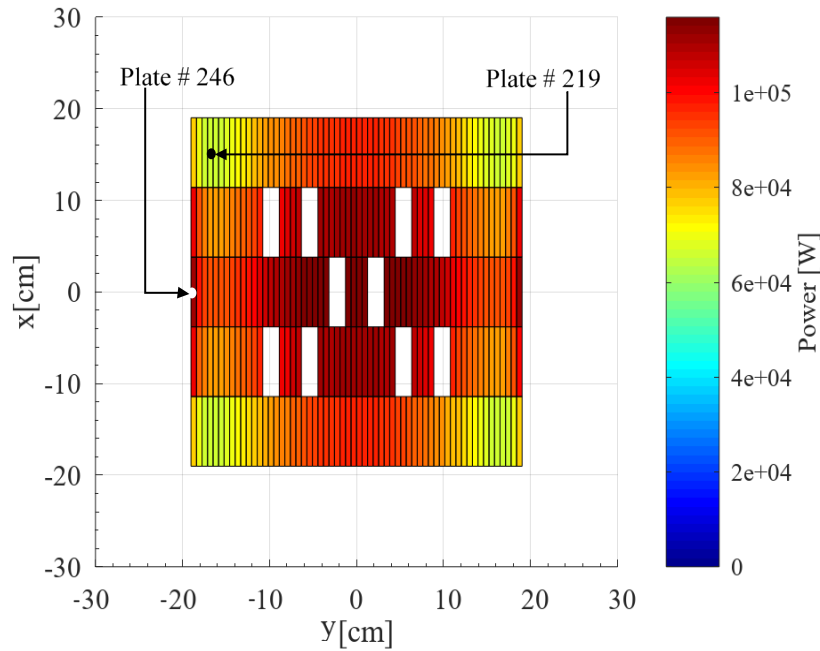


Figure 8.21: Radial power distribution for the SPERT IV reactor calculated by Serpent2/Subchanflow, test B-35 at a discrete time of $t = 4.89$ s after reactivity insertion.

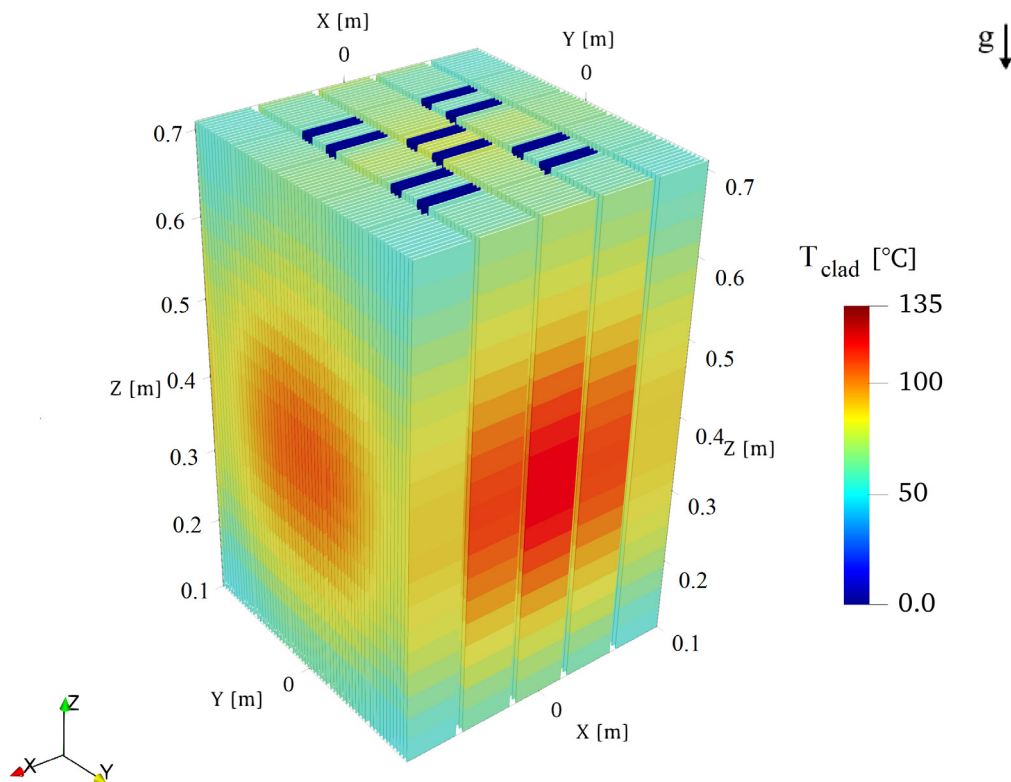
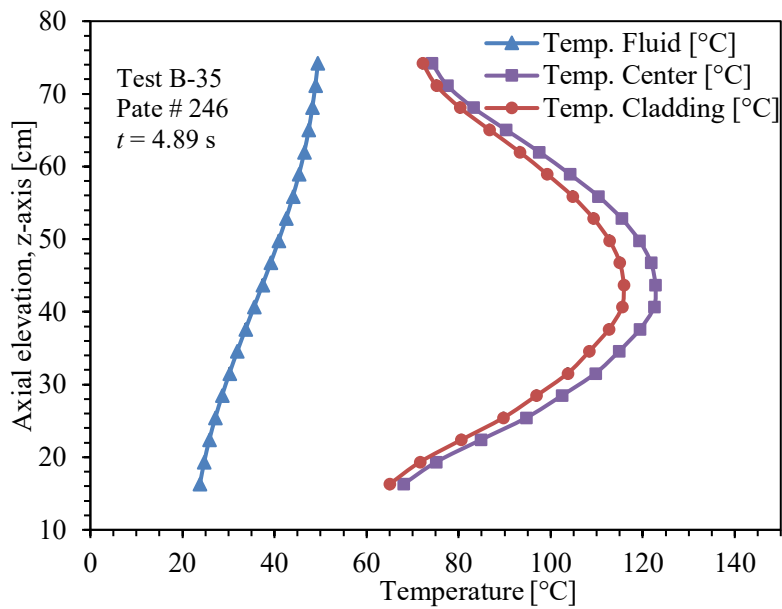
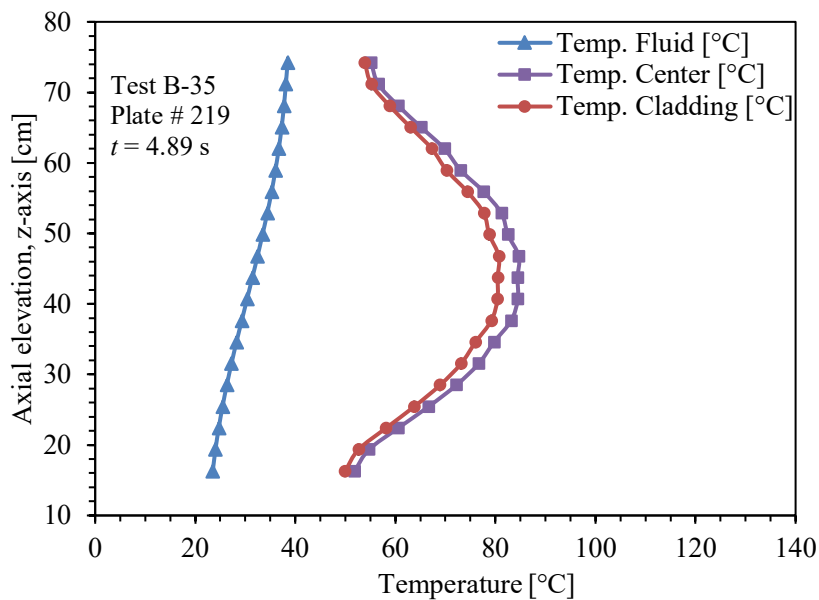


Figure 8.22: 3D cladding temperature distribution of reactor SPERT IV D-12/25 test B-35, predicted using Serpent2/Subchanflow at $t = 4.89$ s.



(a)



(b)

Figure 8.23: Test B-35, axial temperature distribution for coolant, cladding and fuel for: (a) maximum power plate # 246; (b) minimum power plate # 219.

Figure 8.23 shows the axial temperature distribution for the coolant, cladding, and fuel for plates/channels 246 and 219 over a time of 4.89 s. The highest values for the coolant temperature have been found at the reactor core outlet with a value of 72.17 °C and 53.88 °C for channels 246 and 219, respectively. On the other hand, the cladding and fuel temperatures reach their maximum values at a height of 43 cm (115.85 °C 122.74 °C for plate # 246) and 46 cm (80.41 °C and 84.47 °C for plate # 219), which is due to the fact that the neutron flux distribution is different for each

of the plates (see Figure 8.12). The values calculated by Serpent2/Subchanflow do not show unexpected variations and can be used as a reference for other solvers in the absence of experimental data.

Finally, Figure 8.24 shows the evolution of the experimental temperature of the cladding of plate # 136 together with the values calculated by Serpent2/Subchanflow up to a time of 4.89 s. The measured temperature values have been performed with a thermocouple located at coordinates (0, -0.03, 35.08) cm (see Figure 8.3). For test B-35, the maximum temperature measured at $t = 4.89$ s is 72.26 °C. The temperature increase in the cladding is due to the power increase observed in Figure 8.19. Comparing the obtained results with the experimental data, it is observed that Serpent2/Subchanflow tends to overestimate and underestimate the cladding temperature values. Although the calculated power values largely agree with the experimental values (refer to Figure 8.19), the overestimation of the calculated data becomes more pronounced from $t = 3.2$ s, reaching a maximum temperature difference between the predicted (81.62 °C) and experimental values of 9.36 °C. This is due to the fact that the power for the plate # 136 is higher than the average power per plate, which leads to an overestimation of the temperature values. However, considering an uncertainty range of $\pm 10\%$ for the experimental data, it is observed that about 82% of the calculated values are within this range. This shows that Serpent2/Subchanflow provides good agreement with the experimental values despite the discrepancies mentioned above.

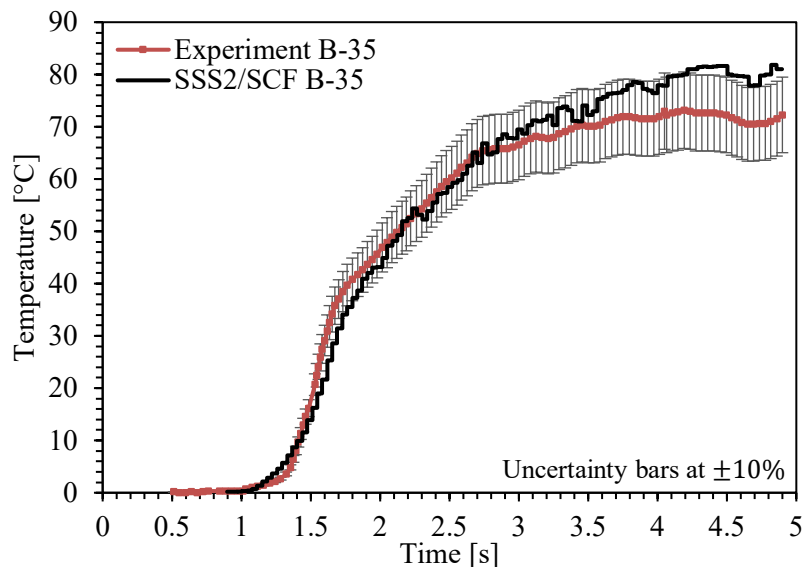


Figure 8.24: Comparison of temporal evolution of the cladding temperature between Serpent2/Subchanflow calculation and experimental data for the plate # 136, test B-35.

8.5 Final comments about the validation using the SPERT IV data

The validation of the transient capability of Serpent2/Subchanflow have demonstrated that the coupled code provides unique access to analyze local data which is superior compared to all

other computational routes used worldwide to analyze MTR-cores with plate-type fuel. The comparison of integral parameters such as the total power and local parameters as the axial cladding temperature of a plate predicted by Serpent2/Subchanflow with the experimental data measured in the tests 34 and 35 of the SPERT IV D-12/25 reactor is in very good agreement considering the complexity of the transients analyzed. These findings are very promising since no similar simulations have been published yet. A validated code version of Serpent2/Subchanflow can be applied for the safety evaluations of new MTR-cores in the frame of a licensing process. The values predicted by Serpent2/Subchanflow show good agreement with the experimental values of power and temperature of the central plate cladding. This is a great step forward compared to the large discrepancy between predictions and measured data observed in previous validation work (Margulis and Gilad, 2018) and (Labit, et al., 2021).

9 Analysis of reactivity insertion accidents in an MTR-core with Serpent2/Subchanflow code

To demonstrate the new capabilities of the validated coupled code Serpent2/Subchanflow performing safety evaluations of MTR-cores the RIA-transients defined in the IAEA MTR benchmark has been selected. The respective neutronic and thermal-hydraulic data of this benchmark are summarized in Appendix C. The generic reactor IAEA MTR benchmark is commonly used as a reference for accident analyzes in research reactors. Usually, the accident types analyzed for this hypothetical reactor focus on fast and slow reactivity insertion for transient calculations. In this section, a high-fidelity analysis for the IAEA MTR benchmark reactor is performed and discussed for the first time. In order to perform FRIA and SRIA transient analysis, assumptions are made and they are explained below.

9.1 IAEA MTR benchmark problem definition

The reactor data and transient scenarios used for these studies are defined by the IAEA in (IAEA, 1980) and (IAEA, 1992b). The core consists of highly enriched uranium and contains 21 standard fuel assemblies (SFA) and 4 control fuel assemblies (CFA). It is radially reflected by graphite on two opposite sides, and surrounded by light water, as illustrated in Figure 9.1. In this analysis, a 77 mm x 81 mm aluminum block with a 50 mm square hole filled with water in the central part of the core is considered (IAEA, 1992b) (p. 15).

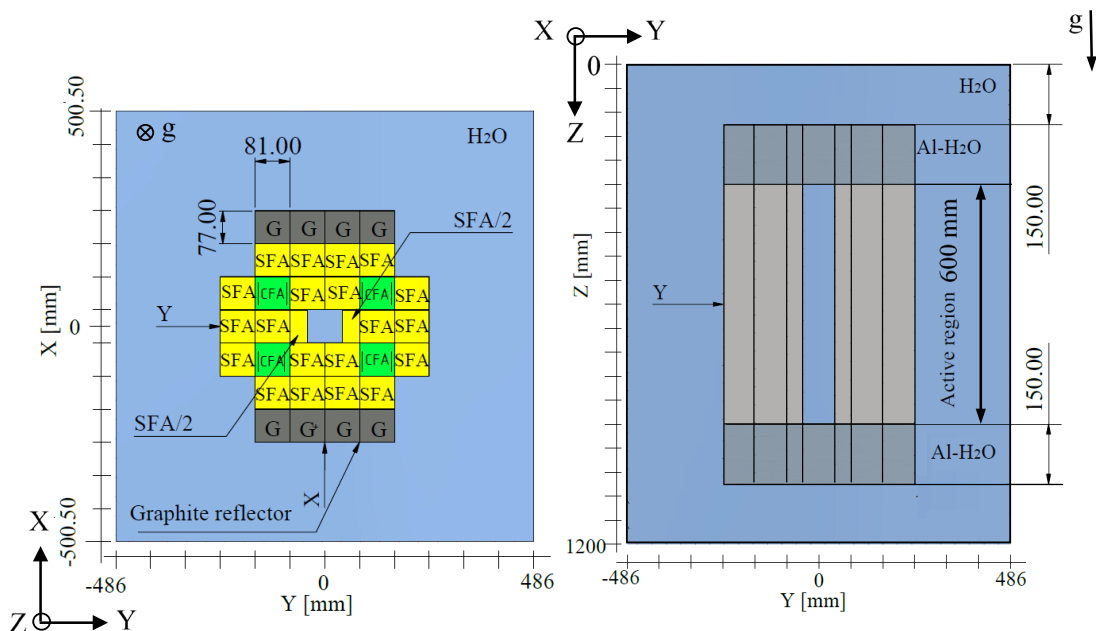


Figure 9.1: Representation of radial (left) and axial (right) slices of the MTR core, obtained from (Almachi, et al., 2022a).

Each SFA has 23 plates and a CFA has 17 plates. At the ends of the CFA, there is an empty region of 5.73 mm that contains the absorber material (AgInCd). Each CFA contains 2 absorber plates with a total of 8 plates throughout the core. Figure 9.2 shows the AgInCd absorber blades. To maintain the symmetry of the core, each half fuel assembly (SFA/2) in the center of the core has 12 plates.

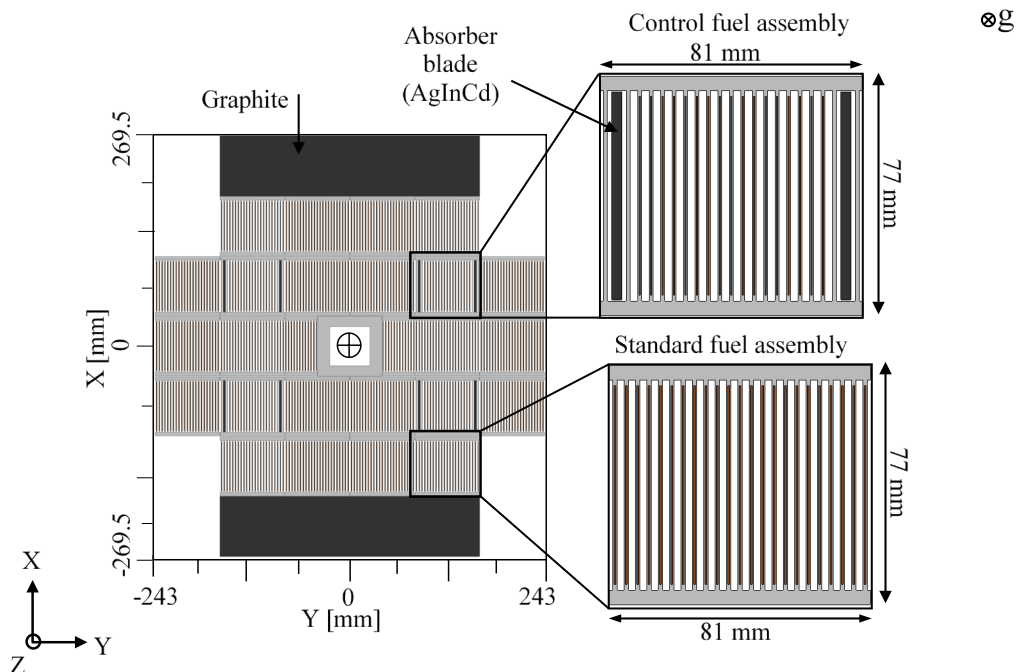


Figure 9.2: XY cross section of the reactor core midplane showing enlargement of the standard and control fuel assemblies with absorber blades modeled in Serpent 2, obtained from (Almachi, et al., 2022a).

The benchmark problem presented consists of two different types of accidents: reactivity-initiated accident (RIA) and loss-of-flow accidents (LOFA). In this work, only the two RIA scenarios, namely fast and slow reactivity insertion, are studied. Table 9-1 shows the main characteristics of these scenarios.

Table 9-1: Transient characteristics for IAEA MTR benchmark

Parameters	RIA HEU-BOL
Initial power	1.0 W for both scenarios
Rate of external reactivity insertion	- Fast RIA scenario: 1.5\$/0.5 s (FRIA) - Slow RIA scenario: 0.1\$/1 s (SRIA)
Scram setpoint	12 MW (120% of nominal power)
Delay time before shutdown	0.025 s for both scenarios
Shutdown reactivity insertion	-10\$/0.5 s for both scenarios
Coolant temperature inlet	311 K
Pressure at top of the core	1.7 bar
Coolant mass flow rate (downward)	1000 m ³ /h
Material fuel HEU	Enrichment 93 wt.% ²³⁵ U 280g ²³⁵ U per fuel element 21 wt. % of uranium in the UAl _x - Al

The core configuration for Beginning of Life (BOL) is shown in Figure 9.3 and the atomic density to HEU is taken from (Margulis and Gilad, 2016).

	A	B	C	D	E	F	g
1	Water	Graphite	Graphite	Graphite	Graphite	Water	
2	Water	SFA BOL 5%	SFA BOL 25%	SFA BOL 25%	SFA BOL 5%	Water	
3	SFA BOL 5%	CFA BOL 25%	SFA BOL 45%	SFA BOL 45%	CFA BOL 25%	SFA BOL 5%	
4	SFA BOL 25%	SFA BOL 45%	SFA BOL 45%	H ₂ O + Al 45%	SFA BOL 45%	SFA BOL 25%	
5	SFA BOL 5%	CFA BOL 25%	SFA BOL 45%	SFA BOL 45%	CFA BOL 25%	SFA BOL 5%	
6	Water	SFA BOL 5%	SFA BOL 25%	SFA BOL 25%	SFA BOL 5%	Water	
7	Water	Graphite	Graphite	Graphite	Graphite	Water	

Figure 9.3: MTR core configuration for Beginning of Life as a function of U-235 depletion, obtained from (Almachi, et al., 2022a).

9.2 Modeling of the IAEA-10 MW MTR reactor core

In order to develop very detailed and coherent models of Serpent 2 and Subchanflow for plate/subchannel level simulations, a radial map has been created showing the location of each plate/channel of the reactor core with a total of 552 plates and channels (see Appendix C Figure C.7). The mapping of the individual plates/channels is the starting point for the development of the multiphysics interface files called IFC. The Subchanflow and Serpent 2 models are created using the following assumptions:

Subchanflow model:

- A plate-centered model is used to create the Subchanflow and IFC models,
- for heat conduction, each plate is divided laterally in the y-direction into 3 and 2 cells for the fuel and cladding, respectively (see Figure 6.6),
- Blasius and Colburn correlations are used for the friction factor and heat transfer coefficient, respectively, based on previous validation work (Almachi, et al., 2021), and
- the axial discretization of each plate/channel is 20 equidistant cells.

Serpent 2 model:

- The IFC type-22 developed for KIT is used for data transfer between Serpent 2 and Subchanflow,

- the criticality calculation is performed with 20 inactive cycles followed by 200 active cycles, with neutron per generation of 150,000,
- nuclear data library: ENDF/B- VII.0 is used,
- for the fast reactivity insertion accident (FRIA), the total number of particles is 8E5 divided into 200 batches, and
- for the slow reactivity insertion accident (SRIA), the total number of particles is 1.6E6, divided into 200 batches.

Estimation of the control rod worth and critical control rod position:

Since there is no detailed information about the position of the control rods, the control rod curve must be estimated by simulations. Figure 9.4 shows the k_{eff} value predicted using Serpent2/Subchanflow, the variation of the effective K_{eff} multiplication factor is calculated for different positions (90 cm: fully inserted, 30 cm: fully withdrawn, see Figure 9.1) of the 8 control plates for the MTR core loaded with HEU at BOL conditions. Then, the critical position of the control rods is calculated by linear interpolation between two points at 30 cm and 40.2 cm, assuming a theoretical k_{eff} value of 1. Then, the core is recalculated using the new control rod positions to obtain a calculated k_{eff} value of 1.00012 ± 0.00015 . The assumed values for the critical position and the effective multiplication factor can be found in Table 9-2.

Table 9-2: Critical control rod position.

CR position [cm]	k_{eff} theoretical	k_{eff} calculated SSS2/SCF
52.46 ± 0.1	1	1.00012 ± 0.00015

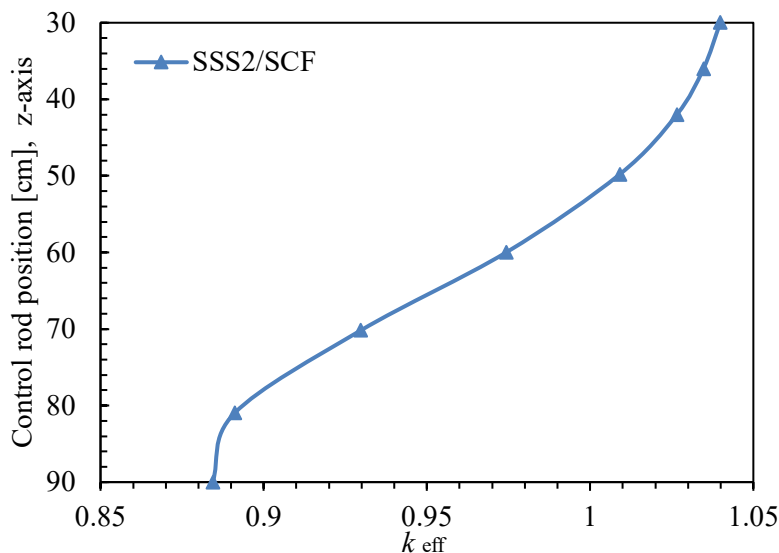


Figure 9.4. k_{eff} depending of the control rod position for HEU and BOL Benchmark Cores.

9.3 Definition of the fast/slow RIA transients

To perform transient calculations, it is first necessary to obtain the live neutron sources and precursors from an independent critical steady-state calculation. Following the above convergence and neutron population criteria, a full 3D model with a power of 1 W is created to generate the neutron sources. The conditions of the core in the critical steady state are characterized by the position of the control rod shown in Table 9-2. Since the extraction and insertion velocities of the control rods in the transient condition are not specified, constant velocity ramps are supposed for the FRIA and SRIA cases.

Figure 9.5 shows the movements of the control rod at each time interval for the fast RIA scenario (FRIA). In the time interval ($\Delta t_1 = 0.5$ s), the control rods are extracted at a constant speed of 0.61 ± 0.1 cm/s. Consequently, it is observed that the reactivity increases linearly from 0\$ to 1.5063 ± 0.007485 \$. After 0.5 s, the control rods remain at rest for $\Delta t_2 \sim 0.09$ s, and the reactivity continues to increase to a maximum of 1.6037 ± 0.007485 \$, at which point it begins to decrease due to the Doppler effect and the insertion of the control rod. This starts at 0.59 s with a velocity of -41 ± 0.1 cm/s to a value of -5.998 ± 0.00749 \$.

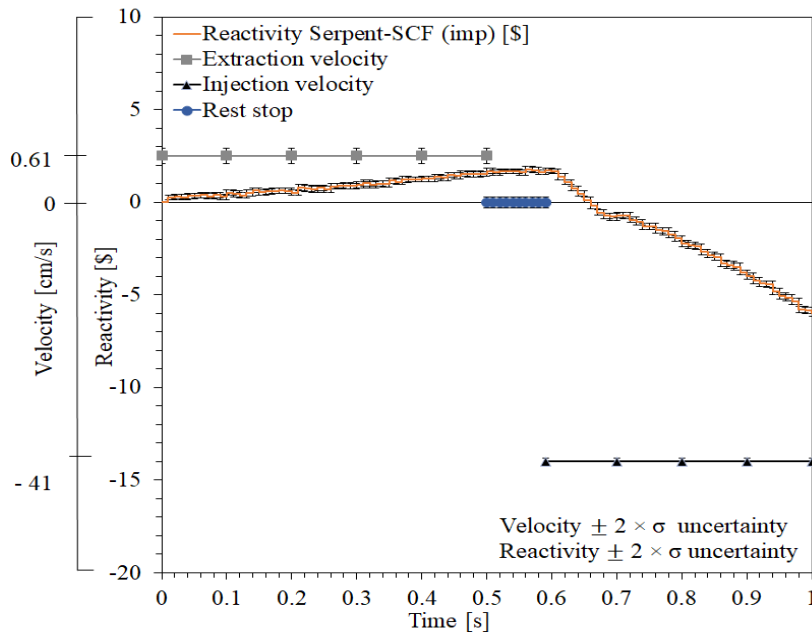


Figure 9.5: Anticipated control rod movements for FRIA event (1.5\$/0.5s) and simulated reactivity.

Control rod motions for the slow RIA event (SRIA) are shown in Figure 9.6. For $\Delta t_1 = 10$ s, the control rods are extracted with a constant velocity of 0.16 ± 0.1 cm/s, resulting in an increase in reactivity of $1.0051 \pm 6.86E-01$ \$. After the 10 s, the control rods are inserted with a constant velocity of -41 ± 0.1 cm/s for $\Delta t_2 = 0.5$ s, resulting in a decrease in reactivity to -9.0027 ± 0.007485 \$. Finally, after 10.5 s, the control rods remain at rest.

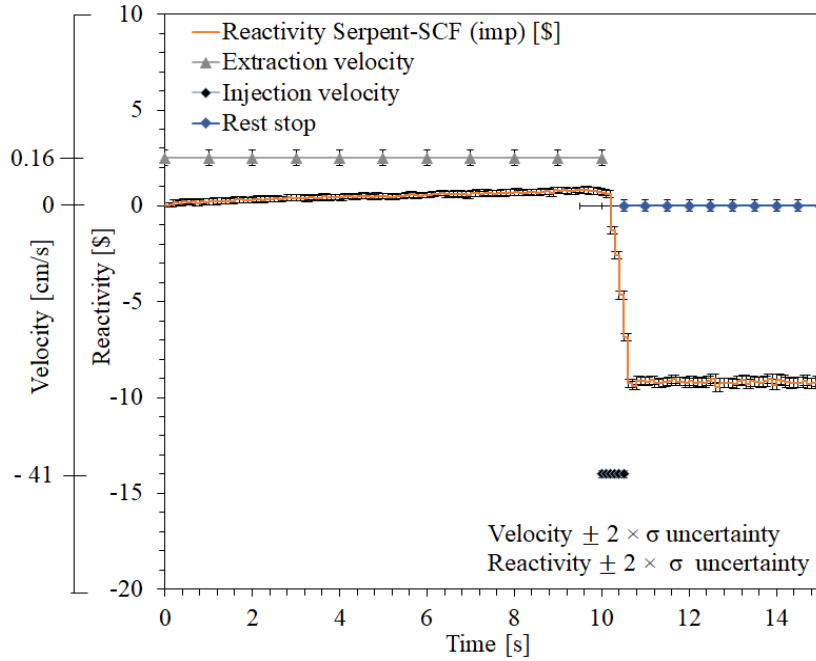


Figure 9.6: Anticipated control rod movements for SRIA event (1\$/10s) and simulated reactivity.

9.4 Convergence criteria

The convergence parameters, e.g., for fuel temperature, are determined based on L_2 according to Eq. (4.10). To obtain a good converges solution with minimal statistical noise, the following values are used as recommended in (Ferraro, et al., 2019): $\epsilon_{T_{\text{fuel}}}^{-t} = 5$ [°C], $\epsilon_{T_{\text{cool}}}^{-t} = 1$ [°C] and $\epsilon_{\rho_{\text{cool}}}^{-t} = 0.01$ [g/cm³]. Furthermore, a relaxation factor in Eq. (4.12) of $\omega = 0.0$ has been used.

9.5 Discussion of global results for FRIA and SRIA

9.5.1 Global results for FRIA

Figure 9.7 shows the evolution of the core power in a time interval of 1 s. It can be observed that the power increases from 1 W to a maximum value of 6.75E07 W at 0.63 s, which is due to the insertion of positive reactivity. After 0.63 s, the power begins to decrease until it reaches a value of 1.57E+05 W at 1 s. The evolution of the reactivity shows that the power increases when it is positive and that the power decreases when the reactivity becomes negative. It can be seen that the power increase is partly stopped by the reactivity coefficients of the Doppler and the moderator and mainly by the reinsertion of the control plates starting from 0.5 s. The statistical error of the power evolution increases until the peak power and remains larger than that of the initial time, while the statistical error of the reactivity remains almost uniform during the whole time of the transient.

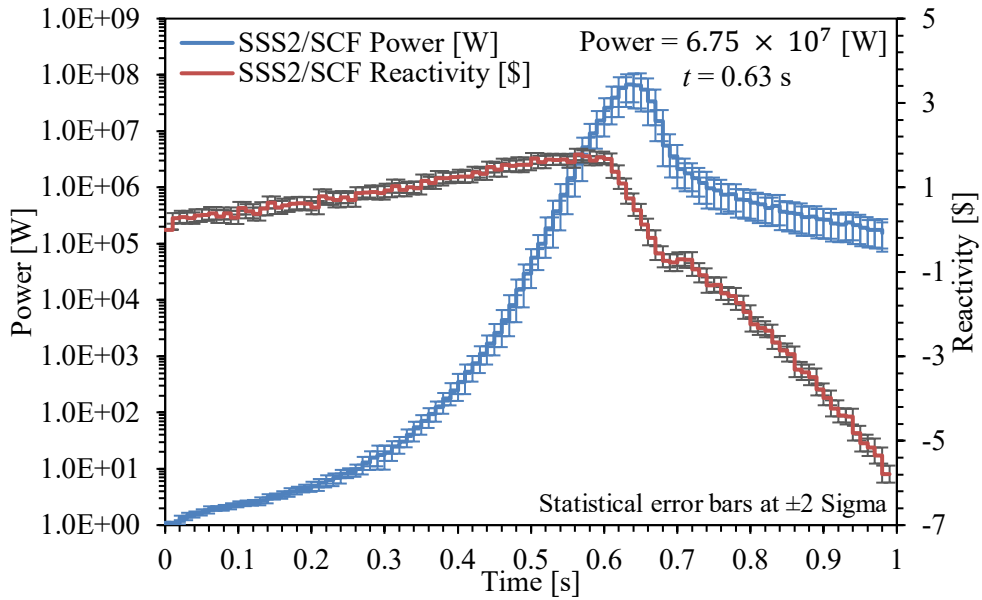


Figure 9.7: Computed temporal evolution of power and reactivity during the FRIA scenario (1.5\$/0.5 s).

On the other hand, the evolution of the average core temperature of the fuel and coolant during the transient time of 1 s is shown in Figure 9.8. It can be observed that the temperature peaks occur at different times. The peak of fuel temperature occurs at 0.67 s, with a maximum value of 362.012 K. The peak of coolant temperature occurs at 0.72 s, with a maximum value of 320.012 K. To understand the time difference between the peaks, one must examine the power profile shown in Figure 9.7, where the maximum power peak occurs at $t = 0.63$ s. The power deposited in the core takes time to heat up the fuel, the cladding and the coolant and to be reflected in the temperature, since each of these elements has its own specific heat. The first delay time is between the released power and the fuel and has a value of 0.04 s. Then, the plate cladding (aluminum) and the cooling liquid are heated. This second delay time is 0.05 s. This type of detailed analysis is one of the major advantages of the Serpent2/Subchanflow code for research reactor analysis.

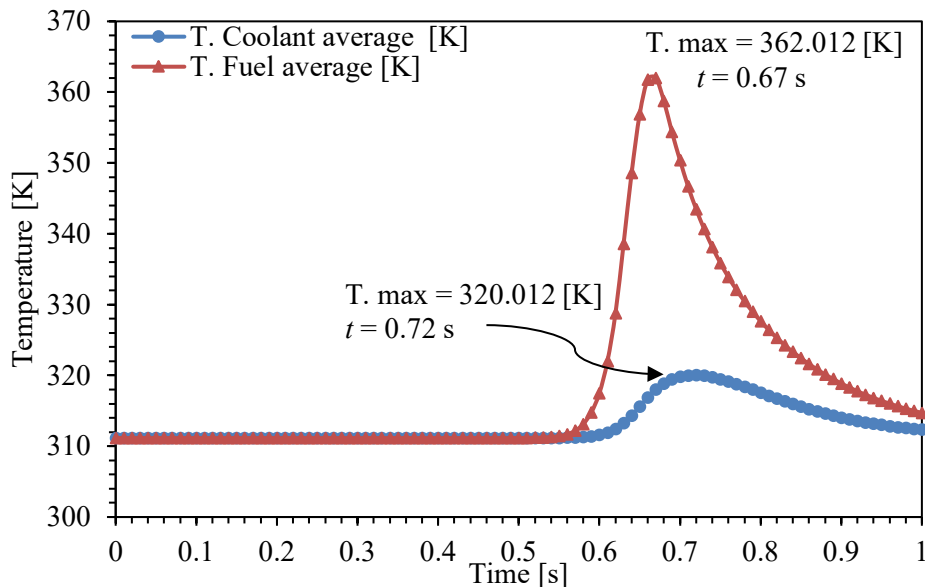


Figure 9.8: Simulated core averaged fuel and coolant temperature evolution for the FRIA scenario (1.5\$/0.5 s) as predicted by Serpent2/Subchanflow.

9.5.2 Global results for SRIA

Figure 9.9 shows the evolution of reactor core power during the first 10 seconds of the transient along with reactivity insertion. It can be seen that the power increases slowly due to the removal of the control plates up to 10.2 s. At 10 s, a maximum power of 1.47×10^7 W is reached. Then the control plates are inserted into the core, resulting in a negative reactivity of about $-9.0027\$/0.5$ s. As a result, the power decreases and reaches a value of 2.10×10^4 W at 15 s. As in the case of FRIA, it can be observed that the statistical error of the power increases with increasing power and is larger after the core is turned off, since the number of neutrons is drastically reduced leading to a high statistical uncertainty.

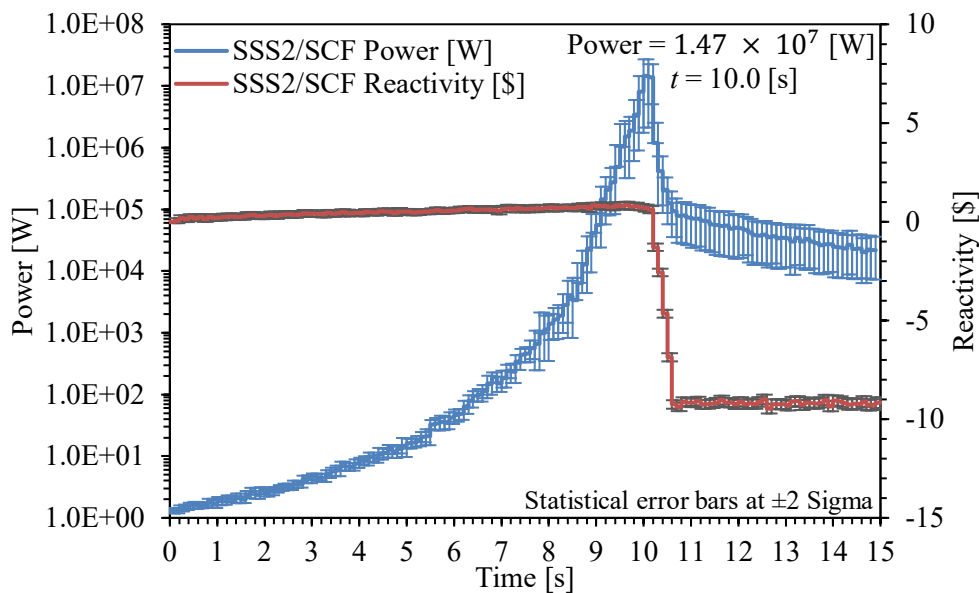


Figure 9.9: Computed temporal evolution of power and reactivity during the SRIA scenario ($1\$/10$ s).

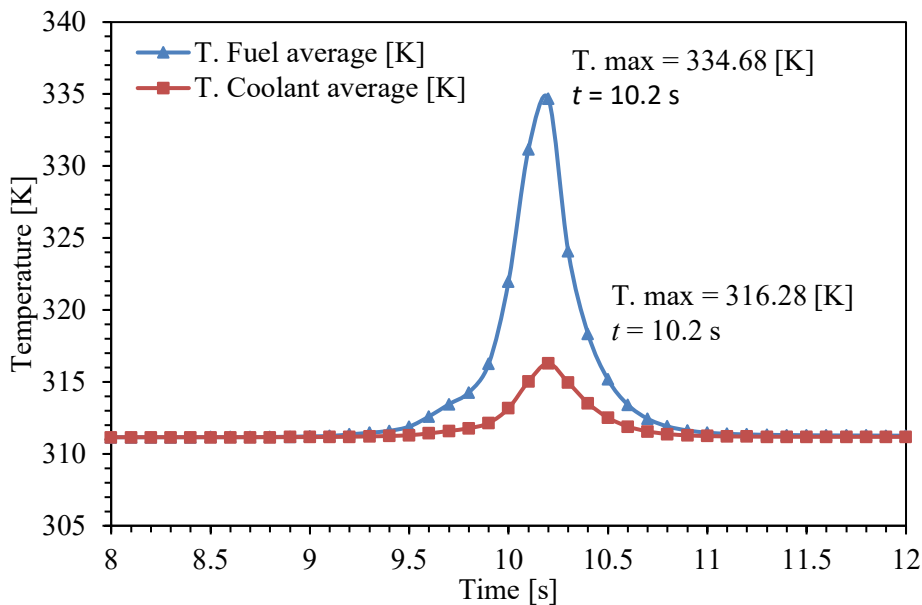


Figure 9.10: Simulated core averaged fuel and coolant temperature evolution for the SRIA scenario ($1\$/10$ s) as predicted by Serpent2/Subchanflow.

As shown in Figure 9.10, the maximum averaged core temperatures of the fuel and coolant are 334.68 K and 316.28 K, respectively. Both are at the same time at 10.2 s. After 11 s, there is no significant difference between the initial and final temperatures. In the case of SRIA, the changes in realized power are slower, so thermal resistances due to the thermal capacities of the fuel, cladding and coolant play no role and therefore no delay is observed.

9.6 Discussion of local results for FRIA and SRIA

9.6.1 Local results for FRIA

The new capability of Serpent2/Subchanflow for the detailed analysis of MTR-cores become apparent when the local parameters are evaluated. Figure 9.11 shows the power of each plate of the full core as predicted by the coupled code. The selected time is 0.63 s and corresponds to the time when the core reaches its highest power value (see Figure 9.7). In Figure 9.11, the value and position of the plates with maximum and minimum power can be easily identified. The plate with the maximum power is # 403 located in the lower right corner of the core (see Appendix C Figure C.7). It can be observed very clear that all the plates have different power and that there is a large variation of the plate power depending of its position within the fuel assembly and of the fuel assembly within the core. The power peaks are located in the center and at the edges of the core near the wider water channels due to higher moderation than in normal subchannels. These results show for the first-time plate-by-plate power distribution using Serpent2/Subchanflow, in contrast to previous analyses with point kinetics or nodal diffusion codes, which generally assumed a uniform power distribution within a fuel assembly or more precisely they predict only one power value per fuel assembly.

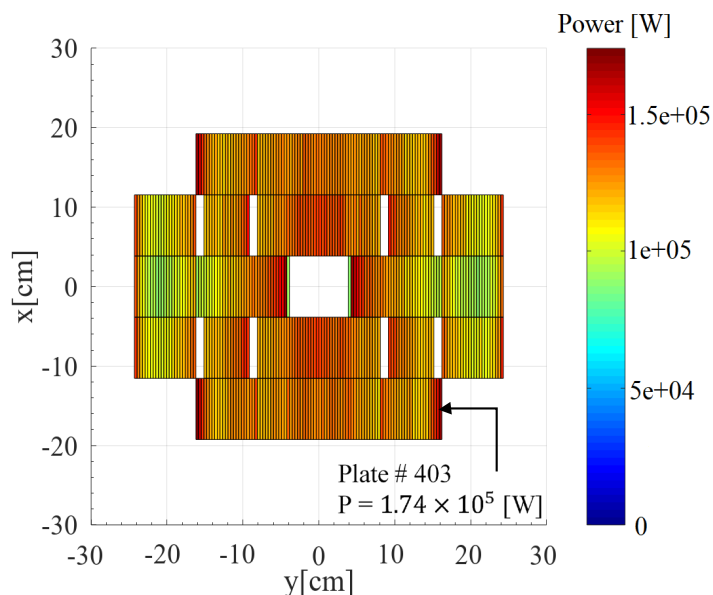
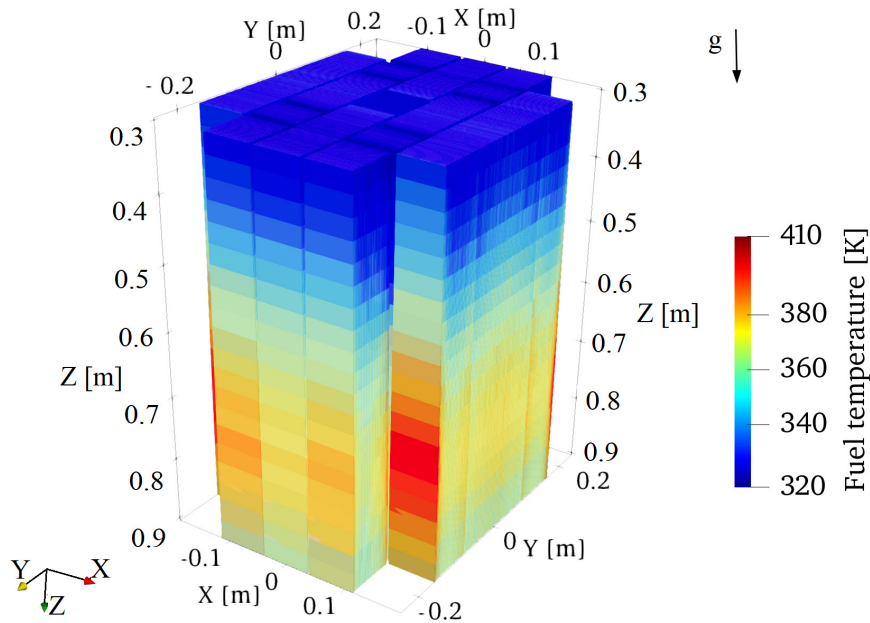
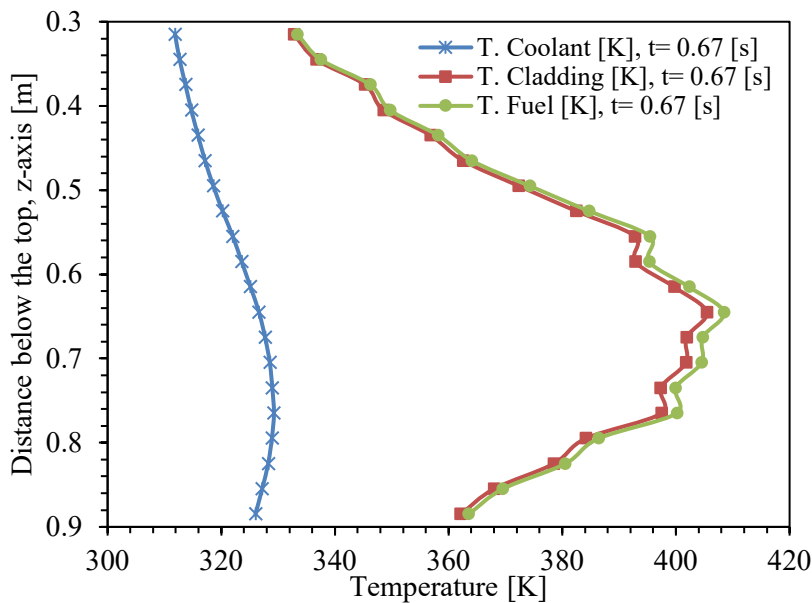


Figure 9.11: Radial power distribution plate by plate predicted for the FRIA scenario at $t = 0.63$ s.

Based on the average fuel and coolant temperature results shown in Figure 9.8, Figure 9.12 (a) and Figure 9.13 (a) show the radial and axial distribution of fuel and coolant temperature at times of 0.67 s and 0.72 s, respectively. Figure 9.12 (b) shows the axial distribution of coolant, cladding, and fuel temperature for plate/channel # 403. The highest values are found at 0.65 cm measured from the top with a value of 408.44 K and 405.44 K for fuel and cladding, respectively.



(a)



(b)

Figure 9.12: Serpent2/Subchanflow prediction at 0.67 s of: (a) Full core 3D fuel temperature; (b) Axial temperature distribution of plate/channel # 403.

Figure 9.13 (b) shows the temperature profiles at 0.72 s, and comparing with Figure 9.12 (b), it can be seen that the maximum temperature values of the cladding and fuel decrease from 408.44 K and 405.44 K to 367.24 K and 368.23 K, respectively, which is due to the fact that at this time the power decreases with a value of $1.45E06$ W (see Figure 9.7). The temperature profile of the

coolant at the core outlet increases from 326.01 K to 334.0 K, and this increase reflects the maximum power reached at $t = 0.63$ s with a delay of 0.09 s.

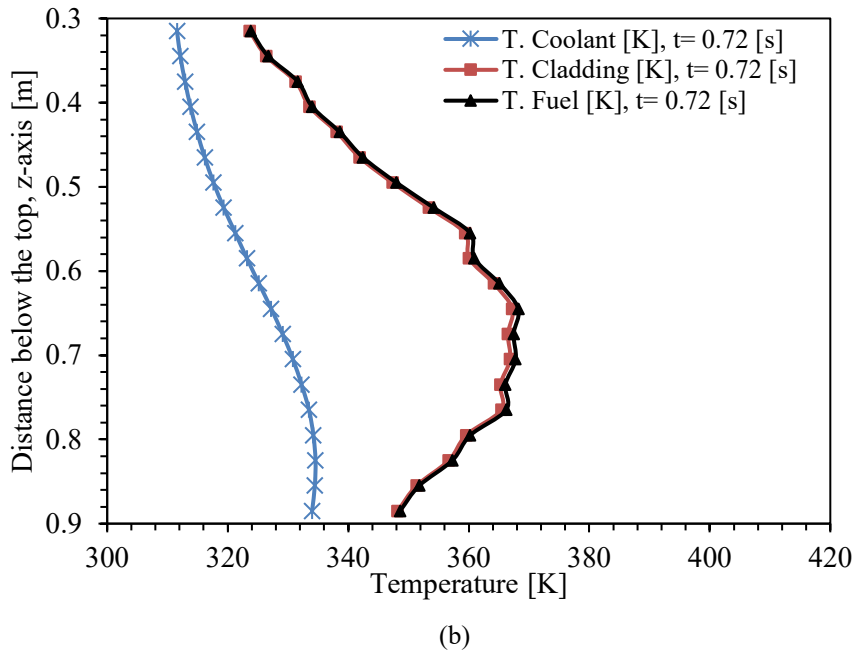
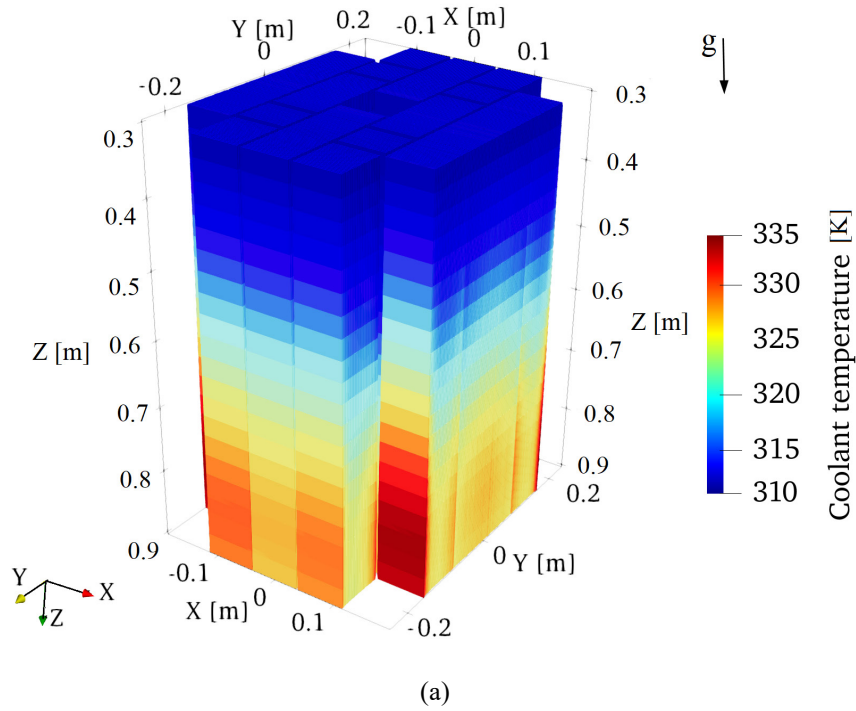


Figure 9.13. Serpent2/Subchanflow prediction at 0.72 s of: (a) Full core 3D fuel temperature; (b) Axial temperature distribution of plate/channel # 403.

9.6.2 Local results for SRIA

The power peak shown in Figure 9.9 has been achieved at a time of 10.0 s. Consequently, shows the power mapping of all plates for this time. As in the case of FRIA, the plate with the highest power is plate # 403 with a value of 38492 W. The radial representation of the power for

each plate is shown in Figure 9.14, where it can be observed that the power peaks coincide in the central part and around the core due to the higher neutron moderation.

It is worth to emphasize that the plate power is quite different depending of its location inside the fuel assembly and of the fuel assembly within the core. The difference of the plate with the highest and lowest power is considerable. Here, again the radial power distribution of the plate power indicates that there is no uniform power distribution within a fuel assembly. The analysis shows that nodal diffusion codes are not able to adequately represent the physics of a complex MTR core and thereby also fail to predict safety parameters.

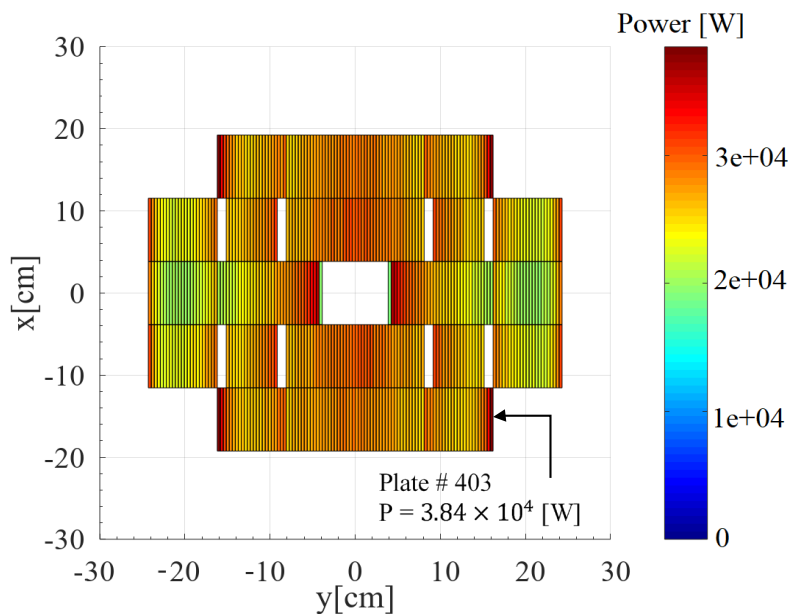


Figure 9.14: Predicted radial power distribution plate-by-plate for the SRIA scenario.

According to Figure 9.10, the temperature peaks for the fuel and coolant have been reached at 10.2 s, and analogous to the FRIA case, Figure 9.15 (a) shows the radial and axial representation of the temperature of each of the plates for this time point. Figure 9.15 (b) shows the axial distribution of the coolant and fuel cladding temperature of plate # 403 at 10.2 s. The maximum temperature values correspond to the cladding at 336.33 K and the fuel at 336.73 K at 72 cm measured from the top. The maximum coolant temperature is found at the core outlet and is 323.68 K.

Comparing the two cases, FRIA and SRIA, it can be seen that the temperature peaks differ from each other and occur at different times. In the FRIA case, there is a delay in the temperature change between the fuel and the coolant. In the SRIA case, however, the temperature peaks generally occur at the same time. In the case of fast transients such as the FRIA, the thermal inertia causes a delay in the temperature change, as can be seen in Figure 9.8, which is not the case in the SRIA case, where the thermal inertia is overcome and the fuel and coolant reach equilibrium in the same time (see Figure 9.10).

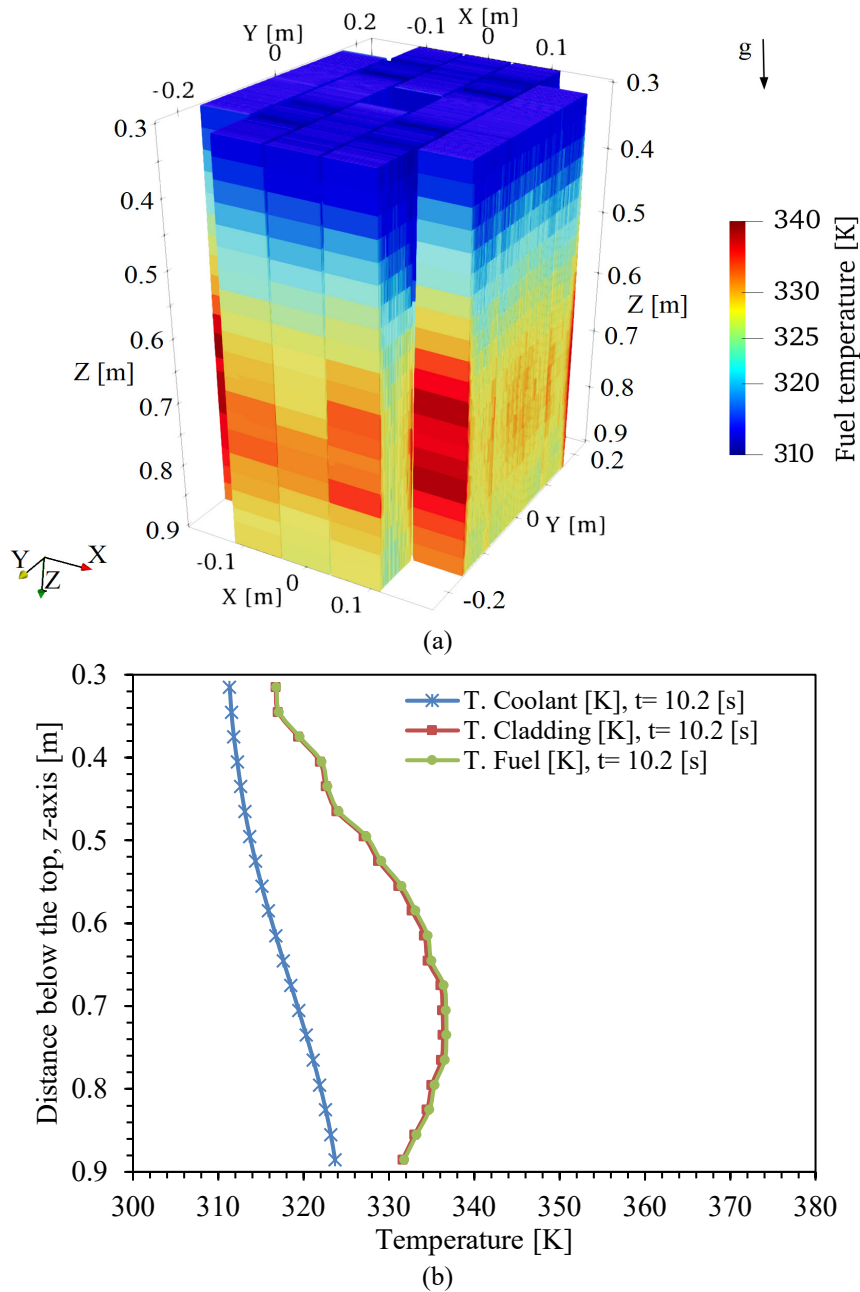


Figure 9.15: Serpent2/Subchanflow prediction at 10.2 s of: (a) Full core 3D fuel temperature; (b) Axial temperature distribution of plate/channel # 403.

These results represent the state of the art in the development of a three-dimensional code for neutronic and thermal-hydraulic analysis of research reactors based on Serpent2/Subchanflow. The unique feature of this research is the level of detail, as each fuel plate and coolant channel are simulated considering the local thermal-hydraulic feedbacks between the Monte Carlo system and the thermal-hydraulic system. This advanced approach enables more accurate and detailed analysis of research reactors and eliminates the need for oversimplifications and approximations, resulting in higher confidence in the prediction of neutronic and thermal-hydraulic phenomena. Serpent2/Subchanflow opens the way to direct prediction of safety parameters without relying on hot-channel factors or heuristic methods, and the results obtained can be used as a reference for lower-level code review.

10 Summary and conclusions

A new safety analysis tool has been developed for simulations of plate-type fuel research reactor cores, known as MTR cores. This tool is based on the original Serpent2/Subchanflow code developed for power reactors, which has been extended and modified to meet the specific requirements of MTR cores. With this new tool, it is possible to perform detailed neutron and thermal-hydraulic analyzes at the plate/subchannel level under both steady-state and transient conditions.

Following extensions and modifications to the Subchanflow thermal-hydraulic code to include appropriate heat transfer correlations, pressure drop for narrow rectangular channels, incorporation of downflow and plate heat conduction that are typical features of MTR reactors, extensive validation with experimental data has been executed. The first phase of validation includes experimental data of plate and channel temperature and pressure drop measured in the devices RA-6 and in the IEA-R1 reactor. Thereby the most appropriate correlations to describe the thermal-hydraulic behavior of the MTR cores under normal and non-normal conditions have been identified.

Validation based on the RA-6 device tests show that Subchanflow under- and over-predicts the temperature values. The coolant temperature predicted by Subchanflow at the outlet of the test section is very close to the measured values with a maximum deviation of ± 0.6 °C. Experimental temperatures measured at 10 axial positions of the heater plate are also compared to the temperatures predicted by Subchanflow. In this data set, it has been observed how the different correlations implemented in Subchanflow impact the prediction of the plate temperature. The results showed that the Colburn correlation best approximates the experimental values with a discrepancy of ± 7 °C.

Further, experimental data from the IAE-R1 reactor are used to validate Subchanflow. The coolant temperature at the outlet of the IFA device, the temperature at three axial positions of three plates, and the pressure drop are compared. The results showed that Subchanflow predicts the overall values of fluid temperature and pressure drop with an accuracy of ± 0.07 °C and a relative error of $\pm 4.52\%$, respectively. The Y-Sudo correlation, developed to analyze the JRR-3 reactor with similar characteristics, has been used to determine the temperature profiles of the plates. In this case, the predicted results showed excellent agreement with the experimental values and had a maximum discrepancy of ± 4.3 °C.

The neutronic analysis has been performed using the Monte Carlo code Serpent 2. The steady-state experimental data of the thermal neutron flux measured at the two critical positions D-4 and E-5 of the SPERT IV D-12/25 reactor have been used for validation. The calculated values agree

very well with the experimental data. The reactivity worth curve of the control rods has been obtained to determine the initial axial positions for the power excursion tests. The main neutron parameters calculated are $\beta_{eff} = 749 \pm 2$ pcm, $K_{eff} = 1.00007 \pm 0.00014$, and excess reactivity of 5.27 ± 0.04 \$. Comparing the difference between the calculated excess reactivity and the experimental value, the value is 0. This clearly indicates that the model developed for the simulation of the SPERT IV reactor is ideal for use in subsequent high-fidelity calculations.

The coupled Serpent2/Subchanflow code has been finally validated against the unique experimental data from the B-34 and B-35 power excursion transient tests performed in the SPERT IV D-12/25 reactor. The transient global and local values calculated by Serpent2/Subchanflow show an excellent agreement with the experimental values, which has not been achieved by any other code before. The statistical error bars for the power evolution as a function of time are fixed at ± 2 sigma, which includes most of the experimental data. Comparison of the measured axial temperature of the cladding of a plate at coordinates (0, -0.03, 35.08) cm with the temperature predicted by Serpent2/Subchanflow during the rod ejection tests (B-34 and B-35) showed excellent agreement, and no major discrepancies have been found. A detailed mapping of the power per plate and maximum and minimum plate/channel temperatures has been determined to serve as a reference for low-level codes.

Based on the validation work using specific tests (RA-6) and tests on two reactors (IAE-R1 and SPERT-IV), as well as the promising results obtained with both the stand-alone codes and the coupled code, it can be concluded that Serpent2/Subchanflow is able to predict key neutronic/thermal-hydraulic parameters relevant to the safety of MTR cores with high accuracy, i.e., at the plate/subchannel level, which has not been done before for both static and transient conditions, such as rod ejection accidents.

Finally, the validated and extended coupled code Serpent2/Subchanflow has been used to analyze the transient behavior of the IAEA 10 MW reactor core loaded with plate fuel. This high-fidelity simulation at the plate/subchannel level is the first to predict the thermal-hydraulic behavior of the core by considering local feedbacks directly between the plate and the surrounding subchannels. This new type of simulation paves the way for direct and more accurate prediction of safety parameters and allows identification of the highest performing core plate and its position within the core. This approach makes the use of hot-channel factors irrelevant in the safety assessments of MTR cores. In general, high-fidelity simulations help reduce conservatism and directly predict local safety parameters such as maximum peak cladding temperature, maximum plate power, etc. In addition, these new types of computational tools can be used to provide benchmark solutions for new research reactor core designs for which experimental data are not available, and to compare them with low-order solutions.

11 Outlook

In the following, several outlooks and lines of research based on the use of the validated Serpent2/Subchanflow code and its application to the analysis of MTR fuel-loaded research reactors, as well as other cores with complex geometry, are presented below:

- *Expanding the Subchanflow validation base:* It is proposed to expand the Subchanflow validation base by identifying new relevant experiments that reflect the conditions of modern MTR fuel assemblies. This includes additional testing and comparison with experimental data to ensure code reliability and accuracy in a wide range of cases. Facilities such as the Dutch government's PALLAS reactor, the Bolivian government's CIDTN reactor, and Argentina's RA -10 multipurpose reactor can be used as benchmarks. In addition, reactors with complex cores such as LVR-1 and the Vietnamese reactor (MPRR) loaded with VVR-KN fuel can also be included.
- *Thermal-hydraulic analysis by natural convection:* it is proposed to implement in Subchanflow the option of thermal-hydraulic analysis by natural convection for core cooling in reactors intended for training programs. This includes simulation and study of the behavior of natural convection in the reactor and its effects on heat transfer and temperature distribution. Experimental data from the IEA-R1 reactor can be used to validate this extension of the code.
- *Improved parallel scalability of the coupled code:* It is proposed to improve the parallel scalability of the Serpent2/Subchanflow coupled code, especially in the case of Serpent 2, to be able to analyze longer transients (larger than 20 seconds) such as LOFA. This includes optimizing code performance on parallel computing systems. Methods such as hybrid parallelism, efficient sampling strategies (variance reduction technique) and optimization of communication and synchronization of both codes can be used.
- *Application of artificial intelligence:* the use of artificial intelligence techniques can be promising to improve the description of heat transfer and pressure drop in research reactors. Using available data from this and other research, models and algorithms can be developed that use the calculated and experimental database to identify patterns and trends. This will allow more accurate estimation of heat and pressure transfer coefficients under various operating conditions.

Bibliography

- Adorni, M., Bousbia-salah, A., and D'Auria, F. (2007). Accident Analysis in Research Reactors. In The International Conference of Nuclear Energy for new Europe. Portoroz, Slovenia. September 10-13, pp 10. ISBN: 978-961-6207-28-7. Retrieved from http://inis.iaea.org/search/search.aspx?orig_q=RN:39095684
- Aksan, N., Bestion, D., D'Auria, F., Galassi, G., Glaeser, H., Hassan, Y., . . . Umminger, K. (2017). *Thermal Hydraulics in Water-Cooled Nuclear Reactors*. Woodhead Publishing is an imprint of Elsevier, Cambridge, MA 02139, USA. ISBN: 978-0-08-100679-5.
- Almachi, J., and Montenegro, J. (2016). Study Thermohydraulic a Fixed Bed for Core of Nuclear Reactor. In COMSOL conference. Boston, USA. October 5-7, pp. 1-6. Paper ID: 37332. Retrieved from www.comsol.com/paper/37332
- Almachi, J., Sánchez-Espinoza, V., and Imke, U. (2021). Extension and validation of the SubChanFlow code for the thermo-hydraulic analysis of MTR cores with plate-type fuel assemblies. *Nuclear Engineering and Design, Vol. 379*, pp. 111221. doi:<https://doi.org/10.1016/j.nucengdes.2021.111221>
- Almachi, J., Sánchez-Espinoza, V., and Imke, U. (2022a). High-Fidelity Steady-State and Transient Simulations of an MTR Research Reactor Using Serpent2/Subchanflow. *Energies, Vol. 15(4)*, pp. 20. doi:<https://doi.org/10.3390/en15041554>
- Almachi, J., Sanchez-Espinoza, V., and Margulis, M. (2022b). Validation of Serpent 2 using experimental data from the SPERT-IV D-12/25 Research Reactor Tests. In European Research Reactor Conference of innovative methods in reactor physics and thermohydraulics. Budapest, Hungary. June 6-10. ISBN: 978-92-95064-38-6, pp. 142-150.
- Ardaneh, K., and Zaferanlouei, S. (2013a). A lumped parameter core dynamics model for MTR type research reactors under natural convection regime. *Annals of Nuclear Energy, Vol. 56*, pp. 243-250. doi:<https://doi.org/10.1016/j.anucene.2013.01.033>
- Ardaneh, K., and Zaferanlouei, S. (2013b). An analytical solution for thermal-hydraulic analysis and safety margins in MTR-type research reactors cooled by natural convection. *Annals of Nuclear Energy, Vol. 51*, pp. 282-288. doi:<https://doi.org/10.1016/j.anucene.2012.07.021>
- Bahadir, T., and Lindahl, S.-Ö. (2009). Studsvik's next generation nodal code SIMULATE-5. In Advances in Nuclear Fuel Management IV. Hilton Head Island, South Carolina, USA, April 12-15. ISBN: 978-1-61567-351-3. Vol. 1, pp. 992-1003. Retrieved from <https://www.proceedings.com/05926.html>

- Bauer, W. (1958). The Monte Carlo Method. *Journal of the Society for Industrial and Applied Mathematics*, Vol. 6(4), pp. 438-451. doi:<https://doi.org/10.1137/0106028>
- Beckert, C., and Grundmann, U. (2008). Development and verification of a nodal approach for solving the multigroup SP3 equations. *Annals of Nuclear Energy*, Vol. 35(1), pp. 75-86. doi:<https://doi.org/10.1016/j.anucene.2007.05.014>
- Bell, G., and Glasstone, S. (1970). *Nuclear Reactor Theory*. Van Nostrand Reinhold Company, New York, USA. ISBN: 978-0-442-20684-0. Retrieved from <https://www.osti.gov/biblio/4074688>
- Björn, B. (2010). On the influence of the resonance scattering treatment in Monte Carlo codes on high temperature reactor characteristics. PhD Thesis, Stuttgart University. Stuttgart, Germany. ISBN: 0173 – 6892. doi:<http://dx.doi.org/10.18419/opus-1881>
- Bodey, I. T. (2014). Thermal Hydraulic Characteristics of Fuel Defects in Plate Type Nuclear Research Reactors. PhD Thesis, University of Tennessee, Tennessee, USA. Retrieved from https://trace.tennessee.edu/utk_graddiss/2680
- Bousbia-Salah, A., and Hamidouche, T. (2005). Analysis of the IAEA research reactor benchmark problem by the RETRAC-PC code. *Nuclear Engineering and Design*, Vol. 235(6), pp. 661-674. doi:<https://doi.org/10.1016/j.nucengdes.2004.10.004>
- Bousbia-Salah, A., Benkharfia, H., Kriangchaiporn, N., Petruzzi, A., D'Auria, F., and Ghazi, N. (2008). MTR benchmark static calculations with MCNP5 code. *Annals of Nuclear Energy*, Vol. 35(5), pp. 845-855. doi:[10.1016/j.anucene.2007.09.016](https://doi.org/10.1016/j.anucene.2007.09.016)
- Britannica. (1999). Nuclear reactor. <https://www.britannica.com/technology/nuclear-reactor/Research-reactors>. Accessed: 09.05.2023.
- Bugis, A. (2020). Modeling a nuclear research reactor and radiation dose estimation in an accident scenario. Phd Thesis, Missouri University of Science and Technology, Rolla, MO, USA. Electronic OCLC 1198488524. Retrieved from https://scholarsmine.mst.edu/doctoral_dissertations/2907/
- Calleja, M., Jimenez, J., Sanchez, U., Imke, U., Stieglitz, R., and Macián, R. (2014). Investigations of boron transport in a PWR core with COBAYA3/SUBCHANFLOW inside the NURESIM platform. *Annals of Nuclear Energy*, Vol. 66, pp. 74-84. doi:<https://doi.org/10.1016/j.anucene.2013.11.034>
- Cao, L., Gerlach, A., Xu, Y., Downar, T., and Lee, J. (2015). Neutronics modeling of the SPERT III E-Core critical experiments with MPACT and KENO. *Annals of Nuclear Energy*, Vol. 80, pp.207-218. doi:<https://doi.org/10.1016/j.anucene.2015.02.013>
- Castellanos-Gonzalez, D., Moreira, J., Maiorino, J., and Carajilescov, P. (2018). Validation of the COTENP Code: A Steady-State Thermal-Hydraulic Analysis Code for Nuclear Reactors with Plate Type Fuel Assemblies. *Science and Technology of Nuclear Installations*, Vol. 2018, pp. 17. doi:<https://doi.org/10.1155/2018/9874196>
- Cengel, Y., and Ghajar, A. (2015). *Heat and mass transfer* (Vol. 5). McGraw-Hill Education, 2 Penn Plaza, New York, NY 10121, USA. ISBN 978-0-07-339818-1. Retrieved from <https://ostad.nit.ac.ir/payaidea/ospic/file8973.pdf>

- Chadwick, M., Obložinský, P., Herman, M., Greene, N., McKnight, R., Smith, D., and Young, P. (2006). ENDF/B-VII.0: Next Generation Evaluated Nuclear Data Library for Nuclear Science and Technology. *Nuclear Data Sheets, Vol. 107*(12), pp. 2931-3060. doi:<https://doi.org/10.1016/j.nds.2006.11.001>
- Chan, V. (2013). *Theory and Applications of Monte Carlo Simulations* (Vol. 1). IntechOpen, Rijeka, Croatia. ISBN 978-953-51-1012-5 . doi:<https://doi.org/10.5772/45892>
- Chaudri, K., and Mirza, S. (2015). Burnup dependent Monte Carlo neutron physics calculations of IAEA MTR benchmark. *Progress in Nuclear Energy, Vol. 81*, pp. 43-52. doi:<https://doi.org/10.1016/j.pnucene.2014.12.018>
- Chen, J., Peng, X., Xie, W., Feng, L., Zhao, A., and Wang, H. (2017). Influence of high dose γ irradiation on the calibration characteristics of type K mineral-insulated metal-sheathed thermocouples. *Journal of Alloys and Compounds, Vol. 696*, pp. 1046-1052. doi:[10.1016/j.jallcom.2016.12.091](https://doi.org/10.1016/j.jallcom.2016.12.091)
- CNEA. (2017). Argentine multipurpose nuclear reactor RA-10. https://www.youtube.com/watch?v=_WcJTHMMXZk . Accessed: 10.05.2023.
- Crocker, J., and Stephan, L. (1964). Reactor Power Excursion Tests in the SPERT IV Facility. Technical Report IDO-17000, NSA-18-044970, Phillips Petroleum Co. Atomic Energy Div., Idaho Falls, Idaho, USA. doi:<https://doi.org/10.2172/4000736>
- Crocker, J., Koch, J., Martinson, Z., McGlinsky, A., and Stephan, L. (1963). Nuclear Start-up of the SPERT IV Reactor. Technical Report IDO-16905, NSA-17-040407, Phillips Petroleum Co. Atomic Energy Div., Idaho Falls, Idaho, USA. doi:<https://doi.org/10.2172/4647654>
- Crocker, J., Martinson, Z., Potenza, R., and Stephan, L. (1965). Reactor Stability Test in the SPERT IV Facility. Technical Report: IDO-17088, NSA-19-042152, Phillips Petroleum Co. Idaho Falls, Idaho. Atomic Energy Div. USA. doi:<https://doi.org/10.2172/4566563>
- Daubler, M., Ivanov, A., Sjenitzer, B., Sanchez, V., Stieglitz, R., and Macian-Juan, R. (2015). High-fidelity coupled Monte Carlo neutron transport and thermal-hydraulic simulations using Serpent 2/SUBCHANFLOW. *Annals of Nuclear Energy, Vol. 83*, pp. 352-375. doi:<https://doi.org/10.1016/j.anucene.2015.03.040>
- de Kruijf, W., and Janssen, A. (1996). The Effective Fuel Temperature to Be Used for Calculating Resonance Absorption in a $^{238}\text{UO}_2$ Lump with a Nonuniform Temperature Profile. *Nuclear Science and Engineering, Vol. 123*(1), pp. 121-135. doi:<https://doi.org/10.13182/NSE94-108>
- Dietrich, S., and Boyd, I. (1996). Scalar and Parallel Optimized Implementation of the Direct Simulation Monte Carlo Method. *Journal of Computational Physics, Vol. 126*(2), pp. 328-342. doi:<https://doi.org/10.1006/jcph.1996.0141>
- Dittus, F. W., and Boelter, L. (1985). Heat transfer in automobile radiators of the tubular type. *International Communications in Heat and Mass Transfer, Vol. 12*(1), pp. 3-22. doi:[https://doi.org/10.1016/0735-1933\(85\)90003-X](https://doi.org/10.1016/0735-1933(85)90003-X)

- Doligez, X., Bouneau, S., David, S., and Ernoult, M. (2017). Fundamentals of reactor physics with a view to the (possible) futures of nuclear energy. *Comptes Rendus Physique, Vol. 18(7)*, pp. 372-380. doi:<https://doi.org/10.1016/j.crhy.2017.10.004>
- Doval, A. (1998). Validation and verification of the MTR_PC thermohydraulic package. In International Meeting on Reduced Enrichment for Research and Test Reactors, Sao Paulo, Brazil. October 10-23, pp. 1-9. Retrieved from <https://www.rertr.anl.gov/Method98/ADoval-abst.html>
- Doval, A., Villarino, E., Hergenreder, D., and Ferraro, D. (2022). INVAP perspectives and initiatives for proliferation resistance as research reactor's designer. In International Meeting on Reduced Enrichment for Research and Test Reactors. Vienna, Austria. October 3-4, pp. 1-10. Paper ID: S2-P4. Retrieved from <https://www.rertr.anl.gov/RERTR42/index.shtml>
- Duderstadt, J., and Hamilton, L. (1976). *Nuclear reactor Analysis*. John Willey & sons Inc., New York, USA. ISBN: 0-471-22363-8. Retrieved from <https://books.google.de/books?id=xWvsswEACAAJ>
- Durazzov, M., Umbehaun, P., Torres, W., Souza, J., Silva, D., and Andrade, D. (2019). Procedures for manufacturing an instrumented nuclear fuel element. *Progress in Nuclear Energy, Vol. 113*, pp. 166-174. doi:<https://doi.org/10.1016/j.pnucene.2019.01.021>
- El-Din El-Morshedy, S. (2011). Prediction, analysis and solution of the flow inversion phenomenon in a typical MTR-reactor with upward core cooling. *Nuclear Engineering and Design, Vol. 241(1)*, pp. 226-235. doi:<https://doi.org/10.1016/j.nucengdes.2010.10.006>
- El-Khatib, H. (2013). Thermal-hydraulic simulation and analysis of Research Reactor Cooling Systems. Phd thesis, Benha University, Cairo, Egypt. INIS-EG--487. Retrieved from http://inis.iaea.org/search/search.aspx?orig_q=RN:46135156
- Everts, M., and Meyer, P. (2020). Laminar hydrodynamic and thermal entrance lengths for simultaneously hydrodynamically and thermally developing forced and mixed convective flows in horizontal tubes. *Experimental Thermal and Fluid Science, Vol. 118*, pp. 110153. doi:<https://doi.org/10.1016/j.expthermflusci.2020.110153>
- Ferraro, D. (2021). Monte Carlo-based multi-physics analysis for transients in Light Water Reactors. PhD Thesis, Karlsruhe Institute of Technology, Eggenstein-Leopoldshafen, Germany. McSAFE (EU, H2020, 755097). doi:<https://publikationen.bibliothek.kit.edu/1000131803>
- Ferraro, D., Garcia, M., Imke, U., Valtavirta, V., Leppänen, J., and Sanchez-Espinoza, V. (2019). Serpent/SCF pin-level multiphysics solutions for the VERA Fuel Assembly benchmark. *Annals of Nuclear Energy, Vol. 128*, pp. 102-114. doi:<https://doi.org/10.1016/j.anucene.2018.12.047>
- Ferraro, D., García, M., Valtavirta, V., Imke, U., Tuominen, R., Leppänen, J., and Sanchez-Espinoza, V. (2020). Serpent/SUBCHANFLOW pin-by-pin coupled transient calculations for the SPERT-III hot full power tests. *Ann. Nucl. Energy, Vol. 142*, pp. 107387. doi:10.1016/J.ANUCENE.2020.107387
- Fevotte, F., and Lathuiliere, B. (2013). MICADO: Parallel implementation of a 2D-1D iterative algorithm for the 3D neutron transport problem in prismatic geometries. In International Conference on

- Mathematics and Computational Methods Applied to Nuclear Science & Engineering, Sun Valley, Idaho, USA, May 5-9. ISBN 978-0-89448-700-2, pp. 1-12. Retrieved from <https://www.fevotte.net/publications/fevotte2013.pdf>
- Forrest, E., Hu, L., Buongiorno, J., and McKrell, T. (2016). Convective Heat Transfer in a High Aspect Ratio Minichannel Heated on One Side. *Journal of Heat Transfer, Vol. 138(2)*, pp. 10. doi:<https://doi.org/10.1115/1.4031646>
- Frei, W. (2017). Which Turbulence Model Should I Choose for My CFD Application? COMSOL Blog, <https://www.comsol.com/blogs/which-turbulence-model-should-choose-cfd-application/>. Accessed: 24.05.2023.
- Gaheen, M., and Abdelaziz, M. (2019). Analysis of natural circulation loop in MTRs using CONVEC code. *Progress in Nuclear Energy, Vol. 117*, pp. 103097. doi:<https://doi.org/10.1016/j.pnucene.2019.103097>
- Gambill, W. R., and Bundy, R. D. (1961). HFIR Heat-Transfer Studies of Turbulent Water Flow in Thin Rectangular Channels. Technical Report ORNL-3079, NSA-15-023623, Oak Ridge National Lab. (ORNL), Oak Ridge, TN, USA. Retrieved from <https://www.osti.gov/biblio/4033513>
- García, J. C., Delmastro, D. F., Chasseur, A. F., Silin, N., and Masson, V. (2008). Numerical Modeling of Heat Transfer in the Core Channels of a MTR Type Reactor. *Computational Mechanics, Vol. 27(20)*, pp. 1545-1554. Retrieved from <https://cimec.org.ar/ojs/index.php/mc/article/view/1504>
- Garcia, M. (2021). A high-fidelity multiphysics system for neutronic, thermalhydraulic and fuel-performance analysis of Light Water Reactors. PhD Thesis, Karlsruhe Institute of Technology, Eggenstein-Leopoldshafen, Germany. doi:10.5445/IR/1000140281
- Gill, D., Griesheimer, D., and Aumiller, D. (2017). Numerical Methods in Coupled Monte Carlo and Thermal-Hydraulic Calculations. *Nuclear Science and Engineering, Vol. 185(1)*, pp. 194-205. doi:<https://doi.org/10.13182/NSE16-3>
- Goltsev, A., Davidenko, V., Tsibulsky, V., and Lekomtsev, A. (2000). Computational Problems in the Calculation of Temperature Effects for Heterogeneous Nuclear Reactor Unit Cells. *Annals of Nuclear Energy, Vol. 27(2)*, pp. 175-183. doi:[https://doi.org/10.1016/S0306-4549\(99\)00067-5](https://doi.org/10.1016/S0306-4549(99)00067-5)
- Haghighat, A. (2020). *Monte Carlo methods for particle transport*. CRC Press, Taylor & Francis Group, Boca Raton, USA. ISBN: 9780429198397. doi:<https://doi.org/10.1201/9780429198397>
- Hainoun, A., Doval, A., Umbehaun, P., Chatzidakis, S., Ghazi, N., Park, S., . . . Shokr, A. (2014). International benchmark study of advanced thermal hydraulic safety analysis codes against measurements on IEA-R1 research reactor. *Nuclear Engineering and Design, Vol. 280*, pp. 233-250. doi:<https://doi.org/10.1016/j.nucengdes.2014.06.041>
- Hainoun, A., and Schaffrath, A. (2001). Simulation of subcooled flow instability for high flux research reactors using the extended code ATHLET. *Nuclear Engineering and Design, Vol. 207(2)*, pp. 163-180. doi:[https://doi.org/10.1016/S0029-5493\(00\)00410-6](https://doi.org/10.1016/S0029-5493(00)00410-6)

- Hedayat, A., and Davari, A. (2022). Feasibility study to increase the reactor power at natural convection mode in Tehran Research Reactor (TRR) through a hybrid thermal-hydraulic simulation and analysis using the RELAP5 code and Computational Fluid Dynamic (CFD) modeling by ANSYS-FLUENT. *Progress in Nuclear Energy, Vol. 150*, pp. 104285. doi:<https://doi.org/10.1016/j.pnucene.2022.104285>
- Heffner, R., Morris, E., Jones, D., Seaman, D., and Shane, M. (1962). SPERT IV FACILITY. Technical Repor IDO-16745, NSA-16-014339, Phillips Petroleum Co. Atomic Energy Div., Idaho Falls, Idaho. USA. doi:<https://doi.org/10.2172/4785456>
- IAEA. (1980). Research Reactor Core Conversion from the Use of Highly Enriched Uranium Fuels: Guidebook. Technical Report IAEA-TECDOC-233, INTERNATIONAL ATOMIC ENERGY AGENCY, Vienna, Austria. Retrieved from <https://www.iaea.org/publications/484/research-reactor-core-conversion-from-the-use-of-highly-enriched-uranium-fuels-guidebook>
- IAEA. (1992a). Research Reactor Core Conversion Guidebook, Volume 4: Fuels (Appendices I-K). Technical Report IAEA-TECDOC-643/4, INTERNATIONAL ATOMIC ENERGY AGENCY, Vienna, Austria. ISSN: 1011-4289. Retrieved from <https://www.iaea.org/publications/899/research-reactor-core-conversion-guidebook-volume-4-fuels-appendices-i-k>
- IAEA. (1992b). Research Reactor Core Conversion Guidebook; Volume 3: Analytical Verification (Appendices G and H). Technical Report IAEA-TECDOC-643/3, INTERNATIONAL ATOMIC ENERGY AGENCY, Vienna, Austria. ISSN: 1011-4289. Retrieved from <https://www.iaea.org/publications/901/research-reactor-core-conversion-guidebook-volume-3-analytical-verification-appendices-g-and-h>
- IAEA. (2002). Accident analysis for nuclear power plant. Safety Reports Serie No. 23, International Atomic Energy Agency, Vienna, Austria. ISBN: 92-0-115602-2. Retrieved from <https://www.iaea.org/publications/6388/accident-analysis-for-nuclear-power-plants>
- IAEA. (2008). Innovative methods in research reactor analysis: Benchmark against experimental data on neutronics and thermal-hydraulic computational methods and tools for operation and safety analysis of research reactors. Report of the 1st RCM of CRP 1496, J7-RC-1111.1, International Atomic Energy Agency, Vienna, Austria. Retrieved from http://www-naweb.iaea.org/napc/physics/research_reactors/crps/crp3/document.html
- IAEA. (2014). Applications of Research Reactors. Series No. NP-T-5.3, INTERNATIONAL ATOMIC ENERGY AGENCY, Vienna, Austria. ISBN: 978-92-0-145010-4. Retrieved from <https://www.iaea.org/publications/10491/applications-of-research-reactors>
- IAEA. (2015). Research Reactor Benchmarking Database: Facility Specification and Experimental Data. Technical Reports Series No. 480, INTERNATIONAL ATOMIC ENERGY AGENCY, Vienna, Austria. ISBN: 978-92-0-151714-2. Retrieved from <https://www.iaea.org/publications/10578/research-reactor-benchmarking-database-facility-specification-and-experimental-data>
- IAEA. (2019). Benchmarking Against Experimental Data of Neutronics and Thermohydraulic Computational Methods and Tools for Operation and Safety Analysis of Research Reactors.

- IAEA-TECDOC-1879, INTERNATIONAL ATOMIC ENERGY AGENCY, Vienna, Austria. ISBN: 978-92-0-109619-7. Retrieved from <https://www.iaea.org/publications/13547/benchmarking-against-experimental-data-of-neutronics-and-thermohydraulic-computational-methods-and-tools-for-operation-and-safety-analysis-of-research-reactors>
- IAEA. (2022). *Research Reactor Database*. Retrieved from <https://nucleus.iaea.org/rrdb/#/home> . Accessed: 16.12.2022.
- Imke, U., and Sanchez-Espinoza, V. (2012). Validation of the subchannel code SUBCHANFLOW using the NUPEC PWR tests (PSBT). *Science and Technology of Nuclear Installations, Vol. 2012*, pp. 12. doi:<https://doi.org/10.1155/2012/465059>
- Incropera, F., and DeWitt, D. (1996). *Fundamentals of Heat and Mass Transfer*. John Wiley & Sons, Inc., New York City, USA, ISBN: 9780471386506. Retrieved from <https://www.worldcat.org/de/title/45951568>
- INVAP. (2023). *World leader in nuclear technology*. Retrieved from <https://www.invap.com.ar/en/divisions/nuclear/>. Accessed: 10.03.2023.
- Jo, D., Al-Yahia, O., Altamimi, R., Park, J., and Chae, H. (2014). Experimental Investigation of Convective Heat Transfer in a Narrow Rectangular Channel for Upward and Downward Flows. *Nuclear Engineering and Technology, Vol. 46(2)*, pp. 195-206. doi:<https://doi.org/10.5516/NET.02.2013.057>
- Joo, H., Cho, J., Kim, K., Lee, C., and Zee, S. (2004). Methods and Performance of a Three-Dimensional Whole-Core Transport Code DeCART. In PHYSOR 2004 - The Physics of Fuel Cycles and Advanced Nuclear Systems: Global Developments, Chicago, Illinois, April 25-29. On CD-ROM, American Nuclear Society, pp. 1-14. Retrieved from <https://www.ipen.br/biblioteca/cd/physor/2004/PHYSOR04/papers/95595.pdf>
- Kandlikar, S., and Grande, W. (2003). Evolution of Microchannel Flow Passages--Thermohydraulic Performance and Fabrication Technology. *Heat Transfer Engineering, Vol. 24(1)*, pp 3-17. doi:<https://doi.org/10.1080/01457630304040>
- Khedr, A., Adorni, M., and d'Auria, F. (2005). The effect of code user and boundary conditions on RELAP calculations of MTR research reactor transient scenarios. *Nuclear Technology and Radiation Protection, Vol. 20(1)*, pp. 16-22. doi:<https://doi.org/10.2298/NTRP0501016K>
- Khedr, K. (2013). Thermal-Hydraulic Analysis of Heated Plate under Asymmetrical Cooling Conditions. *Arab Journal of Nuclear Science and Applications, Vol. 46(3)*, pp. 219-230. Retrieved from http://inis.iaea.org/search/search.aspx?orig_q=RN:45013719
- Kim, H.-J., Yim, J.-S., Lee, B.-H., Oh, J.-Y., and Tahk, Y.-W. (2014). Drop impact analysis of plate-type fuel assembly in research reactor. *Nuclear Engineering and Technology, Vol. 45(4)*, pp. 529-540. doi:<https://doi.org/10.5516/NET.09.2013.103>
- Labit, J.-M., Seiler, N., Clamens, O., and Merle, E. (2021). Thermal-hydraulic two-phase modeling of reactivity-initiated transients with CATHARE2 – Application to SPERT-IV simulation. *Nuclear*

- Engineering and Design, Vol. 381*, pp. 111310. doi:<https://doi.org/10.1016/j.nucengdes.2021.111310>
- Lahey, R., and Moody, F. (1993). *The Thermal-hydraulic of a boiling water nuclear reactor* (Vol. 2). American Nuclear Society, Illinois, USA. ISBN: 0-89448-037-5. Retrieved from <https://www.ans.org/store/item-300026/>
- Lai, P.-C., Huang, Y.-S., and Sheu, R.-J. (2019). Comparing the performance of two hybrid deterministic/Monte Carlo transport codes in shielding calculations of a spent fuel storage cask. *Nuclear Engineering and Technology, Vol. 51*(8), pp. 2018-2025. doi:<https://doi.org/10.1016/j.net.2019.06.019>
- Lassmann, K., and Hohlefeld, F. (1987). The revised URGAP model to describe the gap conductance between fuel and cladding. *Nuclear Engineering and Design, Vol. 103*(2), pp. 215-221. doi:[https://doi.org/10.1016/0029-5493\(87\)90275-5](https://doi.org/10.1016/0029-5493(87)90275-5)
- Leppänen, J. (2007). Development of a New Monte Carlo reactor physics code. PhD thesis, Helsinki University of Technology, Espoo, Finland. ISBN: 978-951-38-7018-8. Retrieved from <http://montecarlo.vtt.fi/download/P640.pdf>
- Leppänen, J., Aufiero, M., Fridman, E., Rachamin, R., and van der Marck, S. (2014). Calculation of effective point kinetics parameters in the Serpent 2 Monte Carlo code. *Annals of Nuclear Energy, Vol. 65*, pp. 272-279. doi:<https://doi.org/10.1016/j.anucene.2013.10.032>
- Leppänen, J., Pusa, M., Viitanen, T., Valtavirta, V., and Kaltiaisenaho, T. (2015). The Serpent Monte Carlo code: Status, development and applications in 2013. *Annals of Nuclear Energy, Vol. 82*, pp. 142-150. doi:<https://doi.org/10.1016/j.anucene.2014.08.024>
- Leppänen, J., Valtavirta, V., Tuominen, R., Kaltiaisenaho, T., Pusa, M., and Viitanen, T. (2022). *Serpent Wiki on-line user Manual for Serpent 2*. Retrieved from http://serpent.vtt.fi/mediawiki/index.php/Main_Page. Accessed: 25.8.2022.
- Levy, S., Fuller, R. A., and Niemi, R. O. (1959). Heat Transfer to Water in Thin Rectangular Channels. *Journal of Heat Transfer, Vol. 81*(2), pp. 129-140. doi:<https://doi.org/10.1115/1.4008156>
- Lewis, E., and Miller, W. (1984). *Computational methods of neutron transport*. John Wiley and sons, New York, USA. ISBN: 0-471-09245-2. Retrieved from <https://www.osti.gov/biblio/5538794>
- Li, L., and Zhang, Z. (2010). Development of Real-Time Thermal-Hydraulic Analysis Code for Plate Type Fuel Reactor. In The International Conference on Nuclear Engineering, Xi'an, China. May 17-21. Vol 2, pp. 497-505. doi:<https://doi.org/10.1115/ICONE18-29297>
- Li, L., Fang, D., Zhang, D., Wang, M., Tian, W., Su, G., and Qiu, S. (2019). Flow and heat transfer characteristics in plate-type fuel channels after formation of blisters on fuel elements. *Annals of Nuclear Energy, Vol. 134*, pp. 284-298. doi:<https://doi.org/10.1016/j.anucene.2019.06.030>
- Liu, K., Wang, M., Gan, F., Tian, W., Qiu, S., and Su, G. (2021). Numerical investigation of flow and heat transfer characteristics in plate-type fuel channels of IAEA MTR based on OpenFOAM. *Progress in Nuclear Energy, Vol. 141*, pp. 103963. doi:<https://doi.org/10.1016/j.pnucene.2021.103963>

- Maiorino, J. (2000). The utilization and operational experience of IEA-R1 Brazilian research reactor. In The international symposium on research reactor utilization, safety and management; Lisbon, Portugal. September 6-10. ISSN: 1562-4153, Vol. 31, pp. 1-10. Retrieved from http://inis.iaea.org/search/search.aspx?orig_q=RN:31043003
- Margulis, M., and Gilad, E. (2016). Monte Carlo and nodal neutron physics calculations of the IAEA MTR benchmark using Serpent/DYN3D code system. *Progress in Nuclear Energy, Vol. 88*, pp. 118-133. doi:<https://doi.org/10.1016/j.pnucene.2015.12.008>
- Margulis, M., and Gilad, E. (2018). Simulations of SPERT-IV D12/15 transient experiments using the system code THERMO-T. *Progress in Nuclear Energy, Vol. 109*, pp. 1-11. doi:<https://doi.org/10.1016/j.pnucene.2018.07.005>
- Marin-Lafleche, A., Smith, M., and Lee, C. (2013). PROTEUS-MOC: a 3D deterministic solver incorporating 2D Method of Characteristics. In The International Conference on Mathematics and Computational Methods Applied to Nuclear Science and Engineering, Sun Valley, USA. May 5-9. ISBN: 978-0-89448-700-2, pp. 2759-2770. Retrieved from <https://www.osti.gov/biblio/22212914>
- Masson, V., Silin, N., Azcona, A., Delmastro, D., Garcia, J. C., and Mateos, D. (2008). Experimental Investigation on the Heat Transfer Characteristics of a Minichannel in Transition Flow. In Proceedings of the 16th International Conference on Nuclear Engineering, Orlando, Florida, USA. May 11-15. Vol. 3: Thermal Hydraulics; Instrumentation and Controls, pp. 443-448. doi:<https://doi.org/10.1115/ICONE16-48451>
- Masterson, R. (2020). *Nuclear reactor thermal hydraulics*. CRC Press is an imprint of Taylor & Francis Group, an Informa business, Boca Raton, FL 33487-2742, USA. Identifiers: LCCN 2018058907 | ISBN 9781138035379. Retrieved from <https://lcn.loc.gov/2018058907>
- Meijer, G. C., and Voorwinden, C. H. (1991). A novel BIMOS signal processor for Pt 100 temperature sensors with microcontroller interfacing. *Sensors and Actuators A: Physical, Vol. 27*(1), pp. 613-620. doi:[https://doi.org/10.1016/0924-4247\(91\)87059-C](https://doi.org/10.1016/0924-4247(91)87059-C)
- Meulekamp, R., and van der Marck, S. (2006). Calculating the Effective Delayed Neutron Fraction with Monte Carlo. *Nuclear Science and Engineering, Vol. 152*(2), pp. 142-148. doi:<https://doi.org/10.13182/NSE03-107>
- Moorthi, A., Kumar Sharma, A., and Velusamy, K. (2018). A review of sub-channel thermal hydraulic codes for nuclear reactor core and future directions. *Nuclear Engineering and Design, Vol. 332*, pp. 329-344. doi:<https://doi.org/10.1016/j.nucengdes.2018.03.012>
- Motalab, M., Mahmood, M., Khan, M., Badrun, N., Lyric, Z., and Altaf, M. (2014). Benchmark analysis of SPERT-IV reactor with Monte Carlo code MVP. *Annals of Nuclear Energy, Vol. 65*, pp. 365-369. doi:<https://doi.org/10.1016/j.anucene.2013.11.043>
- Nasir, R., Kamram Butt, M., Mirza, S., and Mirza, N. (2015). Simultaneous multiple reactivity insertions in a typical MTR-type research reactor having U3Si2-Al fuel. *Annals of Nuclear Energy, Vol. 85*, pp. 869-878. doi:<https://doi.org/10.1016/j.anucene.2015.07.003>

- Nelson, A., Kasam-Griffith, A., Atz, M., and Heidet, F. (2021). Performance of HALEU and HEU-Fueled Nuclear Thermal Propulsion Reactors. Technical Report ANL/NSE-20/55, 166537, Argonne National Lab. (ANL), Argonne, USA. doi:<https://doi.org/10.2172/1825887>
- Nhi-Dien, N., Kien-Cuong, N., Ton-Nghiem, H., Doan-Hai-Dang, V., and Hoai-Nam, T. (2020). Conceptual Design of a 10 MW Multipurpose Research Reactor Using VVR-KN Fuel. *Science and Technology of Nuclear Installations*, Vol. 2020, pp. 11. doi:<https://doi.org/10.1155/2020/7972827>
- Nimal, J., and Vergnaud, T. (1990). TRIPOLI: A general Monte Carlo code, present state and future prospects. *Progress in Nuclear Energy*, Vol. 24(1), pp. 195-200. doi:[https://doi.org/10.1016/0149-1970\(90\)90036-5](https://doi.org/10.1016/0149-1970(90)90036-5)
- Nogarin, M. (2016). Bolivia: The New Nuclear Research Center in El Alto. *atw - International Journal for Nuclear Power*, Vol. 61(5), pp. 297-300. Retrieved from <https://www.kernd.de/kernd-wAssets/docs/fachzeitschrift-atw/2016/>
- Olsher, R. (2006). A practical look at monte carlo variancereduction methods in radiation shielding. *Nuclear Engineering and Technology*, Vol. 28(3), pp. 225-230. Retrieved from <https://koreascience.kr/article/JAKO200603018219944.page>
- Osipovich, S., Kuatbekov, R., Lukichov, V., Sokolov, S., Tretiyakov, I., and Trushkin, V. (2011). A New Generation of Research Reactors Fuelled with LEU. In The International Conference on Research Reactors: Safe Management and Effective Utilization; Rabat, Morocco. November 14-18. ISSN 1991-2374, pp. 15. Retrieved from http://inis.iaea.org/search/search.aspx?orig_q=RN:44019521
- Pecchia, M., Kotev, G., Parisi, C., and D'Auria, F. (2012). MOx benchmark calculations by deterministic and Monte Carlo codes. *Nuclear Engineering and Design*, Vol. 246, pp. 63-68. doi:<https://doi.org/10.1016/j.nucengdes.2011.10.005>
- Primm, T., Maldonado, G., and Chandler, D. (2008). Validating MCNP for LEU Fuel Design via Power Distribution Comparisons. Technical Report ORNL/TM-2008/126, NN9002000; MDGA518; TRN: US0807267; Oak Ridge National Lab. (ORNL), Oak Ridge, USA. doi:<https://doi.org/10.2172/940800>
- Prinja, A., and Larsen, E. (2010). *General Principles of Neutron Transport* (Vol. 1). (D. G. Cacuci, Ed.) Springer US, Handbook of Nuclear Engineering, Boston, USA, ISBN: 978-0-387-98130-7. doi:https://doi.org/10.1007/978-0-387-98149-9_5
- Rearden, B., and Jessee, M. (2016). SCALE Code System. Technical Report ORNL/TM-2005/39 Version 6.2, Oak Ridge National Lab. (ORNL), Oak Ridge, USA. doi:<https://doi.org/10.2172/1424483>
- Rhodes, J., Smith, K., and Lee, D. (2006). CASMO-5 Development and Applications. In PHYSOR-2006: American Nuclear Society's Topical Meeting on Reactor Physics - Advances in Nuclear Analysis and Simulation, Vancouver, Canada, September 10-14. ISBN 0-89448-697-7, pp. 11. Retrieved from <https://www.osti.gov/biblio/22039682>

- Rohsenow, W., Hartnett, J., and Cho, Y. (1998). *Handbook of heat transfer*. The McGraw-Hill Companies, Inc, New York, USA. ISBN: 0-07-053555-8. Retrieved from <http://160592857366.free.fr/joe/ebooks/Mechanical%20Engineering%20Books%20Collection/H-EAT%20TRANSFER/handbook%20of%20HeatTransfer.pdf>
- Rowe, D. (1973). COBRA IIIC: digital computer program for steady state and transient thermal-hydraulic analysis of rod bundle nuclear fuel elements. Technical Report BNWL-1695/NSA-28-007436, Battelle Pacific Northwest Labs., Richland, Wash. WA, USA. doi:<https://doi.org/10.2172/4480166>
- Russell, B., Luckow, W., and Gomberg, H. (1956). The Ford nuclear reactor and phoenix memorial laboratory. *Chem. Eng. Progr., Vol. 52(19)*, pp. 9-13. Retrieved from http://um2017.org/Phoenix_Project_files/The%20Ford%20Nuclear%20Reactor%20%26%20The%20Phoenix%20Memorial%20Project.pdf
- Salko Jr, R., Avramova, M., Wysocki, A., Toptan, A., Hu, J., Porter, N., . . . Kelly, J. (2019). CTF 4.0 Theory Manual. Technical Report ORNL/TM-2019/1145, Oak Ridge National Lab. (ORNL), Oak Ridge, USA. doi:<https://doi.org/10.2172/1550750>
- Sánchez, F., Cintas, A., and Blaumann, H. (2014). RA-10: Argentinean Multipurpose Reactor. *Neutron News, Vol. 25(4)*, pp. 6-8. doi:<https://doi.org/10.1080/10448632.2014.955416>
- Sánchez, V., Imke, U., and Gomez, R. (2010). SUBCHANFLOW: a thermal hydraulic sub-channel program to analyse fuel rod bundles and reactor cores. In The Proceedings of the 17th Pacific Basin Nuclear Conference. Nuclear energy: an environmentally sound option, Cancun, Q.R. Mexico. October 24-30. ISBN 978-607-95174-1-0, pp. 18. Retrieved from <https://www.osti.gov/etdeweb/biblio/21420219>
- Schaaf, B., Broekhaus, K., Linden, N., and Wijtsma, F. (2011). The Infrastructure for Pallas, the New Nuclear Reactor in the Netherlands. In European Research Reactor Conference, Rome, Italy. ISBN 978-92-95064-11-9, pp. 21-25. Retrieved from http://inis.iaea.org/search/search.aspx?orig_q=RN:42043845
- Silin, N., Masson, V., and García, J. C. (2010). Convection in a rectangular channel with a flow of water in laminar-turbulent transition with high heat fluxes. *Latin American applied research, Vol. 40(2)*, pp. 125-130. Retrieved from <http://ref.scielo.org/r8z98f>
- Silin, N., Masson, V., and Marino, R. (2012). Heat Transfer in a Short Parallel-Plate Channel in the Transition Regime. *Experimental Heat Transfer, Vol. 25(1)*, pp. 12-29. doi:<https://doi.org/10.1080/08916152.2011.556312>
- Silin, N., Vertullo, A., Masson, V., and Hilal, R. (2009). Thermohydraulic calculations in rectangular channels for RA-6 type reactors with transition regime. In The Annual meeting of the Argentine Association of Nuclear Technology: Nuclear energy in the present world, Buenos Aires, Argentina. November 16-20. INIS-AR-V--269, pp. 13. Retrieved from http://inis.iaea.org/search/search.aspx?orig_q=RN:42004365

- Sjenitzer, B. (2013). The Dynamic Monte Carlo Method for Transient Analysis of Nuclear Reactors. PhD thesis, Delft University of Technology, Delft, Netherlands. ISBN 978-90-8891-657-1. doi:<https://doi.org/10.4233/uuid:6a4bfa4c-2d1f-4648-9698-6eb7ec7e2d11>
- Sjenitzer, B. L., and Hoogenboom, J. E. (2011). A Monte Carlo method for calculation of the dynamic behaviour of nuclear reactors. *Progress in Nuclear Science and Technology*, Vol. 49(28), pp. 716-721. doi:<http://dx.doi.org/10.15669/pnst.2.716>
- Slabbert, R. (2011). Thermal-hydraulics simulation of a benchmark case for a typical Materials Test Reactor Using Flownex. Master thesis, at the Potchefstroom Campus of the North-West University, South Africa. Retrieved from <https://repository.nwu.ac.za/handle/10394/7575?show=full>
- Smith, K., and Forget, B. (2013). In The International Conference on Mathematics and Computational Methods Applied to Nuclear Science and Engineering, Sun Valley, USA. May 5-9. ISBN 978-0-89448-700-2, pp. 1809-1825. Retrieved from <https://www.osti.gov/biblio/22212838>
- Soares, H., Aronne, I., Costa, A., Pereira, C., and Veloso, M. (2014). Analysis of Loss of Flow Events on Brazilian Multipurpose Reactor Using the Relap5 Code. *International Journal of Nuclear Energy*, Vol. 2014, pp. 12. doi:<https://doi.org/10.1155/2014/186189>
- Spano, A., and Miller, R. (1962). SPERT I Destructive Test Program Safety Analysis Report. Technical Report, NSA-17-001010, IDO-16790, Phillips Petroleum Co. Atomic Energy Div., Idaho Falls, Idaho. USA. doi:<https://doi.org/10.2172/4775396>
- Spurgeon, D. (1969). Preliminary desing studies for a high flux MIT reactor. Master Thesis, Massachusetts Institute of Technology, Monterey, California USA. Retrieved from <https://hdl.handle.net/10945/12868>
- Sudo, Y., Kaminaga, M., and Minazoe, K. (1990). Experimental study on the effects of channel gap size on mixed convection heat transfer characteristics in vertical rectangular channels heated from both sides. *Nuclear Engineering and Design*, Vol. 120(2), pp. 135-146. doi:[https://doi.org/10.1016/0029-5493\(90\)90368-8](https://doi.org/10.1016/0029-5493(90)90368-8)
- Sudo, Y., Miyata, K., Ikawa, H., and Kaminaga, M. (1985). Experimental Study of Differences in Single-Phase Forced-Convection Heat Transfer Characteristics between Upflow and Downflow for Narrow Rectangular Channel. *Journal of Nuclear Science and Technology*, Vol. 22(3), pp. 202-212. doi:<https://doi.org/10.1080/18811248.1985.9735648>
- Todreas, N., and Kazimi, M. (1990). *Nuclear Systems I Thermal Hydraulic Fundamentals* (Vol. 1). Taylor & Francis., Massachusetts, USA. ISBN: 1-56032-051-6. doi:<https://doi.org/10.1201/9781351030502>
- Umbehaun, P. (2016). Development of an Instrumented Fuel Assembly for the IEA-R1 Reseach Reactor. PhD Thesis, Nuclear and Energy Research Institute, São Paulo, Brazil. IPEN-CNEN/SP. doi: DOI: 10.11606/D.85.2016.tde-24102016-144026

- Umbehaun, P., Torres, W., Batista Souza, J., Yamaguchi, M., Teixeira e Silva, A., Navarro de Mesquita, R., . . . Alves de Andrade, D. (2018). Thermal Hydraulic Analysis Improvement for the IEA-R1 Research Reactor and Fuel Assembly Design Modification. *World Journal of Nuclear Science and Technology*, Vol. 8(2), pp. 54-69. doi:10.4236/wjnst.2018.82006
- Valtavirta, V., Hessian, M., and Leppänen, J. (2016). Delayed Neutron Emission Model for Time Dependent Simulations with the Serpent 2 Monte Carlo Code: First Results. In PHYSOR 2016: Unifying Theory and Experiments in the 21st Century American Nuclear Society (ANS), Sun Valley, USA. May 1-5. ISNS:978-0-89448-762-2, pp. 44 . Retrieved from <https://cris.vtt.fi/en/publications/delayed-neutron-emission-model-for-time-dependent-simulations-wit>
- Van Uffelen, P., Konings, R., Vitanza, C., and Tulenko, J. (2010). *Analysis of Reactor Fuel Rod behaviour* (Vol. 1). (D. G. Cacuci, Ed.) Springer US, Handbook of Nuclear Engineering, Boston, USA, ISBN: 978-0-387-98130-7. doi:<https://doi.org/10.1007/978-0-387-98149-9>
- Viitanen, T., and Leppänen, J. (2012). Explicit Treatment of Thermal Motion in Continuous-Energy Monte Carlo Tracking Routines. *Nuclear Science and Engineering*, Vol. 171(2), pp. 165-173. doi:<https://doi.org/10.13182/NSE11-36>
- Viitanen, T., and Leppänen, J. (2014). Target Motion Sampling Temperature Treatment Technique with Elevated Basis Cross-Section Temperatures. *Nuclear Science and Engineering*, Vol. 177, pp. 77-89. doi:<https://doi.org/10.13182/NSE13-37>
- Villarino, E., and Doval, A. (2011). INVAP's Research Reactor Designs. *Science and Technology of Nuclear Installations*, Vol. 2011, pp. 6. doi:<https://doi.org/10.1155/2011/490391>
- Wemple, C., and Simeonov, T. (2017). Advances in HELIOS2 nuclear data library. *Kerntechnik*, Vol. 82(4), pp. 445-447. doi:<https://doi.org/10.3139/124.110811>
- Werner, C., Bull, J., Solomon, C., B. Brown, F., McKinney, G., Rising, M., . . . Cox, L. (2018). MCNP Version 6.2 Release Notes. Technical Report 1419730, LA-UR-18-20808, AC52-06NA25396. Los Alamos National Lab. (LANL), Los Alamos, NM USA. doi:<https://doi.org/10.2172/1419730>
- Wheeler, C., Stewart, C., Cena, R., Rowe, D., and Sutey, A. M. (1976). COBRA-IV-I: an interim version of COBRA for thermal-hydraulic analysis of rod bundle nuclear fuel elements and cores. Technical Report BNWL-1962/TRN: 76-018139, Battelle Pacific Northwest Labs., Richland, Wash. (USA). doi:<https://doi.org/10.2172/7359476>
- Woodcock, E., and Murphy, T. (1965). Techniques Used in the GEM Code for Monte Carlo Neutronics Calculations in Reactors and Other Systems of Complex Geometry. In Proceedings of the Conference on Applications of Computing Methods to Reactor Problems. In Proceedings of the Conference on the Application of Computing Methods to Reactor Problems. Argonne National Lab., ILL. USA. May 17-19. ANL-7050, pp. 557-579 . Retrieved from <https://ntrl.ntis.gov/NTRL/dashboard/searchResults/titleDetail/ANL7050.xhtml>
- Woodruff, W. L. (2017). A Kinetics and Thermal-Hydraulics Capability for the Analysis of Research Reactors. *Nuclear Technology*, Vol. 64(2), pp. 196-206. doi:<https://doi.org/10.13182/NT84-A33342>

- Woolstenhulme, N. E., Wachs, D. N., Meyer, M. K., Glunz, H. W., and Nielson, R. B. (2012). Using PARET Code for Analyzing Research Reactor Cores with Two Fuel Geometries. In *The International Meeting on Reduced Enrichment for Research and Test Reactor*, Warsaw, Poland. October 14-17, pp. 1-6. Paper ID: S8-P1. Retrieved from <https://www.rertr.anl.gov/RERTR34/index.shtml>
- X-5 Team. (2008). *MCNP- A General Monte Carlo N-Particle Transport Code*. Version 5 Volume I: Overview and Theory. Number LA-UR-03-1987 in Nuclear Energy Series. Los Alamos National Security, LLC.
- Yoo, Y., Hwang, D., and Sohn, D. (1999). Development of a Subchannel Analysis Code MATRA Applicable to PWRs and ALWRs. *Journal of the Korean Nuclear Society*, Vol. 31(3), pp. 314-327. Retrieved from <https://koreascience.kr/article/JAKO199911921632938.page>
- Zhang, K., Campos Muñoz, A., and Sanchez-Espinoza, V. (2021). Development and verification of the coupled thermal–hydraulic code – TRACE/SCF based on the ICoCo interface and the SALOME platform. *Annals of Nuclear Energy*, Vol. 155, pp. 108169. doi:<https://doi.org/10.1016/j.anucene.2021.108169>
- Zheng, L., Wang, W., and Wang, K. (2020). On-the-fly temperature-dependent cross section treatment under extremes in RMC code. *EPJ Web Conf.*, Vol. 239, pp. 22009. doi:<https://doi.org/10.1051/epjconf/202023922009>
- Zuccaro-Labelarte, G., and Fagerholm, R. (1996). Safeguards at research reactors: Current practices, future directions. *International Atomic Energy Agency Bulletin*, Vol. 38(4), pp. 20-24. Retrieved from <https://www.osti.gov/etdeweb/biblio/458058>

Appendix A Implementation of the conduction solver in SCF

For the implementation of heat conduction, the routines *heat_pin.f90*, *heat_input.f90* and *powinit.f90* are extended. Figure A.1 shows the flow chart of the *heat_pin.f90* routine, which calculates the surface heat flux in each rod as a function of reactor power.

This routine allows obtaining the internal temperatures of the rods (*Tem_rod*) and plates (*Tem_plate*) using a built-in solver for heat conduction based on the Thomas algorithm.

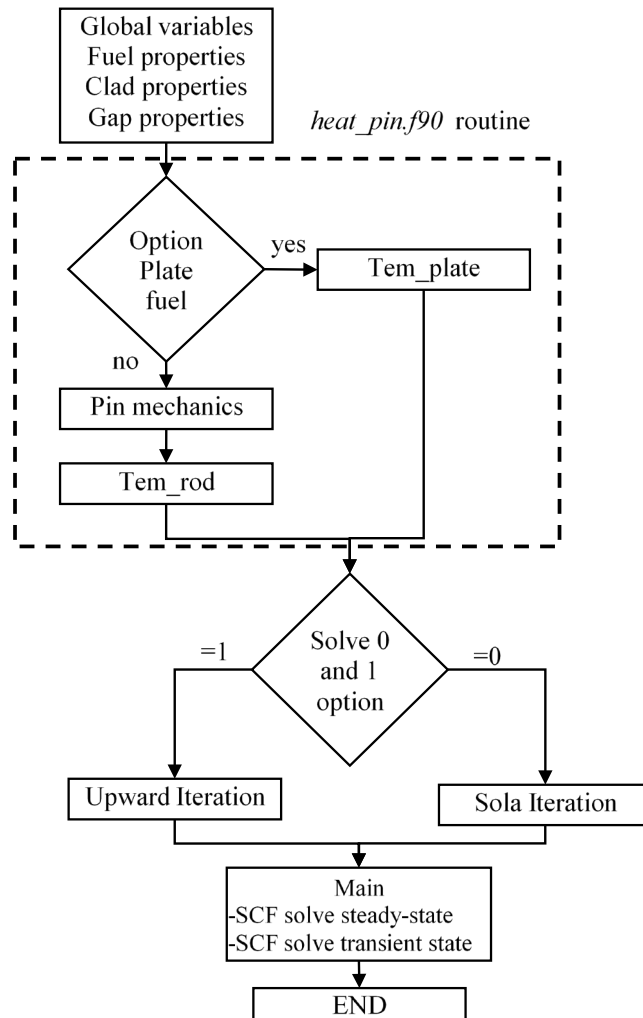


Figure A.1: Flowchart of Subchanflow code corresponding to *heat_pin.f90*.

On the other hand, Figure A.2 shows the flowchart for the *heat_input.f90* routine which calculates the linear heat input to each channel using the surface heat flux. This routine uses the global variables declared earlier. When the analysis option (rods or plates) is specified, the sub-routine calculates the fuel perimeter and subsequently the linear heat input.

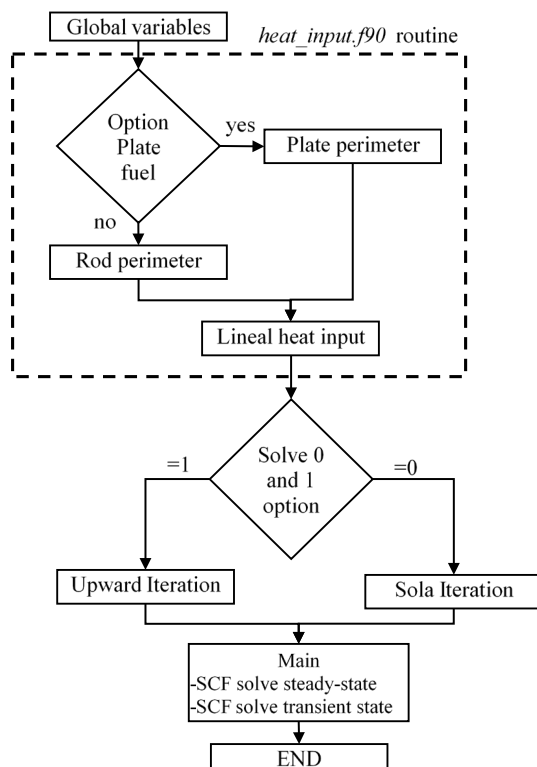


Figure A.2: Flowchart of Subchanflow code corresponding to *heat_input.f90*.

Finally, Figure A.3 shows the flowchart for the routine *powinit.f90*, which initiates the call to the global variables and utilities for the calculation of fuel used to calculate the spatial power distribution.

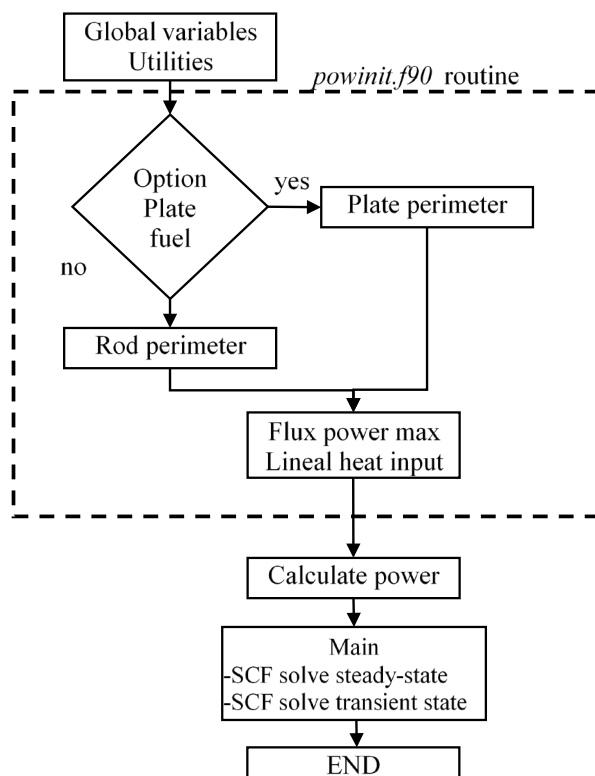


Figure A.3: Flowchart for the *powinit.f90* routine.

Appendix B Description of the SPERT IV reactor elements

B.1 Geometric details of the SPERT IV reactor components

To reduce the metrological differences when converting from imperial to metric units, a 3D model has been created using the Autodesk Inventor program (Almachi, et al., 2022b). Figure B.1 shows the dimensions of the 6061-T6 aluminum bottom grid in mm. This grid contains 81 internal cavities and houses the active core shown in Figure 8.3.

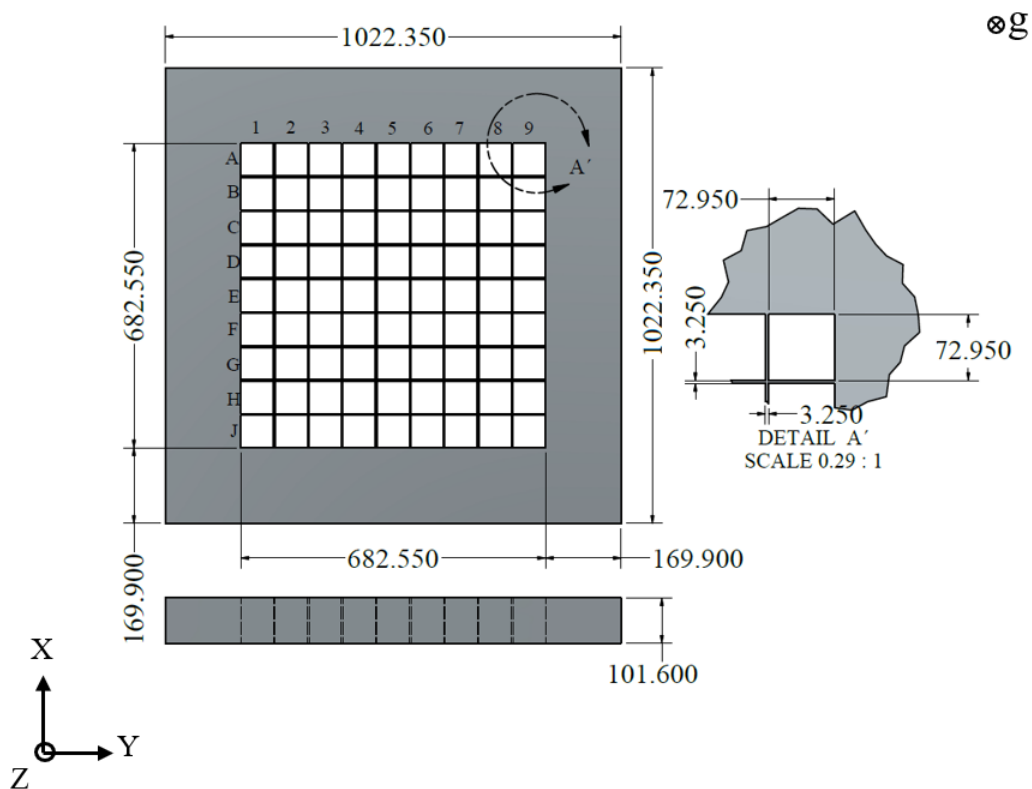


Figure B.1: Grid plate and lattice spacing for SPERT IV reactor, dimensions in mm and are symmetrical in x-y directions.

Figure B.2 shows an aluminum box housing the standard, control, and transient fuel assemblies. This box has been fabricated using aluminum to the same specifications as the grid. In the lower radial section of the box, it can be seen that the dimensions are smaller compared to the upper radial section, creating a sort of "flange" that allows the box to fit inside the grid. All dimensions of the box are symmetrical in the x and y directions and are given in millimeters.

Figure B.3 shows a front view of a fuel plate in the x - z plane. The active region where the fuel is distributed has a height of 609.00 mm and a width of 62.23 mm. The thickness of the fuel is 0.5080 mm. The entire cladding is made of 6061-T6 aluminum.

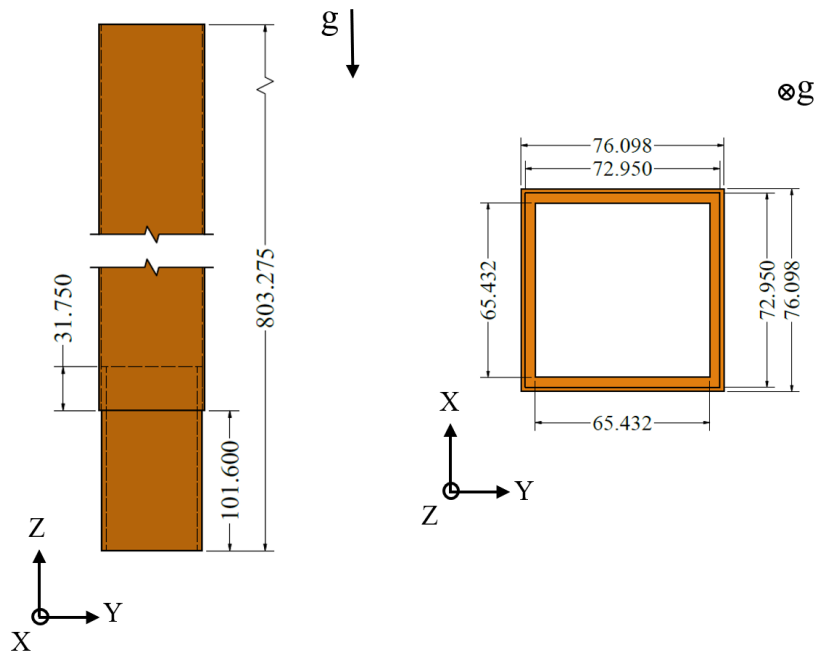


Figure B.2: Axial and radial view of the aluminum box that houses the fuel assemblies, all dimensions are in mm.

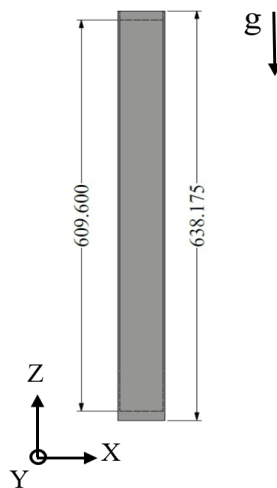


Figure B.3. Front view of a fuel plate, dimensions in mm.

The dimensions of the standard and control fuel assemblies are shown in the upper part of Figure B.4. The standard fuel assembly consists of 12 plates spaced 4,547 mm apart. The black area represents the 93% highly enriched uranium fuel. Figure B.4. also shows the control fuel assembly, which is located in the lower part. It can be seen that it consists of 4 central plates and one plate at each end. The missing plates in the center of the assembly allow for the inclusion of a rectangular aluminum guide in which the neutron absorbing material, represented by the red color, moves axially. The transient fuel assembly has similar features to the control assembly. Both the cladding surrounding the nuclear fuel and the lateral support plates are made of aluminum.

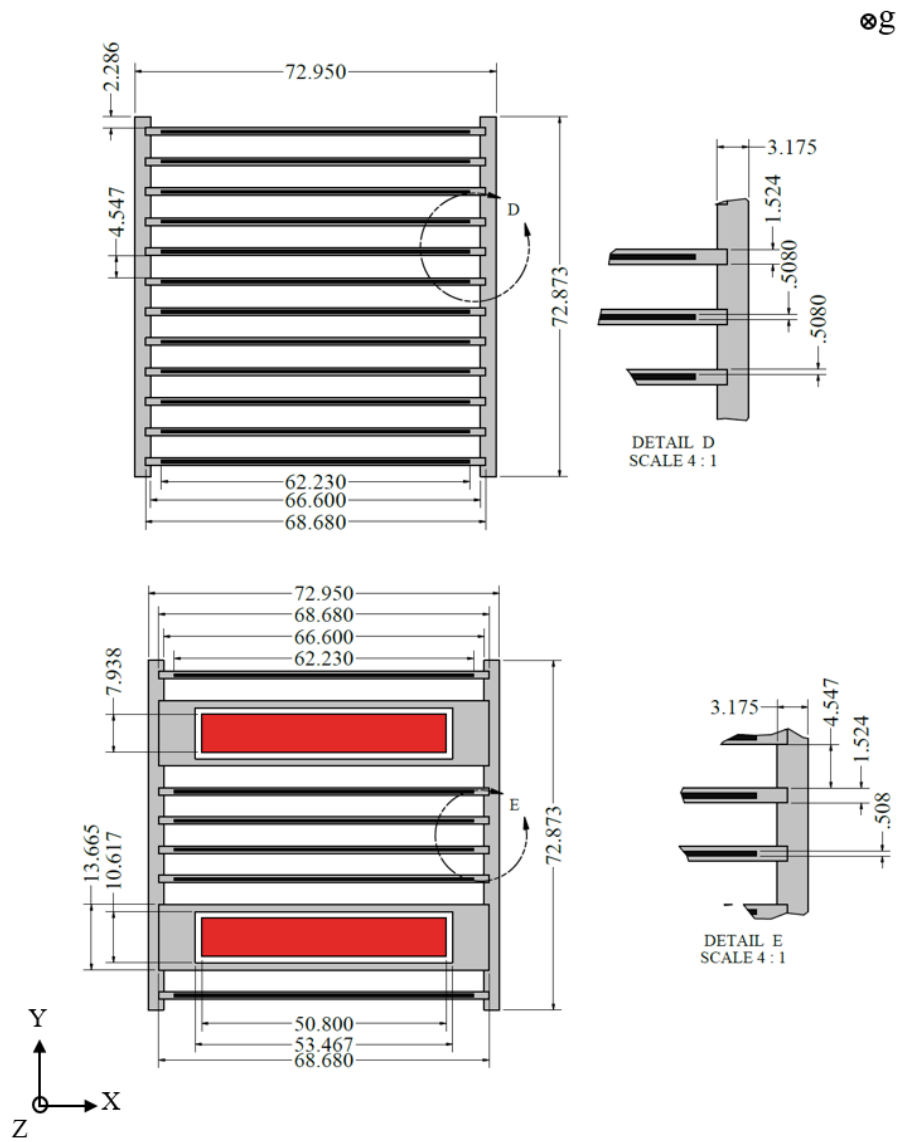


Figure B.4: Top view of the standard fuel assembly (top) and control/transient (bottom), all dimensions are in mm.

B.2 Radial numbering of plates and cooling channels for SPERT-IV reactor

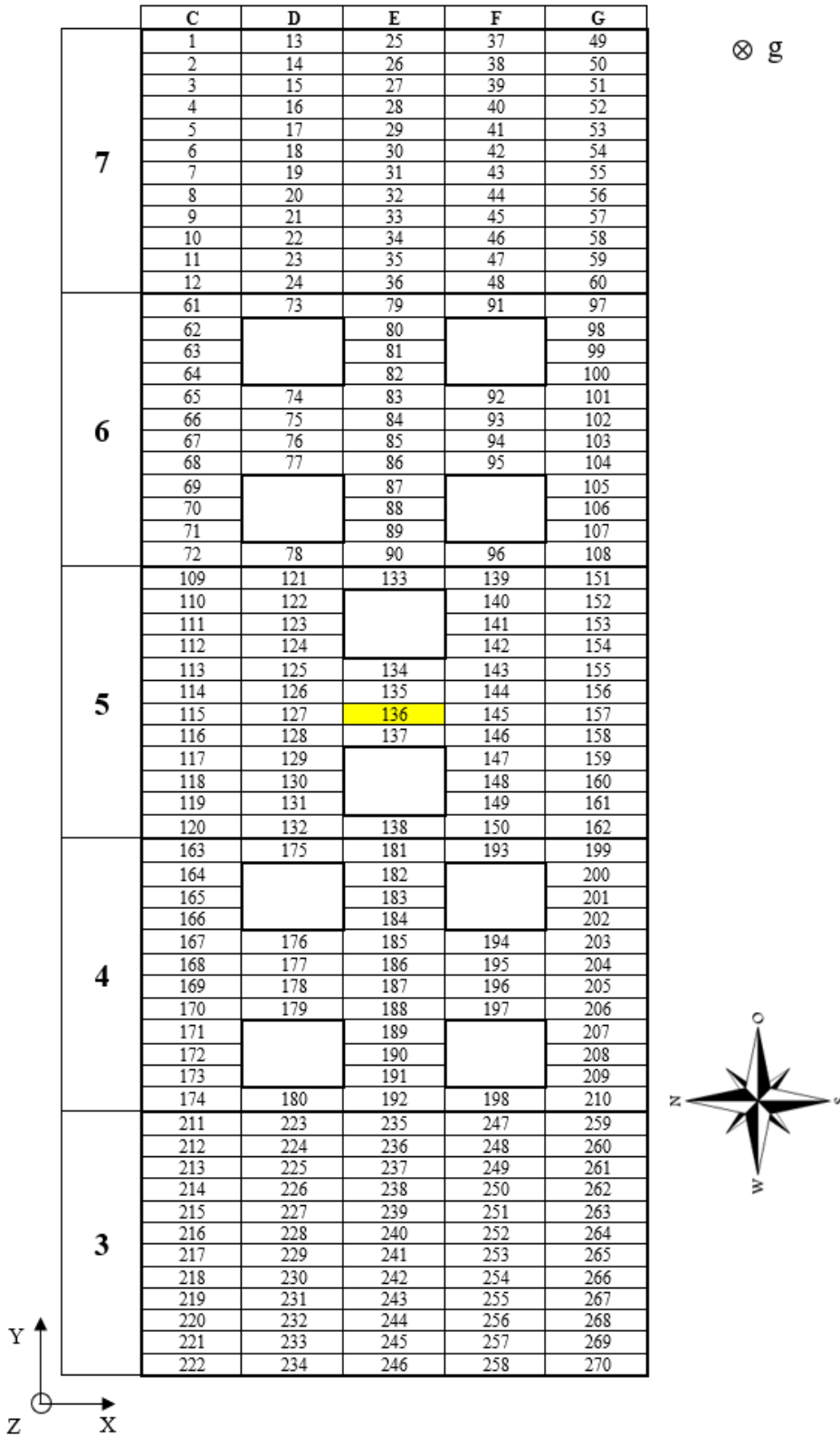


Figure B.5: Identification of plates and cooling channels, for remapping between Serpent 2 and Subchanflow, SPERT-IV reactor.

Appendix C Additional data for the IAEA 10-MW reactor

C.1 Description of the benchmark IAEA 10 MW

In the current work the IAEA 10MW core is considered. The core configuration consists of 6x5 grid containing 21 Standard Fuel Assemblies and 4 Control Fuel Assemblies. The core is reflected by graphite on two opposite sides and surrounded by light water. In the axial all fuel assemblies (SFA and CFA) are reflected in their edges by 15 cm of Al-H₂O with 20% Al and 80% of H₂O, (Woolstenhulme, et al., 2012), (Ardaneh and Zaferanlouei, 2013b), (Khedr K. , 2013), (Ardaneh and Zaferanlouei, 2013a), (Woodruff, 2017). The SFA has 23 plates and CFA has 17 plates. The Control Fuel Assemblies have a special region for the four-fork type absorber (see Figure C.1 and Figure C.2). The main specifications are summary in Table C.1 and have been obtained from (IAEA, 1980), pg. 514.

Table C.1: Benchmark specification.

Density clad aluminum	2.7 g/cm ³
Density graphite element:	1.7 g/cm ³
$UAl_x - Al$ fuel, HEU	Enrichment 93 wt. % ²³⁵ U, 280g ²³⁵ U per fuel element 21 wt. % of uranium in the $UAl_x - Al$
$UAl_x - Al$ fuel, LEU	Enrichment 20 wt. % ²³⁵ U, 390g ²³⁵ U per fuel element 72 wt. % of uranium in the $UAl_x - Al$
Total power	10 MW _{th}
Water temperature	20°C
Fuel temperature	20°C
Pressure at the core height	1.7 bar

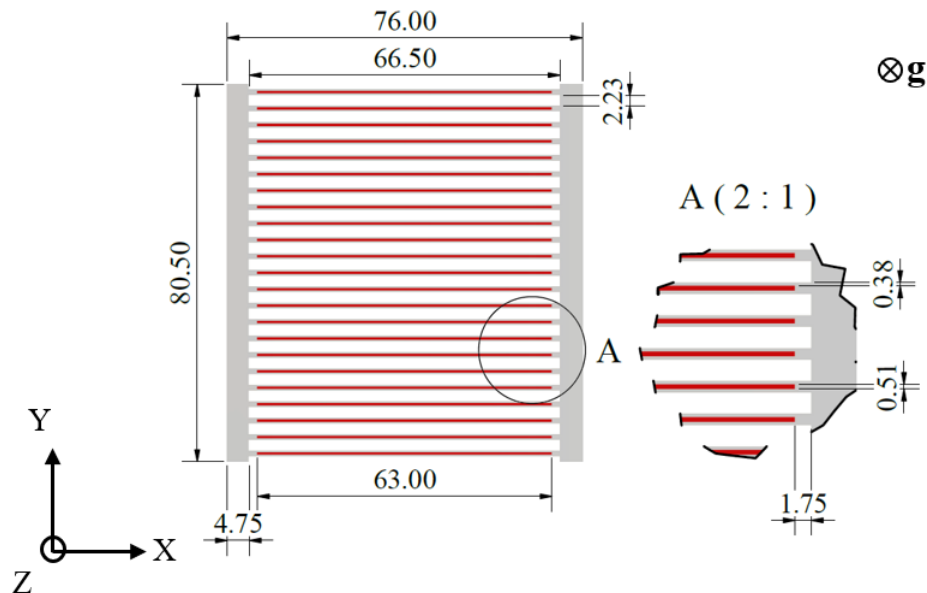


Figure C.1: Standard fuel assembly, dimensions in mm.

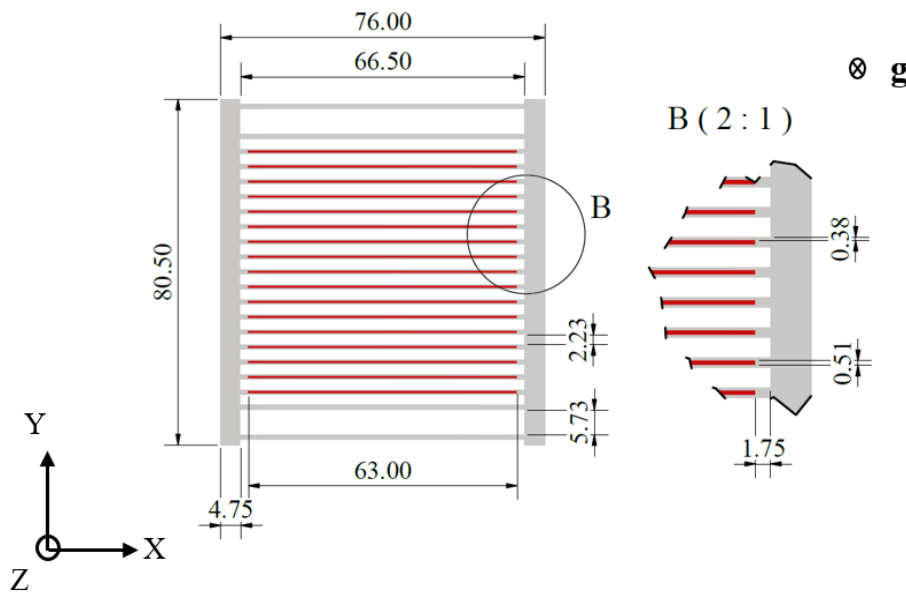


Figure C.2: Control fuel assembly, dimensions in mm.

The core configuration for High Enrichment of Uranium (HEU), Low Enrichment of Uranium (LEU) for the Beginning of Life (BOL) as a function of ^{235}U depletion is showed in Figure 9.3. The atomic density for HEU-BOL and LEU-BOL have been taken from the work presented by (Bousbia-Salah, et al., 2008) which presents a good agreement with those presented in Appendix F of (IAEA, 1980).

C.2 Serpent 2 modeling results

The Serpent 2 calculation are performed with 20 inactive cycles followed by 200 active cycles, each consisting of 150,000 histories and the source neutron, additionally the library ENDF/B-VIII has been used. The energy is considered as the following:

- Thermal group from 0 eV to 0.625 eV,
- epithermal group from 0.625 eV to 5.531 keV,
- fast group up to 5.531 keV.

k_{eff} results

Table C.2 shows the K_{eff} values when the ENDF/B-VIII (293 K) libraries are used. The values calculated by MCNP 5 are different from those calculated with Serpent 2, one of the reasons is the type of library used (ENDFBVII at 300 K), apparently (Bousbia-Salah, et al., 2008) ignores this detail even though the benchmark analyzed should be at 293 K.

Table C.2: Comparison of k_{eff} calculated by different code and library (MCNP5/Serpent2).

Cross sections	ENDF/B-VI (300 K)	ENDF/B-VIII (294 K)	Diff
Cases	MCNP5	Serpent 2	pcm
HEU Fresh	1.18962	1.18691	192
HEU BOL	1.05768	1.05588	161
LEU Fresh	1.17238	1.16959	203

Table C.3 shows a complementary comparison, the values calculated by (Chaudri and Mirza, 2015) have been made using OpenMC with a modified ENDF/B-VII.1 library at 293 K. On this occasion it is observed that the pcm values show in Table C.3 are bigger that Table C.2.

Table C.3: Comparison of K_{eff} calculated by different code and library (OpenMC/Serpent2).

Cross sections	NDF/B-VII.1 (293.6 K)	ENDF/B-VIII (294 K)	Diff
Cases	OpenMC *	Serpent 2	pcm
HEU Fresh	1.19382	1.18691	488
HEU BOL	1.06094	1.05588	452
LEU Fresh	1.15494	1.16959	-1085
LEU BOL	1.05916	1.05407	456

* Axial reflector of graphite.

Flux distribution results

An important part of research reactor analysis is the flux distribution. Serpent 2 allows to obtain the thermal flux, fast flux and epithermal flux. The flux is normalized by the mesh volume and the mesh is created according the benchmark specifications, 51 intervals in the x-direction and 56 in the y-directions (Chaudri and Mirza, 2015). The results presented in, Figure C.3, Figure C.4, Figure C.5, and Figure C.6 show good approximation with those presented by ANL (DIF2D) (IAEA, 1980) pages 461-470.

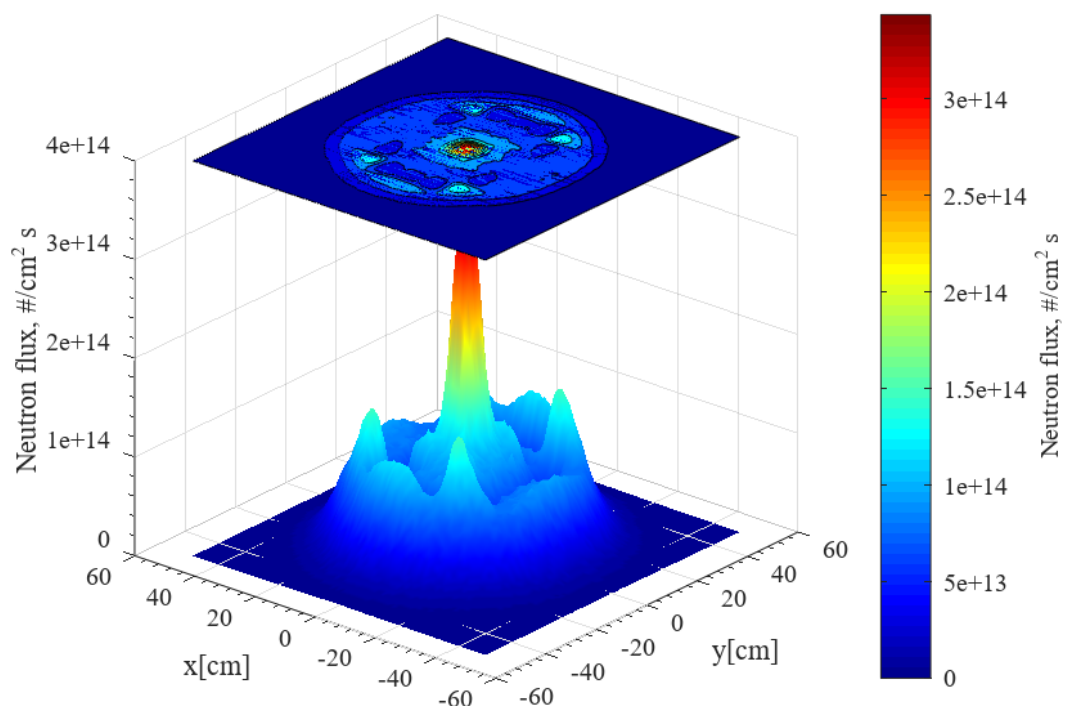


Figure C.3: Mid-plane radial thermal flux distribution HEUBOL core.

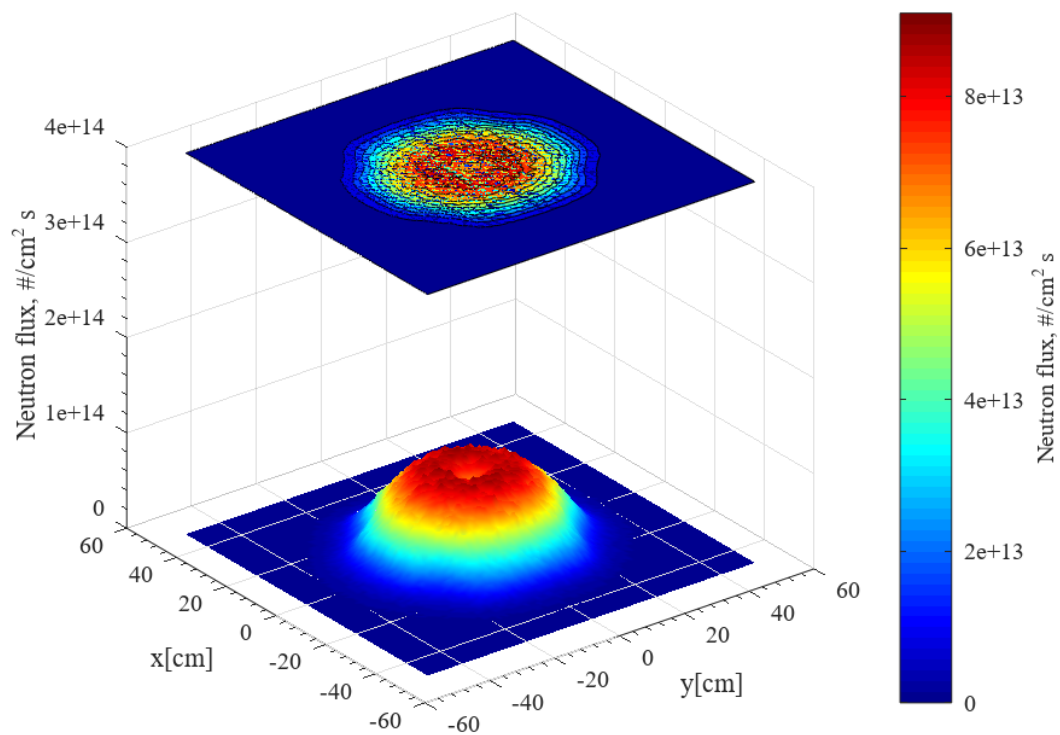


Figure C.4: Mid-plane radial epithermal flux distribution HEUBOL core.

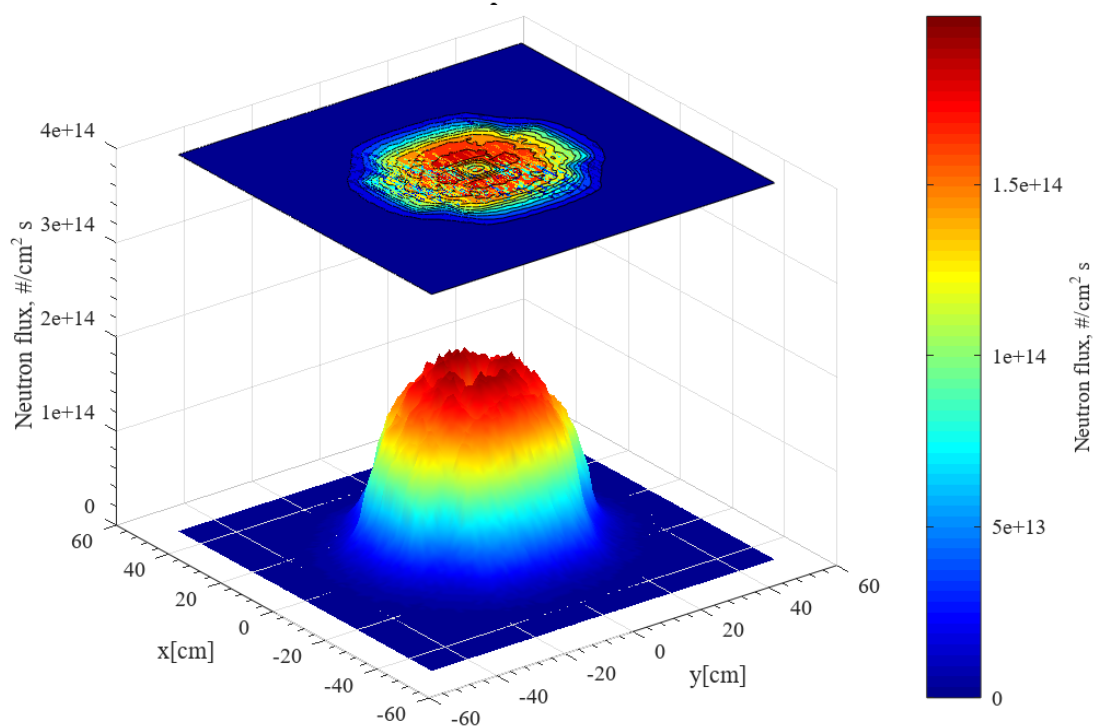


Figure C.5: Mid-plane radial fast flux distribution HEUBOL core.

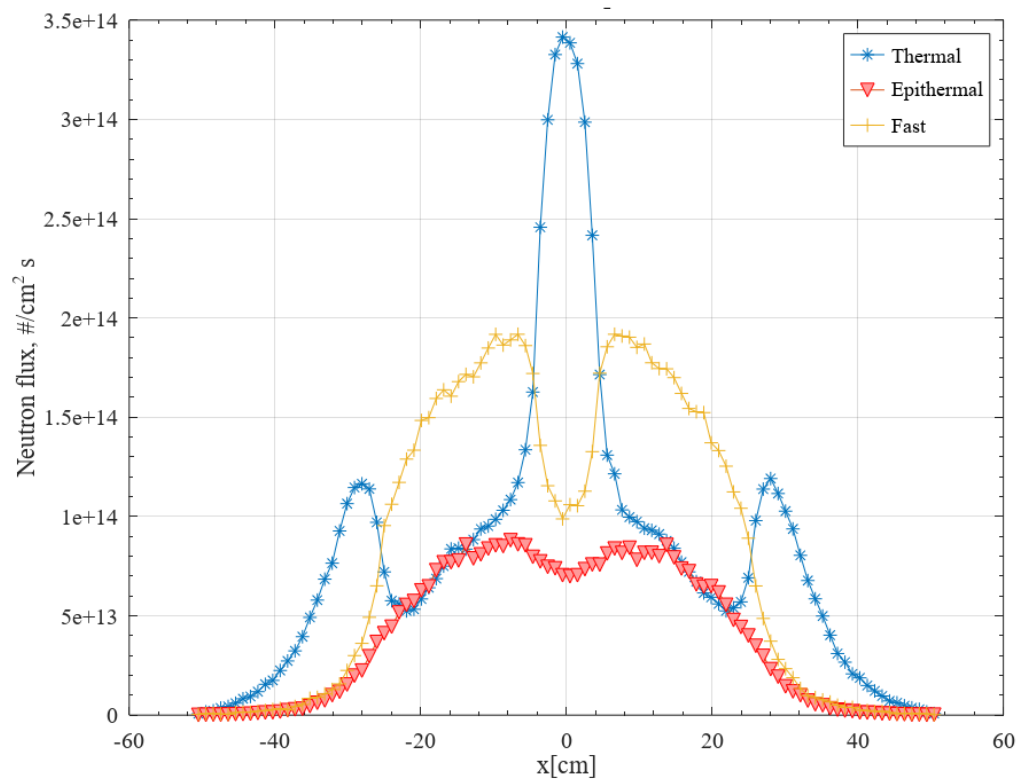


Figure C.6: Neutron fluxes along x-direction to HEUBOL.

C.3 Radial numbering of plates and cooling channels for IAEA 10 MW reactor

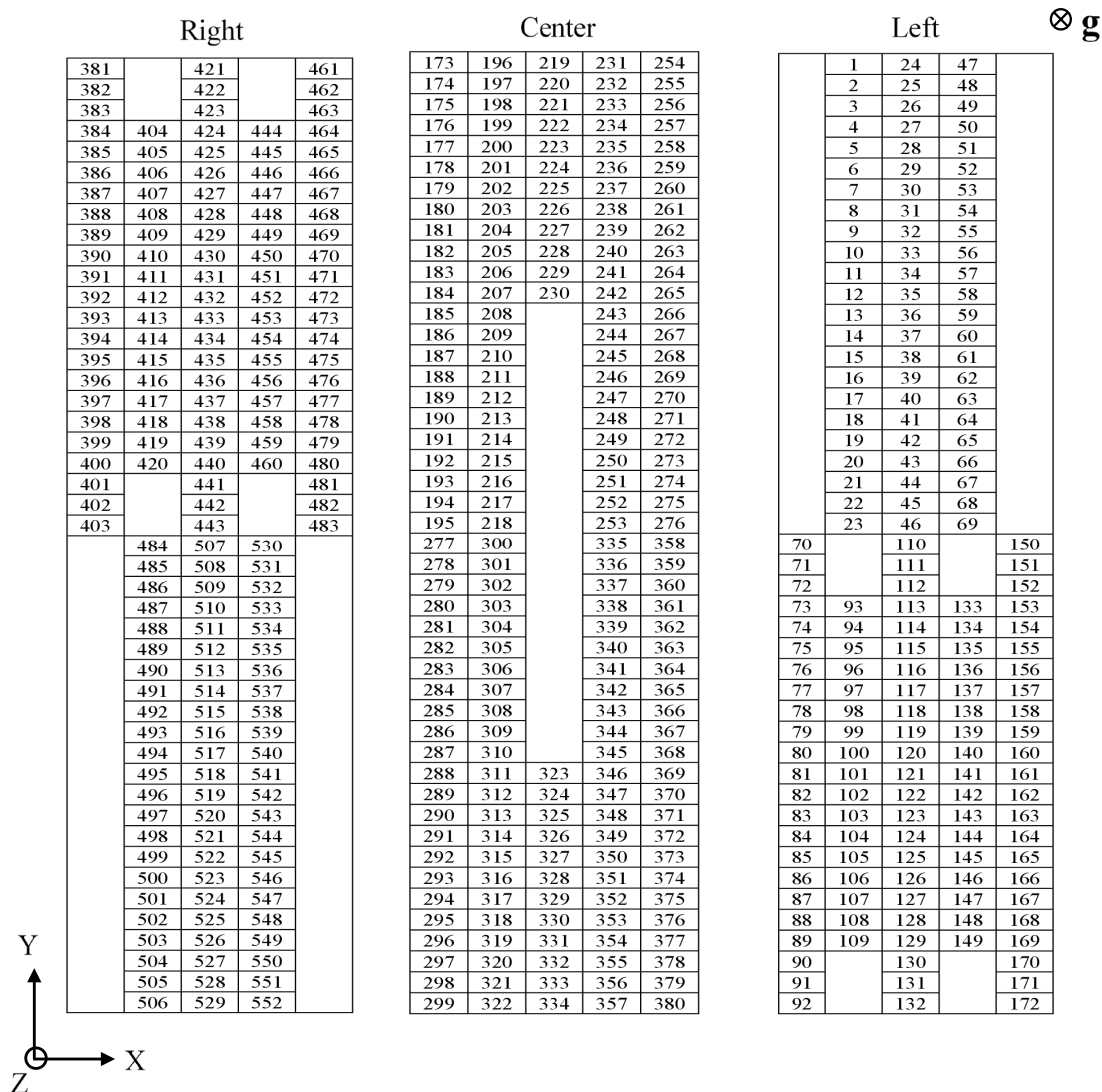


Figure C.7: Identification of plates and cooling channels, for remapping between Serpent 2 and Subchanflow, IAEA 10 MW benchmark reactor.